

LITHIUM INTERCALATION IN B_zC_{1-z} SOLID SOLUTIONS

by

Brian Way
B.Sc., Simon Fraser University, 1991

**THESIS SUBMITTED IN PARTIAL FULFILLMENT OF
THE REQUIREMENTS FOR THE DEGREE OF
DOCTOR OF PHILOSOPHY**

in the Department
of
Physics

© Brian Way 1995
SIMON FRASER UNIVERSITY
September 1995

All rights reserved. This work may not be
reproduced in whole or in part, by photocopy
or other means, without permission of the author.

Approval

Name: Brian Michael Way
Degree: Doctor of Philosophy
Title of thesis: Lithium Intercalation in B_2C_{1-z} Solid Solutions

Examining Committee:

Chair: Dr. Robert Frindt

Dr. Jeffrey Dahn
Senior Supervisor

~~Dr. John Cochran~~

Dr. Simon Watkins

~~Dr. George Kirzenow~~
Internal Examiner

~~Dr. Manfred Jericho~~
External Examiner
Department of Physics
Dalhousie University

Date Approved:

September 8, 1995

PARTIAL COPYRIGHT LICENSE

I hereby grant to Simon Fraser University the right to lend my thesis, project or extended essay (the title of which is shown below) to users of the Simon Fraser University Library, and to make partial or single copies only for such users or in response to a request from the library of any other university, or other educational institution, on its own behalf or for one of its users. I further agree that permission for multiple copying of this work for scholarly purposes may be granted by me or the Dean of Graduate Studies. It is understood that copying or publication of this work for financial gain shall not be allowed without my written permission.

Title of Thesis/Project/Extended Essay

Lithium Intercalation in BzCl-z Solid Solutions.

Author: _____
(signature)

Brian M Way

(name)

15 September 1995

(date)

Abstract

A series of B_zC_{1-z} solid solution films with $0 \leq z \leq 0.17$ were synthesized by chemical vapor deposition (CVD) from benzene and boron trichloride. The boron concentrations were measured by means of Auger Electron Spectroscopy of the films. The structure was determined using standard and grazing incidence X-ray diffraction to be a disordered graphite, with the degree of disorder decreasing with increasing boron concentration. Using synchrotron radiation, measurements of the near-edge X-ray absorption of the carbon and boron 1s edges as a function of the angle between the photon beam and the substrate were made. The dependence of the absorption with angle at both edges suggests that the boron is substitutional in the graphite structure. Heat treatment of these materials resulted in phase separation into carbon and boron carbide, for temperatures greater than 1100°C.

$Li/Li_x(B_zC_{1-z})_6$ electrochemical cells were produced for the range of boron concentrations $0 \leq z \leq 0.17$. The voltage as a function of the concentration of intercalated lithium, x , and the reversible capacities of these cells were measured. These cells show an increased voltage for a given lithium concentration compared with a cell using a pure carbon electrode. In addition, all cells for $z > 0$ showed reversible capacities greater than Li/Li_xC_6 cells for carbons produced at the same temperature, and for $z > 0.10$ the capacities exceeded that of graphite.

We attempted to understand the voltage curves and capacities of these cells using a lattice gas model of intercalation, and solving in the mean field approximation. The future of

these materials as anodes in lithium-ion batteries is questionable, due to their high cost and non-optimum voltage characteristics. Nevertheless their study has helped lead to new classes of high capacity carbons.

Quotation

The storage battery is, in my opinion, a catch-penny, a sensation, a mechanism for swindling the public by stock companies. The storage battery is one of those peculiar things which appeal to the imagination, and no more perfect thing could be desired by stock swindlers than that very self-same thingJust as soon as a man gets working on the secondary battery it brings out his latent capacity for lying....Scientifically, storage is all right, but, commercially, as absolute a failure as one can image.

THOMAS EDISON in The Electrician (London) February 17, 1883, pp. 329-331 as quoted in Bottled Energy: Electrical Engineering and the Evolution of Chemical Energy Storage by Richard H. Schallenberg

Acknowledgments

I would first like to thank my supervisor, Jeff Dahn, for his constant guidance, interest and help throughout my time as a graduate student. Without his assistance and encouragement, I'm sure this thesis would have taken much longer to complete.

In the time that I have been a graduate student, the many students in Jeff's busy lab have made it an enjoyable experience. I would particularly like to thank Hang Shi, Alf Wilson, Oliver Schilling and Tao Zheng for useful discussions.

I would like to acknowledge the financial support of Simon Fraser University, the Natural Sciences and Engineering Research Council, the British Columbia Science Council and Moli Energy Ltd. (1990) of Maple Ridge, B.C.

On a more personal note, I cannot adequately express my gratitude to my brother, David Way, without whose generous gift, the completion of this thesis would have been impossible. Finally I would like to thank my wife, Toni, for her love, support, and patience throughout the long years required to complete a graduate degree.

Table of Contents

APPROVAL	ii
ABSTRACT	iii
QUOTATION.....	v
ACKNOWLEDGMENTS	vi
1. INTRODUCTION.....	1
2. INTERCALATION IN CARBONS.....	11
2.1 STRUCTURE OF CARBONS	11
2.1.1 <i>Structure of Graphite</i>	11
2.1.2 <i>Disordered Carbons</i>	12
2.2 INTERCALATION.....	15
2.2.1 <i>Rigid-Band model of Intercalation</i>	16
2.2.2 <i>Staging</i>	18
2.3 LITHIUM INTERCALATION IN CARBONS	19
2.3.1 <i>General Description of Lithium Intercalation in Graphite</i>	20
2.3.2 <i>Intercalation in Disordered Carbons</i>	21
3. EXPERIMENTAL - PART I: SYNTHESIS OF B_2C_{1-z}.....	24
3.1 PREVIOUS WORK ON SYNTHESIS OF B_2C_{1-z} SOLID SOLUTIONS	24
3.1.1 <i>Synthesis by Solid State Reaction</i>	24
3.1.2 <i>Synthesis by Chemical Vapor Deposition</i>	27
3.2 INTRODUCTION TO CHEMICAL VAPOR DEPOSITION.....	29
3.2.1 <i>Factors Affecting Deposition</i>	29
3.2.2 <i>Deposition of Carbon Compounds</i>	31
3.2.3 <i>Deposition of Boron Carbide</i>	31
3.3 APPARATUS	32
3.4 LOW PRESSURE SYNTHESIS	33
3.4.1 <i>General Deposition Method</i>	34
3.4.2 <i>Chemical Sources (Precursors)</i>	35
3.4.3 <i>Temperature</i>	36
3.4.4 <i>Substrates</i>	36
3.5 HIGH PRESSURE SYNTHESIS.....	37
3.6 TABLE OF MATERIALS DISCUSSED IN THESIS	38
4. EXPERIMENTAL - PART II: CHARACTERIZATION OF MATERIALS.....	40
4.1 DESCRIPTION OF TECHNIQUES AND EXPERIMENTAL METHODS	40
4.1.1 <i>X-ray diffraction</i>	40
4.1.2 <i>Chemical Composition Determination</i>	44
4.1.3 <i>X-ray Absorption Spectroscopy</i>	47
4.1.4 <i>Heat Treatment Study</i>	52
4.2 RESULTS AND DISCUSSION.....	53
4.2.1 <i>Films</i>	53
4.2.2 <i>Powder Samples</i>	66
4.2.3 <i>Heat Treatment Study</i>	71

5. EXPERIMENTAL - PART III: ELECTROCHEMICAL PROPERTIES OF $Li_x(B_2C_{1-z})_6$	77
5.1 INTRODUCTION TO ELECTROCHEMICAL METHODS	77
5.1.1 <i>Chemical Potential</i>	77
5.1.2 <i>Types of Experiments</i>	79
5.2 ELECTROCHEMICAL INTERCALATION IN CARBONACEOUS MATERIALS	82
5.2.1 <i>Electrochemical Intercalation of Li in Graphite</i>	82
5.2.2 <i>Electrochemical Intercalation in Disordered Carbons</i>	87
5.3 CELL CONSTRUCTION AND TESTING	88
5.3.1 <i>Electrode Fabrication</i>	88
5.3.2 <i>Cell Assembly</i>	89
5.3.3 <i>Cell Testing</i>	91
5.4 AS-DEPOSITED SAMPLES - RESULTS AND DISCUSSION.....	92
5.4.1 <i>Films</i>	92
5.4.2 <i>Powders</i>	93
5.5 IN-SITU DIFFRACTION	105
5.6 HEAT TREATED SAMPLES - RESULTS AND DISCUSSION	112
5.7 CONCLUSIONS.....	118
6. LATTICE GAS MODEL OF INTERCALATION	119
6.1 INTRODUCTION	119
6.1.1 <i>Thermodynamics of Intercalation</i>	119
6.1.2 <i>Lattice Gas Model Applied to Lithium Intercalation</i>	120
6.2 LATTICE GAS MODEL FOR LITHIUM INTERCALATION IN CARBON	120
6.2.1 <i>Mean Field Solution for Graphite</i>	120
6.2.2 <i>Mean Field Solution for Disordered Carbon</i>	124
6.2.3 <i>Mean Field Solution for B_2C_{1-z}</i>	128
6.2.4 <i>Mean Field Solution for BC_3</i>	135
7. RECENT ADVANCES IN CARBONACEOUS ANODES	138
7.1 THE EFFECT OF PHOSPHORUS, BORON, NITROGEN AND SILICON ON LITHIUM INTERCALATION IN CARBON	139
7.2 HIGH CAPACITY DISORDERED CARBONS	143
7.2.1 <i>Region 1:</i>	146
7.2.2 <i>Region 2:</i>	146
7.2.3 <i>Region 3:</i>	148
7.3 CONCLUSIONS.....	150
8. CONCLUSIONS	151
8.1 SUMMARY OF CONTRIBUTIONS OF THIS THESIS	151
8.2 FUTURE WORK	153
8.3 TECHNOLOGICAL APPLICATION OF B_2C_{1-z}	153
REFERENCES	156

List of Tables

<i>Table 1-1 Performance of AA-size cells for several existing rechargeable battery technologies.....</i>	<i>1</i>
<i>Table 3-1 Synthesis conditions of materials discussed in this thesis.</i>	<i>39</i>
<i>Table 4-1 Boron concentrations of B_2C_{1-x} powders as determined by laser-ablation-ICPMS.....</i>	<i>69</i>
<i>Table 4-2 Boron concentrations and diffraction results for materials discussed in this thesis. AES is Auger Electron Spectroscopy. Estimated boron concentrations were determined from Figure 4-11 and Figure 4-12.</i>	<i>76</i>

List of Figures

Figure 1-1 Binding energy of lithium in various lithium compounds.....	4
Figure 1-2 Schematic drawing of the discharge of a Lithium-Ion cell.....	6
Figure 1-3 Schematic drawing comparing the filling of the density of states for intercalated graphite and intercalated boron-substituted graphite, in the rigid band model.....	9
Figure 2-1 (a) single graphite layer (b) structure of 2H graphite (c) structure of 3R graphite.....	12
Figure 2-2 Schematic drawing of the organized (low strain) and unorganized regions in a low temperature carbon. L_a and L_c refer to the size of the regions which scatter X-rays coherently.....	13
Figure 2-3 The probabilities P , P_b , $1-P$, and $1-g$	14
Figure 2-4 Intercalation in a layered material.....	16
Figure 2-5 Rigid band model of intercalation.....	17
Figure 2-6 Staging phenomena in a layered material.....	18
Figure 2-7 Stage-2 in the Daumas-Herold domain model of staging.....	19
Figure 2-8 The single layer structure of LiC_6	20
Figure 2-9 Reversible capacity versus P for soft carbons heated above 2200°C , from reference 86.....	23
Figure 3-1 Boron-carbon phase diagram from reference 16.....	25
Figure 3-2 Variation of graphite a and c lattice constants with boron concentration from reference 16.....	26
Figure 3-3 Proposed single layer structure of BC_3 from reference 42. The unit cell is outlined by the dashed line.....	27
Figure 3-4 Proposed mechanism steps for deposition of B_2C_{1-2} from reference 45.....	28
Figure 3-5 Schematic drawing of CVD system.....	33
Figure 4-1 Geometry of grazing incidence diffraction.....	41
Figure 4-2 $1/e$ penetration depth versus angle of incidence for Cu K_α radiation incident on carbon. The solid line is given by Equation 4-3 and the dashed curve is $\Lambda = (\sin \alpha_{inc})/\mu$. The inset is a close up of the penetration depth below the critical angle.....	43
Figure 4-3 Schematic of KL_1L_2 auger process.....	45
Figure 4-4 Schematic drawing of the excitation of a core electron to an unoccupied state above the Fermi level.....	48
Figure 4-5 Drawing of the incidence of X-rays on an oriented carbon film.....	49
Figure 4-6 Relative orientation of incident beam, sample and microchannel plate detector.....	51
Figure 4-7 Auger electron spectrum, $dN/dE (E)$, for a B_2C_{1-2} film made at 900°C with 76% BCl_3 in the flow mixture.....	54
Figure 4-8 Stoichiometry of B_2C_{1-2} films as a function of BCl_3 volume percentage in the flow mixture.....	55

Figure 4-9 Grazing incidence diffraction pattern of a thin B_zC_{1-z} film on a quartz substrate, in the carbon (002) region. The top two patterns are shifted up by 400 and 800 counts, respectively, for clarity. The incident angle of the X-ray beam is listed by each curve.....	56
Figure 4-10 The (002) Bragg peak of B_zC_{1-z} samples made at 900°C. The numbers at the right, above each data set, are the percentage of BCl_3 in the gas flow. The data have been offset for clarity, from the bottom, by: 0, 250, 500, 950, 1200, 1450, 1700, 1950 and 2200.	57
Figure 4-11 (002) Layer spacing as a function of z in B_zC_{1-z}	58
Figure 4-12 Full width at half maximum of the (002) diffraction peak as a function of z in B_zC_{1-z} . The solid line is a guide to the eye.....	59
Figure 4-13 Rocking curve for the (002) Bragg peak of $B_{0.17}C_{0.83}$. The rocking angle, θ_R is 0° when the angles of the incident and diffracted rays with respect to the normal to the substrate are the same.....	60
Figure 4-14 Rocking curve for the (004) Bragg peak of $B_{0.17}C_{0.83}$	61
Figure 4-15 Carbon 1s X-ray absorption for (a) oriented graphite powder pressed on Cu tape and (b) a pure carbon film on a quartz substrate, made by CVD. The data have been corrected.....	62
Figure 4-16 Carbon 1s X-ray absorption for (a) $B_{0.05}C_{0.85}$ and (b) $B_{0.17}C_{0.83}$ films on quartz substrates, prepared by CVD. The arrows indicate empty π -bonding orbitals created by the incorporation of boron.....	64
Figure 4-17 Boron 1s X-ray absorption for (a) $B_{0.05}C_{0.85}$ and (b) $B_{0.17}C_{0.83}$ films on quartz substrates, prepared by CVD. The XAS spectrum for B_2O_3 powder is shown in (b) for comparison.	65
Figure 4-18 The (002) Bragg peak of B_zC_{1-z} powder samples made at 900°C. Estimated boron concentration are at right, above each data set. The data have been scaled and offset for clarity.....	67
Figure 4-19 Diffraction patterns of B_zC_{1-z} powder samples produced at 30 torr, for $z=0, 0.08, 0.15, 0.17$	68
Figure 4-20 Diffraction pattern of $B_{0.15}C_{0.85}$ powder sample as a function of temperature. Unlabeled Miller indices refer to the graphite structure.....	70
Figure 4-21 (002) Bragg peak for (a) $B_{0.15}C_{0.85}$ and (b) pure carbon powders, at 900°C and 1500°C.....	72
Figure 4-22 Average layer spacing, d_{002} , of B_zC_{1-z} powder samples as a function of heat treatment temperature.....	73
Figure 4-23 Full width at half maximum of the (002) peak of B_zC_{1-z} powder samples as a function of heat treatment temperature.....	74
Figure 5-1 Schematic drawing of a lithium test cell. The current direction shown corresponds to the recharge of the cell.....	79
Figure 5-2 Second cycle voltage curve of Li/JMI graphite cell.....	83
Figure 5-3 Derivative curve of JMI graphite with staged phase transitions labeled.	84
Figure 5-4 The first discharge and subsequent cycle of a Li/graphite (Lonza KS-44) cell.	85
Figure 5-5 The effect of 12-Crown-4 ether on the irreversible capacity of Li/Graphite cells with 1M $LiClO_4$ PC/EC electrolyte (from reference 67). Only the first discharge is shown.	86

Figure 5-6 Cell voltage vs. x in Li_xC_6 for the first cycle and second discharge of cells made from KS900, cycled at 7.44 mA/g. The inset shows the derivative, dx/dV , for the same cells.....	88
Figure 5-7 Exploded view of a typical lithium coin cell.....	90
Figure 5-8 Structure of common electrolyte solvents.....	91
Figure 5-9 Cell voltage vs. x in Li_xC_6 for the first cycle and second discharge of cells made from a $\text{B}_{0.17}\text{C}_{0.83}$ film on Cu foil. The lithium concentration, x , is approximate.	93
Figure 5-10 Cell voltage vs. x in $\text{Li}_x(\text{B}_z\text{C}_{1-z})_6$ for the first cycle and second discharge of cells made from $\text{B}_{0.03}\text{C}_{0.97}$ (solid), cycled at 7.44 mA/g, and pure carbon produced by CVD from benzene at 900°C. The inset shows the derivative, dx/dV , for the same two cells.....	94
Figure 5-11 Cell voltage vs. x in $\text{Li}_x(\text{B}_z\text{C}_{1-z})_6$ for the first cycle and second discharge of cells made from $\text{B}_{0.08}\text{C}_{0.92}$ (solid), cycled at 3.72 mA/g, and pure carbon produced by CVD from benzene at 900°C. The inset shows the derivative, dx/dV , for the same two cells.....	95
Figure 5-12 Cell voltage vs. x in $\text{Li}_x(\text{B}_z\text{C}_{1-z})_6$ for the first cycle and second discharge of cells made from $\text{B}_{0.10}\text{C}_{0.90}$ (solid), cycled at 3.72 mA/g, and pure carbon produced by CVD from benzene at 900°C. The inset shows the derivative, dx/dV , for the same two cells.....	96
Figure 5-13 Cell voltage vs. x in $\text{Li}_x(\text{B}_z\text{C}_{1-z})_6$ for the first cycle and second discharge of cells made from $\text{B}_{0.115}\text{C}_{0.885}$ (solid), cycled at 7.44 mA/g, and pure carbon produced by CVD from benzene at 900°C. The inset shows the derivative, dx/dV , for the same two cells.....	97
Figure 5-14 Cell voltage vs. x in $\text{Li}_x(\text{B}_z\text{C}_{1-z})_6$ for the first cycle and second discharge of cells made from $\text{B}_{0.17}\text{C}_{0.83}$ (solid), cycled at 7.44 mA/g, and pure carbon produced by CVD from benzene at 900°C. The inset shows the derivative, dx/dV , for the same two cells.....	98
Figure 5-15 Cell voltage vs. x in $\text{Li}_x(\text{B}_z\text{C}_{1-z})_6$ for the first cycle and second discharge of cells made from a mixture of XP Coke and 20% boron powder (solid), cycled at 7.44 mA/g, and pure carbon produced by CVD from benzene at 900°C. The inset shows the derivative, dx/dV , for the same two cells.....	99
Figure 5-16 A comparison of voltage curves of $\text{Li}/\text{Li}_x(\text{B}_z\text{C}_{1-z})_6$ cells as a function of boron concentration. Each curve is shifted up sequentially by 1.0 V for clarity.....	100
Figure 5-17 Reversible capacity vs. boron concentration in $\text{Li}/\text{Li}_x(\text{B}_z\text{C}_{1-z})_6$ cells made from B_zC_{1-z} . Capacities are calculated from the average of the first charge and second discharge.	101
Figure 5-18 Schematic drawing of the lithium sites on a single layer of boron-substituted carbon. The dashed circle represents the site for additional lithium beyond $x=1$ in $\text{Li}_x(\text{B}_z\text{C}_{1-z})_6$	102
Figure 5-19 Qualitative sketch of the voltage curves of (a) graphite, and (b) disordered carbon, both unsubstituted and boron-substituted; $3J$ is the nearest neighbor repulsion between lithium ions on the lattice, separated by 2.45Å; Δ is the increase in binding energy caused by the addition of boron. The region below $V=0$ is not accessible for intercalation.	104
Figure 5-20 Exploded view of X-ray diffraction in-situ cell.....	106

<i>Figure 5-21 Determination of the equilibrium voltage for a $\text{Li}/\text{Li}_x(\text{B}_{0.17}\text{C}_{0.83})_6$ cell.....</i>	<i>108</i>
<i>Figure 5-22 Average layer spacing versus lithium concentration in $\text{Li}_x(\text{B}_{0.17}\text{C}_{0.83})_6$. The solid line is a guide to the eye.</i>	<i>109</i>
<i>Figure 5-23 Average layer spacing versus lithium concentration in $\text{Li}_x(\text{B}_{0.08}\text{C}_{0.92})_6$. The solid line is a guide to the eye.</i>	<i>110</i>
<i>Figure 5-24 Drawing of nested and unnested coordination of lithium ions</i>	<i>111</i>
<i>Figure 5-25 Puckering of intercalated lithium layers.....</i>	<i>111</i>
<i>Figure 5-26 Voltage versus capacity for cells made from a pure carbon produced by CVD of benzene at 900°C, heated to a series of temperatures. The capacity scale is continuous, and actual cycle capacity is the difference between the capacities at the beginning and end of the cycle.</i>	<i>113</i>
<i>Figure 5-27 Voltage versus capacity for cells made from $\text{B}_{0.15}\text{C}_{0.85}$, heated to a series of temperatures. The capacity scale is continuous, and actual cycle capacity is the difference between the capacities at the beginning and end of the cycle.</i>	<i>114</i>
<i>Figure 5-28 Derivative curves for charge only of Li test cells made from heat treated B_zC_{1-z} samples.</i>	<i>115</i>
<i>Figure 5-29 2nd discharge capacity versus heat treatment temperature for Li test cells made from heat treated B_zC_{1-z} samples.</i>	<i>116</i>
<i>Figure 5-30 Derivative curves for the charge only in the region of the 0.95 V peak for B_zC_{1-z} samples heated to 1500°C and Conocco petroleum pitch heated to 2200°C.</i>	<i>117</i>
<i>Figure 6-1 The in-plane structure of graphite, showing the three sublattices.....</i>	<i>121</i>
<i>Figure 6-2 Mean field calculation of Li/Graphite voltage curve (solid) and number of iterations required to reach self-consistency (short-dash). The voltage of lithium metal is marked by the long dashes at zero volts.....</i>	<i>124</i>
<i>Figure 6-3 Mean field calculation of Li/Coke voltage curve, for $\Delta=0.8$ eV, 0.4 eV, and 0.01 eV.....</i>	<i>126</i>
<i>Figure 6-4 Mean field calculation of $\text{Li}/\text{B}_z\text{C}_{1-z}$ voltage curve, for $z=0.15$, 0.075, and 0.0, using double rectangular density of sites. Other parameters are described in the text.</i>	<i>127</i>
<i>Figure 6-5 (a) Double rectangular and (b) double Gaussian models of the density of sites versus binding energy in B_zC_{1-z}</i>	<i>129</i>
<i>Figure 6-6 Mean field calculation of $\text{Li}/\text{B}_z\text{C}_{1-z}$ voltage curve, for $z=0.15$, 0.075, and 0.0, using double Gaussian density of sites. Other parameters are described in the text.</i>	<i>131</i>
<i>Figure 6-7 Mean field calculation of $\text{Li}/\text{B}_{0.15}\text{C}_{0.85}$ voltage curve using double Gaussian density of sites, and varying the distribution widths, σ_b and σ_c. Other parameters are described in the text.....</i>	<i>132</i>
<i>Figure 6-8 Comparison of $\text{Li}/\text{B}_{0.17}\text{C}_{0.83}$ voltage, from average of first charge and second discharge, with mean field calculation of voltage using double Gaussian density of sites and parameters described in the text.....</i>	<i>133</i>
<i>Figure 6-9 Comparison of the derivative curves of the charge of a $\text{Li}/\text{B}_{0.17}\text{C}_{0.83}$ cell (solid) with that calculated in mean field approximation. Parameters are the same as for Figure 6-8.</i>	<i>134</i>

<i>Figure 6-10 In plane structure of BC₃ showing the four sublattices.</i>	135
<i>Figure 6-11 Mean field calculation of Li/BC₃ voltage curve, for $\Delta=0.6$ eV, 0.3 eV, and 0.1 eV. Also shown are the number of iterations required to reach self-consistency for the $\Delta=0.1$ eV calculation.</i>	136
<i>Figure 7-1 Voltage curve of phosphorus-containing polyfurfuryl alcohol, pyrolyzed at 600°C.</i>	140
<i>Figure 7-2 Schematic drawing of (a) disordered carbon and (b) nano-dispersed silicon in disordered carbon.</i> 142	
<i>Figure 7-3 Voltage curve for Li/Si₂C₁₋₂ cells from reference 82. The solid curve is for a sample prepared from 1:1 (CH₃)₂Cl₂Si:C₆H₆, and the dashed curve corresponds to a sample produced from pure benzene. Both samples were prepared by CVD at 950°C.</i>	143
<i>Figure 7-4 The master graph of reversible capacity for lithium plotted versus heat-treatment temperature for a variety of carbon samples from reference 85. The three regions of commercial relevance are marked.</i> .	144
<i>Figure 7-5 Second cycle voltage curves of carbons representative of regions 1,2 and 3. a)Johnson-Matthey Synthetic Graphite, b) Crowley petroleum pitch heated to 550°C and c) resole resin heated to 1000°C.</i> 145	
<i>Figure 7-6 Reversible capacity of carbons from region 2 as a function of their hydrogen to carbon ratio. The samples include Crowley Pitch (CRO), Kureha Pitch (KS Series A and B), polyvinylchloride (PVC) and polyvinylidene fluoride (PVDF) heated to temperatures between 550°C and 1000°C as well as data from reference 87.</i>	147
<i>Figure 7-7 The reversible capacity of region 3 carbons prepared from epoxy-novolac resins heated between 900°C and 1100°C as a function of their single-layer fraction. The square point is a calculation corresponding to complete absorption on both sides of a carbon consisting of only single-layers. The line is a guide to the eye.</i>	149

Chapter One

1. Introduction

The first primary battery was invented by Volta in 1800¹, followed by the lead acid secondary or rechargeable battery in the 1850's.² Since then the secondary battery has been significantly improved, in terms of energy density, power capability and cycle life. However, in the last twenty years improvements to energy density have not kept up with the miniaturization of consumer electronics, especially now with the rapidly growing use of notebook computers and cellular phones. The size and weight of the battery present serious impediments to further miniaturization, and the poor capacity restricts usage. Another group making demands for better battery performance is the electric vehicle (EV) producers. California has enacted legislation to force manufacturers to sell a certain percentage of vehicles with no polluting emissions. This basically means battery or fuel cell powered EVs. Fuel cell technology is hampered by the necessity of carrying hydrogen, and the lack of a hydrogen infrastructure. Thus, huge efforts have been started to produce electric vehicles with existing battery technology and to improve battery performance. With the California Zero Emission Vehicle (ZEV) laws spreading to many states with pollution problems, caused in great part by vehicle emissions, the demand for better battery performance is at an all-time high.

<i>Rechargeable Battery System</i>	<i>Discharge Voltage(V)</i>	<i>Specific Energy (Wh/kg)</i>	<i>Energy Density (Wh/l)</i>
Nickel Cadmium	1.2V	45	120
Nickel Metal Hydride	1.25V	70	180
Lithium-ion	3.5-3.9V	120	240

Table 1-1 Performance of AA-size cells for several existing rechargeable battery technologies³

There are a number of new battery technologies that are being developed to meet these needs. Nickel metal hydride (NiMH) batteries outperform the older nickel cadmium and have been used in laptop computers, and are being developed for EV use.⁴ Although they have large volumetric energy density (Energy/Volume), they also have large mass density and therefore relatively low specific gravimetric energy density (Energy/Mass). High specific energy lithium batteries are the current state-of-the-art. Primary lithium batteries are now extremely common for applications requiring high energy density, such as in autofocus cameras, and long life applications such as computer memory back-up and smoke-detectors. For applications having high power demands, however, primary batteries are not practical, due to their high replacement cost. Early rechargeable lithium batteries have proved unsafe due to the extreme reactivity of the lithium metal anode. The next generation of secondary lithium batteries are called *lithium-ion* batteries and contain no metallic lithium. Although suffering from somewhat lower energy density compared to cells containing lithium metal, these new batteries have much improved cycle life and safety characteristics. Laptop computers containing lithium-ion batteries have the longest battery life ever and have been favorably reviewed, in part due to this feature⁵. This technology is in its infancy however, and much room for improvement still exists in the areas of energy density, cost and safety. It is to these ends that materials research can be useful, studying new materials for use as anodes or cathodes in lithium-ion cells.

Intercalation is the process by which guest atoms or molecules (called intercalants) are reversibly inserted into a host, without causing a significant structural change in the host. Secondary electrochemical cells based on intercalation have been studied since the late 1970's⁶. Early work focused on a cell with a lithium metal foil anode and a layered material, such as MoS₂, spread onto aluminum foil as the cathode. The electrolyte consisted of a lithium salt (ie. LiAsF₆) dissolved in a non-aqueous solvent (ie. propylene carbonate / ethylene carbonate). In the standard 'jelly roll' configuration a sandwich would be made of the two electrodes, with a microporous polypropylene separator between them. The three layers would then be rolled up and placed into a cell can, where electrolyte is added and the cell sealed.

Unfortunately these early cells suffered from a subtle, but basic flaw. Lithium metal is thermodynamically unstable in all known non-aqueous electrolytes. Spontaneous exothermic reaction results from any direct contact between the metal and the electrolyte. The only reason that such cells work at all, is due to the formation of an insoluble passivation film on the lithium metal, consisting of lithium compounds including Li_2O , Li alkyl carbonate and LiOH .⁷ This film prevents direct contact between the lithium and the liquid electrolyte, while acting as a conductor for lithium ions, allowing intercalation to continue. Upon cycling, however, the lithium is repeatedly stripped and redeposited onto the foil. During redepositing, or plating, the lithium tends to form dendritic growths, leading to increased surface area. This behaviour can be reduced by use of pressure applied to the lithium surface (referred to in the battery industry as *stack pressure*), but cannot be entirely avoided for all cycling conditions.⁸ As these dendrites continue to grow, they may penetrate the separator and produce an internal short, which can increase the temperature of the cell. The total Li surface area may start to react, sometimes leading to self-heating, melt down of the lithium, and finally a runaway exothermic reaction. This is a fundamental flaw in the use of lithium metal in rechargeable intercalation cells, which may only be circumvented if an electrolyte which is not reactive with lithium metal could be found. Even in this case the future for this type of cell is limited, because uneven stripping and plating eventually lead to holes in the lithium foil, which cause the failure of the cell, setting an upper limit on the number of cycles possible.

A simple solution to this problem is the *lithium-ion* or '*rocking-chair*' cell.⁹ In this type of cell the lithium metal anode is replaced by an intercalation material. Thus, the cell consists of two intercalation hosts, into which lithium is shuttled back and forth on discharge and charge. These materials are chosen so that there is a large difference in the chemical potential of the lithium in the two hosts, leading to a large cell voltage. The cell voltage is given by:

$$V = -\frac{(\mu_{\text{cathode}} - \mu_{\text{anode}})}{e} \quad \text{Equation 1-1}$$

where μ_{cathode} is the chemical potential of lithium in the cathode, μ_{anode} is the chemical potential of lithium in the anode, and e is the magnitude of the charge on an electron.

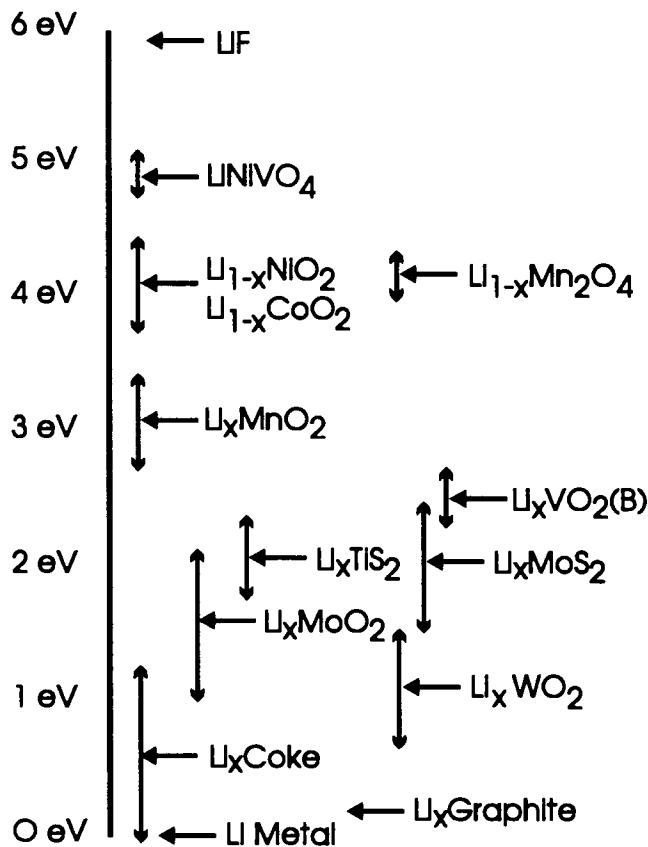
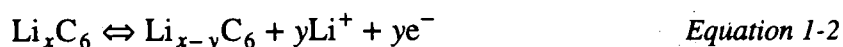


Figure 1-1 Binding energy of lithium in various lithium compounds.

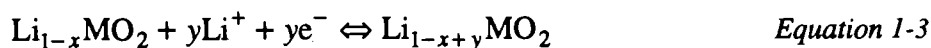
Due to the lack of metallic lithium, one of the hosts in a Li-ion cell must be synthesized containing lithium atoms, which may be removed by de-intercalation. Currently the materials of choice are: a lithium transition metal oxide as the cathode (high voltage side), and a carbon, either disordered or graphitic, for the anode (low voltage side). The criteria for choosing the cathode material are that they are air stable, contain a large amount of lithium that can be reversibly de-intercalated, and have a large voltage versus lithium metal. Referring to the diagram of binding energies of lithium in lithium compounds in Figure 1-1, one can see that the transition metal oxides LiNiO₂, LiCoO₂, or LiMn₂O₄ are good choices as cathodes^{7,10,11}. LiNiVO₄ does not have a high enough reversible capacity to be considered a good cathode material, and LiF, which is an ionic solid will not intercalate at

all. Carbon, in the form of coke or graphite is chosen primarily because it has a voltage near that of lithium metal, leading to a large cell voltage, and can intercalate up to 1 lithium per 6 carbon atoms.¹² It should be noted that lithiated carbon will also react with organic electrolytes, suggesting the possibility that the safety problem may still exist. However, because there is no formation of dendrites when intercalating into carbon, the surface area remains essentially constant during cycling, and thus a carbon that is initially safe, will remain so, regardless of the cycling conditions.¹³

The cell is assembled in its discharged state, with lithium in the transition metal oxide, where it is most tightly bound. To charge the cell a voltage is applied across the electrodes, forcing electrons out of the cathode and onto the anode. The potential is increased until the binding energy of the least tightly bound lithium atoms is reached, at which time lithium ions are forced out of the cathode and into solution. Lithium ions diffuse through the electrolyte, across the separator, and into the anode. In a galvanostatic charge, the voltage is increased at such a rate as to cause the rate of transfer of electrons (and therefore lithium) to be constant with time. Once a predetermined voltage is reached the cell is called 'charged'. After this the cell can be removed from the current source, connected across a load and it will spontaneously discharge, with the reverse process occurring. With no external circuit the cell will remain charged, because there is no electrically conducting path for the electrons to take from the anode to the cathode. Figure 1-2 schematically illustrates the discharge process. The half cell reactions for a lithium transition metal oxide / carbon cell are:



at the carbon anode, and:



at the transition metal oxide cathode. The forward direction of both reactions corresponds to discharge of the cell.

Li-ion cells now exist in the market place in applications such as laptop computer and videocamera batteries. They possess higher specific energies (Wh/kg) and lower self-discharge rates compared to Ni-Cd and Ni-Metal Hydride batteries. Yet there is still much room for improvement in this technology. Ongoing research is making improvements in the areas of higher specific capacities for both anode and cathode materials, safety, cost, electrolyte stability and cycle life. The primary goal of the battery scientist is to increase that amount of lithium that can be intercalated into the electrode in question, called the *reversible capacity*, while decreasing the amount of lithium lost to side reactions, called the *irreversible capacity*. For graphite the limit is 372 mAh/g, which corresponds to LiC_6 , when fully intercalated. Because graphite is considered a benchmark, the reversible capacity for other carbons is often quoted as x_{max} in Li_xC_6 , the fraction of the LiC_6 capacity.

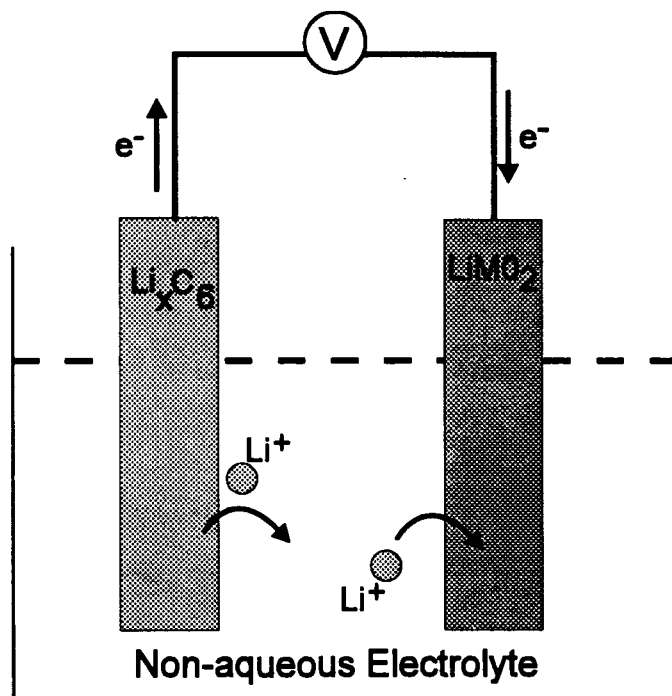


Figure 1-2 Schematic drawing of the discharge of a Lithium-Ion cell.

The work presented here involves the study of a relatively new class of carbonaceous materials, boron substituted carbons, as possible anode materials in lithium-ion cells. The method used to study the intercalation of lithium in carbons involves the production of Li/Carbon test cells. These cells are basically the same as the early lithium cells, containing

an anode of lithium metal and a cathode of the carbonaceous material that is being studied. The purpose of studying carbons in these test cells, rather than in lithium-ion cells, is that the chemical potential of lithium in lithium metal is constant throughout the intercalation process, so the voltage of the cell depends only on the chemical potential of the intercalated lithium in the material being studied. In a lithium-ion cell, the chemical potentials of lithium in both electrodes are changing together, making the results more difficult to interpret.

There are thousands of carbonaceous compounds that could be tested for their ability to intercalate lithium. The structure of carbons depends strongly on the method and the experimental conditions used to produce them, and the electrochemical performance depends strongly on the structure.¹⁴ Therefore, one must try to make rational choices of what should be tested, on the basis of some factors such as anticipated performance or low cost of production. The choice of boron substituted carbon was made on the basis of both anticipated performance, based in part on some earlier work on boron substituted graphite¹⁵, and scientific interest. Until recently the only boron substituted carbons available had less than 2.35 atomic percent boron, and were produced at relatively high temperatures, around 2300°C, by the method of Lowell.¹⁶ In the late eighties however, Bartlett's group discovered a low temperature (<1000°C) synthesis route, that produced solid solutions with up to 25 atomic percent boron.¹⁷ It is these new materials that we were interested in synthesizing and studying.

These boron substituted carbons, which are often referred to as BC₃ regardless of their exact boron concentration, will be referred to here as B_zC_{1-z}, where z is the estimated atomic fraction of boron. They have been the subject of much research over the past few years since their discovery. Probably one of the main reasons has been the interest in their electronic properties. The electronic properties of the older boron substituted graphites are well reviewed by Klein in the *Chemistry and Physics of Carbon, Volume 2*.¹⁸ Although graphite has no bandgap, the Fermi level is between two bands, giving it few free carriers, making it a semimetal. Boron atoms have one fewer valence electron than carbon and are thus thought to act as electron acceptors, producing hole-carriers, and lowering both the in-plane and c-axis electrical resistance.¹⁸ Theoretical studies of BC₃ have confirmed that the

conductivity should be increased, relative to graphite.¹⁹

Boron also has the interesting property that it reduces the rate of oxidation of carbons when heated in an oxidizing atmosphere. Boron substituted graphite, with less than 2.35% boron, is currently marketed as "oxidation resistant" graphite. When heated in air, carbon is oxidized to CO₂ and CO, which vaporize, but the boron becomes B₂O₃, which is a stable solid. After sufficient exposure to heated air, the B₂O₃ layer that forms is sufficient to dramatically slow further reaction with air, in analogy with Al₂O₃ on aluminum. This is a very important property because graphites are very strong, and mechanically stable to very high temperatures, when not subject to oxidation. Thus these new, high-boron-concentration-carbons are technologically very interesting, as coatings on graphite, or graphite fiber substrates. They have proved to have superior oxidation resistance properties.²⁰

The question then arises: Why would we believe that B₂C_{1-z} would make a good anode material? Some previous work on the intercalation of lithium in boron-carbon solid solutions was done by Dahn *et al.*¹⁵ using samples with low boron concentration, prepared by the method of Lowell. They calculated the voltage versus x , in Li _{x} (B₂C_{1-z})₆, curves for $z \leq 0.01$. Using the rigid band model (as described in *Chapter 2*), and treating boron as an electron acceptor in the carbon host, the effect of the boron was shown to be the lowering of the Fermi level relative to the shape of the bands. They calculated that an additional plateau at low x in Li _{x} (B₂C_{1-z})₆ in the voltage curve of the boron substituted graphite should be formed due to the filling of the unoccupied one-electron states below the previous Fermi level in graphite. This plateau was observed experimentally, and could be well understood by means of the model.

From this behaviour of boron-doped graphite we hypothesized that if sufficient boron was substituted, the carbon could intercalate significantly more lithium. The reason for this increased capacity would be that the number of unoccupied electron states that are lower in energy than the donor lithium 2s states is increased compared to pure carbon. It is for this

reason that we anticipated a larger capacity for the B_2C_{1-z} solid solutions than for graphite. An illustration of the filling of these newly available states by the lithium 2s electrons is shown in Figure 1-3, in the rigid band approximation, discussed in Section 2.2.1.

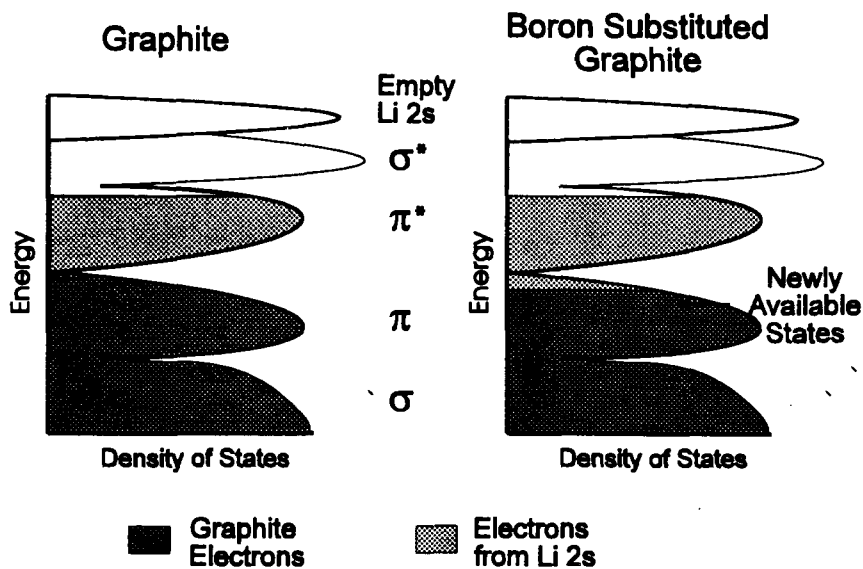


Figure 1-3 Schematic drawing comparing the filling of the density of states for intercalated graphite and intercalated boron-substituted graphite, in the rigid band model.

The goal of this thesis is to understand the relationship between the intercalation of lithium, the boron concentration and structure of B_2C_{1-z} solid solutions, and to evaluate the usefulness of these materials as anodes for lithium-ion cells. The method used to reach this goal is comprised of four major steps. First, we synthesize a series of B_2C_{1-z} films with $0 \leq z \leq 0.17$. We then characterize these materials by a variety of techniques, to determine boron concentration, crystal structure, purity and electronic structure. Thirdly, we produce Li/B_2C_{1-z} electrochemical cells and study the intercalation of lithium by constant current cycling and *in-situ* X-ray diffraction. Finally we model the system using a lattice gas model to calculate voltage curves as a function of boron concentration.

When we measured a reversible capacity of 420mAh/g for $B_{0.17}C_{0.83}$ in 1992, this was the most lithium that had ever been intercalated into a carbon, exceeding the previous limit of 372mAh/g, in graphite. This was very interesting both from a scientific and a technological point of view, due to its potential application in lithium-ion cells. Because of

the large financial stakes in the battery industry, an immense research effort has gone on among many battery companies and research institutions around the world in the last five years to produce higher capacity carbons. This research has led to a series of disordered carbons with reversible capacities up to almost 1000 mAh/g, through a variety of different mechanisms, which are still not well understood. A review of the recent advances in high capacity carbons, and the proposed mechanisms is given in *Chapter 7*. The technological applications of B_2C_{1-z} are uncertain, but understanding the mechanisms for lithium intercalation is still very important.

The organization of this thesis is as follows. *Chapter 2* contains a description of the structure of graphitic and pre-graphitic carbons, the phenomenon of intercalation, and the state of knowledge of intercalation in carbons when this thesis was begun. In *Chapter 3* we begin by describing the previous work done on the synthesis of boron substituted carbons, both graphitic and disordered, and then discuss the synthesis of the materials studied in this thesis. *Chapter 4* includes the characterization of these materials by X-ray diffraction, Auger Electron Spectroscopy, and X-ray Absorption Spectroscopy, as well as a study of the effects of heat treatment temperature. *Chapter 5* begins by describing the electrochemical methods used to study lithium intercalation, reviews the previous work on intercalation in boron substituted carbons and continues by outlining the electrochemical and *in-situ* diffraction experiments performed on the Li/B_2C_{1-z} cells. It concludes by providing a simple physical model for understanding the electrochemical results. Next, in *Chapter 6* we outline a lattice gas model of the intercalation system, propose a mean field solution, and solve for the voltage as a function of intercalated lithium for a series of boron concentrations. We conclude by interpreting the results in the context of our experimental findings. *Chapter 7* contains a review of the recent advances in the use of carbons as anodes in lithium-ion cells, to place the knowledge gained in this thesis in an historical context. Finally, in *Chapter 8* we summarize the information from this thesis, evaluate the usefulness of these B_2C_{1-z} materials as lithium-ion anodes and present some conclusions.

Chapter Two

2. Intercalation in Carbons

The subject of this thesis is the intercalation of lithium into B_zC_{1-z} solid solutions. We will show later that the structure of these materials is that of a disordered graphite, and that the boron is substitutional in this structure. A considerable amount of work has been done on intercalation in graphite, and to a lesser extent, disordered carbons. Many of the basic concepts related to that work are directly applicable to the study of these substituted carbons. Therefore it is instructive to review the structure of pure, unsubstituted carbons, the phenomena of intercalation in general, and the specifics of lithium intercalation in graphitic and pre-graphitic carbons. Issues related directly to electrochemical intercalation will be covered in *Chapter 5*, and recent advances in the reversible capacity of carbonaceous materials, that have occurred only in the last three years, will be covered in *Chapter 7*.

2.1 Structure of Carbons

There are a large variety of forms of carbons, with different crystal structures, microstructure, and varying levels of disorder. Traditionally there were two crystalline forms of carbon: graphite and diamond. These were joined by the fairly recent discovery of C_{60} "Buckminster Fullerene" or "Bucky-Balls", which crystallize to form face centered cubic (FCC) single crystals. Other forms of carbon include: petroleum coke, carbon blacks, carbon fibers, pyrolyzed polymers, nanotubes, mesocarbon microspheres, and the list goes on. Only descriptions of the structures of graphite and disordered, pre-graphitic carbons follow because these most closely relate to the boron substituted carbons.

2.1.1 Structure of Graphite

The structure of graphite is well known. The basic building blocks are hexagonal, honeycomb lattices of carbon atoms in 2-dimensions, as seen in Figure 2-1a, and these

graphene layers are stacked along the third direction, the *c*-axis, in a registered fashion. The in-plane lattice constant, *a*, is approximately 2.45Å and the stacking distance (*d*₀₀₂) is 3.35Å. The bonding between layers is due to van der Waal's (induced dipole-dipole) forces, and is therefore quite weak. There are two natural forms of graphite, each with different stacking along the *c*-axis. The more common form is the hexagonal or 2H form and has layers stacked with registry ABABAB.... The second, less common, polymorph of graphite is the rhombohedral or 3R form that has ABCABC... stacking. Both natural and synthetic graphites often have a fair amount of stacking disorder, with both random stackings and 3R intergrowths in a predominantly 2H structure.²¹ The 2H and 3R structures are shown in Figure 2-1b and Figure 2-1c respectively.

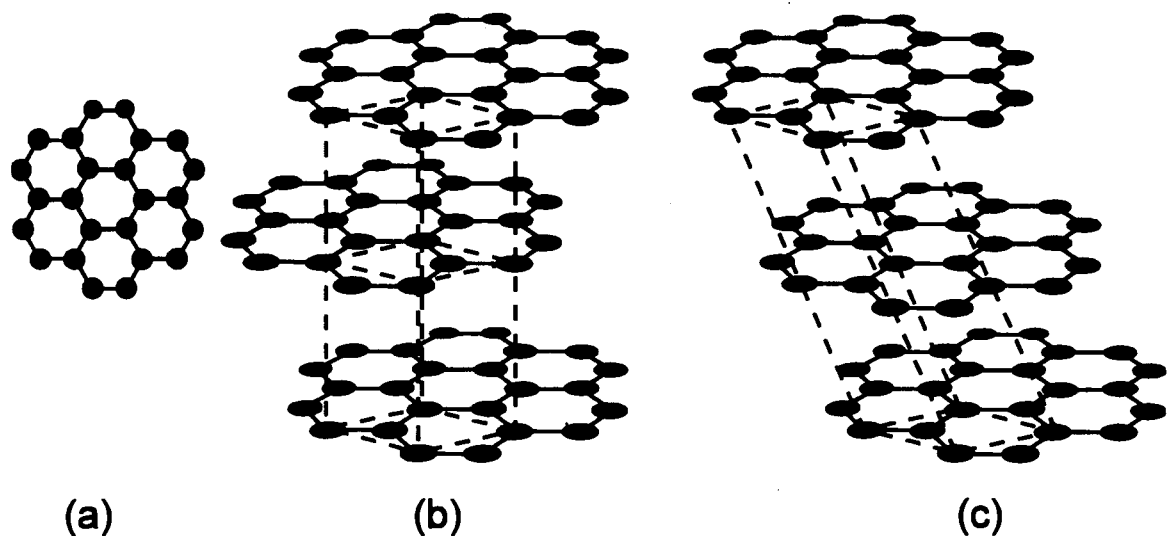


Figure 2-1 (a) single graphite layer (b) structure of 2H graphite (c) structure of 3R graphite

2.1.2 Disordered Carbons

Carbons such as petroleum coke and pyrolyzed polymers, that are produced at relatively low temperatures (900-1300°C) have disordered graphite structures, and are sometimes referred to as *pre-graphitic*. Both the layer extent and the height of the stacks, denoted by *L*_{*a*} and *L*_{*c*} respectively, are much smaller than for graphite. In addition, there is strain in the *c*-axis layer spacing (*d*₀₀₂), and there is a large probability that adjacent carbon layers are randomly stacked. This random stacking consists of random shifts and rotations

between adjacent layers, leading to a loss of registry, and is referred to as *turbostratic disorder*²². There are two classes of disordered carbons, soft and hard. With *soft* or *graphitizable* carbons the turbostratic disorder can be removed by heating in the range from 2000°C to 3000°C, producing a synthetic graphite. Petroleum coke and petroleum pitch are common examples of soft carbons, produced by pyrolysis of petroleum products. These carbons pass through a liquid or liquid crystalline state during heating that allows parallel layers to form. On the other hand, the layers of *hard* or *non-graphitizable* carbons, will not register under almost any conditions.²² Hard carbons are typically produced from the pyrolysis of cross-linked polymers, and have bonding between layers that prevents proper registry.

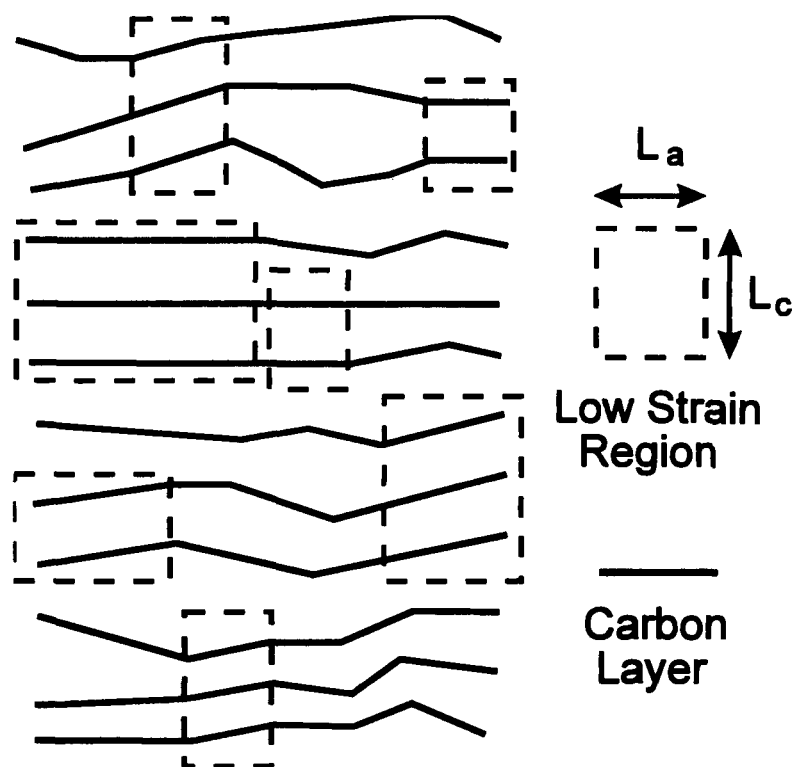


Figure 2-2 Schematic drawing of the organized (low strain) and unorganized regions in a low temperature carbon. L_a and L_c refer to the size of the regions which scatter X-rays coherently.

The structure of disordered carbons is quite difficult to determine. The powder X-ray diffraction patterns of the low temperature carbons (ie. formed at temperatures lower than 1000°C) are difficult to interpret because there are only a few, broad peaks, which are

typically at positions that correspond to the (002),(004),(100) and (110) peaks of graphite. The information generally taken from this data is the average layer spacing, d_{002} , the in-plane lattice constant, a , and the crystallite dimensions, L_a and L_c , which are determined from the X-ray peak widths using the Scherrer equations.²³ But for some samples L_a and L_c are as small as 10\AA , while the surface area estimated by gas adsorption (BET method) is less than $1\text{ m}^2/\text{g}$. Therefore these L_a and L_c can not represent the true particle size of the crystallites, because the surface area would be much larger than the measured one. Instead they are correlation lengths within a larger particle, that correspond to regions that scatter X-rays coherently. These regions which scatter coherently within themselves will be referred to as *organized carbon*. Franklin proposed that the organized regions were separated by highly strained, *unorganized carbon*, consisting of groups of tetrahedrally bonded carbon, or highly buckled graphitic sheets.²² This picture is illustrated in Figure 2-2, where the organized regions will not scatter coherently with respect to each other.

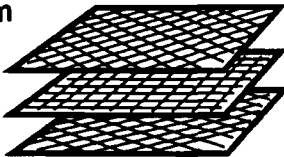
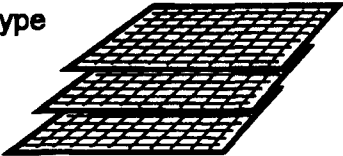
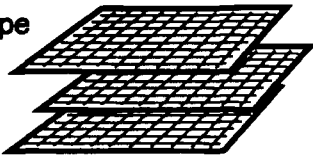

Probs	Layer Stacking
P	Random 
P_t	3R-type 
1-P- P_t	2H-type 
1-g	Buckled Layers 

Figure 2-3 The probabilities P , P_t , 1-P- P_t , and 1-g.

A model for understanding disordered carbons can now be created, based on these concepts. The important parameters are:

P - the probability that adjacent layers are randomly stacked

P_t - the probability of having 3R type stacking

$1-P-P_t$ - the probability of having 2H type stacking

g - the fraction of carbon that is made up of organized regions

and these are illustrated in Figure 2-3. The probability P_t is only relevant within organized regions. In unorganized regions, $P=1$.

Using these parameters, Hang Shi *et al.* developed a structure refinement program that minimizes the difference between measured powder diffraction data and a calculated pattern.²⁴ Using this program accurate values of g , P , and P_t can be determined for a wide variety of disordered carbons. The application of this information to intercalation in disordered carbons will be discussed in section 2.3.2.2

2.2 Intercalation

The process of *intercalation* has been studied for many years²⁵. It is the process by which guest atoms or molecules (called intercalants) are reversibly inserted into a host, without causing a 'significant' structural change in the host (Figure 2-4). The term 'significant' is generally thought to allow expansion, either isotropic or anisotropic, but not a reordering of atoms, as in alloying. Intercalants include a wide range of species, from lithium to large organic molecules. In this work we will be looking only at the intercalation of lithium. Lithium is a common intercalant because its small size can be more easily incorporated into a host, and because it has a large oxidation potential. For intercalation to proceed to any great extent there must be empty sites in the host available to accommodate intercalants to reside in, and these sites must be accessible from the surface. For this reason intercalation hosts tend to be materials with either a layered or tunnel structure, allowing easy diffusion of intercalants throughout the structure. The traditional example of an

intercalation host is graphite, which is capable of intercalating many different atoms and molecules, forming a class of materials called *graphite intercalation compounds* (GICs). Much of the early work on GICs was reviewed by Dresselhaus and Dresselhaus in 1981,²⁶ and this continues to be an active area of study for many researchers.

There are several methods used to prepare intercalation compounds. The traditional method is to expose the host to the vapor of the intercalant²⁶. The concentration of the intercalant in the host is controlled by varying the vapor pressure of the intercalant used. A second method is the use of chemical reagents such as n-butyl lithium, C_4H_9Li , that can react in an irreversible redox reaction with many hosts to provide an intercalated compound.²⁷ The third, and most recent, method, used to prepare intercalation compounds is carried out in a specific type of electrochemical cell. It is this method that was used in the experiments reported in this thesis. Intercalation processes are now being studied for use in electrochromic windows and mirrors, and electrochemical cells. In this section, some useful concepts relevant to intercalation will be discussed.

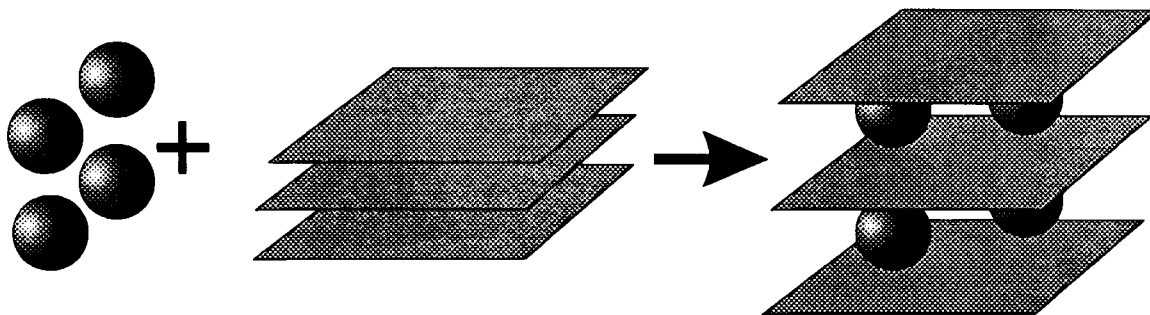


Figure 2-4 Intercalation in a layered material

2.2.1 Rigid-Band model of Intercalation

When a lithium atom is intercalated, it donates all or part of its 2s electron to the host. In the rigid band model, as lithium is intercalated its 2s electrons sequentially fill the lowest unoccupied one-electron levels of the host, causing the Fermi level to rise with respect to the shape of the bands. In this model the shape of these bands is unaffected by the presence of the lithium, as illustrated by Figure 2-5. This is in general not quite true, because the lithium atoms are closer to some host atoms than others, lowering the energy of the

electrons on the closer atoms, and thus deforming the bands²⁸. For many systems the rigid-band model provides a useful description of the electron states of the system, though. One other important point is that the Fermi level does not necessarily move up with respect to the vacuum as intercalation occurs. The conduction electrons of the host will move to screen the charge of the positive ion. This screening was shown by Friedel to lower the energy of the bands²⁹ with respect to the vacuum. In fact, in the dilute limit, where there is no interaction between adjacent screening clouds, and in a metallic system, where the density of conduction electrons is high, the upward motion of the Fermi level is exactly matched by the downward motion of the bands. In that case the binding energy of the lithium to the host remains approximately constant as the concentration of lithium is varied.²⁸

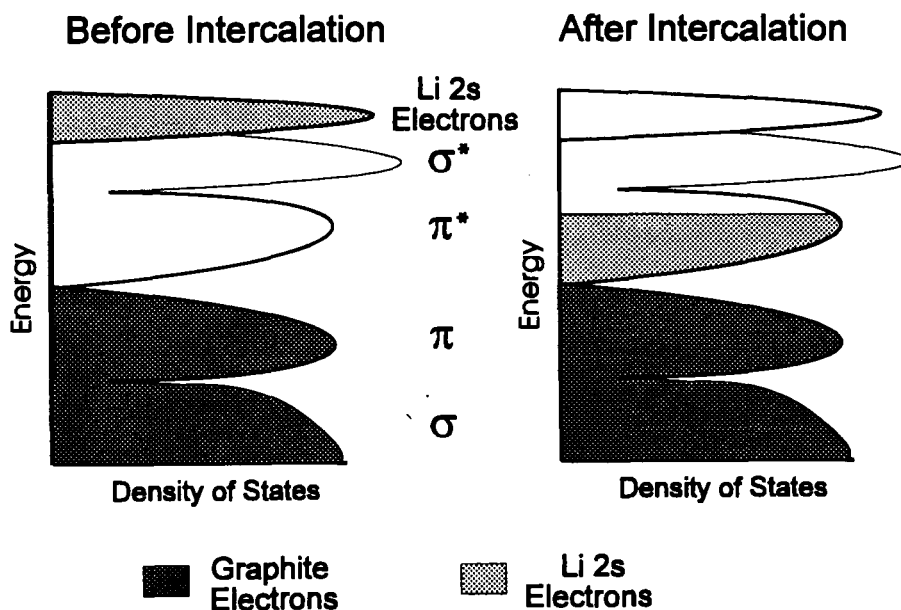


Figure 2-5 Rigid band model of intercalation

The intercalated lithium can be thought of as either atoms or ions. They have donated part of their electron density to the host, making them charged to some extent, but the host reacts to their presence with a screening cloud of electron density. In this thesis intercalated lithium will generally be referred to as atoms, except when the ionic nature is of direct importance for the discussion.

2.2.2 Staging

Another important concept when dealing with intercalation in layered materials is *staging*. Staging occurs when guest atoms in the same layer attract one another, and those in different layers repel each other. This attractive interaction is thought to be strain-mediated.^{30,31} After one guest atom has expanded the layer spacing between two host layers, the sites in this expanded region become more favourable than sites in neighboring unexpanded regions. The repulsive interaction may arise from a screened Coulomb interaction between the intercalated ions in different layers. This leads to staged phases, where every n^{th} guest layer is almost fully occupied and all other layers are almost empty. Stage 2 and stage 3 are illustrated in Figure 2-6. Transitions between staged phases lead to plateaus in chemical potential as the intercalated lithium concentration changes. As the transition progresses, the relative concentrations of the two phases change, but the chemical potential is constant, because the chemical potentials of phases in equilibrium are equal. Graphite intercalation compounds are the most well known example of materials that exhibit staging behaviour. The phase diagram of the staged phases have been well studied for several intercalants in graphite, including lithium³².

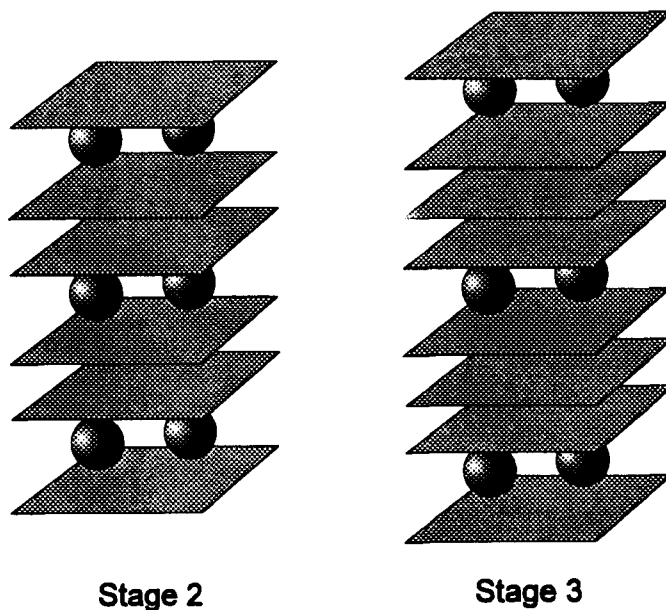


Figure 2-6 Staging phenomena in a layered material

It may be difficult to understand how transitions between staged phases may occur in a layered material, since in general intercalants cannot diffuse perpendicular to the layers. For example in the transition between stage-2 and stage-3 one might think that some of the intercalant must come out of the lattice and move into an adjacent layer. Experiments have shown, however, that this does not occur. This dilemma was resolved by the introduction of the Daumas-Herold island model of staging in 1969.³³ In this model each layer contains approximately the same amount of intercalant, distributed between high and low concentration regions, with the regions of high concentration often referred to as *islands*. The islands within the same layer repel each other, and the high and low concentration regions in successive layers are stacked, forming stages. An illustration of stage-2 according to this model is shown in Figure 2-7. As the phase transition occurs, in some layers intercalants move from regions of high concentration to low concentration, while in others the opposite occurs, rearranging the relative position and size of islands in different layers. The net effect is that the domains of the crystallite in one phase grow and the other diminish.

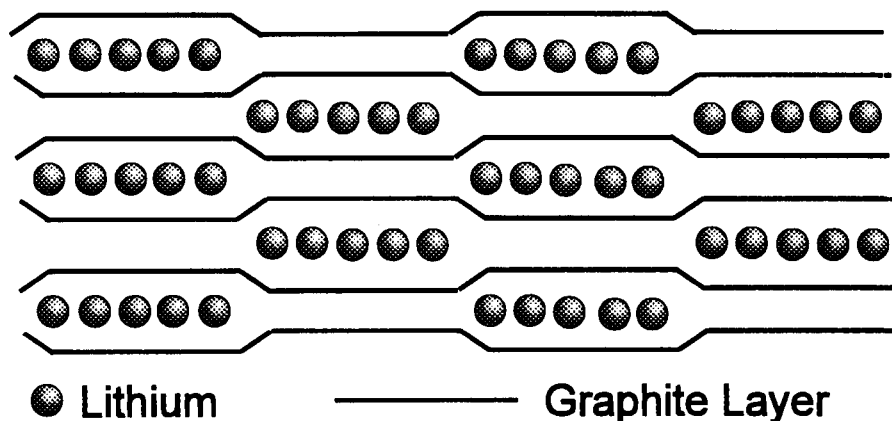


Figure 2-7 Stage-2 in the Daumas-Herold domain model of staging

2.3 Lithium Intercalation in Carbons

Although graphite is used as an anode in some lithium-ion cells, most of the carbons under consideration for this role are disordered to some extent. Historically however, graphite was the carbon of choice for the study of intercalation, both because its structural perfection allowed for easier study, and because it exhibits better ordering, both in-plane and

through staging. For use as an anode though, the most important factor is the maximum amount of lithium that can be intercalated into a specific mass of carbon, and neither ease of study nor interesting ordering phenomena are major considerations. On the other hand it is useful to understand intercalation in these better described materials first, before trying to tackle the more difficult, less well understood disordered carbons.

2.3.1 General Description of Lithium Intercalation in Graphite

Since its discovery by Herold in 1955,²⁵ the intercalation of lithium in graphite has been very well studied. Much of this work has focused on the formation of staged phases, and the determination of x -Temperature phase diagrams for Li_xC_6 . Fischer's group has done a great deal of work on phase diagrams, using intercalation from the vapor phase to make the samples, and X-ray and neutron diffraction to study the resulting structures as a function of temperature and composition. A good review of this work is provided by Fischer in *The Chemical Physics of Intercalation*.³⁴ At room temperature they observed the following phases: stage-1, stage-2, stage-2L (liquid-like), stage-3 and stage-4, with a maximum intercalation of 1 lithium per 6 carbon atoms. We will discuss staging here in its simplest approximation, keeping in mind that the Daumas-Herold island model is probably a more accurate representation, but within each domain the simple model is satisfactory.

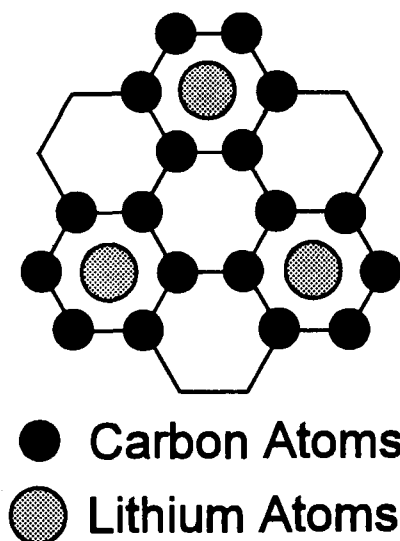


Figure 2-8 The single layer structure of LiC_6

In all phases of Li_xC_6 , Li atoms reside in the center of the van der Waals gap between layers, occupying the centers of the carbon hexagons, both above and below. This is possible because the carbon layers shift from ABABAB... to AAAA... stacking as lithium is intercalated. For the fully intercalated graphite at room temperature, stage-1 LiC_6 , Li atoms within each lithium layer occupy sites on a triangular lattice, forming a $\sqrt{3}a \times \sqrt{3}a$ hexagonal superlattice, as seen in Figure 2-8. According to Kambe *et al.*,³⁵ at temperatures below 220 K, the Li on successive layers occupy each of the three available superlattices, in what is referred to as an α, β, γ arrangement. Furthermore as LiC_6 is heated above 720 K, the superlattice melts entirely, allowing the Li atoms to occupy all honeycomb sites randomly.³⁴

Stage-2 is observed for $\text{Li}_{0.5}\text{C}_6$ at room temperature. As noted previously, this means that only every second gap between graphite layers contains intercalated lithium. Stacking is also AAA for stage-2. Within each occupied layer the structure is the same as for stage-1 LiC_6 . The stage-2L phase also has intercalant in every second gap, but not all of the superlattice sites are occupied, leading to a composition of $x \approx 0.35$. The structure of the higher phases, stage-3 and stage-4, are not very well understood.

Another area of considerable interest is the degree of charge transfer (CT) between the intercalant and graphite upon intercalation. Because lithium is extremely electropositive it is a strong electron donor. Charge transfer in this class of materials, donor GICs, is much better understood than in acceptor GICs, in which the graphite transfers charge to the intercalant. For lithium in graphite the charge transfer is thought to be almost completely ionic, with CT values from 0.9 to 1.0, signifying that almost all of the lithium's one valence electron is donated to the graphite host.³⁶

2.3.2 Intercalation in Disordered Carbons

The study of intercalation in disordered carbons is a fairly recent endeavor, and most of this work has been done by electrochemical intercalation, the details of which will not be covered until *Chapter 5*. The basic results of this research are applicable to intercalation in general, and will be described here.

2.3.2.1 Disorder and the Suppression of Staging in Carbons

For disordered carbons, such as coke below 2000°C, the formation of staged phases has not been observed. Instead the average layer spacing increases continuously as lithium is intercalated, as determined by *in-situ* X-ray diffraction experiments.³⁷ These experiments also showed that the disorder of the coke, as measured by the width of the (002) diffraction peak, was unaffected by the intercalation process. Upon de-intercalation the average layer spacing returns to its previous value.

In graphite, the layer registry adjusts from ABAB stacking, to AAAA stacking as lithium is intercalated, with the lithium atoms occupying 'nested' sites between the AA stacked layers, in the centers of the honeycombs above and below.³⁵ This gives all sites the same binding energy, and the major contribution to the variation in chemical potential of the intercalated lithium is due to lithium-lithium interactions. However, in disordered carbons, the turbostratic layers are unable to register, leading to a variation in site energy depending on the local environment. Assuming this variation is large enough, the lithium atoms will therefore fill the sites lowest in energy first, and not cluster on adjacent sites of the same layer. Thus the disorder of the host will suppress the formation of staged phases. This was shown experimentally and modeled phenomenologically by Dahn *et al.* for disordered petroleum cokes.³⁷ They also showed that as the coke was heated above 2200°C, and the turbostratic disorder was relieved, staged phases could once again be observed.

2.3.2.2 The Reversible Capacity of Soft Carbons

For soft carbons heated to 1000°C the reversible capacity, x_{\max} in Li_xC_6 , is approximately 0.8. As the carbon is heated to 2000°C, x_{\max} drops steadily to a value of 0.4. Further heating leads to an increasing reversible capacity, reaching a maximum $x_{\max} > 0.9$ at 3000°C, close to that of graphite. As discussed in section 2.1.2, the major parameters describing the disorder of soft carbons are g , the fraction of organized carbon, and P , the probability that adjacent layers are not registered. These parameters can also be used to explain the variation in reversible capacity as a function of heat treatment temperature. For

the low temperature carbons, the fraction of organized carbon is near 0.5 and the random stacking probability is 1. These extremely disordered carbons can intercalate about 0.9 lithium per carbon. As they are heated g increases to 1 by 2000°C, while P remains virtually unchanged. These organized, but turbostratically disordered carbons do not intercalate well because there are few sites where the lithium atoms can nest properly. Finally as the carbon is heated to 3000°C the turbostratic disorder is relieved, P approaches 0, and the carbon becomes graphitic, allowing 1 lithium per 6 carbon atoms to be intercalated. The effect of P on the reversible capacity of a wide variety of soft carbons heated above 2000°C (where $g=1$) is shown in Figure 2-9. The capacity can be well fit by the dashed line, which has the equation $Q=372(1-P)$ mAh/g, where Q is the capacity. This suggests that no lithium can be intercalated between layers that are organized, but not registered.

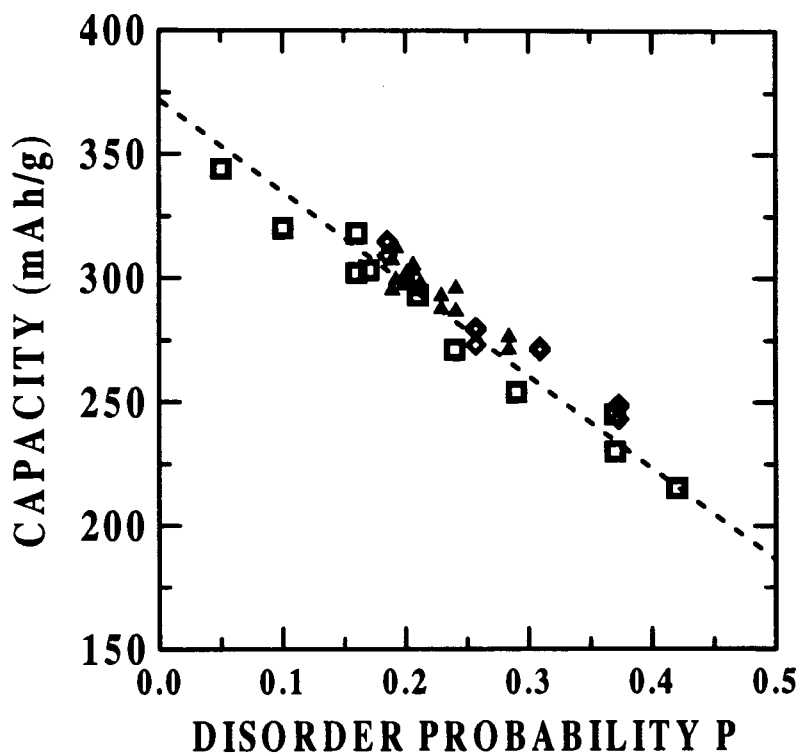


Figure 2-9 Reversible capacity versus P for soft carbons heated above 2200°C, from reference 86.

Chapter Three

3. Experimental - Part I: Synthesis of B_2C_{1-z}

3.1 Previous Work on Synthesis of B_2C_{1-z} Solid Solutions

The study of boron solubility in carbon has gone on for about a century, primarily due to the fact that the addition of boron containing compounds to a carbon has a catalytic effect on the graphitization process. This work will be discussed in two parts: The classical synthesis by solid state reaction under equilibrium conditions, generally at temperatures above 2000°C, and the newer synthesis by chemical vapor deposition in the range 800°C to 1000°C.

3.1.1 Synthesis by Solid State Reaction

Early work on the substitutional solid solubility of boron, silicon and phosphorus in carbon and graphite is well reviewed by Marinkovic in *The Chemistry and Physics of Carbon, Volume 19*.³⁸ Most of the research on the solid solution of boron in graphite by direct reaction was performed in the 1960's. Typically the synthesis was performed by grinding together graphite and boron carbide (B_4C), and heating under inert atmosphere to some final temperature. In 1967 Lowell published an equilibrium phase diagram for the boron-carbon system.¹⁶ It is reproduced in Figure 3-1, and shows that the maximum boron concentration attainable is approximately 2.35%, at 2350°C. Graphite was shown to have an a -axis expansion and a c -axis contraction with increasing boron concentration, as illustrated by Figure 3-2. The reasons for these relationships were not given. The amount of dissolved boron was measured by assuming that the unit cell dimensions are linearly dependent on the boron concentration, however the method for normalizing to the actual concentration was not discussed. Lowell's argument for substitutional, rather than interstitial boron, was based on the variation of the unit cell dimensions as well as the density of the final product. No

other evidence for the substitutional incorporation of the boron was presented.

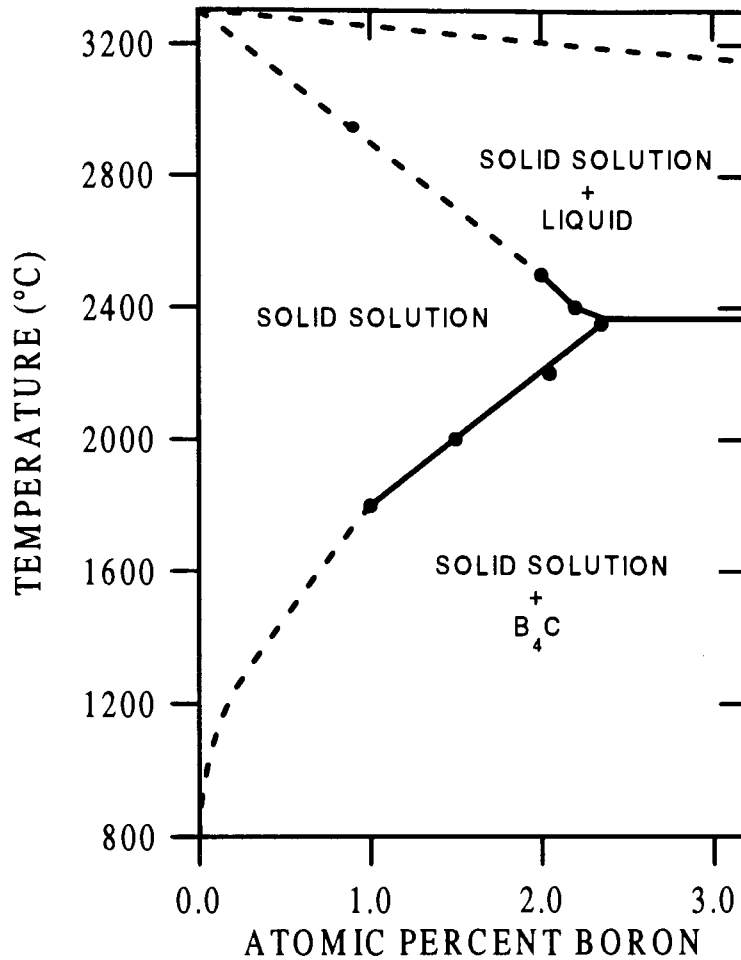


Figure 3-1 Boron-carbon phase diagram from reference 16.

There were also several studies of the effects of low levels of boron doping ($\leq 0.5\%$) on the electronic and magnetic properties of single crystal and polycrystalline graphite in order to determine the shift in the Fermi level as a function of boron concentration.^{39,40,41} Specifically, measurements of the diamagnetic susceptibility and Hall coefficient were compared to calculations to determine the shift. The Fermi level was seen to shift downwards with the addition of boron, from 0.027 eV above the bottom of the conduction band in pure graphite, through the conduction band edge at 1.40×10^{-4} B/C atomic ratio, and finally to -0.24 eV at 0.5% boron.⁴¹ The electrical conductivity of doped single crystal graphite was observed to decrease with increasing boron concentration, thought to be due to

the increased scattering by the boron atoms more than compensating for the additional holes produced in the valence band. By contrast, the conductivity of polycrystalline graphite, which is substantially lower than single crystal graphite to begin with, was found to increase with boron concentration. This is most likely because the number of boron atoms added compared to the number of defects already present is small, and thus the addition of holes is the dominant effect.³⁸

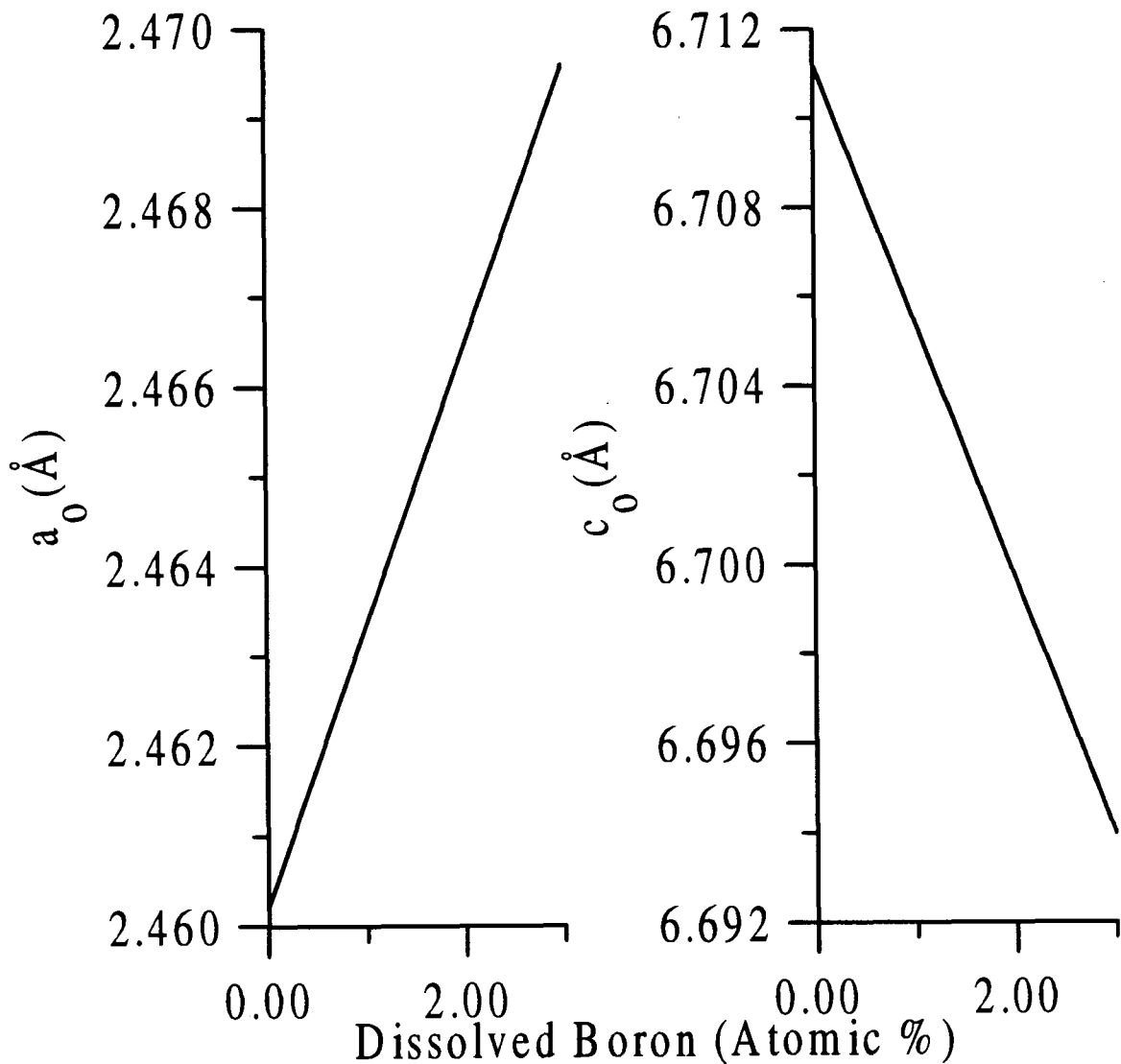


Figure 3-2 Variation of graphite a and c lattice constants with boron concentration from reference 16.

3.1.2 Synthesis by Chemical Vapor Deposition

The situation remained basically unchanged until the mid to late 1980's, when Bartlett's group produced a series of $B_xC_yN_z$ materials (N is nitrogen) at relatively low temperatures, by chemical vapor deposition (CVD)^{17,42,43}. For the purely boron and carbon containing materials, the carbon sources used were typically benzene (C_6H_6) or acetylene (C_2H_2), and the boron source was boron trichloride (BCl_3). Films were deposited in a quartz tube on a variety of substrates, resistively heated to temperatures from 800°C to 1000°C. The total pressure was approximately 800 torr. These films were reported to have up to 25% boron, as determined by Rutherford Backscattering.

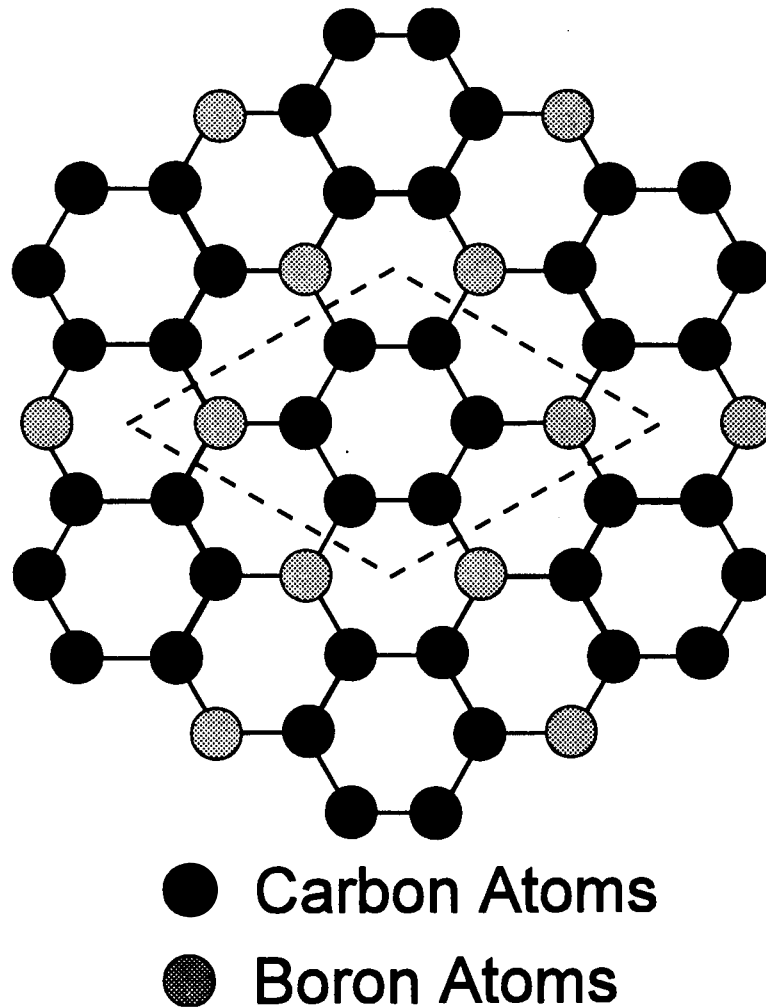


Figure 3-3 Proposed single layer structure of BC_3 from reference 42. The unit cell is outlined by the dashed line.

The investigators suggest the existence of a hexagonal BC_3 phase shown in Figure 3-3. The reason that these high boron concentrations are possible, seemingly in conflict with the phase diagram of Lowell, is that CVD is not an equilibrium process. It is an atom by atom or molecule by molecule process, with temperatures too low for rearrangement to the equilibrium structure. Although they intercalated some of these materials with fluorine, fluorides⁴³ and potassium,⁴⁴ no studies of lithium intercalation were performed. Again there was limited evidence for substitutional boron.

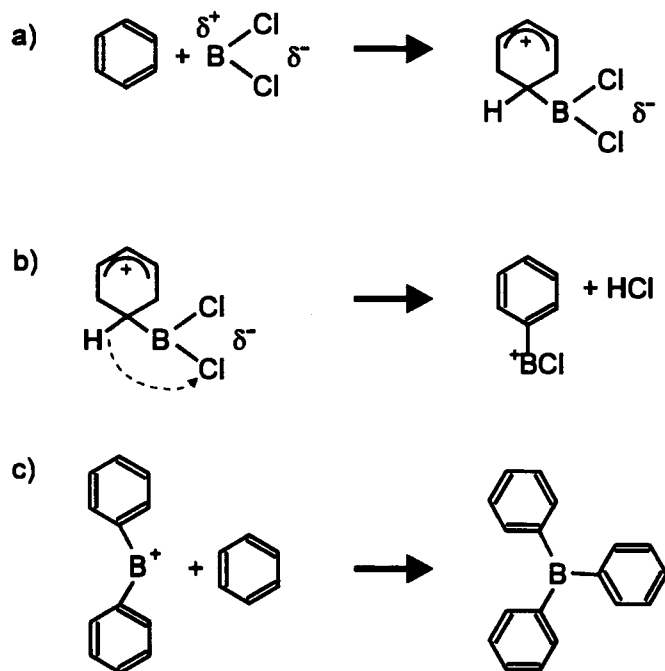


Figure 3-4 Proposed mechanism steps for deposition of B_2C_{1-2} from reference 45.

3.1.2.1 Proposed Mechanism

The mechanism for this vapor phase reaction has not been well studied, but a reasonable suggestion for the formation of BC_3 has been made by Jones *et al.*⁴⁵ They propose a Friedel-Craft-like reaction, most of which is presented in Figure 3-4. The initial step is the electrophilic substitution of a boron radical, or some polarized form of boron chloride (Figure 3-4a), leading to the elimination of HCl and the formation of a boron phenyl free-radical (Figure 3-4b). This complex attacks another benzene ring (not shown), leading to another boron free-radical containing two phenyl rings. The process continues with the

attack of a third benzene ring, forming the stable triphenyl boron molecule (Figure 3-4c). Each hydrogen atom on each of the incorporated benzene rings is then substituted by a boron radical until all the hydrogen atoms are gone, and the final BC_3 product illustrated in Figure 3-3 is formed. Although this mechanism is sufficient for the formation of BC_3 , an additional mechanism is required for the formation of B_zC_{1-z} solid solutions with $z < 0.25$. It is likely that this additional mechanism is similar to the pyrolytic decomposition of benzene, but some form of boron chloride must play a catalytic role, since the rate of deposition of films at $900^\circ C$ is much greater than for the deposition from pure benzene at the same temperature.

3.2 Introduction to Chemical Vapor Deposition

Chemical Vapor Deposition (CVD) has become a very important tool in the last few decades for the production of semiconductor thin films for electronics applications. The technique itself is much older though, tracing its history back to 1880 when it was used to deposit pyrolytic carbon for incandescent lamp filaments.⁴⁶ CVD is defined by Powell as “a method of plating in which the deposits are produced by heterogeneous gas-solid or gas-liquid chemical reactions at the surface of a substrate.”⁴⁷ An important feature of CVD for our work is that it is an atomistic process, meaning that the film is created atom by atom, allowing the deposition of materials that are too unstable to be created via an equilibrium process. It can be used to produce films that are amorphous, poly-crystalline, or single-crystal depending on the chemistry and conditions involved in the deposition. There is a lot of available information related to the growth of high quality films for electronics applications. Most of this is not extremely important to the work discussed in this thesis, because the goal here is to produce a material rather than a film, and the properties of the film itself are of less interest. It is useful, however, to understand the basics of chemical vapor deposition to be able to control the properties of the material. These are reviewed by Powell in *Vapor Deposition (1966)*.⁴⁷

3.2.1 Factors Affecting Deposition

There are many factors that affect the chemical and physical properties of the deposited film. This is both useful and an annoyance. It enables fine control over the

properties of the film, but it also produces a huge phase space that must be searched to completely understand the deposition process. In the following sections, there are descriptions of some of the most common parameters, and their likely effects on the deposited product.

3.2.1.1 Effect of the Substrate

The substrate can play an important role both in the deposition of a film and in the adhesion of the film after deposition. In some cases the substrate plays an essential role in the chemistry of the deposition. For example, the substrate may act as a reducing agent for a metal halide vapor, while it is in turn converted to a volatile metal halide. The film may also be dissolved in the substrate, forming an alloy, or react with the depositing material to form a stable coating. There can be catalytic effects involved, where the deposition only occurs at active sites, which would lead one to expect that the reaction would stop once these sites are covered. However under some conditions, such as in the deposition of a liquid, the geometry can be arranged so that deposited material flows or diffuses away from the active site. The substrate may provide good nucleation sites for the growth of the film, increasing the rate of initial deposition. Finally, the substrate is of course of great importance in the production of epitaxial semiconductor films, where it acts as a template for the ensuing deposition.

3.2.1.2 Temperature Effects

Probably the single most important factor affecting the deposition process, after choosing the chemistry, is the temperature. It obviously has a great effect on the final products because of the temperature dependence of the competing reactions that are occurring over the substrate. This aspect will not be discussed here however, because it is entirely dependent on the individual chemistry involved. There are some more general ways in which the temperature affects the nature of the deposited film. In most cases the higher the temperature the larger the crystallites, ranging from virtually amorphous to macroscopic single crystals. This is because the atoms or molecules have enough kinetic energy at high temperature to allow rearrangement to the lowest available energy configuration, whereas those at low temperature are generally confined to the region where they first interact with

the film surface.

The film properties may also be affected by the temperature in other ways. If the precursors are not very stable, they may react at greater distances from the substrate as the temperature is increased. This can produce a fine powder "snow" that drops down upon the substrate, and is not a coherent film. The adhesion of the film to the substrate can also be affected by temperature since the interdiffusion of the film and the substrate is usually temperature dependent.

3.2.1.3 Other factors

Other important parameters of the deposition process are the total pressure, the residency time and the concentrations of reactants. These parameters are all interrelated, and their effects vary greatly with the chemistry in question. Generally though, the higher the pressure or concentration, the more finely crystalline the deposit.

3.2.2 Deposition of Carbon Compounds

More carbon has been deposited than any other material.⁴⁷ Several million tons per year of carbon blacks, produced by the partial combustion of organic materials, are now used primarily in the rubber industry, but also in inks, plastics, carbon papers, toner, and many other applications. The organic precursors used in industrial processes are typically methane, ethane, acetylene or aromatics such as benzene. Although many of these depositions have been studied in detail, mechanisms are not known for many of the reactions. The exact elemental make-up, crystal structure, microstructure, and morphology have all been shown to depend on the type and concentrations of the source materials, the temperature both at the substrate surface and above it, the pressure, the nature of the substrate, and the amount of recirculation of the product gases, making a thorough understanding of the processes involved all but impossible.

3.2.3 Deposition of Boron Carbide

We know that the equilibrium condition for a mixture of boron and carbon, when the boron concentration is greater than about two percent, is a two phase mixture of carbon and boron carbide, B_4C . Since this is exactly what we want to avoid in the production of B_zC_{1-z}

solid solutions, it is instructive to briefly study how the deposition of various boron carbides are accomplished.

A film of B_6C was deposited by heating a carbon rod in the range $1750^\circ C$ to $1950^\circ C$ in the presence of BCl_3 and H_2 .⁴⁸ In another study, a mixture of B_4C and B_2O_3 was obtained on a tungsten filament heated to incandescence in an atmosphere of BCl_3 , CO and H_2 .⁴⁹ These processes are probably not relevant to the work involved here because neither of them involve the deposition of carbon from a hydrocarbon. In one case however, toluene (methyl benzene), boron trichloride and hydrogen were mixed over a molybdenum substrate at $800^\circ C$ to $1200^\circ C$, producing a B_4C film.⁴⁷ This suggests that toluene should probably be avoided as a carbon source.

3.3 Apparatus

The CVD system used for these syntheses was a CVD-300-M (Vactronic, Bohemia, New York). The system is pictured schematically in Figure 3-5. The gaseous precursors are fed through Brooks 5850D mass flow controllers. These controllers determine the flow rate by measuring the temperature difference between sensors upstream and downstream of a heater coil, and adjusting a piston to keep the flow rate to a constant, calibrated value. They have a rated error of $\pm 1\%$ of full scale, which is 200 scc/min (cubic centimeters per minute under standard conditions). However, the pressure of the benzene source was outside the linear region of the controllers, and thus a manual calibration was required. This consisted of evacuating the chamber, flowing the source gas through the controller and timing the rise in pressure, over the pressure region of interest. Normalization was done using the ideal gas law.

From the flow controllers, the gases pass through control valves and into a 75 mm diameter quartz reactor tube, where they are mixed. The tube is heated by a 16 inch long hot-wall furnace, capable of $\sim 1000^\circ C$. Deposition occurs on the walls of the quartz tube, and on substrates placed in the hot zone. From the reactor, the output gases pass through a particle filter, a process valve, and into liquid nitrogen cooled cold trap where most of the waste gases solidify. The remaining gases then pass through an automatic pressure control valve, a

manual shut-off valve and into a direct drive roughing pump. Exhaust from the pump goes to the fume hood line. Pressure measurement is by a MKS Baratron Absolute Pressure Transducer, which is located just forward of the reactor hot zone. Two models were used for this work with pressure ranges of 0-10 torr and 0-1000 torr, each with an accuracy of 0.5% of the reading. The transducer capacitively measures the flexing of one membrane relative to a reference membrane and outputs a voltage proportional to the pressure, from 0 to 10V. The voltage is applied to a MKS 252C Exhaust Valve Controller which regulates the automatic pressure control valve, thus producing a stable feedback system to maintain a constant pressure.

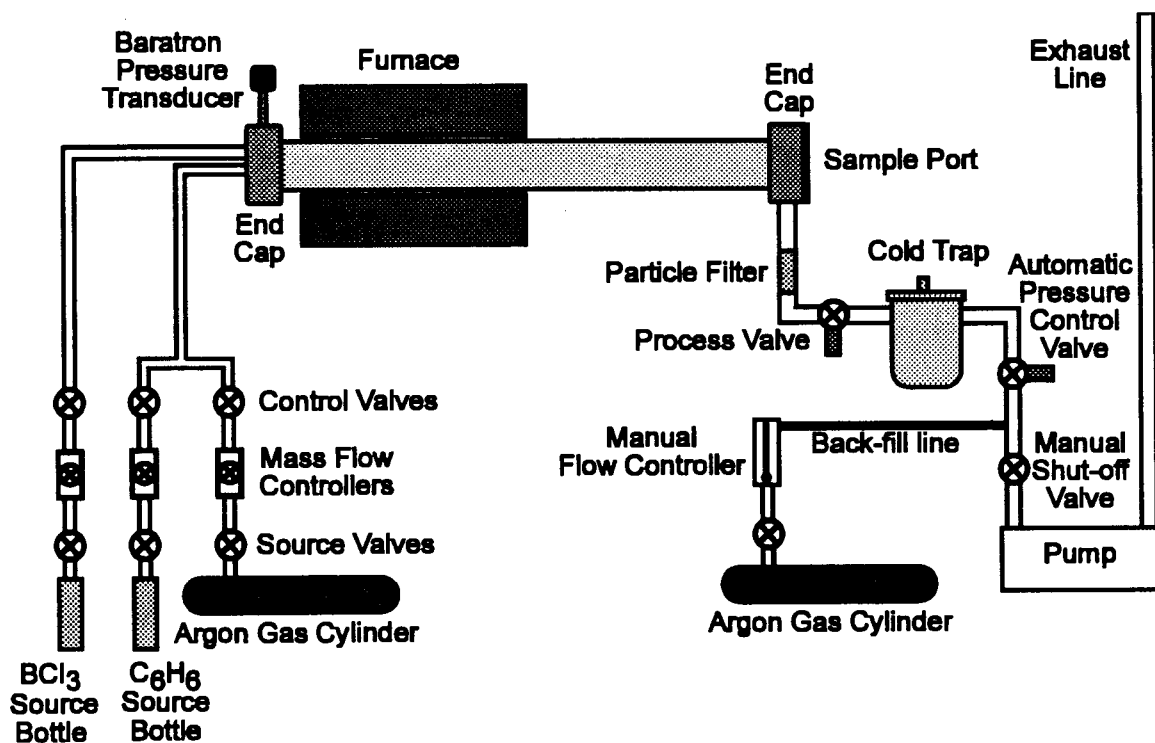


Figure 3-5 Schematic drawing of CVD system

3.4 Low Pressure Synthesis

The first group of syntheses was made using the 0-10 torr Baratron pressure transducer, usually at 5 torr total pressure. Materials produced in this way will be referred to as 'Low Pressure' samples. What follows is a description of the general procedure for the

deposition of films. The parameters that were varied from run to run will be mentioned, but the effects of these variations on the deposition will be dealt with subsequently.

3.4.1 General Deposition Method

First, the substrate was slid into the center of the hot-zone of the furnace via the sample port in the reactor tube endcap, which was subsequently sealed. The glass-wool of the particle filter was replaced, and all ports of the system were closed. The system was then pumped down to, typically, less than 20 millitorr. It was impractical to pump below this level due to the large system size, rubber o-ring connections, and out-gassing of previously deposited materials throughout the system. The system was routinely tested for leaks by closing the manual shut-off valve, and looking for a rapid rise in pressure, signaling a leak. Next, with the gases valved off at the source, the mass flow controllers to be used during the experimental run were opened, as were the control valves between them and the system. In this way the gas lines were pumped down until the system came down to its previously attained pressure. Once the system was verified to be "leak-free", the source lines were closed off from the system, and the gas sources opened to their respective lines. The water flow was then started to the reactor tube endcaps, to prevent the o-rings sealing the tube from melting. The temperature controller was then programmed to take the furnace to its operating temperature, usually 900°C. During the temperature ramp, argon gas (UHP) was fed into the system through a mass flow controller at ~100 scc/min to flush the reactor tube of gases produced by the outgassing. As the furnace neared the target temperature, the argon was shut off, and the cold trap was filled with liquid nitrogen.

At this point the run is ready to begin. The mass flow controllers were checked for the correct settings, then set to control, and the control valves opened. The valve controller was switched to automatic, with the target pressure set. Within minutes deposition could usually be seen to be occurring on the tube walls at the exit of the furnace, on the downstream side. The deposition was allowed to continue for a specified time, between 30 minutes and 5 hours, with only the addition of liquid nitrogen to the cold trap every 30-60 minutes. The pressure, temperature and flow controller readings were checked periodically

for correct operation.

At the end of the run, the mass flow controllers were shut off, control valves closed, and the furnace switched off. The reactor was allowed to cool to less than 100°C under argon flow, before removing the samples. The cold trap was then valved off, and removed to the fume hood for venting. In later depositions, where the material was collected from the reactor tube walls, the tube was allowed to cool to room temperature, typically overnight, under static argon atmosphere, with the cold trap valved off and removed at 100-200°C. The samples were then marked for orientation in the tube, and stored away. Some samples slated for electron spectroscopy measurements were stored in vials, under argon. If the material deposited on the tube walls was desired, it was scraped out using a steel blade. Generally the different areas of the tube, which were at different temperatures, produced films which varied in appearance, from black and sooty, to gray and dendritic, to gray and optically flat (mirrored). These different morphologies were collected, separated as much as possible, and stored in vials, sorted by appearance.

Once all samples were collected, the tube was replaced, with the ends left open, and the furnace heated to ~900°C in air to “burn-off” the remaining carbonaceous material. In this way the tube was cleaned between runs. In the case of the high boron content films the oxidation resistance made it necessary to wash the inside of the tube between repeated heatings to remove the boron oxide film, and completely remove the unwanted material.

3.4.2 Chemical Sources (Precursors)

Boron trichloride was the only boron source used. BCl_3 and BBr_3 are the most commonly used industrial boron sources. Both methane and benzene were tested as carbon sources. Methane was tried initially, but showed very poor deposition rates, with films barely visible after an hour of depositing. Benzene on the other hand showed very good deposition, and was selected to use for the rest of the syntheses. We hypothesized that a six-member aromatic ring precursor, such as benzene would provide a more organized structure, due to the extended honeycomb aromatic structure of graphite. The rate of deposition with BCl_3 and benzene was significantly higher than for benzene decomposition alone. This is most

likely due to the driving force of the reaction of BCl_3 and benzene to produce HCl , producing reactive radicals that have high reaction rates. The benzene rate was varied from 6 scc/min to 20 scc/min, but was typically held at 16 scc/min, while the BCl_3 flow rate was varied from 0 scc/min to 80 scc/min.

3.4.3 Temperature

We experimented with a range of deposition temperatures, from 800°C to 1000°C . The rate of deposition increased visibly with temperature between 800°C and 900°C , and at 1000°C corrosion of the quartz reactor tube became a serious problem, caused, we believe, by hydrogen free radical attack. Although Shen *et al.*⁴⁴ reported higher boron concentrations for films produced at 800°C , the amount of material deposited was insufficient for the study of intercalation, and thus was not useful for us. In addition to the corrosion problem, we did not want to deposit at higher temperatures in order to keep the B_2C_{1-2} from rearranging to form its equilibrium composition of graphite and B_4C . For these reasons we selected 900°C as the deposition temperature, and to study the effect of subsequent heat treatment of the films separately.

3.4.4 Substrates

The primary substrate used for the materials discussed in this thesis was quartz. It is convenient because it can withstand high temperatures, and is available as microscope slides at reasonable cost. Furthermore, since later depositions would use material deposited on the inside of quartz tube, it made studies conducted on the films deposited on the slides more relevant. Films deposited on the slides were gray, with an optically flat, mirrored finish, while those deposited on unpolished quartz had a dull gray finish. As with all substrates, deposition occurred on both sides, even when the bottom quartz surface was in direct contact with a flat quartz boat used to hold it. The appearance of both sides was usually the same, though the thickness was less on the hidden surface.

Although the majority of films were deposited on quartz, a wide variety of substrate materials were tested. Because a conductive backing was initially desired to make electrochemical cells with the film as deposited, on its substrate, four metal foils were tried:

Stainless steel, nickel, copper and tantalum. The steel reacted with the free chlorine to produce a variety of coloured impurities, some of which were *deliquescent* (spontaneously dissolved in their own waters of hydration), and was thus rejected for future use. Nickel foil reacted with the boron to produce Ni_3B , evident upon X-ray diffraction analysis, apparently consuming all of the available boron in this way, and was thus also rejected. Tantalum foil was used successfully, with no apparent side reactions, but the deposition rate on Ta was quite low, producing a gray, matte finish film. The last metal substrate tested was copper. It too showed no side reactions, and the deposition rate was higher. Unfortunately, at 900°C small amounts of copper compounds are deposited onto the reactor walls, and some copper diffuses into the deposited carbon film. These properties made it less than ideal, but because the film adhered poorly to the copper, due in part to differential thermal contraction with cooling, it made recovery of large amounts of material easier. The films deposited on copper tended to have a shiny metallic appearance, not quite flat enough to be mirrored.

Two other substrates that were evaluated were single crystal silicon wafer, and highly oriented pyrolytic graphite (HOPG). The silicon was polished only on one side, and the films deposited on it were mirrored on that side, but not the reverse, unpolished side. The films were no different than those deposited on quartz, so there was no reason to continue the use of Si wafers. The HOPG substrates were actually intended for use as X-ray monochromators. Again, the film qualities produced were acceptable, but the anticipation that analysis would be more difficult using a carbon substrate, and the limited supply of monochromators led us to discontinue use of the HOPG.

3.5 High Pressure Synthesis

The second group of syntheses was made using the 0-1000 torr Baratron. This group, which we will refer to as 'High Pressure' synthesis, was typically performed at 30-50 torr. The goal of these runs was to produce a larger quantity of deposited material for use in the study of subsequent heat treatment temperature on structure and lithium intercalation. Calibration of the flow controllers was performed again for this pressure range. The general deposition method is basically the same as for the low pressure synthesis. The only major

difference is that the automatic pressure control valve does not function well in this pressure range, and thus the manual valve had to be closed down, and argon gas leaked in through the back-fill line to keep the pressure at the correct value. Depositions were performed only on copper foil and quartz substrates, at 900°C, and the resulting films were gray, with surface appearance depending on the smoothness of the substrate. There was significantly more deposition in the cool-zone of the reactor tube in the high pressure synthesis compared to the low pressure runs. This consisted of black, sooty powder close to the hot-zone, and yellow tar further along. Care was taken not to contaminate the samples with these impurities.

3.6 Table of Materials discussed in Thesis

Sample ID	Temperature (°C)	Substrate	C ₆ H ₆ Flow Rate (scc/m)	BCl ₃ Flow Rate (scc/m)	Pressure (torr)	Deposition Time (hours)
BW62I	900	Quartz	15.9	50	5	1.5
BW64I	900	Quartz	5.9	80	5	1
BW65I	900	Quartz	18.3	20	5	0.5
BW66I	900	Quartz	15.9	0	5	0.5
BW68I	900	Quartz	15.9	5	5	0.5
BW69I	900	Quartz	15.9	10	5	0.5
BW70I	900	Quartz	15.9	3	5	0.5
BW75I	900	Ta	15.9	50	5	1.2
BW77I	900	Quartz	15.9	9	5	0.5
BW78I	900	Quartz	15.9	13	5	0.5
BW130I	900	Quartz	15.9	5	5	1
BW5II	900	Quartz	15.9	0	5	4
BW16II	900	Quartz	15.9	12	5	5
BW21II	900	Quartz	15.9	3	5	4
BW36II	900	Quartz	15.9	30	5	5.3
BW46II	900	Quartz	15.9	5	5	2.7
BW84II	900	Quartz	15.9	20	5	5.2

BW125II	900	Quartz	14.8	34.4	30	5
BW135II	900	Quartz	14.8	0	40	2
BW141II	900	Quartz	14.8	21.3	30	5.2
BW146II	900	Quartz	14.8	8.6	30	2.5
BW16III	900	Quartz	14.8	0	30	5

Table 3-1 Synthesis conditions of materials discussed in this thesis.

Chapter Four

4. Experimental - Part II: Characterization of Materials

4.1 Description of Techniques and Experimental Methods

4.1.1 X-ray diffraction

X-ray powder diffraction was the primary method used to investigate the structure of the samples produced in this work. The three different diffraction techniques employed in this investigation were powder diffraction on the powder samples and grazing incidence and rocking curve diffraction on the films.

4.1.1.1 Powder Diffraction

X-ray measurements of the powder samples that were obtained by grinding the deposited films were performed on two diffractometers. The first was a Siemens D5000 θ - θ diffractometer with a Cu target X-ray tube operating in the Bragg-Brentano and flat-plate sample geometry. In a θ - θ diffractometer, the sample is fixed, and for powder diffraction the tube and detector arms are each stepped in opposite directions through an angle θ , providing a total scattering angle of 2θ . The slits were 0.5° divergence, 0.5° anti-scattering, and 0.6 mm receiving, providing a resolution of $\sim 0.12^\circ$. The other diffractometer is a Phillips θ - 2θ diffractometer, also with a Cu target X-ray tube, operating in the Bragg-Brentano geometry. In this diffractometer the tube position is fixed while the sample and detector are rotated through θ and 2θ , respectively. Slits on this diffractometer were typically 0.5° divergence and 0.2 mm receiving, providing a resolution of $\sim 0.15^\circ$.

Two types of sample holders were used for the powder samples. One was a stainless steel well holder, with well dimensions (in mm) 12 long by 20 wide by 2 deep, that was used

when enough sample existed to fill it. For most powder samples however, a zero background holder was used. This consists of a piece of single crystal Si wafer, cut along the (510) plane, mounted on an aluminum backing. The high quality of the Si crystal means that the destructive interference is nearly complete away from the Bragg condition, and because the structure factor of the (510) diffraction peak is zero for the diamond structure there are no Bragg peaks in the region of interest. This provides a substrate with very low background counts. The sample is attached to the holder by making a slurry of the powder with acetone, and allowing it to dry. The thickness of the samples were typically $<100\ \mu\text{m}$.

4.1.1.2 *Grazing Incidence Diffraction*

Grazing incidence diffraction measurements were made using the Siemens diffractometer on the films as deposited on the quartz substrates. In this geometry, pictured in Figure 4-1, the X-ray tube is held fixed at some small angle, while the detector is scanned through 2θ . The samples, on 1 mm thick quartz slides, were measured in an aluminum holder, with a 1 mm deep recess, which held the surface of the quartz at the zero plane of the diffractometer. Long Soller slits are used on the detector arm to improve angular resolution. The purpose of using this geometry is to eliminate the overwhelming diffuse scattering from the quartz substrate. The theory behind this technique is well described by Feidenhans'1⁵⁰, and is outlined briefly here.

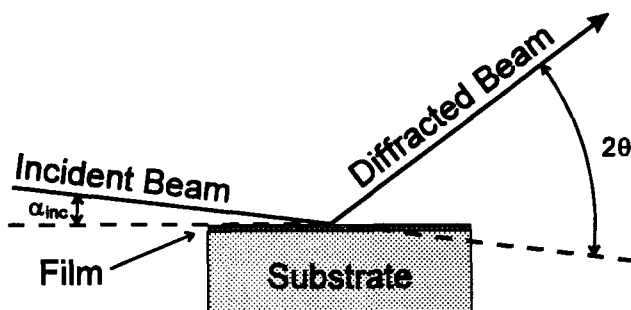


Figure 4-1 Geometry of grazing incidence diffraction

As we know, total reflection of light occurs when it travels from a higher index of refraction material to a lower one at an angle less than the critical angle, where the angle of incidence is taken as the angle between the incident radiation and the plane of the sample. In the visible light regime this phenomenon manifests itself as *total internal reflection*, and is the basis for such processes as light propagation in optical fibers. The index of refraction is wavelength dependent however, and for most materials the index of refraction in the X-ray region is slightly less than that of air. Thus *total external reflection* can occur for sufficiently low incident angle. The critical angle, α_{crit} , is defined as:

$$\cos \alpha_{crit} = n \quad \text{Equation 4-1}$$

where n is the index of refraction of the material. For carbon the critical angle is 0.217° for Cu K_α radiation. Taking

$$\beta = \frac{\lambda\mu}{4\pi} \quad \text{Equation 4-2}$$

as the imaginary part of the index of refraction, due to dispersion, the 1/e penetration depth can be calculated, including absorption as⁵⁰:

$$\Lambda_i = \frac{1}{\sqrt{2}k} \left(\sqrt{(\alpha_{inc}^2 - \alpha_{crit}^2)^2 + 4\beta^2} + \alpha_{crit}^2 - \alpha_{inc}^2 \right)^{-1/2} \quad \text{Equation 4-3}$$

where k is the magnitude of the X-ray wavevector ($2\pi/\lambda$), α_{inc} is the incident angle, λ is the X-ray wavelength (1.54 Å for Cu K_α), and μ is the linear absorption coefficient of the material at the X-ray wavelength. While for incident angles less than α_{crit} , the penetration depth is close to zero, just above it the depth is limited by absorption, and is strongly angle dependent. Figure 4-2 shows the calculated penetration depth versus incident angle for Cu K_α radiation incident on carbon. For angles much larger than the critical angle the penetration depth increases asymptotically to the normal penetration depth, including absorption but neglecting refraction, of

$$\frac{\sin \alpha_{inc}}{\mu}$$

Equation 4-4

shown by the dashed line in the figure. By choosing an angle of incidence between 0.22° and 0.5°, one can control the depth being probed from approximately 1 μm to 20 μm, which is the typical range of thickness of the films, and thus eliminate diffuse scattering from the quartz substrate. In the inset to Figure 4-2 the calculated penetration depth just below the critical angle is shown. For thin carbon films (40-200 Å), an angle of incidence below the critical angle, between 0.1° and 0.22°, can be used to effectively reduce the signal from the substrate.

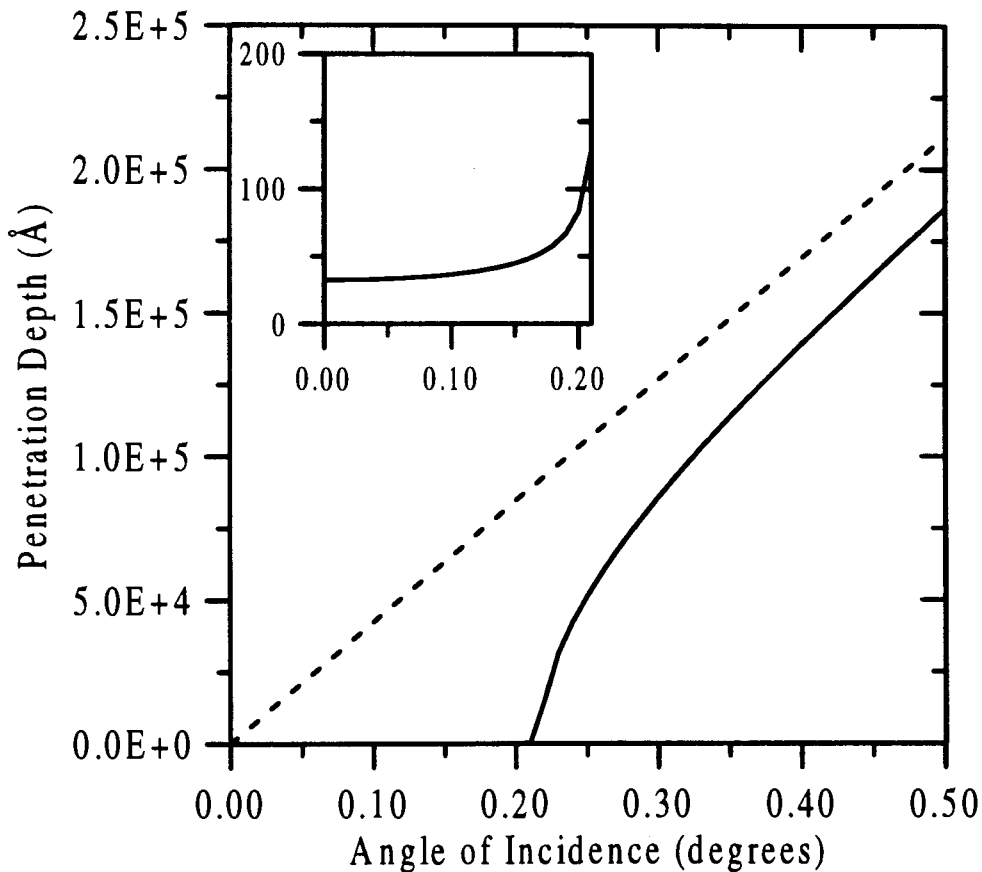


Figure 4-2 $1/e$ penetration depth versus angle of incidence for Cu K_{α} radiation incident on carbon. The solid line is given by Equation 4-3 and the dashed curve is $\Lambda = (\sin \alpha_{inc})/\mu$. The inset is a close up of the penetration depth below the critical angle.

4.1.1.3 Rocking Curves

So called "Rocking Curves" were also measured on several films, for both the (002) and (004) Bragg peaks. Rocking curves were measured with the Siemens D5000 diffractometer by fixing the angle between the X-ray tube and the detector such that the scattering angle, 2θ , is equal to that of a Bragg peak. The tube and detector are then scanned together, maintaining the same 2θ , and the diffracted intensity is approximately proportional to the number of crystallites with the correct orientation to meet the diffraction condition and to diffract into the detector. For an oriented graphitic film, the largest proportion of (002) planes are parallel to the surface, and the number decreases for planes tilted further away from parallel. This technique therefore provides a measurement of the mosaic spread, or the extent to which the crystallites are oriented parallel to the plane of the substrate.

4.1.2 Chemical Composition Determination

It is important to determine the boron to carbon ratio of the samples produced in this work, in order to make quantitative comparison between boron percentage and other properties related to lithium intercalation. Direct determination of boron concentration from X-ray diffraction is not possible because the samples are, for the most part, single phase with no separate boron containing phase. Furthermore there is not enough contrast between the X-ray scattering factors of boron and carbon to fit a single phase reliably with Rietveld-type refinement. Sample sizes are generally too small for neutron diffraction, and in any case the samples are too poorly crystalline for reliable application of the Rietveld method. Other techniques that were considered include X-ray Fluorescence (XRF), which is ineffective for small atomic number elements such as boron and carbon. By elimination, the primary method chosen was Auger Electron Spectroscopy (AES). Comparison of these results with diffraction results provided a calibration curve that allows estimation of boron concentration from the diffraction results.

4.1.2.1 Auger Electron Spectroscopy

AES is a spectroscopy based on the Auger radiationless process that can be used for the chemical analysis of surfaces. In this process, schematically depicted in Figure 4-3, a

core electron is first ionized by an incident electron beam. This vacancy is then filled by an electron from a higher energy level, while a third electron is ejected with the difference in energy of the initial and final states. The kinetic energy of the ejected Auger electron is characteristic of the element and chemical state of the parent atom. Because the Auger electron must reach the analyzer without being scattered to yield useful information, the effective probe depth is only 15-30Å, depending on the energy, and therefore mean free path, of the electron. Therefore it is necessary that the surface being studied is clean of contamination, because of the high surface sensitivity of the measurement.

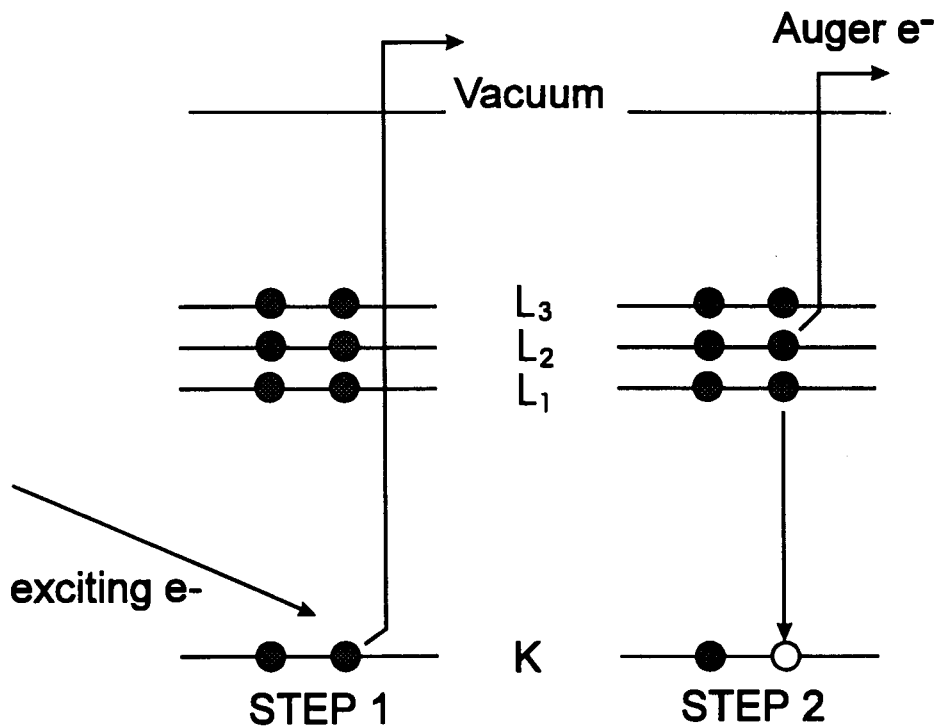


Figure 4-3 Schematic of KL₁L₂ Auger process

The data collected is proportional to the number of electrons in a given kinetic energy interval (N), versus kinetic energy (E). The data is usually differentiated to provide a plot of dN/dE versus E . The Auger intensity of each peak is proportional to the number contributing atoms within the analysis volume. Quantitative analysis for atomic concentrations is performed by comparing the intensity ratios of the peaks in the dN/dE versus E plot with the ratios from a standard containing the same elements in a known

stoichiometry. There are several sources of error associated with this procedure.⁵¹ The electron escape depths in the sample and calibration standard may be different due to differing electronic structure. This leads to a variation in the size of the analysis volume, and thus the number of contributing atoms. Another source of error may occur if the peak shapes are changed due to chemical effects, making the height an inaccurate measure of the intensity. Finally, if the composition of the surface is not the same as that of the bulk, then although the measurement may be accurate, it is not a true indication of the total concentrations in the sample. If sputtering is used to clean the surface, care must be taken to ensure that the composition is not radically changed by the differing sputtering yields of the elements in the film.

The essential components of an AES system include: an ultra high vacuum (UHV) system, an electron gun, and an energy analyzer. Other important accessories are a sputter ion gun for cleaning of the surfaces, and a computer for experiment control and data analysis. The system used was a Perkin Elmer Physical Electronics Division model 595 scanning Auger microscope. The films were transferred to the vacuum chamber (1×10^{-9} Torr) and sputtered using a 3-kV argon-ion beam for about 3 minutes to remove surface species. The boron and carbon KLL Auger electron intensities were measured and then the samples were further sputtered until Auger signals independent of sputter time were obtained. B_4C was used as the calibration standard. When the Auger signals from the sputtered B_4C were corrected for the relative Auger sensitivities from the Handbook of Auger Electron Spectroscopy,⁵¹ the stoichiometry obtained was $B_{4.3}C$, suggesting that the sputter yield of boron and carbon are similar. The compositions of the films were then determined, assuming that the B_4C was stoichiometric. The estimated error in these measurements is $\pm 10\%$.

4.1.2.2 Chemical Analysis

Samples were also sent out to Elemental Research Inc. of North Vancouver for chemical analysis using laser-ablation inductively coupled plasma mass spectroscopy (laser ablation-ICPMS). Calibration is performed by comparison of peak heights to a standard of

similar composition to the sample. This is a fairly new technique and the accuracy for all sample types is unknown. Our experience suggests that it is very poor for substitutional boron in carbon.

4.1.3 X-ray Absorption Spectroscopy

X-ray Absorption Spectroscopy (XAS) can be used to measure properties related to the electronic and local crystal structure of materials. In this technique, the sample is subjected to a beam of X-ray photons and the absorption coefficient is measured as the wavelength of the incident photons is varied over an energy range corresponding to an electronic transition from a core state to an empty state. A schematic diagram of the excitation of a core electron to the unoccupied states above the Fermi level is shown in Figure 4-4. The variable energy photon source is provided by the monochromation of synchrotron radiation produced by an electron storage ring. Measurement of the absorption coefficient can be done by several methods including transmission, fluorescence yield and total electron yield.

In the work presented here, total electron yield (TEY) was used. In the interaction of soft X-rays with matter, photoabsorption followed by emission of a photoelectron dominates by far over all other interactions.⁵² Following this photoemission, the excited atom decays by either fluorescence or an Auger process. Because the photon penetration depth ($\sim 1000\text{\AA}$) is much larger than the electron mean free path, most of the photoelectrons and Auger electrons are inelastically scattered many times on their way to the surface, creating an electron cascade. However, only those electrons produced within $\sim 100\text{\AA}$ of the surface (depending on the material) will have sufficient energy to escape. By collecting all of the electrons that are emitted from the sample and are incident on a detector, regardless of their energy, a signal proportional to the photon absorption within the electron escape depth is obtained. This signal is dominated by electrons with kinetic energy less than 20 eV, often referred to as the “inelastic tail”.⁵²

The two major regions of the XAS spectrum are the X-ray Absorption Near Edge Structure (XANES) (also called the Near Edge X-ray Absorption Fine Structure - NEXAFS)

and the Extended X-ray Absorption Fine Structure (EXAFS). The XANES is the region from the absorption edge to approximately 50 eV above the edge, and the EXAFS is the region beyond that, extending for up to several hundred electron volts. Both of these techniques involve the excitation of core electrons to empty states, however the interpretation of the cause of the modulation in the absorption coefficient is very different in these two regions.

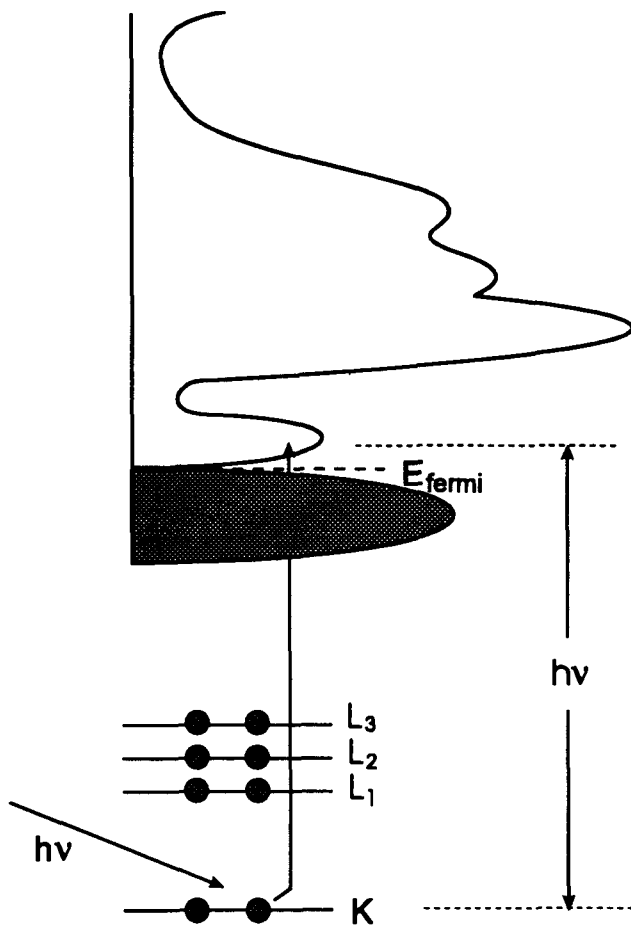


Figure 4-4 Schematic drawing of the excitation of a core electron to an unoccupied state above the Fermi level

In the EXAFS region, the spectrum is dominated by single-scattering of the excited electron back to the absorbing atom, providing information about the distances to neighbouring atoms that is quite easily extracted. Due to the low atomic number of carbon and boron, however, the K shell absorption edges are at fairly low energies (approximately

285 eV and 185 eV respectively), and the EXAFS spectrum is generally much weaker than the XANES features, and is often obscured by other features.

In the near-edge region, the excited electrons have less kinetic energy, giving rise to stronger interactions with atoms and multiple scattering dominates. In this case direct calculation becomes a very difficult problem, requiring complicated approximations.⁵³ Fortunately, there is a simpler, semi-empirical approach. At the absorption edge, the electronic transitions are to empty states just above the Fermi level, and the absorption coefficient exhibits resonance-like features correlated to the density of these unoccupied states.⁵² These empty states may be loosely bound, or a low-lying part of the continuum, and have the symmetry of the atomic orbitals from which they are formed. It is this property that allows us to gain information from the angle dependence of the absorption coefficient.

4.1.3.1 Angle Dependence of X-ray Absorption Spectroscopy

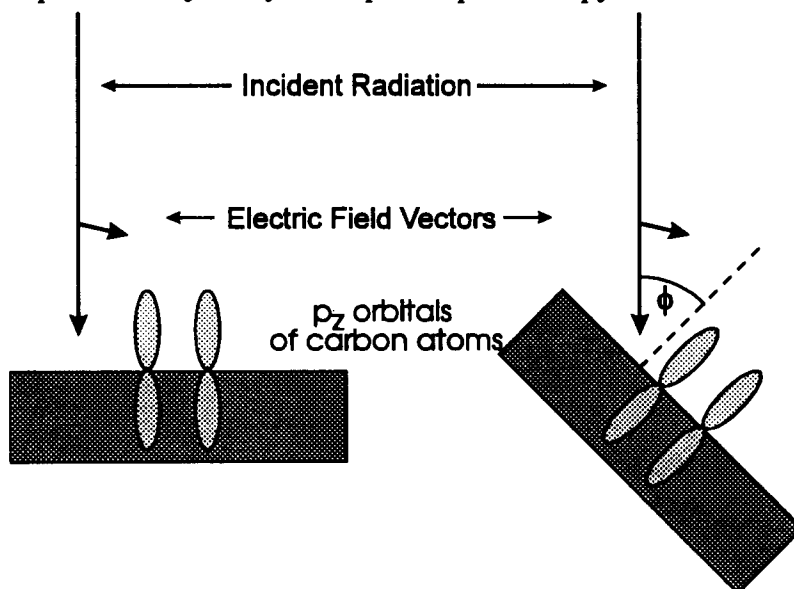


Figure 4-5 Drawing of the incidence of X-rays on an oriented carbon film

If the material under study is a single crystal or an oriented film, the XAS spectrum may depend on the orientation of the sample with respect to the incident photon beam. This is because, according to Fermi's Golden Rule, the transition probability (P_{if}) between the initial and final states depends not only on the density of final states ($\rho(E)$), but also the

magnitude of the perturbation matrix element between the initial and final states:

$$P_{if} = \frac{2\pi}{\hbar} |\langle f | \bar{V} | i \rangle|^2 \zeta(E) \quad \text{Equation 4-5}$$

where \bar{V} is the perturbing potential. For soft X-rays the dipole approximation is valid, and the important matrix elements are:

$$\langle f | \mathbf{e} \cdot \mathbf{p} | i \rangle \quad \text{Equation 4-6}$$

where \mathbf{e} is the electric field of the incident radiation and \mathbf{p} is the linear momentum operator of the electrons. The electric field vector of the X-rays is in the plane normal to the propagation direction of the incident beam, as seen in Figure 4-5. For graphite, the lowest lying unoccupied states (immediately above the Fermi level) are due to the π^* anti-bonding orbitals, constructed from the carbon p_z orbitals, and lie out of the plane of the graphene sheets of carbon atoms.⁵⁴ If the sample is oriented, with the graphite layers parallel to the surface, and the incident beam is normal to the surface, then the electric field is perpendicular to the angular momentum of the p_z orbitals, and the dipole transition probability for a transition from the carbon $1s$ orbital to the carbon $2p_z$ orbital is zero. Of course in real films there is a mosaic spread in the orientation, and thus the transition probability is small, but non-zero. As the film is tilted away from normal, the matrix element becomes increasingly larger, until at 90° a maximum is reached. Experimentally it is not possible to measure to 90° incidence, because the beam is no longer striking the face of the sample.

Approximately 8 eV higher in energy than the states due to the π^* anti-bonding orbitals are the σ^* anti-bonding states.⁵⁴ These states are constructed from the $2p_x$ and $2p_y$ orbitals, and lie in the plane of the carbon atoms. As expected, the peak due to transitions to the σ^* states shows the opposite behaviour to the π^* peak. The dipole matrix element is maximum for normal and minimum for 90° incidence. It should be noted that for synchrotron radiation the beam is partially polarized, but this does not affect the angle

dependence under discussion, because the orientation of the field within the plane perpendicular to the direction of propagation is unimportant.

4.1.3.2 Experimental

The XAS experiments were performed at the Canadian ERG beamline located at the Synchrotron Research Center of the University of Wisconsin. The monochromator is a Mark IV "Grasshopper" grazing incidence monochromator, with an energy range from 50-800 eV.⁵⁵ The instrumental resolution provided is approximately 0.2 eV at the boron edge and 0.4 eV at the carbon edge. The beamline is maintained at $\sim 10^{-10}$ torr, while the measurement chamber is typically at $\sim 10^{-9}$ torr.

The electron yield measurement was made using a microchannel plate detector, with a small positive bias for total electron yield. The angle between the incident beam and the line connecting the beam spot on the sample and the detector was 90° , as illustrated in Figure 4-6. The sample could be rotated about an axis perpendicular to the plane containing the incident photon beam and the electron-yield detector, so that the angle of incidence of the beam with respect to the normal to the film could be controlled between 0° and 70° .

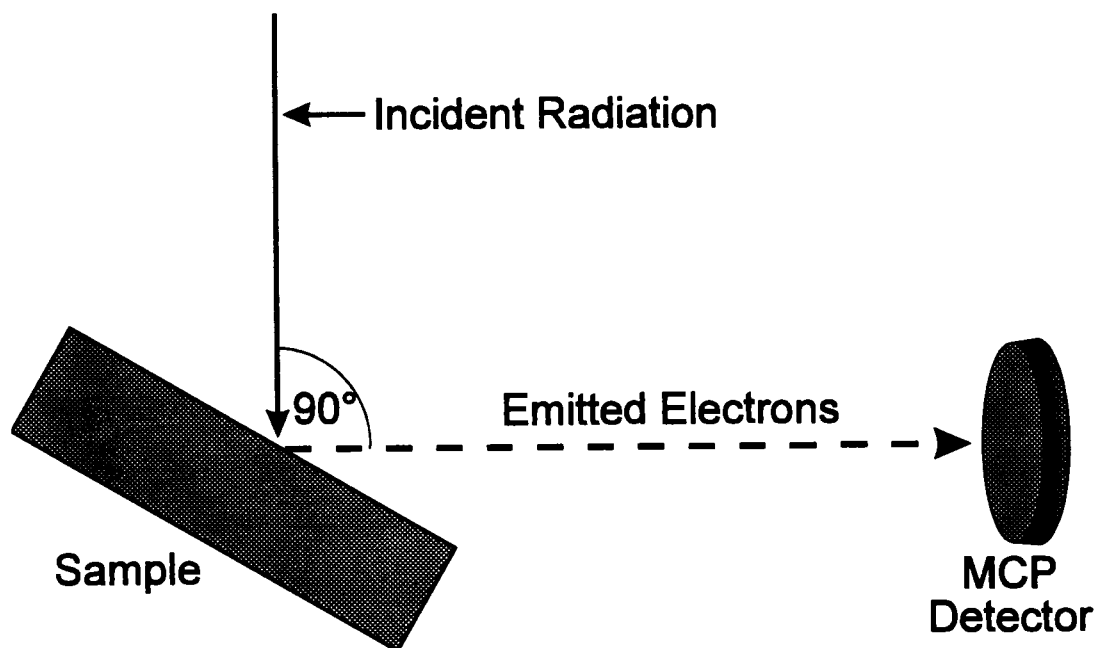


Figure 4-6 Relative orientation of incident beam, sample and microchannel plate detector.

To obtain reliable XAS spectra at the carbon K-edge, one must accurately measure the variation of the synchrotron beam intensity, I_0 , with photon energy, because carbon contamination of the beamline optics leads to intensity variations in the region of interest. We made three independent measurements of the I_0 variation: (1) the current flow from the gold grid placed in the beam in front of the sample, (2) the absorption from a thick gold film deposited on Si, and (3) the absorption of a Si(100) wafer that had been freshly etched in HF prior to insertion into the vacuum chamber. The first measurement was made simultaneously with each of our measurements at the carbon edge, since it is also used to track the variation of beam current with time, while the other two measurements were made independently. These measurements are useful because there are no features in the absorption spectra silicon or gold in the region of the C K-edge. The data for the boron-carbon samples were divided by the I_0 signals provided by these measurements, and the results were approximately the same for all three. We elected to use the gold film as the standard I_0 . Subsequent trips to the same beamline showed that the gold grid gave different results, probably due to carbon contamination of the grid itself.

4.1.4 Heat Treatment Study

The structure of disordered carbons varies greatly with heat treatment temperature between 700°C and 3000°C.²⁴ The two classes of disordered carbons - hard carbons and soft carbons - behave very differently with heating. Initially they act similarly, with the release of hydrogen (remaining from their synthesis from hydrocarbons) between 700°C and 1000°C. As both types of carbons are heated above 1000°C, crystallite size increases as layers flatten and join. Between 2000°C and 3000°C the turbostratic disorder of soft carbons is relieved as the layers rotate and shift into ABAB... stacking and the sample becomes very graphitic. By contrast, the turbostratic disorder of hard carbons is difficult to remove at any temperature, due to cross-linking between layers. All of these structural changes lead to vastly different electrochemical properties.¹⁴ Specifically, as the carbon becomes more graphitic both the variation of chemical potential with lithium concentration and the average intercalation voltage become smaller. These are useful properties for a lithium-ion anode material. In addition, as turbostratic disorder is relieved, the reversible capacity of pure carbons to

intercalate lithium is increased. For the B_zC_{1-z} materials, we thought that heat treatment may be useful to make the electrochemical properties more desirable and to make structural study easier by increasing crystallinity.

Heat treatment was performed at Moli Energy (1990) Ltd. of Maple Ridge, B.C., using a resistively heated graphite tube furnace under argon gas flow. This special furnace was used because the temperature range desired (1000-1600°C) is outside that easily obtained at SFU. Ground powder samples were weighed, transferred into graphite crucibles, and loaded into the center of the furnace. The furnace was pumped with a roughing pump to 100 millitorr, backfilled with ultra high purity (UHP) argon to +3 psig (regulated by a pressure relief valve), and this process repeated several times to remove all oxygen. The tube was filled once again to +3 psig, and the argon flow adjusted to 0.2 l/min. The temperature was then slowly increased to 200°C over one hour to avoid cracking of the graphite tube due to rapid desorption of water. After this gentle warming period, the temperature controller was programmed to take the furnace to the desired treatment temperature in one hour. The sample was then soaked at this temperature for a further hour, after which the power was shut off, and the sample cooled to <100°C in approximately two hours. Finally the sample was removed, weighed and sealed in a glass vial.

4.2 Results and Discussion

4.2.1 Films

Figure 4-7 shows a typical Auger electron spectrum, dN/dE versus E , for a B_zC_{1-z} film made at 900°C, with 76% BCl_3 in the reaction flow mixture. The film has been sputtered with 3 keV argon for three minutes. The peak at 180 eV corresponds to a boron KLL Auger process. The carbon KLL peak is at 273 eV. The peak at 216 eV is due to argon, that has been implanted through the sputtering process. The boron concentration is calculated from:

$$\%B = \frac{1.23I_b}{I_c + 1.23I_b} \quad \text{Equation 4-7}$$

and yields a stoichiometry of $B_{0.17}C_{0.83}$.

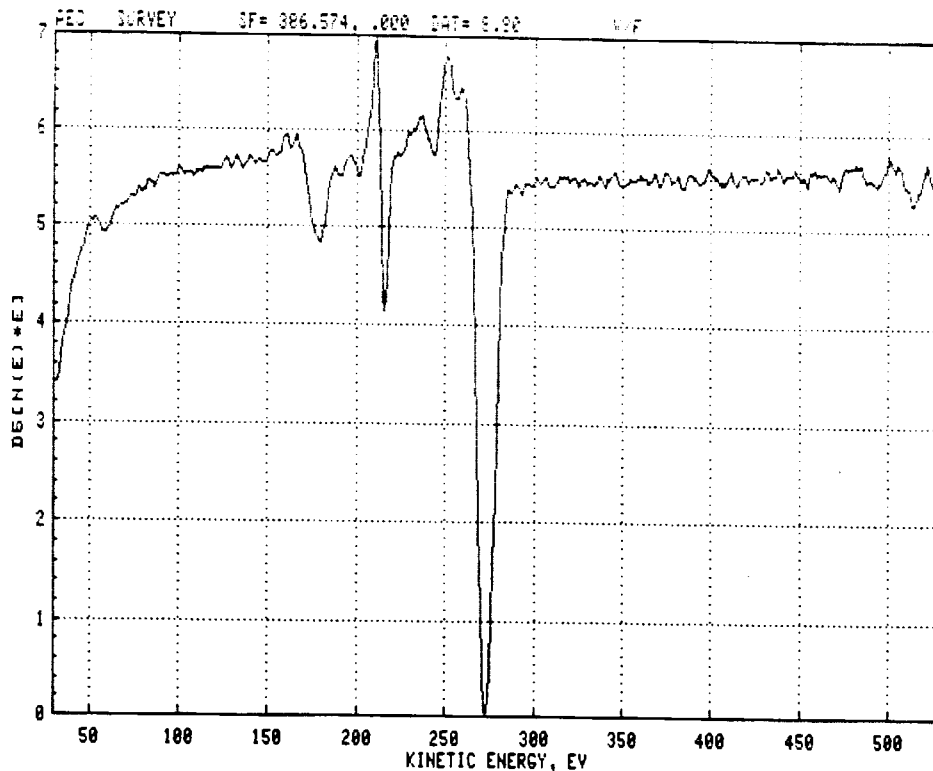


Figure 4-7 Auger electron spectrum, $dN/dE(E)$, for a B_2C_{1-z} film made at 900°C with 76% BCl_3 in the flow mixture.

Figure 4-8 shows the atomic percent of boron in B_2C_{1-z} films deposited at 900°C as determined by AES, as a function of the volume percentage of BCl_3 in the BCl_3 -benzene gas mixture. The most boron that was incorporated in the films under these conditions is about 17%, significantly less than the 25% in BC_3 . The boron concentration appears to saturate for gas mixtures exceeding 50% BCl_3 . Shen *et al.*⁴⁴ used a 2.5 times molar excess of BCl_3 (~70% by volume), in their syntheses, and claimed to make BC_3 at 900°C . However, they showed that the maximum attainable boron concentration dropped rapidly with temperature to 19.6% at 910°C and then to 15% at 1000°C . Their deposition was at atmospheric pressure, not low-pressure (5 Torr) as was ours. In a more recent paper,⁵⁶ Cermignani *et al.* produced films at 900°C and atmospheric pressure, and measured the boron concentration using SIMS. Their Figure 6 is very similar to our Figure 4-8, with a maximum attainable

boron concentration of 15 to 16%. They show a more smooth variation in the film concentration, with no complete saturation until 100% BCl_3 .

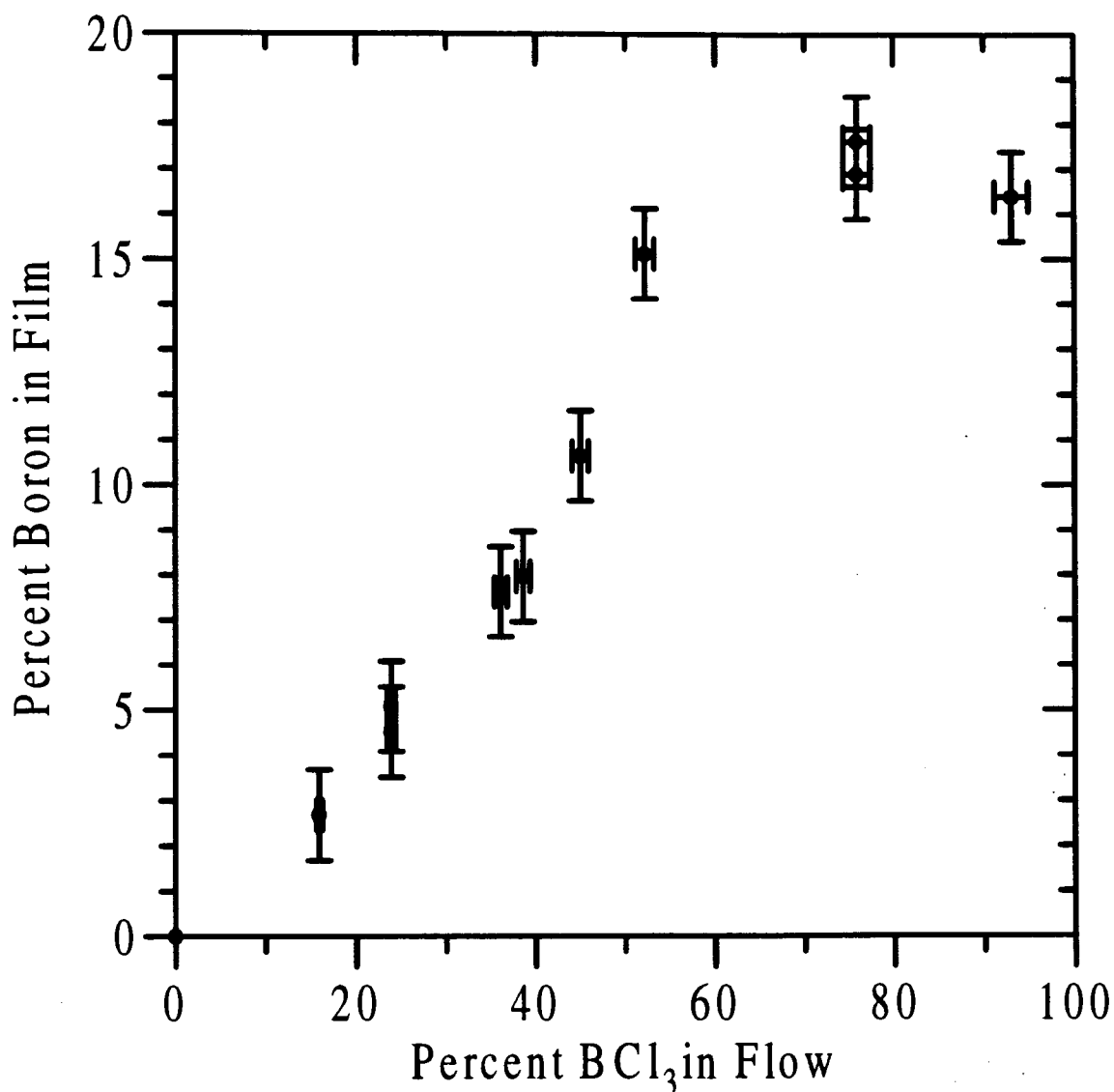


Figure 4-8 Stoichiometry of B_2C_{1-2} films as a function of BCl_3 volume percentage in the flow mixture

Figure 4-9 shows the diffraction pattern in the region of the graphite (002) peak for a thin ($<1 \mu\text{m}$) $\text{B}_{0.17}\text{C}_{0.83}$ film, measured by grazing incidence diffraction at $0.5^\circ, 0.25^\circ$ and 0.125° incident angles. The (002) peak is almost completely obscured by diffraction from the quartz substrate at $\alpha_{\text{inc}}=0.5^\circ$, but is the dominant feature at $\alpha_{\text{inc}}=0.125^\circ$, illustrating the

power of grazing incidence diffraction to make X-ray measurements on relatively thin films.

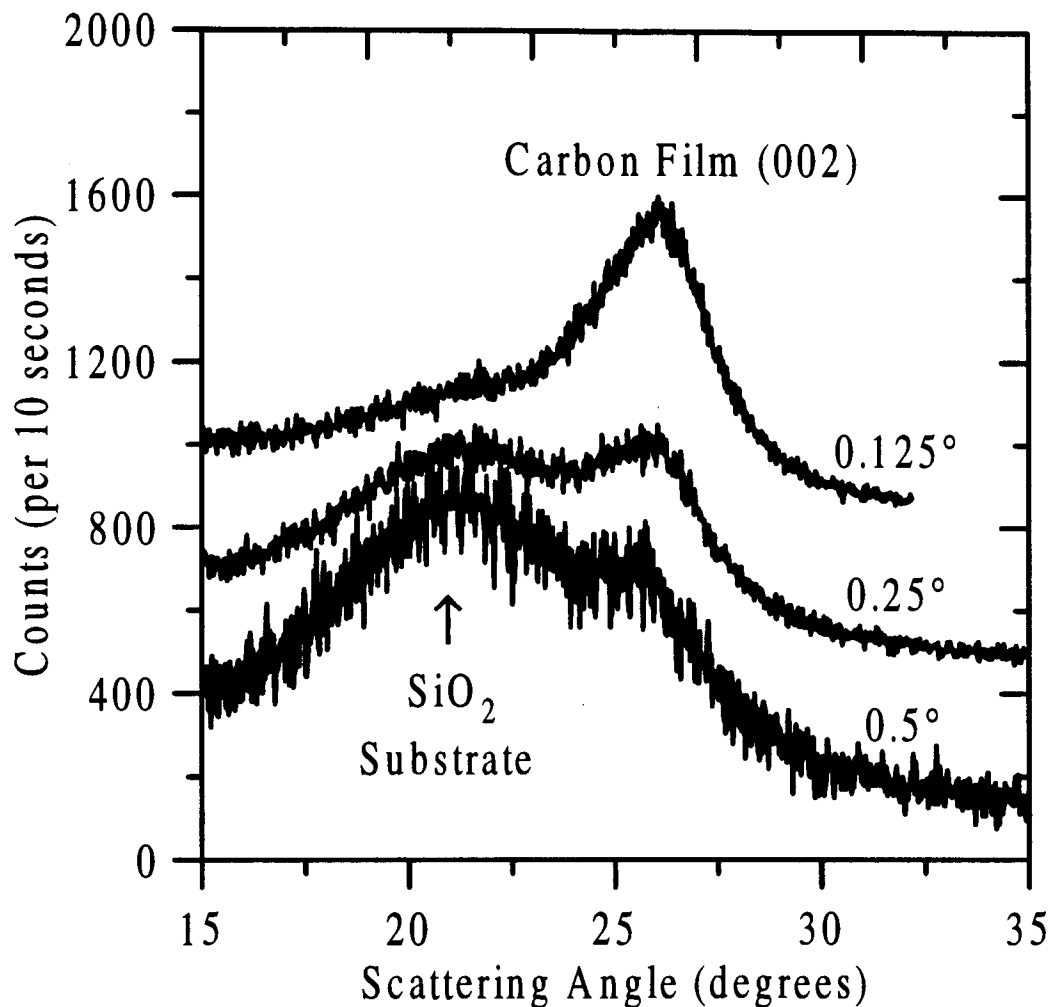


Figure 4-9 Grazing incidence diffraction pattern of a thin B_2C_{1-2} film on a quartz substrate, in the carbon (002) region. The top two patterns are shifted up by 400 and 800 counts, respectively, for clarity. The incident angle of the X-ray beam is listed by each curve.

Figure 4-10 shows the (002) Bragg peak of a series of B_2C_{1-2} films collected using the grazing incidence method. The (002) peak moves to larger scattering angle (smaller plane spacing) and sharpens as the boron concentration of the films increases. The (002) spacing directly measures the average distance between the boron-carbon layers, analogous to the distance between carbon layers in pure graphite. All films appear quite disordered, as indicated by the large width of the (002) peaks.

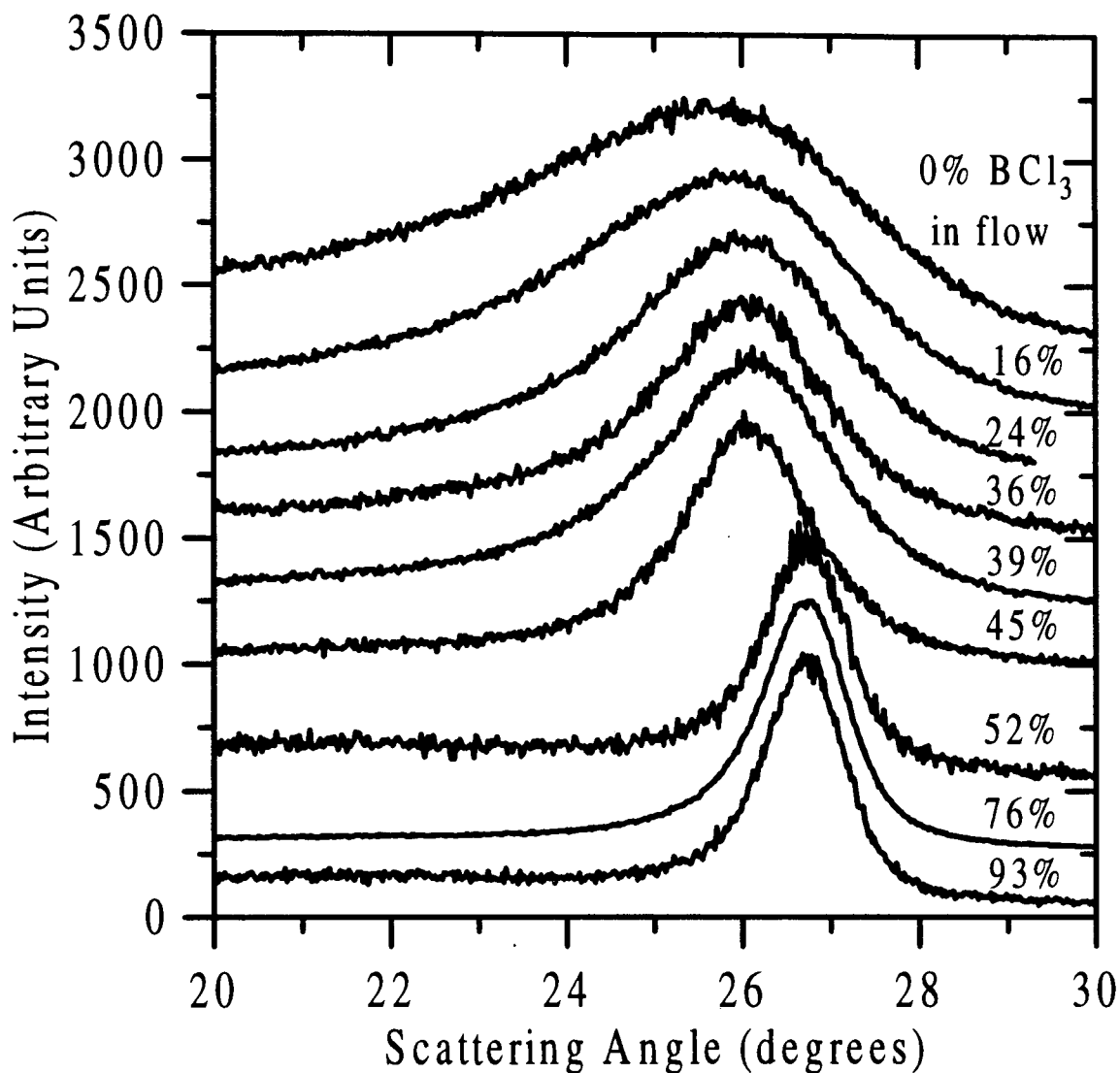


Figure 4-10 The (002) Bragg peak of B_2C_{1-z} samples made at 900°C . The numbers at the right, above each data set, are the percentage of BCl_3 in the gas flow. The data have been offset for clarity, from the bottom, by: 0, 250, 500, 950, 1200, 1450, 1700, 1950 and 2200.

Figure 4-11 and Figure 4-12 show the variation in the spacing between the (002) planes and the full width at half maximum (FWHM) of the (002) peak, respectively, as a function of the boron concentration in the film. For soft carbons, the (002) plane spacing decreases with heat treatment from $\sim 3.45 \text{ \AA}$ at 1300°C to $\sim 3.35 \text{ \AA}$, the same as for graphite, at 3000°C .⁵⁷ This is due to the relief of strain between the layers as they flatten, and become more organized. This also causes the narrowing of the (002) peak, as the coherence length in

the c-direction, L_c , increases. These same phenomena are observed for the B_2C_{1-z} films as a function of z , at 900°C , far below the temperatures needed in pure carbons. For the $B_{0.17}C_{0.83}$ film the (002) plane spacing is 3.336 \AA , significantly smaller than for pure graphite (3.348 \AA)⁵⁸. Lowell¹⁶ showed that small additions of boron in crystalline graphite do cause a contraction in the c axis, in accord with our result. The contraction of the layer spacing is most likely due to an increase in structural ordering.

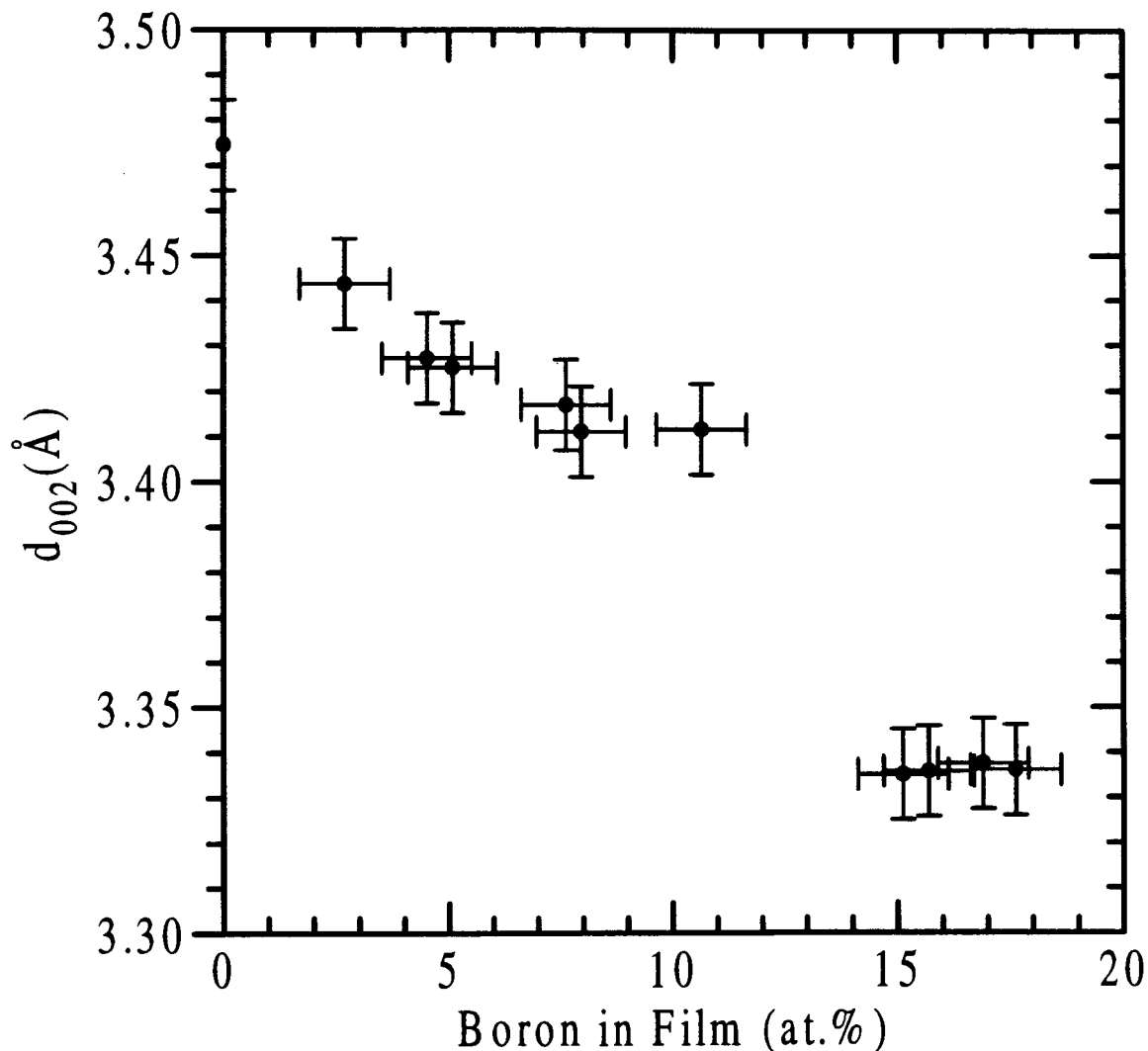


Figure 4-11 (002) Layer spacing as a function of z in B_2C_{1-z}

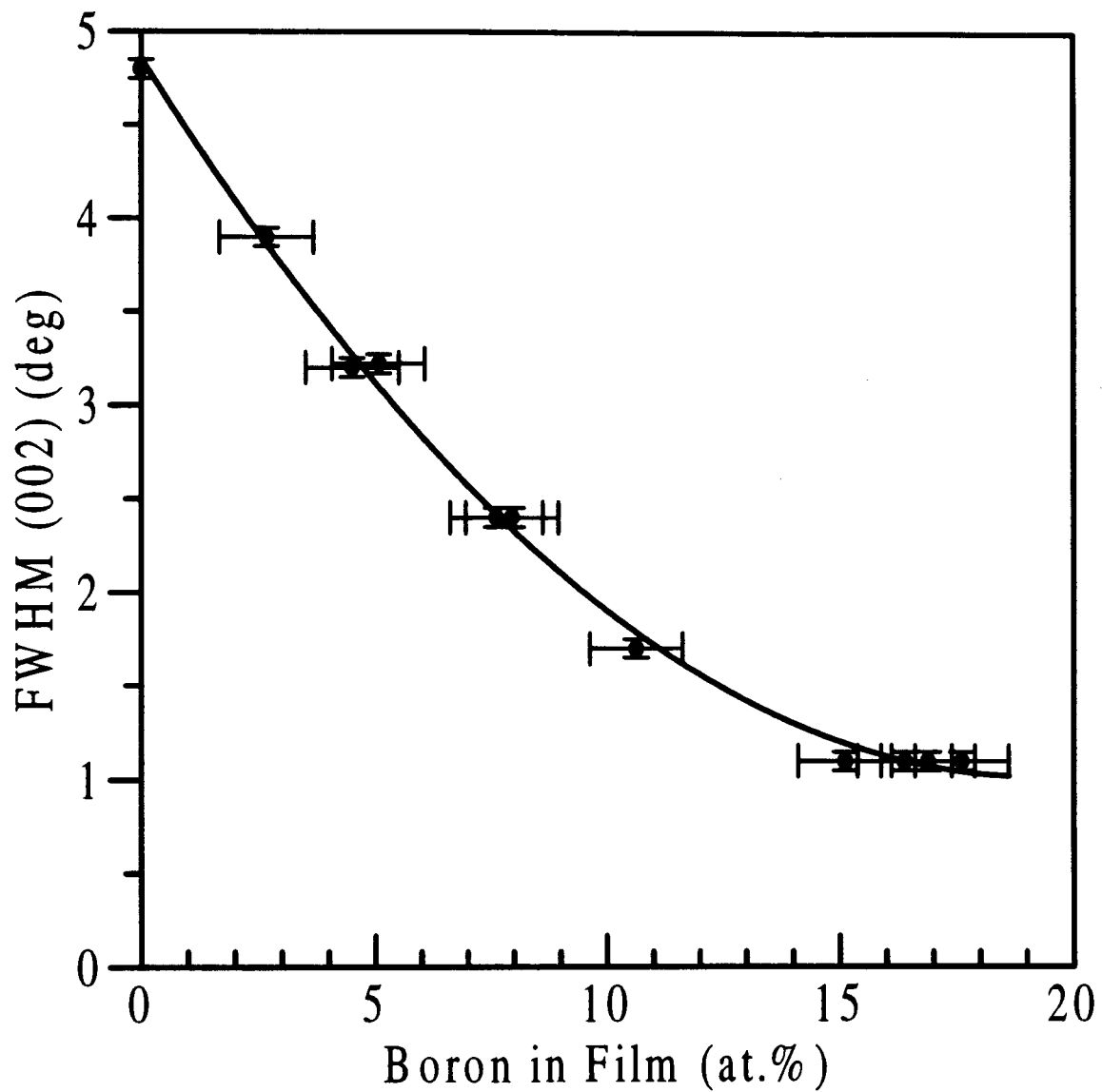


Figure 4-12 Full width at half maximum of the (002) diffraction peak as a function of z in B_zC_{1-z} . The solid line is a guide to the eye.

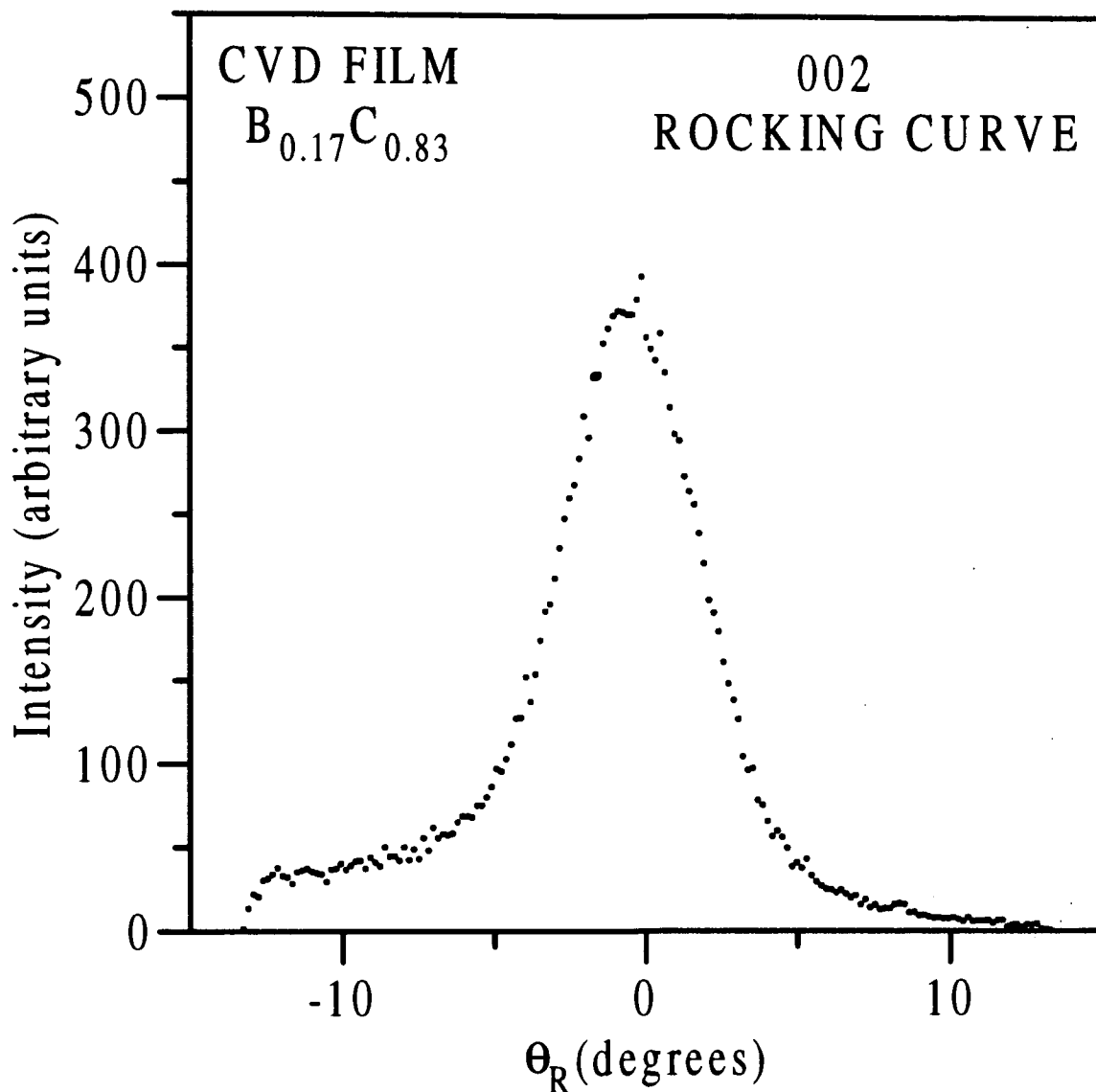


Figure 4-13 Rocking curve for the (002) Bragg peak of $B_{0.17}C_{0.83}$. The rocking angle, θ_R , is 0° when the angles of the incident and diffracted rays with respect to the normal to the substrate are the same.

Figure 4-13 and Figure 4-14 show the rocking curves collected on the (002) and (004) Bragg peaks of the film made at highest BCl_3 concentration. These curves show that the majority of crystallites in the film are oriented with their c -axes within $\pm 5^\circ$ of the normal to the substrate. This implies that only a small fraction of the crystallites are contributing to the (002) intensity measured in grazing incidence, where the c -axis must be tipped approximately 13° away from the normal to satisfy the Bragg condition. Rocking curves

were only measured on the films with the highest boron concentrations. For those films with low boron concentrations, where the (002) peak is broad, the scattering from the quartz substrate is large compared with the (002) signal unless grazing incidence is used, making the rocking-curve measurement impossible.

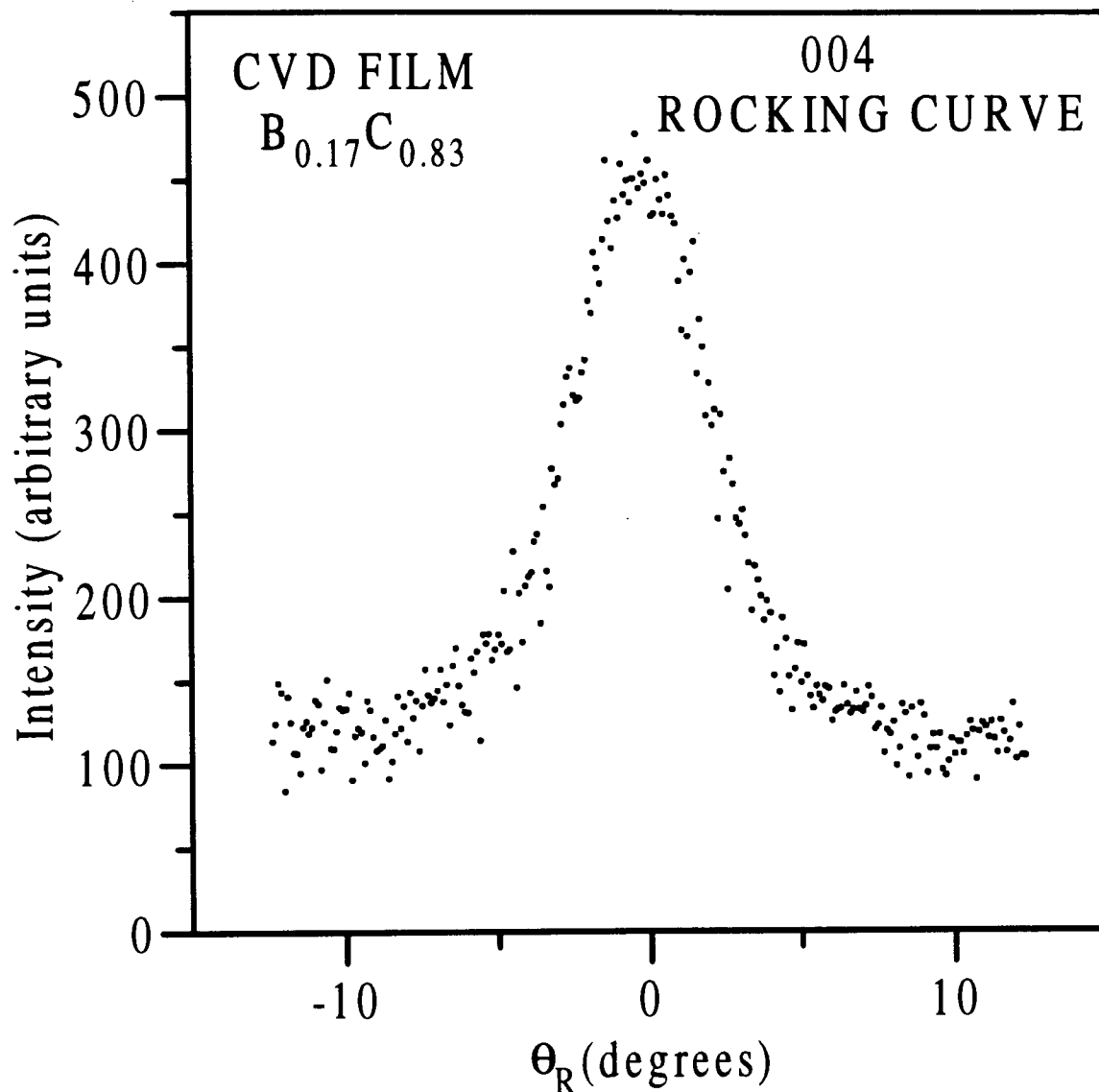


Figure 4-14 Rocking curve for the (004) Bragg peak of $B_{0.17}C_{0.83}$.

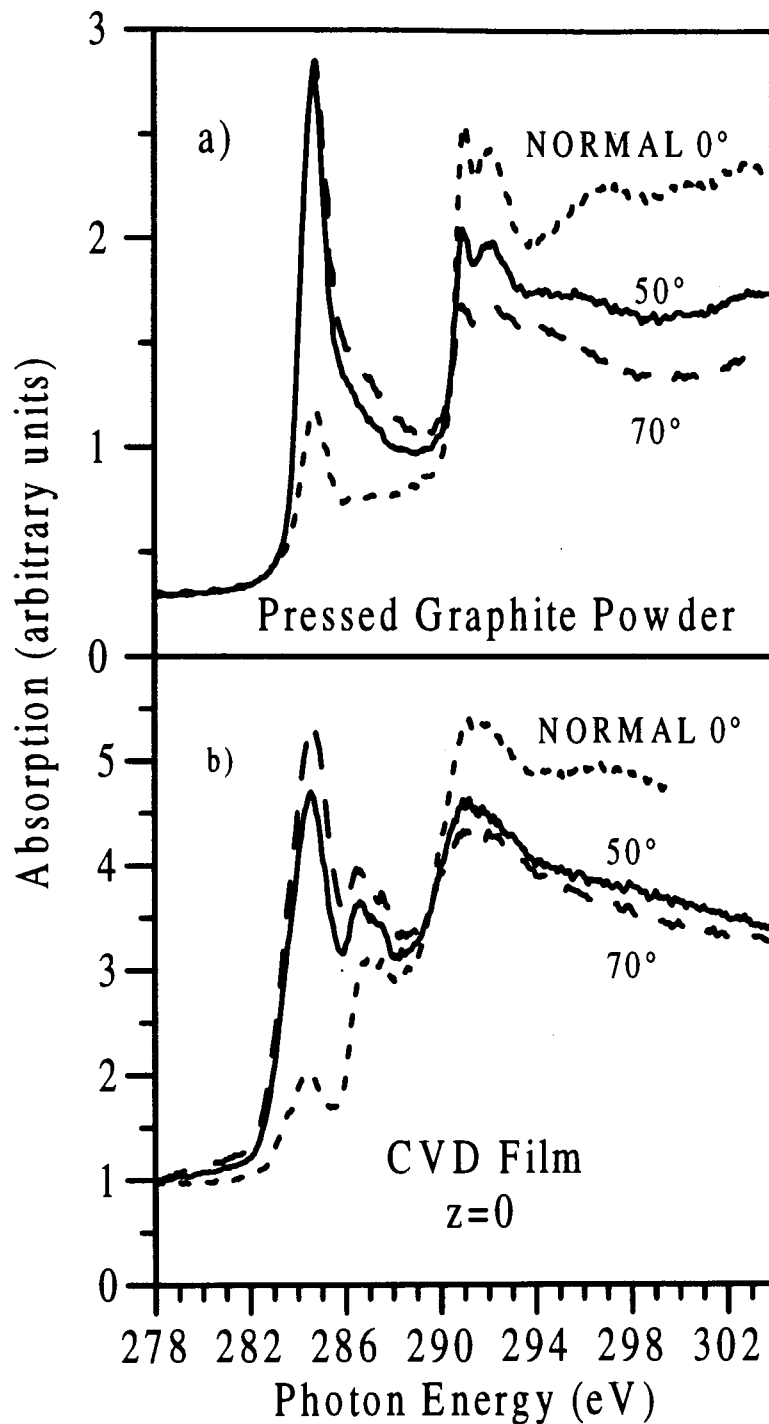


Figure 4-15 Carbon 1s X-ray absorption for (a) oriented graphite powder pressed on Cu tape and (b) a pure carbon film on a quartz substrate, made by CVD. The data have been corrected for I_0 variations. The angle of incidence of the photon beam with respect to the normal to the sample is indicated near each data set.

Figure 4-15a shows the X-ray absorption at the carbon K edge, measured at three angles of incidence for graphite powder (Johnson-Matthey) pressed onto copper tape. The pressing substantially orients the powder with the c axis normal to the tape. The data have been corrected for the I_0 variation as described in Section 4.1.3.2, and scaled so that the absorption below the edge is the same. Figure 4-15b shows similar results for a CVD film prepared from pure benzene. The large peak near 285 eV in both spectra is due to transitions from the carbon 1s state to unfilled states in the π^* band, and the large absorption commencing near 291 eV corresponds to transitions to unfilled σ^* bands. For both samples, the π^* peak is minimum for normal incidence and maximum at the highest angle available (70°), while the σ^* peaks show the opposite behaviour. This is as expected for samples that are predominantly aligned with their c axes normal to the surface of the film. The peak near 287 eV in the CVD film has been attributed in the past to “interlayer states.”⁵⁹ The results here suggest that these states are associated with turbostratic disorder, which is present in the CVD film, but almost absent in the crystalline graphite powder.

Figure 4-16a and Figure 4-16b show the carbon K-edge for CVD deposited $B_{0.05}C_{0.95}$ and $B_{0.17}C_{0.83}$, respectively. These data show the same general behaviour as observed in Figure 4-15 proving that these films are highly oriented. There is additional structure in the absorption right at the edge, evidenced by a shoulder (indicated by the arrows) at about 283 eV on the main π^* absorption. A similar, although weaker, shoulder has been previously observed⁶⁰ for boron-doped carbons made by the method of Lowell.¹⁶ This shoulder is believed to be caused by the empty π -bonding orbitals created by the incorporation of boron, as expected based on **Figure 1-3**.

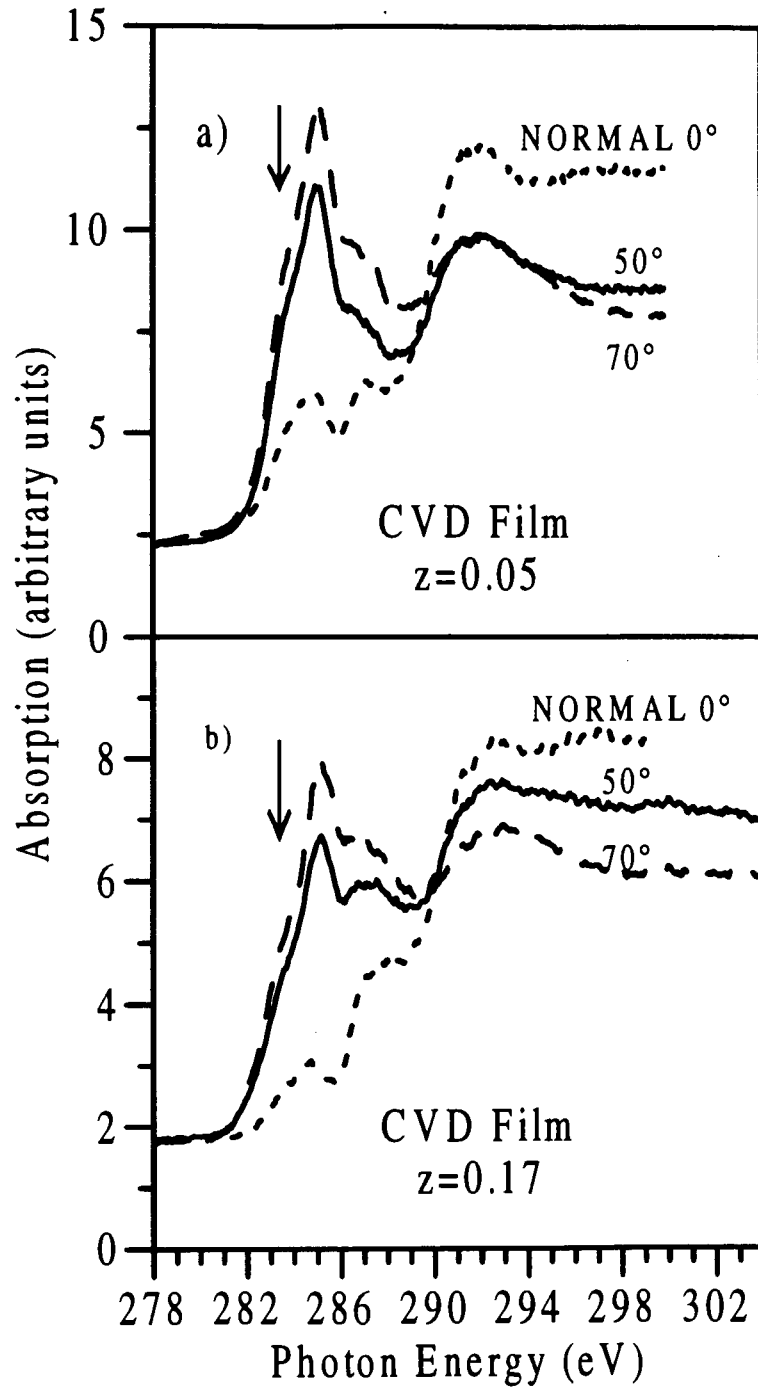


Figure 4-16 Carbon 1s X-ray absorption for (a) $B_{0.05}C_{0.85}$ and (b) $B_{0.17}C_{0.83}$ films on quartz substrates, prepared by CVD. The arrows indicate empty π -bonding orbitals created by the incorporation of boron.

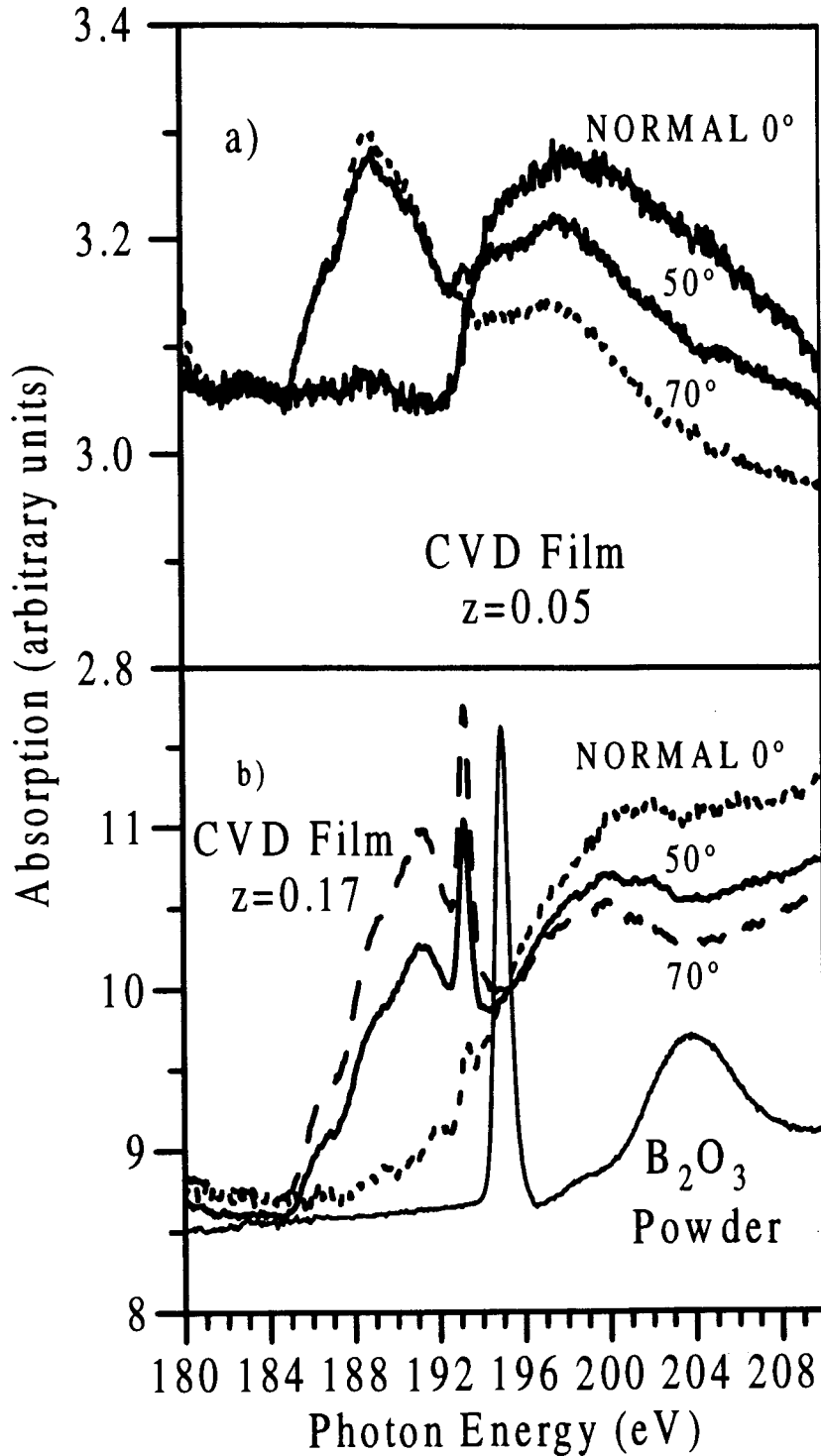


Figure 4-17 Boron 1s X-ray absorption for (a) $B_{0.05}C_{0.85}$ and (b) $B_{0.17}C_{0.83}$ films on quartz substrates, prepared by CVD. The XAS spectrum for B_2O_3 powder is shown in (b) for comparison.

Figure 4-17a and Figure 4-17b show measurements at the boron edge for the same two samples as in Figure 4-16. The dependence of the absorption with incidence angle is qualitatively similar to that at the carbon edge, proving that the boron 1s electron is transferred to final states with the same symmetry as those filled by an electron excited from the carbon 1s level. This strongly suggests that the boron atoms substitute for carbon in these B_2C_{1-z} films. Here the boron 1s electron is transferred to final states with predominantly π^* symmetry for photon energies between 184 eV and 192 eV, and to states with predominantly σ^* symmetry between 194 eV and 202 eV. The sharp peak in the $B_{0.17}C_{0.83}$ spectra near 193 eV shows π character and was only present in the film made with 93% BCl_3 in the gas flow. Due to its sharp absorption profile, it may be due to a boron-containing surface impurity. The spectrum of bulk B_2O_3 is similar, but with the main absorption at 195 eV. It is possible that this is a thin, oriented B_2O_3 film, that is chemically shifted by ~ 1.5 eV. In any case the total area due to this impurity is relatively small, and thus if due to an impurity, the concentration is low. Comparing the height of the boron K-edge absorption over the background for the two samples is also rough quantitative confirmation for the boron concentrations determined by Auger analysis.

4.2.2 Powder Samples

X-ray diffraction measurements were made on the powder samples prepared by grinding the films. Figure 4-18 shows the (002) Bragg peaks of a series of powder samples prepared at 5 torr and $900^\circ C$, offset and scaled for clarity of comparison. The peaks measured by powder diffraction show the same basic behavior as the films did in grazing diffraction: increasing angle and decreasing FWHM with increasing boron concentration. Figure 4-19 shows the diffraction patterns of a series of powder samples produced at 30 torr and $900^\circ C$. The sharpening and shift to higher angle with boron concentration of the 002 ($\sim 26^\circ$), 004 ($\sim 54^\circ$), and 006 ($\sim 87^\circ$) peaks is evident.

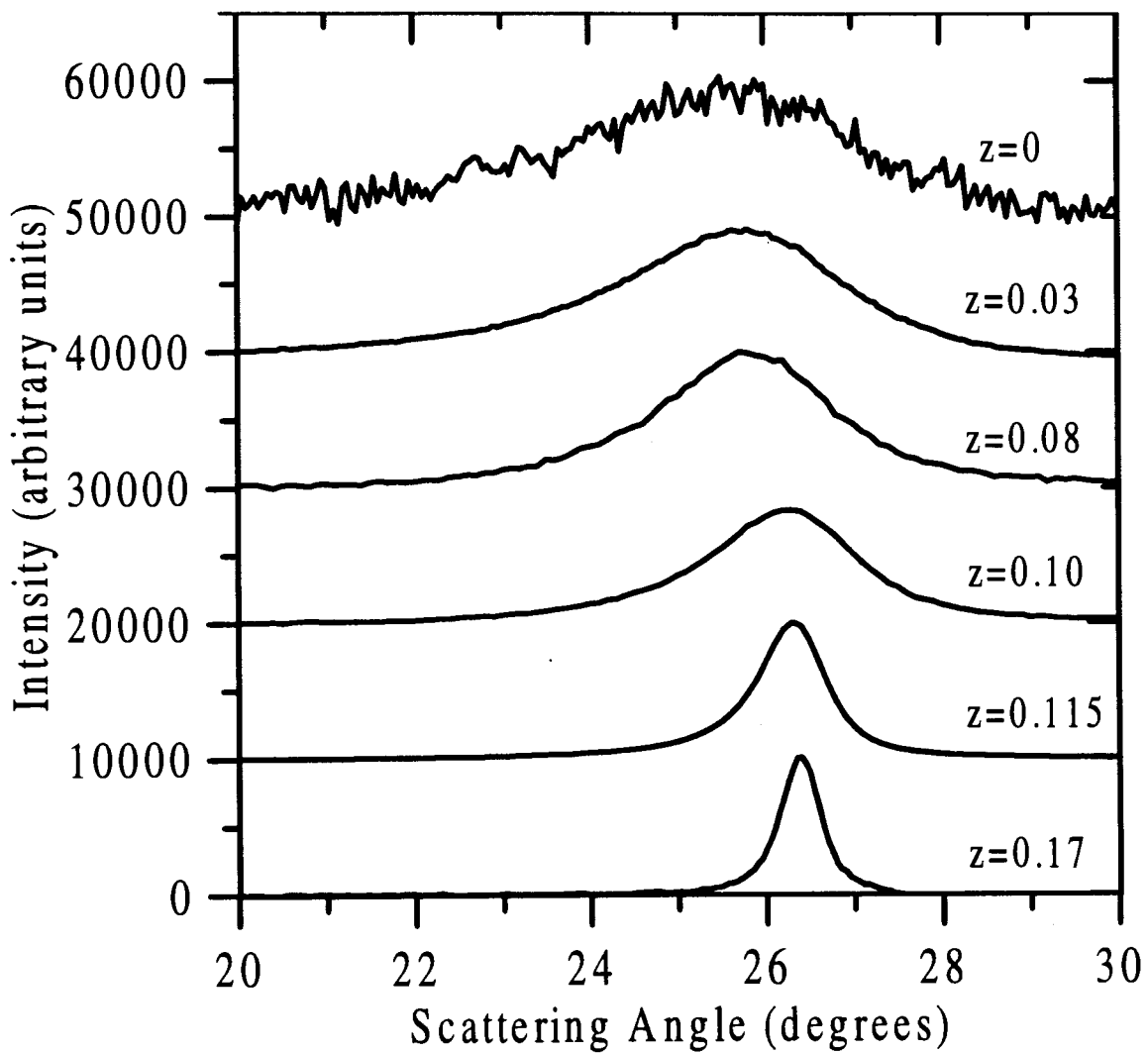


Figure 4-18 The (002) Bragg peak of B_2C_{1-z} powder samples made at 900°C. Estimated boron concentration are at right, above each data set. The data have been scaled and offset for clarity.

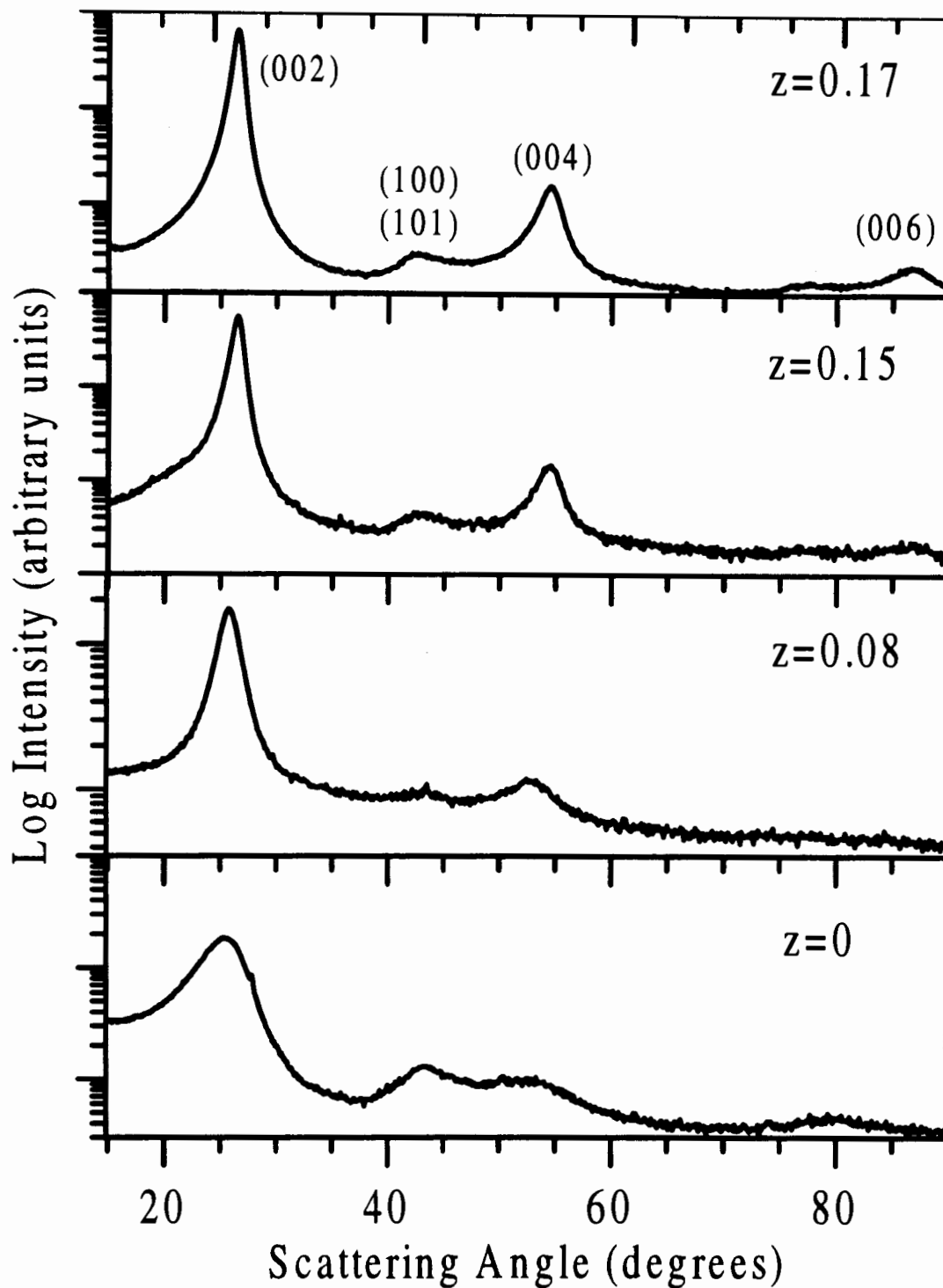


Figure 4-19 Diffraction patterns of B_zC_{1-z} powder samples produced at 30 torr, for $z=0, 0.08, 0.15, 0.17$.

Four samples were sent for elemental analysis by laser ablation inductively-coupled mass spectroscopy. The results are summarized in Table 4-1. The first column is the sample ID sent to Elemental Research Inc. The second column is the boron concentration that we estimated from FWHM of the (002) Bragg peak, using Figure 4-11 and Figure 4-12. The third column contains the first results we received from the company, when the powder samples were affixed to tape for the measurement. Due to the large boron concentration of BW4, which was synthesized with no BCl_3 , we suggested that they measure again, this time with samples affixed to Indium foil, in case the tape contained boron. The results of these subsequent measurements are shown in the fourth column. The pure carbon was still found to contain 6 atomic % boron. Furthermore, all of the values are much higher than measured on the films by AES, or reported by any other researchers. It is also very unlikely that a material with a boron concentration of 67% would have a disordered graphite structure. For all of these reasons, the results of this relatively untested technique were determined to be incorrect and useless for the determination of boron concentrations.

Sample	Boron Concentration from Diffraction	Boron Concentration from laser ablation-ICPMS - on tape	Boron Concentration from laser ablation-ICPMS - on Indium foil
BW1	0.17	0.56	0.53
BW2	0.08	0.56	0.53
BW3	0.15	0.60	0.67
BW4	0	0.33	0.06

Table 4-1 Boron concentrations of B_2C_{1-2} powders as determined by laser-ablation-ICPMS.

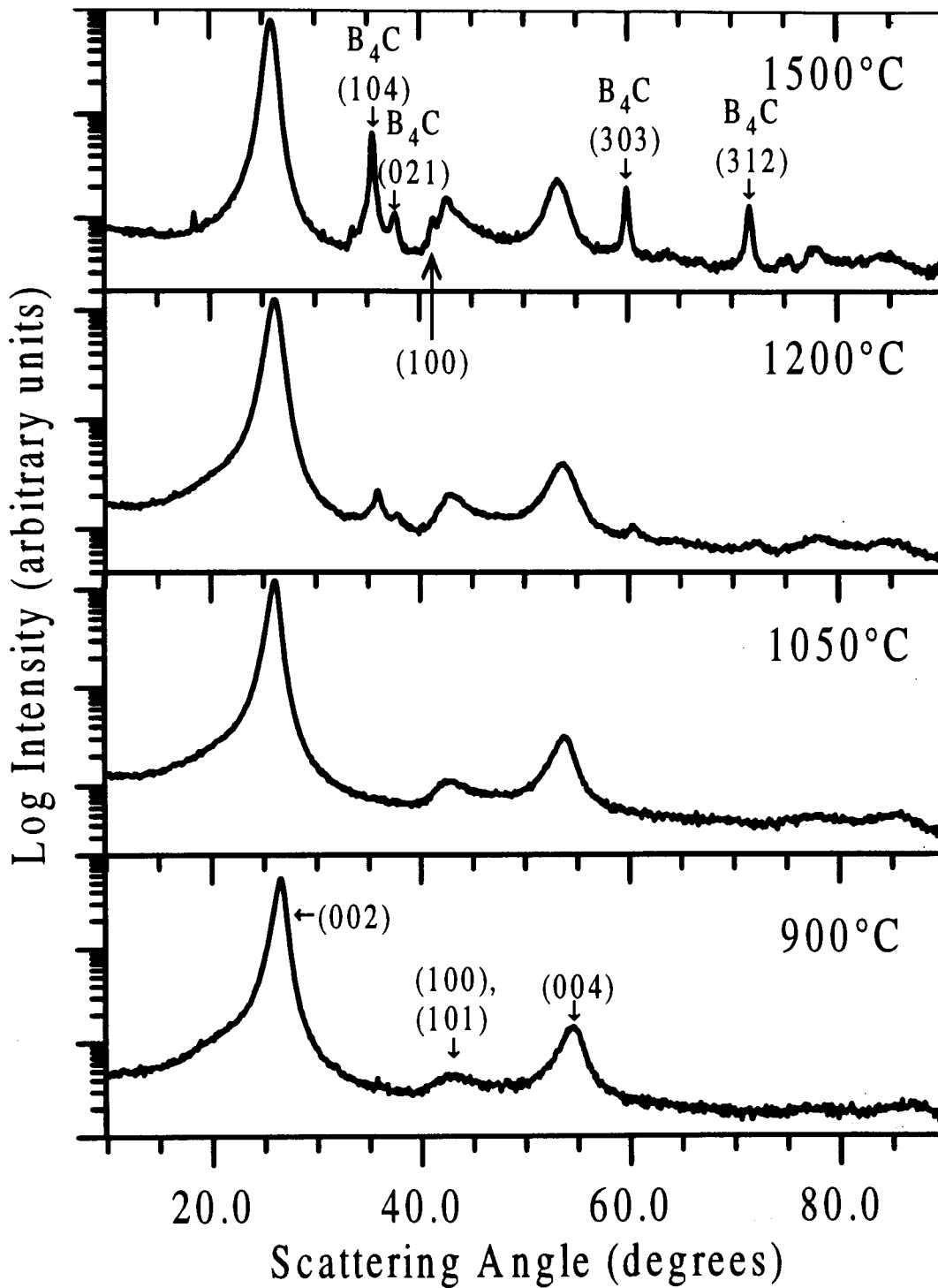


Figure 4-20 Diffraction pattern of $B_{0.15}C_{0.85}$ powder sample as a function of temperature. Unlabeled Miller indices refer to the graphite structure.

4.2.3 Heat Treatment Study

The diffraction patterns of the heat treated samples were measured from 10-90° scattering angle. Figure 4-20 shows these patterns, as a function of heat treatment temperature, for the sample with initial stoichiometry $B_{0.15}C_{0.85}$. These patterns are representative of the high boron concentration samples. There are three distinguishable diffraction peaks in the untreated, 900°C, sample: the (002), the (004), and a single peak which includes both of the (100) and (101) reflections. As the temperature is increased the (002) peak shifts to lower angle (larger layer spacing), and at 1200°C new peaks are evident between 35° and 40°, and at approximately 60° and 72° scattering angle. At 1500° this new phase, identified as B_4C , from the JCPDF CD-ROM database,⁶¹ is clearly visible. The diffraction pattern from the original disordered graphite structure has also changed somewhat. The (002) peak has shifted from 26.274° to 25.848°, and the (100) and (101) peaks have separated and sharpened. The (004) peak has also shifted to lower angle with the (002) peak, as one would expect.

The behaviour of the low boron concentration and pure carbon samples' diffraction patterns with heat treatment temperature is quite different. A comparison of the (002) peaks of the pure carbon and the $B_{0.15}C_{0.85}$ samples at 900°C and 1500°C is shown in Figure 4-21. Note that, while the boron containing sample shifts to lower angle, the pure carbon shifts to slightly higher angle. Also, the width of the (002) peak does not change very much for the $B_{0.15}C_{0.85}$ sample, while the pure carbon (002) peak sharpens considerably with temperature, with a final width close to that of the boron containing sample.

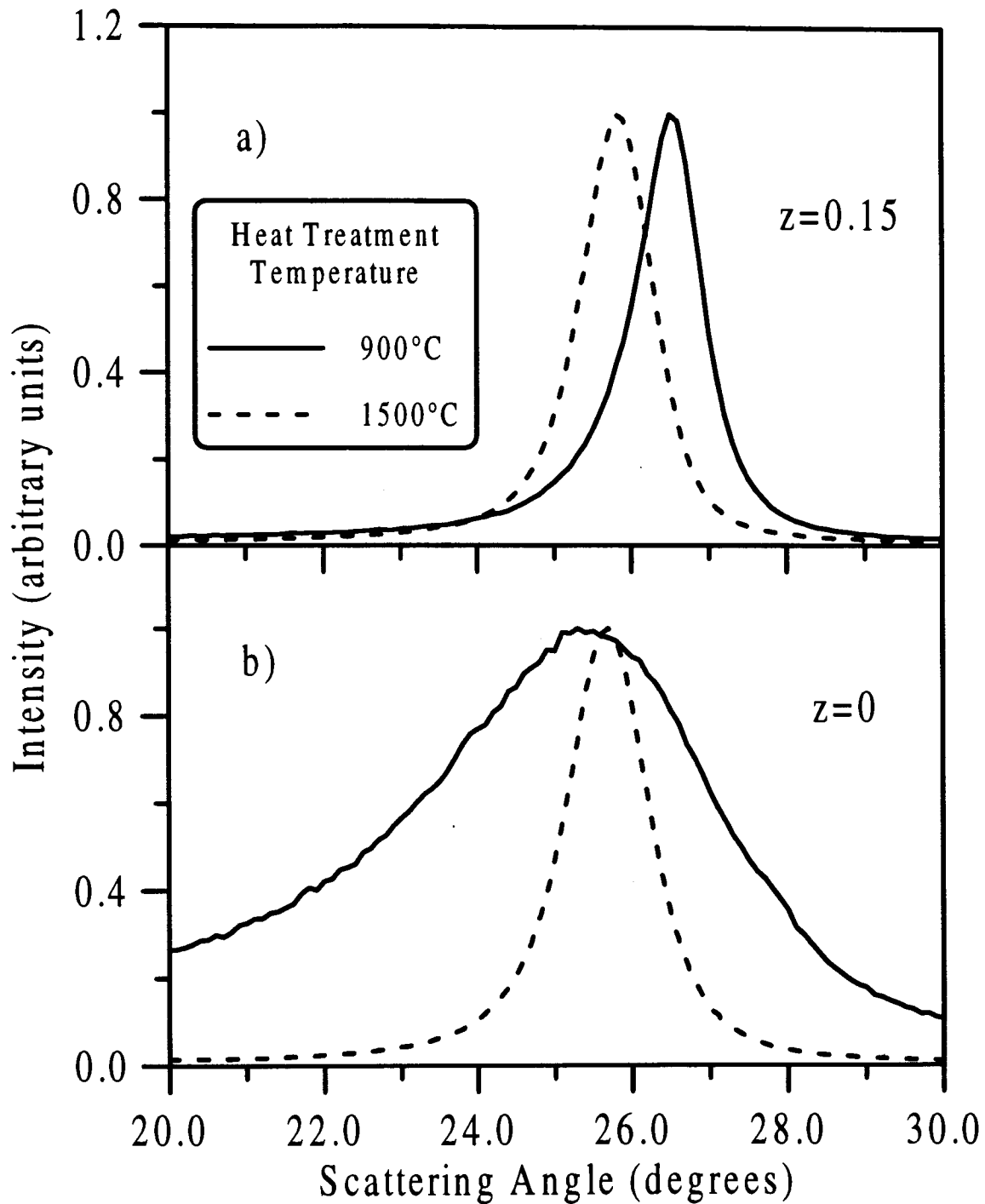


Figure 4-21 (002) Bragg peak for (a) $B_{0.15}C_{0.85}$ and (b) pure carbon powders, at 900°C and 1500°C.

Figure 4-22 shows the average layer spacing (d_{002}) for a series of B_zC_{1-z} powder samples as a function of heat treatment temperature. As seen in the curves in Figure 4-21,

the low boron concentration samples have decreasing layer spacings with increasing temperature, while the higher boron concentrations show the opposite behaviour. The relative final spacings of the $B_{0.08}C_{0.92}$ and $B_{0.15}C_{0.85}$ samples appear somewhat anomalous. The pure carbon sample at 1050°C was not prepared from the same initial sample as the 900°C and 1500°C samples, due to small yields in the synthesis from benzene only.

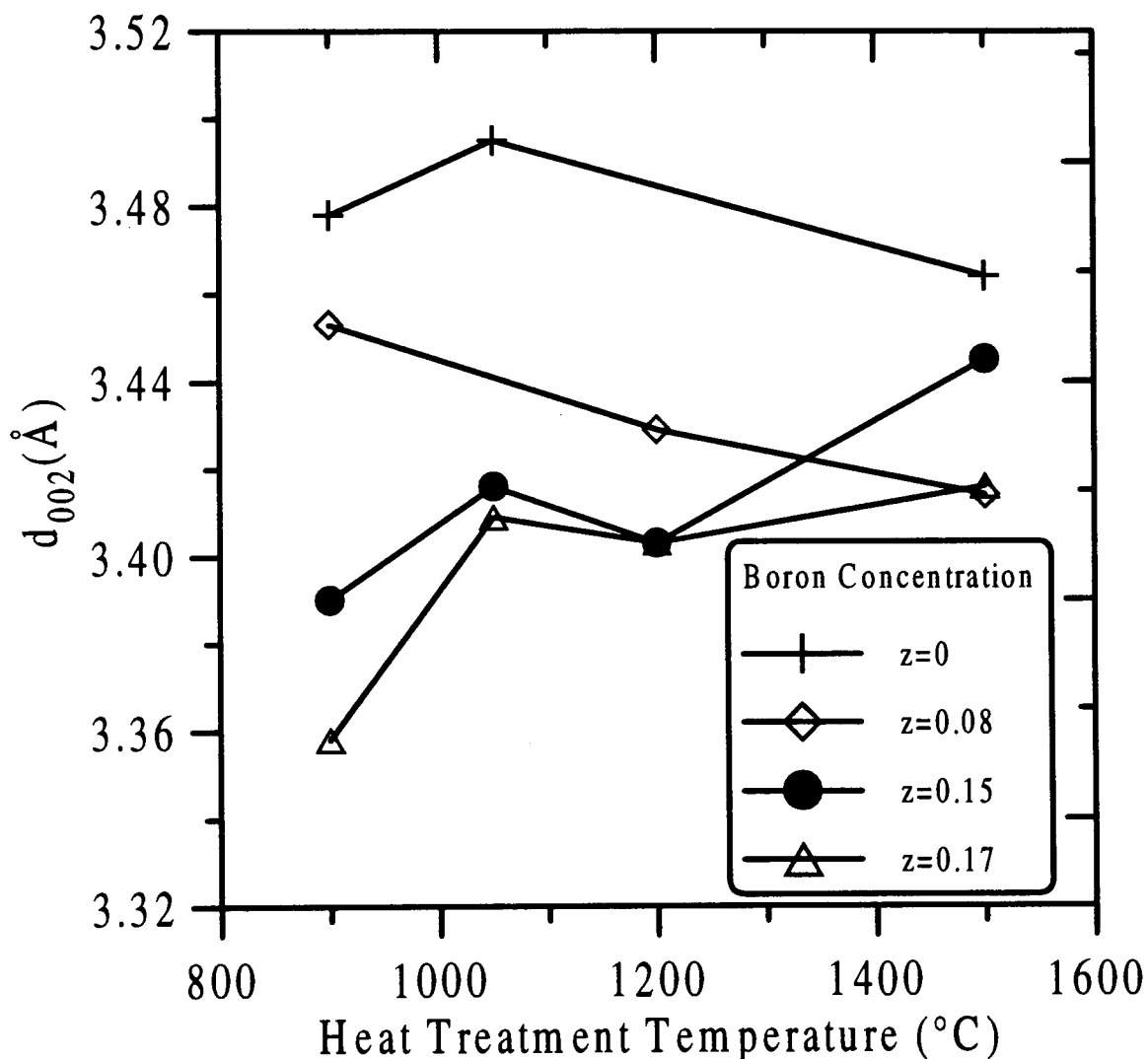


Figure 4-22 Average layer spacing, d_{002} of B_zC_{1-z} powder samples as a function of heat treatment temperature.

Figure 4-23 shows the full width at half maximum (FWHM) of the (002) peak for the same series of B_zC_{1-z} powders. The high boron concentration samples show a slight increase

in the FWHM with increasing temperature, while the FWHM of the low boron concentration samples decrease dramatically. The final FWHM (002) of all the samples is approximately the same.

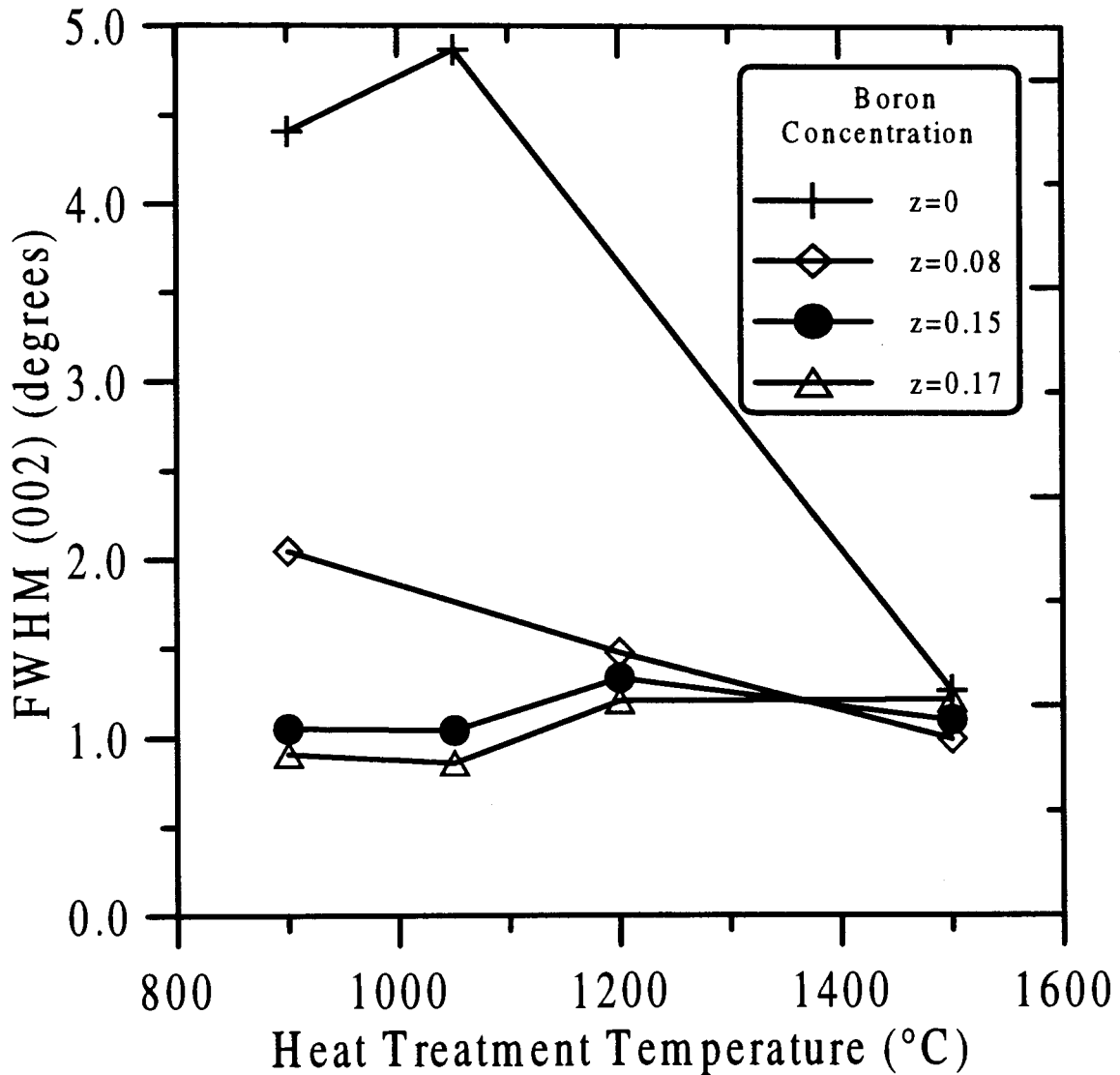


Figure 4-23 Full width at half maximum of the (002) peak of B_2C_{1-z} powder samples as a function of heat treatment temperature.

The behaviour of the B_2C_{1-z} samples with heat treatment can be summarized as follows: As the samples are heated above 1050°C, they start to phase separate into B_4C and B_2C_{1-z} with reduced z . By 1500°C phase separation appears to be complete, but it is not

possible to determine by diffraction whether the B_zC_{1-z} samples have $z=0$ or not. Auger electron spectroscopy on powder samples is unreliable, and it is even more difficult to separate the contributions from boron in B_zC_{1-z} and B_4C . This phase separation is predicted by Lowell's equilibrium phase diagram, reproduced in **Figure 3-1**. The samples with initial $z=0$ and $z=0.08$ graphitize with increasing temperature as expected for soft carbons. The layer spacing decreases, and the correlation length in the c direction increases, as measured by the width of the (002) peak. On the other hand, the layer spacing of the $z=0.15$ and $z=0.17$ samples increases with temperature. The initial layer spacing of these samples is much lower than pure carbons produced at the same temperature, and as the boron leaves the lattice and forms B_4C , the layers are forced apart, and become more disorganized, also causing a slight increase in the (002) peak width. The net effect is to produce (at 1500°C) a series of samples that are very similar, except for the amount of B_4C phase. It seems unlikely that a highly crystalline B_zC_{1-z} solid solution with $0.1 < z < 0.2$ can be produced by CVD, followed by heat treatment.

Sample ID	% BCl ₃ in Flow Mixture	Boron Concentration by AES (atomic percent)	Estimated Boron Concentration (atomic percent)	d ₀₀₂ (Å)	FWHM (002) (degrees)
BW62I	75.9	16.9		3.338	1.1
BW64I	93.1	16.4		3.336	1.1
BW65I	52.2	15.1		3.335	1.1
BW66I	0	0		3.475	4.8
BW68I	23.9	4.5		3.427	3.2
BW69I	38.6	8.0		3.411	2.4
BW70I	15.9	2.7		3.444	3.9
BW75I	75.9	17.6		3.336	1.1
BW77I	36.1	7.6		3.417	2.4
BW78I	45.0	10.6		3.412	1.7
BW130I	23.9	5.1		3.425	3.2
BW5II	0		0	3.478	4.2
BW16II	43.0		10	3.402	2.1
BW21II	15.9		3	3.445	3.6
BW36II	65.4		17	3.372	0.7
BW46II	23.9		8	3.423	2.3
BW84II	55.7		11.5	3.383	1.4
BW125II	69.9		17	3.358	0.9
BW135II	0		0	3.495	4.9
BW141II	59.0		15	3.390	1.1
BW146II	36.8		8	3.453	2.0
BW16III	0		0	3.478	4.4

Table 4-2 Boron concentrations and diffraction results for materials discussed in this thesis. AES is Auger Electron Spectroscopy. Estimated boron concentrations were determined from Figure 4-11 and Figure 4-12.

Chapter Five

5. Experimental - Part III: Electrochemical Properties of $\text{Li}_x(\text{B}_z\text{C}_{1-z})_6$

5.1 Introduction to Electrochemical Methods

There are a vast number of techniques and spectroscopies that may be applied when studying the physical and electronic structure of a material. For materials that can intercalate lithium however, electrochemical measurements made on a cell with lithium as one electrode and the material of interest as the other, can provide a relatively simple yet sensitive probe of numerous properties. Many materials that are indistinguishable by powder X-ray diffraction show vastly different electrochemical properties, suggesting differences in crystal structure⁶² or in other cases microstructure⁶³, that are not distinguishable by the powder method. When studying intercalation in solids, the electrochemical cell is probably the most convenient method, since the intercalated lithium concentration can be changed continuously in a single experiment. The most commonly used electrochemical tests in battery materials research are constant current cycling (charging and discharging of cells between upper and lower voltage limits) and cyclic voltametry.

5.1.1 Chemical Potential

The electrochemical cell provides a convenient means of measuring changes in thermodynamic quantities of an intercalation material as a function of lithium concentration. A cell basically consists of an anode and a cathode, with chemical potentials for the transferred species of μ_{anode} and μ_{cathode} respectively, separated by an ionically conducting electrolyte which allows transfer of the intercalating ions, but not electrons. The chemical potential is defined by:

$$\mu = \partial G / \partial n$$

where G is the Gibb's Free Energy and n is the number of transferred atoms. The spontaneous intercalation process consists of an ion of positive charge ze moving from the anode, into solution, diffusing across the electrolyte, and intercalating into the cathode. Simultaneously, z electrons leave the anode, travel through the external circuit, doing work, and finish in the cathode, to maintain charge neutrality at both electrodes. This process is driven by the difference in the chemical potential of the intercalated species between the two electrode materials. Ignoring losses, the change in free energy of both electrodes, for each transferred atom

$$\Delta\mu = \mu_{cathode} - \mu_{anode}$$

equals the work done in the external circuit:

$$W = -zeV$$

Setting $W = \Delta\mu$, we get an expression for the equilibrium voltage of a cell in terms of the chemical potential of the electrodes:

$$V = -\frac{(\mu_{cathode} - \mu_{anode})}{ze}$$

For convenience we will discuss only the case where lithium metal is the anode. Because the anode is a single homogeneous phase, whose composition does not change, μ_{anode} is a constant throughout the experiment. For this reason, materials of interest for lithium-ion cells are usually studied in cells with lithium metal anodes, as shown in Figure 5-1. If both electrodes were intercalation compounds, both of their chemical potentials would vary as the lithium concentration changed. The variation of cell voltage with charge would then be difficult to interpret. Measuring the voltage of a cell with a lithium anode as a function of state of charge is therefore a direct measurement of the chemical potential of intercalated lithium in the cathode as a function of the intercalated lithium concentration (with respect to lithium metal), which we will call $\mu(x)$.

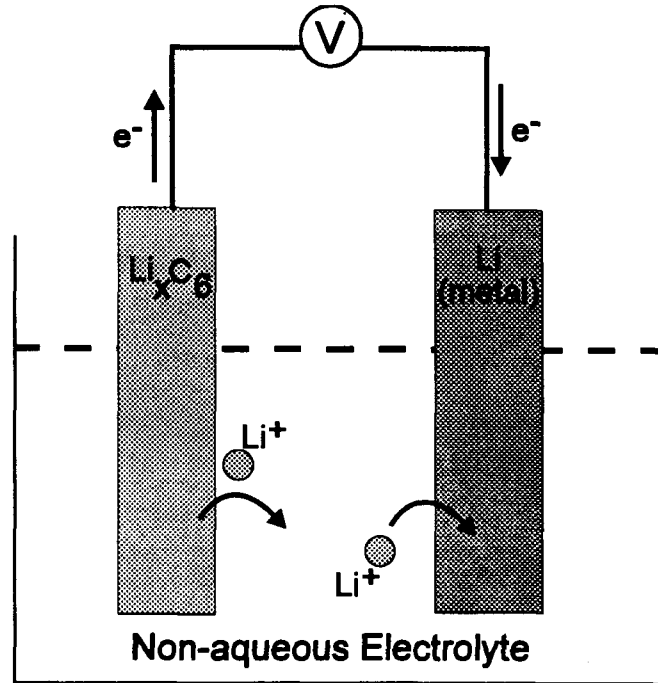


Figure 5-1 Schematic drawing of a lithium test cell. The current direction shown corresponds to the recharge of the cell.

5.1.2 Types of Experiments

5.1.2.1 Voltage Curves

There are several useful tests that may be performed on an intercalation-based electrochemical cell. The simplest of these is galvanostatic cycling. In this technique, the cell is fixed at constant temperature and cycled (repeatedly charged and discharged) between upper and lower voltage trip points. During charge, a current source is used to provide a constant current until the measured cell voltage exceeds the upper trip voltage, at which time the current direction is reversed, and the cell is discharged to the lower voltage trip. This process is repeated a number of times, depending on the type of information that is desired. The voltage is measured as a function of time.

The information gained from this process can be analyzed in a number of ways. A plot of the voltage versus time, $V(t)$, for one charge or discharge can be converted to voltage versus lithium concentration, $V(x)$, according to the following equation:

$$x = \frac{t \times I}{C \times M}$$

where t is the time in hours, I is the current in mA, M is the active mass of the electrode in grams, and C is the specific capacity of the intercalation host in mAh/g (often referred to as the “magic number”). The theoretical specific capacity in mAh/g of a compound Li_xM_n is calculated as:

$$C = \frac{F}{3.6 \times n \times M.W.} \quad \text{for a change of } \Delta x=1,$$

where F is Faraday’s number (96480 Coulombs/mole), and $M.W.$ is the molecular weight of M in grams/mole. Because the current changes direction, and therefore the sign of dx/dt , twice per cycle, a computer program is used to convert $V(t)$ to $V(x)$ for multiple cycles.

Care must be taken in identifying x in $V(x)$ with the concentration of intercalated lithium, since it includes *all* lithium that is transferred, whether it is intercalated, reacts with the electrolyte, or reacts irreversibly with the intercalation host. Subtracting the capacity of the first charge from the capacity of the first discharge yields the irreversible capacity of the first cycle. Usually the majority of the irreversible capacity occurs on the first cycle, because the reaction that is consuming lithium goes to completion, and the reactive species are all consumed. A plot of the capacity of the charge and discharge versus cycle number is called the capacity fade curve, and illustrates the loss of capacity versus cycle number. In a commercial system it is desirable to minimize capacity fade. Sometimes, instead of converting $V(t)$ to $V(x)$, it is better to convert to $V(Q)$, where Q is the capacity in mAh. The shape of the curve is the same, but makes no assumptions about the final disposition of the lithium, only stating the voltage as a function of the net amount of charge that has been transferred.

5.1.2.2 dx/dV

From the $V(x)$ data, the derivative, $-(\partial x/\partial V)_T$, can be calculated. We drop the subscript T in the following. A plot $-\partial x/\partial V$ versus voltage is a useful means of understanding voltage curves. As mentioned previously, the voltage of an electrochemical cell should be

constant during a first-order phase transition where two phases are coexisting, leading to a divergence in the derivative, $-\partial x/\partial V$. In a real cell however, the voltage decreases slightly (during discharge) over the two phase region, due to kinetic effects, producing a peak in $-\partial x/\partial V$ rather than a divergence.²⁸ Thus a sharp peak in $-\partial x/\partial V$ signals the likely existence of a first-order phase transition. Higher order or continuous phase transitions manifest themselves as a divergence in $-\partial x/\partial V$ at a single composition. Similarly, a $-\partial Q/\partial V$ versus V plot can be produced from $V(Q)$ data, and contains the same information.

Another useful way to interpret the derivative plot is in terms of the density of sites for intercalated atoms as a function of voltage, in analogy to the density of one-electron states versus energy. A peak in $-\partial x/\partial V$ corresponds to a large number of sites with approximately the same voltage. This is true for a system whether it involves a first-order transition or a continuous transition. If the chemical potential is dominated by the binding energy of the intercalated atoms to the host, rather than by interactions between them or by the configurational entropy of site occupation, then the $-\partial x/\partial V$ versus V plot can be thought of as approximately corresponding to the density of sites versus binding energy. Qualitatively, the integrated area under the $-\partial x/\partial V(V)$ curve is equal to the total capacity per voltage increment, just as the area under the density of states plot is the number of states per energy increment

5.1.2.3 Cyclic Voltametry

Another common electrochemical test that can be performed is cyclic voltametry. In this method the voltage applied across a cell is swept, typically linearly with time, and the resulting current is measured. A plot of I vs V looks very similar to a plot of $-\partial x/\partial V$ vs V which follows from:

$$I = \frac{dQ}{dt} = \frac{dQ}{dV} \frac{dV}{dt} = Q_0 \frac{dx}{dV} \frac{dV}{dt}$$

where Q_0 is the charge corresponding to $\Delta x=1$. Since Q_0 and dV/dt are constant, I is proportional to dx/dV , neglecting kinetic effects. The advantage of the voltamogram is that it

can often be performed more quickly than the constant current cycling required to produce a noise-free derivative curve. One disadvantage is that the areas of interest are the peaks in current. Thus if the experiment is performed on a two-electrode cell, such as a standard coin cell, then the measured data is shifted in voltage by IR_{int} , where R_{int} is the internal resistance of the cell. Because the current changes throughout the peak, the amount of shift changes continuously and the peak shape is deformed. Another disadvantage of cyclic voltametry is that an equal amount of time is spent on each voltage increment, unlike the derivative curve where the time spent on the peaks is much greater than the time spent in the less-interesting valleys.

5.1.2.4 *In-situ X-ray Diffraction*

Another very powerful technique is that of *in-situ* X-ray diffraction. In this experiment a cell is constructed with a Beryllium window, and the cell is cycled either galvanostatically, or potentiostatically, in voltage steps, and the diffraction pattern is measured as a function of intercalated lithium concentration. This technique will be described further in Section 5.5.

5.2 *Electrochemical Intercalation in Carbonaceous Materials*

The details of intercalation in carbonaceous materials were described in Chapter 2, and so only the specific differences that exist for electrochemical intercalation will be described here.

5.2.1 *Electrochemical Intercalation of Li in Graphite*

5.2.1.1 *The Voltage Curve of Li/Graphite Cells*

As discussed previously, the intercalation of lithium in graphite produces a series of staged phases, which vary with lithium concentration. In fact, the phase diagram of Li_xC_6 has recently been studied in detail using *in-situ* diffraction on an electrochemical cell.³² Because $V(x) = -\mu(x)/e$, a two phase region produces a plateau in the voltage. By measuring the length of the voltage plateaus, the composition range of the two phase regions can be determined. To do this successfully, care must be taken to avoid parasitic side reactions between the

electrolyte and the carbon electrode on the first discharge, which can obscure the reversible intercalation that gives rise to the staged phases. These parasitic side reactions will be dealt with in Section 5.2.1.2. A representative voltage curve for lithium intercalation in Johnson-Matthey Synthetic Graphite (JMI) is shown in Figure 5-2. Note the visible voltage plateaus.

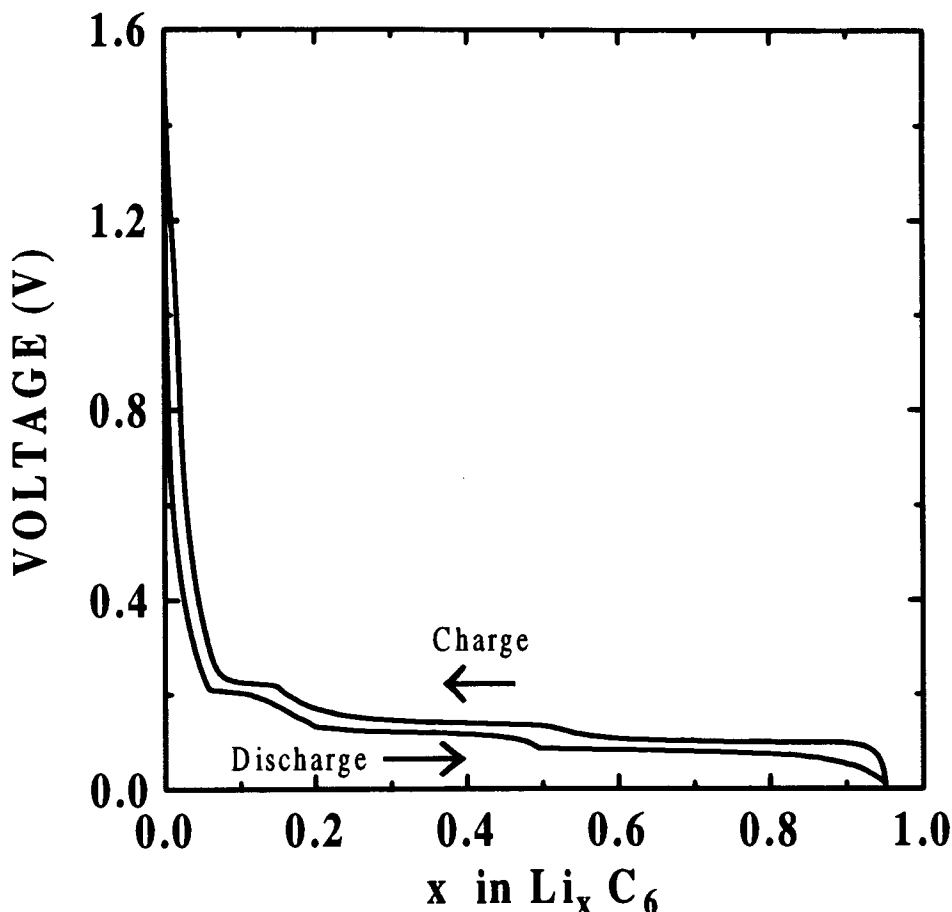


Figure 5-2 Second cycle voltage curve of Li/JMI graphite cell

Although several plateaus are visible on this scale, a plot of the derivative, $-\partial x/\partial V$, versus voltage is a much more sensitive probe. Plateaus in the voltage show up as peaks in the derivative, as seen in the derivative curve of JMI graphite shown in Figure 5-3. The phase transitions, as described in Chapter 2, are labeled, as identified by X-ray diffraction. In this, and all subsequent, derivative curves, for plotting clarity, the charge is assigned a positive value and the discharge a negative value, even though $\partial x/\partial V$ is always negative

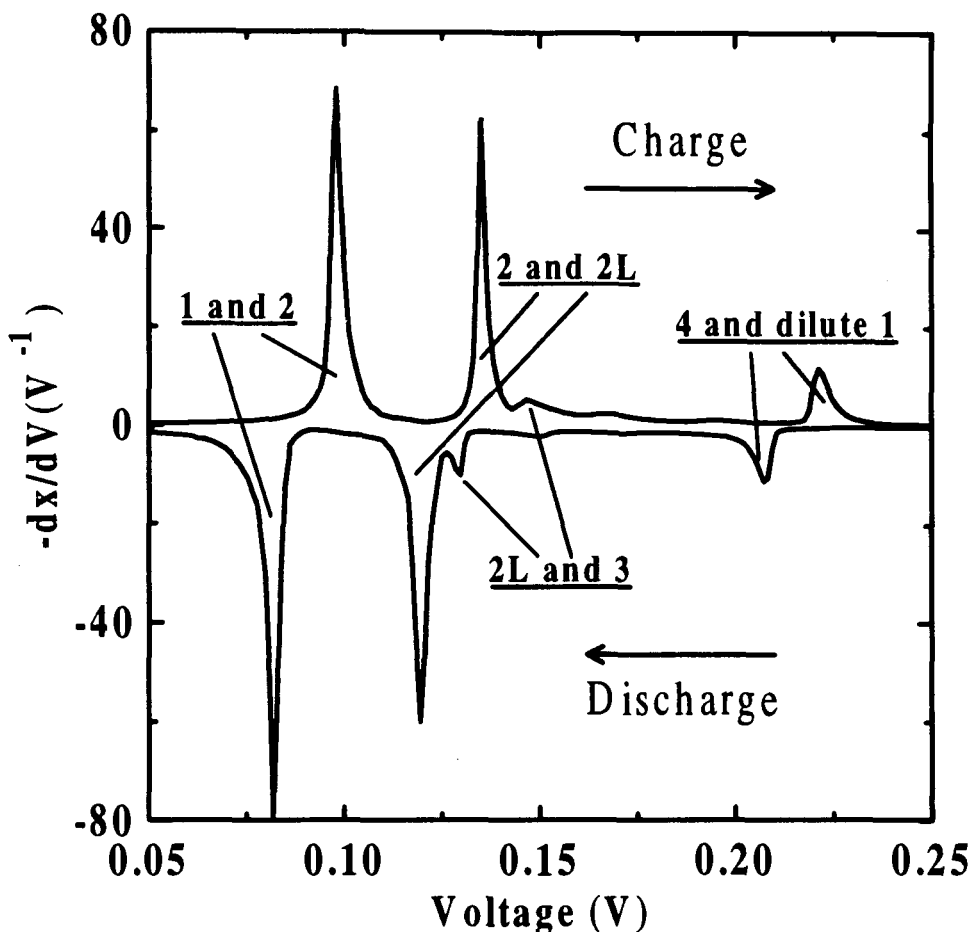


Figure 5-3 Derivative curve of JMI graphite with staged phase transitions labeled⁶⁴.

5.2.1.2 Electrolyte Decomposition, Passivation Film Formation and Cointercalation

Several parasitic side reactions can occur while intercalating lithium into graphite electrochemically. As discussed in Chapter 1, lithium metal will react with non-aqueous electrolytes to produce an electronically insulating, but ionically conducting film on the surface of the lithium. This film, often referred to as the solid electrolyte interphase (SEI)⁶⁵, grows until it is thick enough to prevent electrons tunneling from the lithium to the electrolyte. At this point the reaction is stopped and the surface is passivated. A similar reaction can occur on the surface of a carbon electrode during the first discharge. Although carbon is stable in non-aqueous solvents, Li_xC_6 , which has a voltage only about 0.1 V above lithium metal, is not. During the first discharge of a Li/graphite cell, some of the lithium ions

transferred to the carbon electrode combine with electrons and react with the electrolyte, forming a passivating film. This reaction stops when the film becomes thick enough to prevent tunneling of electrons across it, but allows intercalation to continue because the film conducts lithium ions.⁶⁶ The voltage curve of a Li/graphite cell, using Lonza KS-44 graphite and an electrolyte solution of 1M LiN(CF₃SO₂)₃ and 1M 12-Crown-4 ether in a 50:50 (v/v) mixture of propylene carbonate and ethylene carbonate, is shown in Figure 5-4. The extra capacity above 0.25 V on the first discharge corresponds to the irreversible reaction of lithium with the electrolyte, and the formation of a passivating film. The first charge is shorter than the first discharge by the amount of this extra capacity, because only the intercalated lithium can be removed, not the lithium that has been consumed in the formation of the SEI. The following discharge is the same length as the charge, proving that the formation of the SEI is complete.

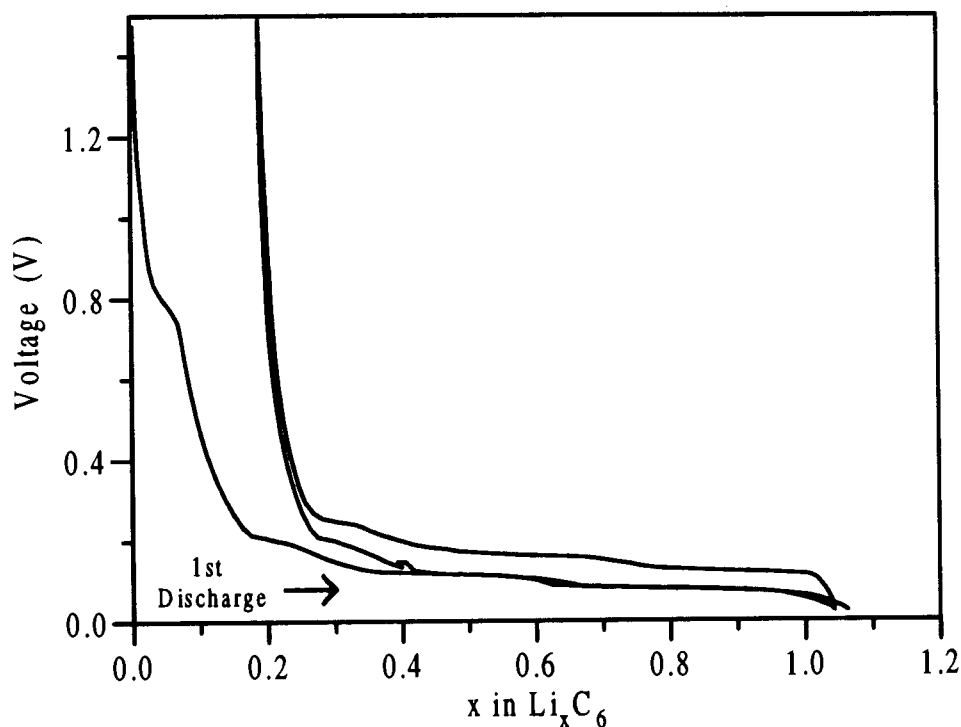


Figure 5-4 The first discharge and subsequent cycle of a Li/graphite (Lonza KS-44) cell.

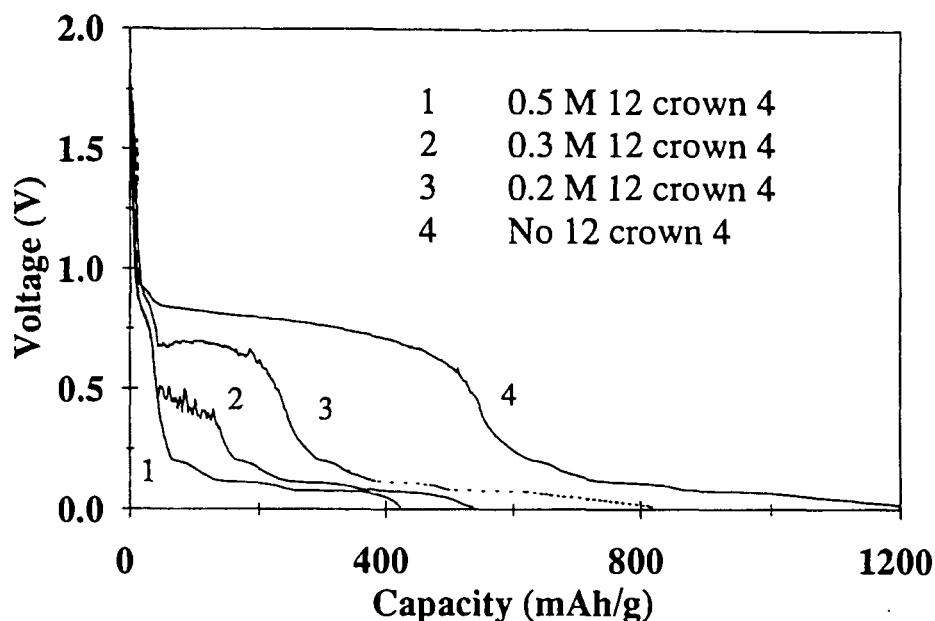


Figure 5-5 The effect of 12-Crown-4 ether on the irreversible capacity of Li/Graphite cells with 1M LiClO₄ PC/EC electrolyte (from reference 67). Only the first discharge is shown.

Another type of side reaction is cointercalation, a process in which two or more guests enter the same host. There are two distinct types of cointercalation: (1) where both guests donate electrons to the host, and (2) where only one donates and the other is neutral and surrounds the other.²⁸ The latter is the case of interest when studying graphite because the solvent molecules which form the solvation sphere around the lithium ions in solution can be intercalated along with the lithium into the host. In a material such as graphite with weak bonding between the layers, this can lead to exfoliation of the layers, causing a drastic increase in surface area. As all of this new surface area is passivated by reaction of lithium atoms with the solvent, a great deal of lithium is consumed, and large amounts of gas are produced. Because of this effect the evidence of cointercalation in the voltage curve is similar to that of passivation film formation, except that it continues much longer, until a larger fraction of the graphite is exfoliated. This is known to occur for the solvent propylene carbonate (PC). One might think that another solvent should be chosen to avoid cointercalation, but until recently there weren't any better choices that had all the other properties necessary for a good commercial electrolyte. One solution was to add 12-Crown-4

ether, a large crown-shaped molecule that chelates the Li^+ ion and thus prevents the cointercalation of PC.⁶⁷ The effect of additions of 12-Crown-4 ether on the irreversible capacity of Li/Graphite cells are seen in Figure 5-5. The capacity at greater than 0.25 V is mostly irreversible, and can be seen to decrease with the addition of the ether. This is a reasonable solution for the laboratory, but not for industry, due to its high cost. Recently (during the time this work was being done), better electrolytes that do not contain PC have been discovered, making cointercalation a problem of the past. One such electrolyte consists of LiPF_6 dissolved in an ethylene carbonate/diethyl carbonate solution.

5.2.2 Electrochemical Intercalation in Disordered Carbons

The suppression of staging due to disorder in the carbon host, and the trend in reversible capacity with heat treatment temperature were discussed in Chapter 2. The experiments that yielded those results were all performed by electrochemical intercalation, but the results were generally applicable to intercalation by any method. In this section we will discuss only issues directly related to electrochemical intercalation in heated petroleum pitches. The new, high capacity disordered carbons will be dealt with in Chapter 7.

The parasitic side reactions which have been such a problem when dealing with intercalation in graphite can also occur in disordered carbons. The irreversible capacity associated with the formation of a passivating film is proportional to surface area, which depends strongly on the method and conditions of production of the carbon. On the other hand, co-intercalation of electrolyte followed by exfoliation do not occur unless the carbon is quite graphitic.

Figure 5-6 shows the voltage curve of a lithium test cell with an electrode made from petroleum pitch heated to 900°C . It is typical of the low temperature disordered carbons, with a sloping voltage curve, and no evidence of plateaus due to staged phase transitions. The irreversible capacity of the first cycle is about $x=0.2$ or 75 mAh/g, as seen by the fact that after the first complete cycle $x=0.2$. The lithium corresponding to $x=0.2$ in Li_xC_6 has reacted, and is not intercalated. In the inset derivative curve, the peaks that appear only on

the first discharge correspond to irreversible reactions of lithium with the electrolyte. On subsequent cycles, only the broad peaks remain, due to the gradually sloping voltage curve, with no evidence of staging. As soft carbons are heated, the reversible capacity decreases to a minimum at 2000°C. Above this temperature staging begins to occur and the reversible capacity increases, as the voltage curve flattens and moves to lower voltage.

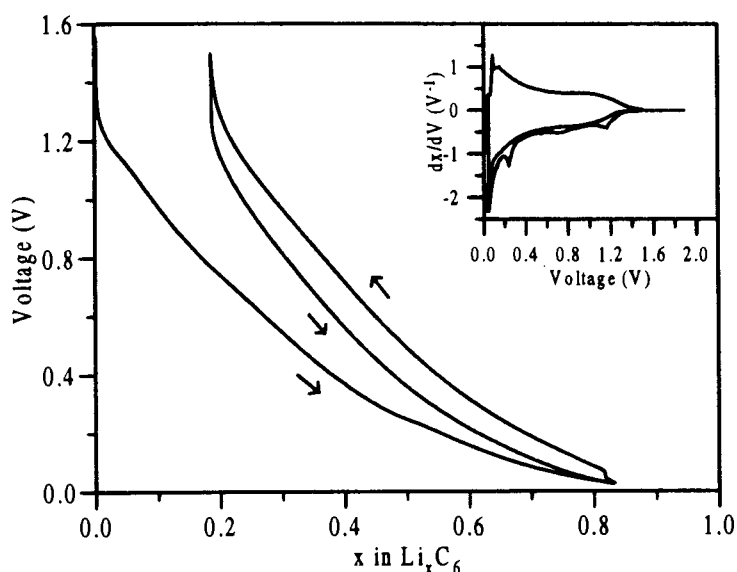


Figure 5-6 Cell voltage vs. x in Li_xC_6 for the first cycle and second discharge of cells made from KS900, cycled at 7.44 mA/g. The inset shows the derivative, dx/dV , for the same cells.

5.3 Cell Construction and Testing

Cell construction consists of several distinct steps. In many of the steps there are trade secrets that lead to successful cells and therefore meaningful results. The first step involved is electrode fabrication.

5.3.1 Electrode Fabrication

The electrode materials must be acquired, either by synthesis or purchase. In our case the B_2C_{1-z} film was synthesized, as described in Chapter 2, and the lithium foil electrodes were provided by Moli Energy (1990) Ltd. The lithium foil is 125 μm thick, and may be used as received. It is important however that the lithium be stored in an inert atmosphere to

avoid oxidation.

Some films were used as deposited, on Ta, Cu or Ni foil, and no further preparation was necessary. Most electrodes, however, were prepared as follows. The B_2C_{1-z} films were scraped from their substrate and ground in a mortar and pestle to a fine powder. Many of the samples were then mixed with 5% by mass of Super S Carbon Black (from MMM Carbon, Belgium). The purpose of adding this carbon is to provide a conductive matrix that will maintain electrical contact to all of the sample grains throughout the expansions and contractions produced by intercalation and de-intercalation. Super S is a good choice for this role because it is composed of long filaments that each can connect several grains. A slurry of this powder was then made using a solution of polyvinylidene fluoride (PVDF) in N-methylpyrrolidinone (NMP). The slurry, which has the consistency of paint, was then spread onto copper foil and dried in air at $\sim 110^\circ\text{C}$ for several hours. The resulting electrodes were typically $100\mu\text{m}$ - $200\mu\text{m}$ thick, and contained 5-10% by weight of PVDF binder. These electrodes were then cut into $1.2\text{cm} \times 1.2\text{cm}$ squares and weighed. The active mass of each electrode was then determined by subtracting the weight of the copper backing and the PVDF binder.

5.3.2 Cell Assembly

All cells produced for this work, except where otherwise noted, are stainless steel 2320-type coin cells (23mm OD, 2.0mm thick), similar to those found in watches and calculators. The cell structure is illustrated schematically in Figure 5-7. The basic components are the top and bottom casings, the two electrodes, a microporous, polypropylene separator, a stainless steel spacer, a disc spring, and a polypropylene gasket. The cell assembly procedure changed during the course of this work, due to an improvement in electrolytes. The first electrolyte used was 1M $\text{LiN}(\text{CF}_3\text{SO}_2)_2$ dissolved in 50/50 (v/v) propylene carbonate and ethylene carbonate (PC/EC). Most of the cells made using this electrolyte also contained 1M 12-Crown-4 ether, to prevent cointercalation of the propylene carbonate. For this electrolyte it was necessary to “pressure wet” the separator and the carbon powder-based electrode, prior to assembly. During this procedure, the separators and

electrodes are first anchored to the bottom of a glass vial containing the electrolyte. The vials are then sealed in a pressure bomb which is evacuated by roughing pump for ~10 minutes, to remove trapped gasses from the pores of the items being wetted. The vacuum is then released and the argon pressure in the bomb is slowly increased to 830 kPa (gauge) for another 10-15 minutes, to force the electrolyte into the pores. After this period, the pressure is released and the items are recovered. The appearance of each item is checked to ensure proper wetting.

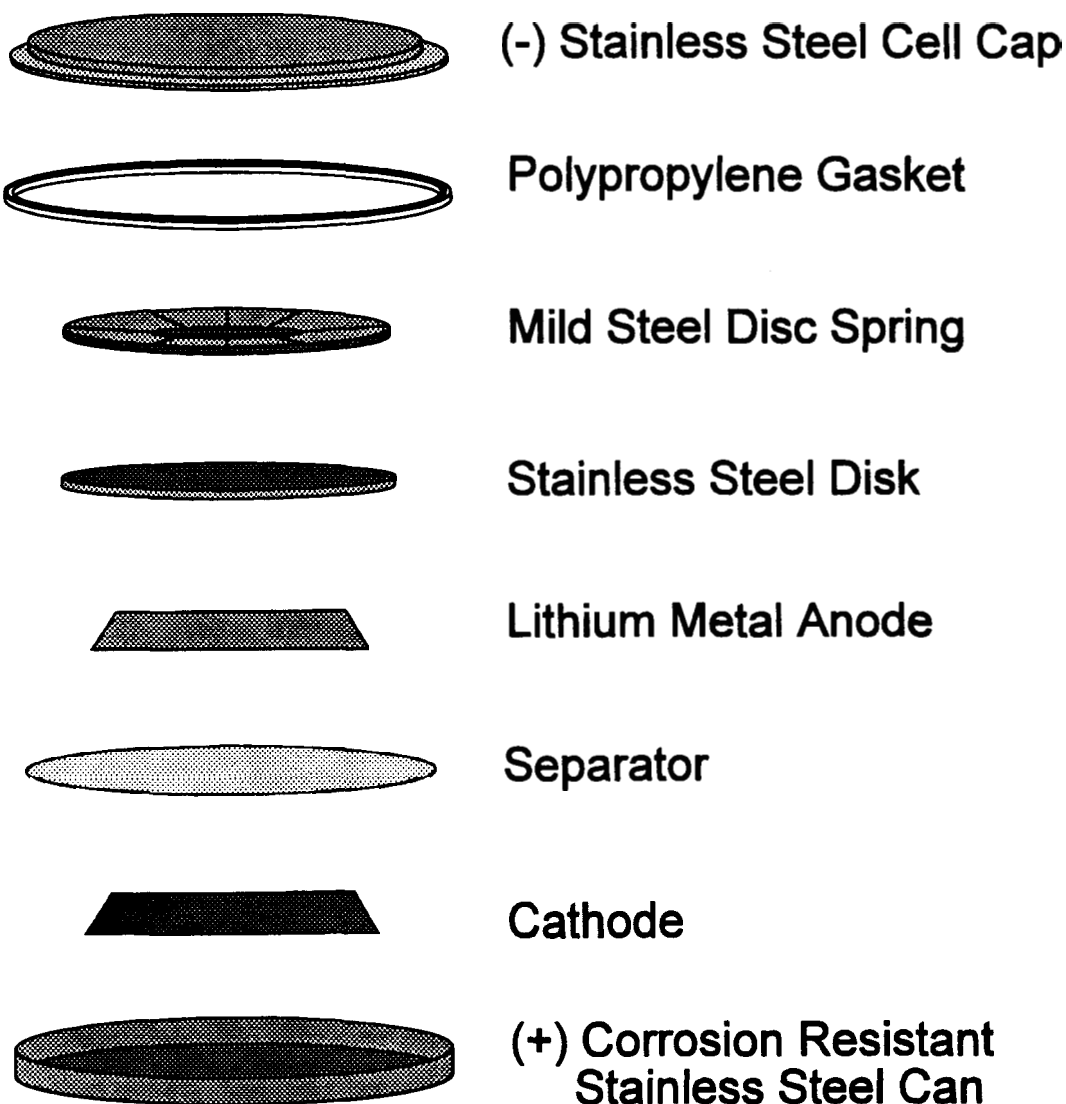


Figure 5-7 Exploded view of a typical lithium coin cell

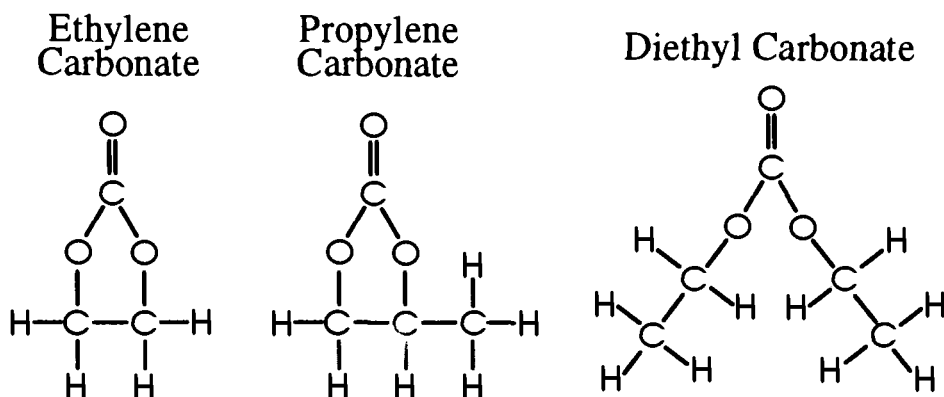


Figure 5-8 Structure of common electrolyte solvents

The second type of electrolyte used was 1M LiPF₆ dissolved in 30/70 (v/v) ethylene carbonate/diethyl carbonate (EC/DEC). This electrolyte is much easier to use since it will self-wet separators and electrodes at atmospheric pressure, and thus does not require the vacuum and pressurization process. In addition, it does not contain PC and therefore does not suffer from the problem of cointercalation.

5.3.3 Cell Testing

Cell testing was done on two charger systems. The early cells, made from films deposited on metals, were measured on a system built by Dr. J.R.Dahn. It consisted of a bank of manual chargers (Techware TF-66) that supplied the current and switched at the voltage trip points. Voltage was measured by a Keithley 196 voltmeter ($\pm 5 \mu\text{V}$), controlled by a Keithley 705 scanner, and read into a 286 computer via an IEEE bus. Later cells were measured on a computer controlled charger system from Moli Energy (1990) Ltd. All voltage and current set points were programmed and sent to the individual charger boards. In this system voltage was also measured by an integrated Keithley 196 voltmeter. For both systems the temperature was controlled at $30 \pm 1^\circ\text{C}$ in insulated boxes, with temperature measured by resistance temperature devices (RTDs) and heating controlled by Omega 4201A-PC2 temperature controllers. Some cells were also measured at 45°C .

The upper and lower voltage trip points for all cells were 2.5 V and 0.01 V respectively. The currents used varied, but for the samples of known active mass, a 50 or 100 hour rate was typically used. This means that the current was calculated so that in 50 (or 100) hours the total charge transferred corresponded to $\Delta x=1$ in Li_xC_6 . Since this amount of charge is equal to 372 mAh/g, a 50 hour rate corresponds to 7.44 mA/g and a 100 hour rate corresponds to 3.72 mA/g.

5.4 As-Deposited Samples - Results and Discussion

Two types of untreated samples were used to produce electrochemical cells: films, deposited on metal foil, and powders produced by the grinding of films deposited on quartz and copper foil. The majority of the data is for powders, because the active mass of the sample in the cell is well known, whereas for the films it is not, due to the large mass of the foil compared to the film, and the fact that the film is deposited on both sides of the substrate.

5.4.1 Films

Cells were made directly from the films deposited on metals before CVD runs that produced enough material to make powder electrodes had been carried out. Because the mass of these films was not well known, the purpose of these cells was to make a preliminary determination of: (1) whether any significant amount of reversible intercalation was occurring, and (2) the voltage profile if intercalation did indeed occur.

Cells made from depositions on Ta and Cu, showed interesting voltage curves, with very high voltage for carbon, starting at around 2 V, and appeared mostly reversible. Figure 5-9 shows the voltage curve for a $\text{B}_{0.17}\text{C}_{0.83}$ film deposited on copper foil, for a cell held at 30°C and 45°C on cycles 6 and 9, respectively. The total mass of the film was estimated to be 1.4 mg, about 5% of the mass of the substrate, and thus the lithium concentration was only estimated. The polarization of the cell was large, indicating a high cell impedance. The polarization causes a difference between charge and discharge voltage that can be eliminated when the current approaches zero. It is smaller for the cycle measured at 45°C than for the one at 30°C. This is because the impedance is mostly due to slow diffusion of lithium

through the film, which is temperature dependent. If the impedance were less, the capacity would be greater before the cell reaches 0 V, suggesting that the theoretical reversible capacity could be much higher than the estimated $x=0.75-0.85$ for this cell.

The voltage curves of the cells made from deposition on Ni appeared like pure graphite, showing staging plateaus. It is well known that Ni catalyzes the formation of graphite.⁶⁸ No indication of the effect of boron was apparent, and X-ray diffraction indicated that a significant amount of Ni_3B was present.

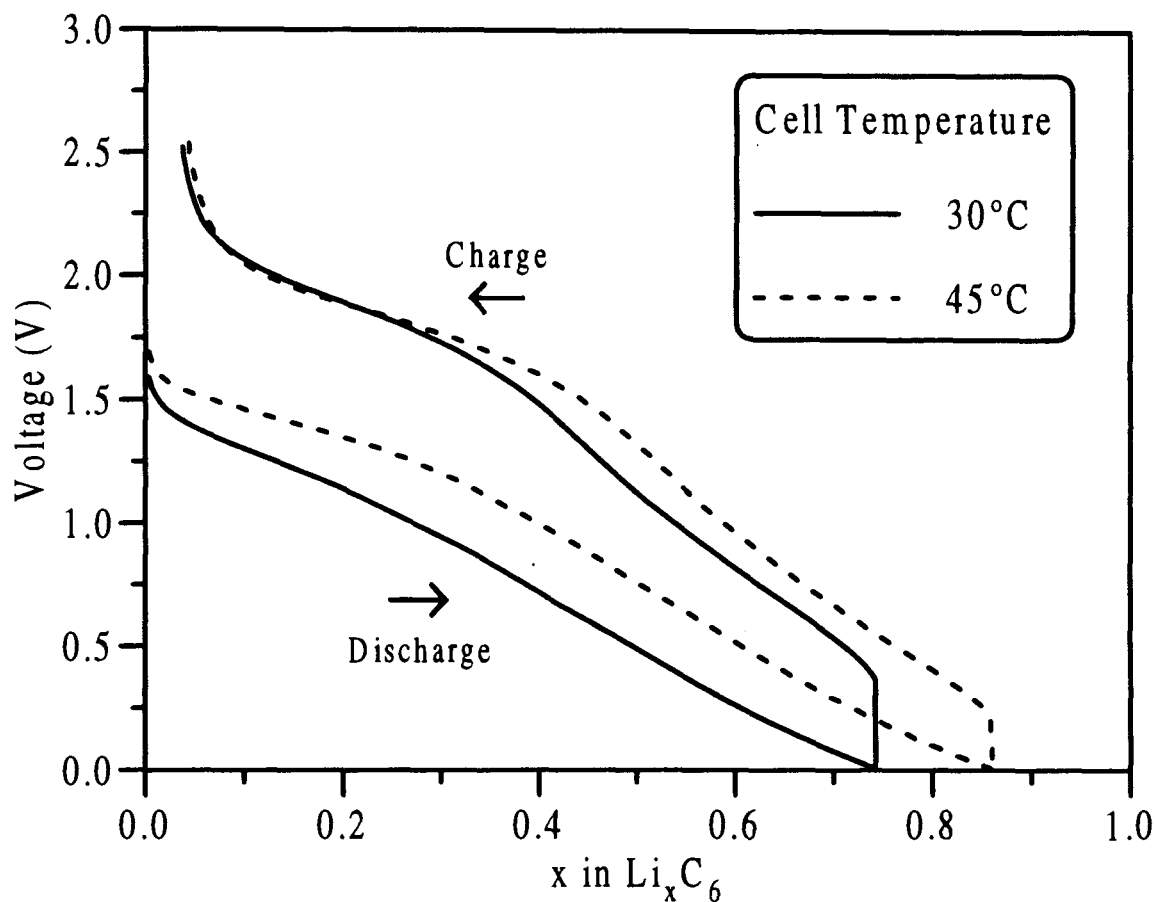


Figure 5-9 Cell voltage vs. x in Li_xC_6 for the first cycle and second discharge of cells made from a $B_{0.17}C_{0.83}$ film on Cu foil. The lithium concentration, x , is approximate.

5.4.2 Powders

Figure 5-10 compares the voltage curve of a cell using a pure carbon deposited at $900^\circ C$ by CVD from benzene to a $Li/Li_x(B_{0.03}C_{0.97})_6$ cell cycled at 7.44 mA/g. The first discharge and

subsequent cycle of the cells are shown. Irreversible capacity caused by reaction between lithium and the electrolyte on the carbon surface is evident in both cells by the fact that the first discharge is longer than the first charge.

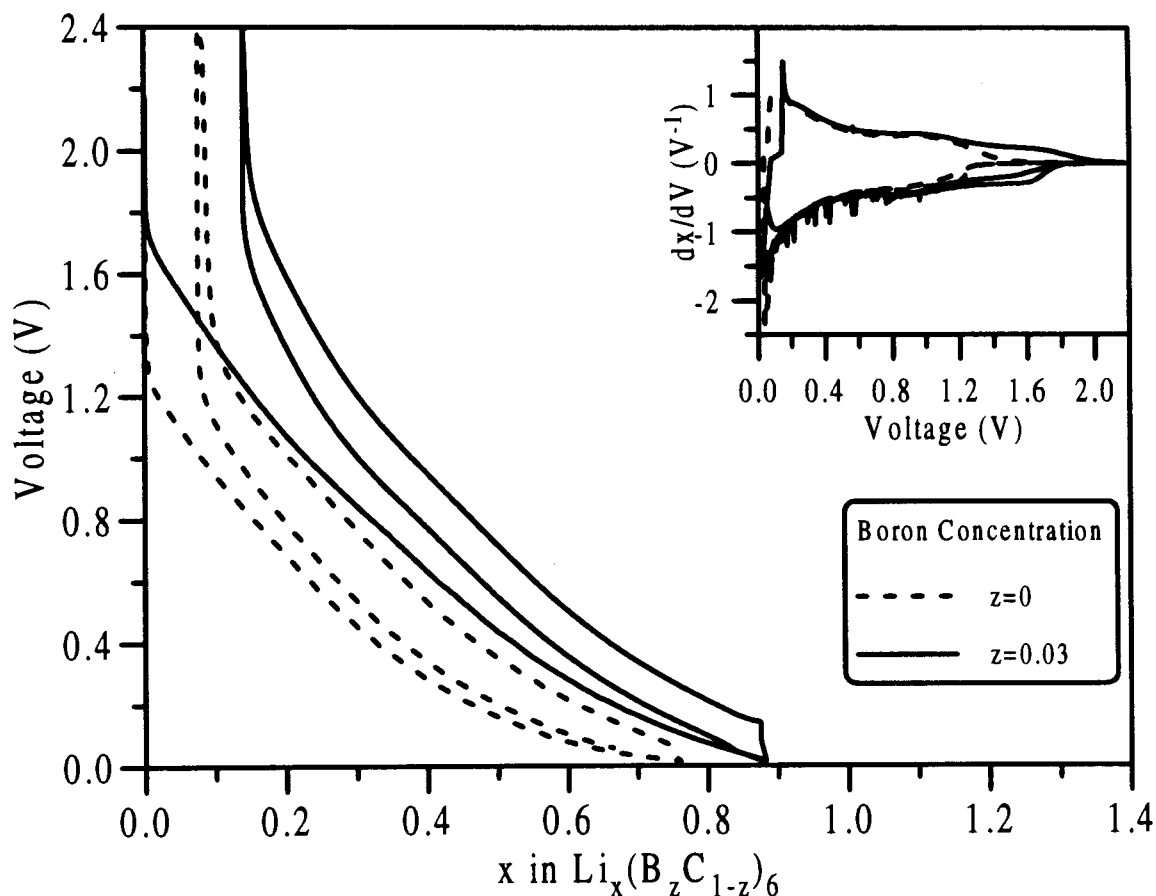


Figure 5-10 Cell voltage vs. x in $\text{Li}_x(\text{B}_z\text{C}_{1-z})_6$ for the first cycle and second discharge of cells made from $\text{B}_{0.03}\text{C}_{0.97}$ (solid), cycled at 7.44 mA/g, and pure carbon produced by CVD from benzene at 900°C. The inset shows the derivative, dx/dV , for the same two cells.

Subsequent charges and discharges are approximately the same length, suggesting that no further reaction is taking place. Two differences are already evident at this low boron concentration: the initial voltage of the $\text{Li}/\text{Li}_x(\text{B}_{0.03}\text{C}_{0.97})_6$ cell is higher than the pure carbon cell, and the reversible capacity is somewhat larger. The capacity is given by the integrated area under the curve. The difference in capacity between these two cells can be seen by area between the two derivatives on either charge or discharge. Further, the voltage at which this new capacity occurs can be observed easily. In these cells it is evident that most of the

additional capacity in the boron-containing electrode is found at relatively high voltage, between 1.2 and 1.8 V. This is not desirable for a lithium-ion anode material, because it reduces the average voltage of the complete cell. The irreversible capacity can be observed in the derivative curve as the area between two subsequent discharges of the same cell. This is between 0.5 and 1.25 V for the pure carbon cell, and between 1.2 and 1.65 V for the boron-carbon cell.

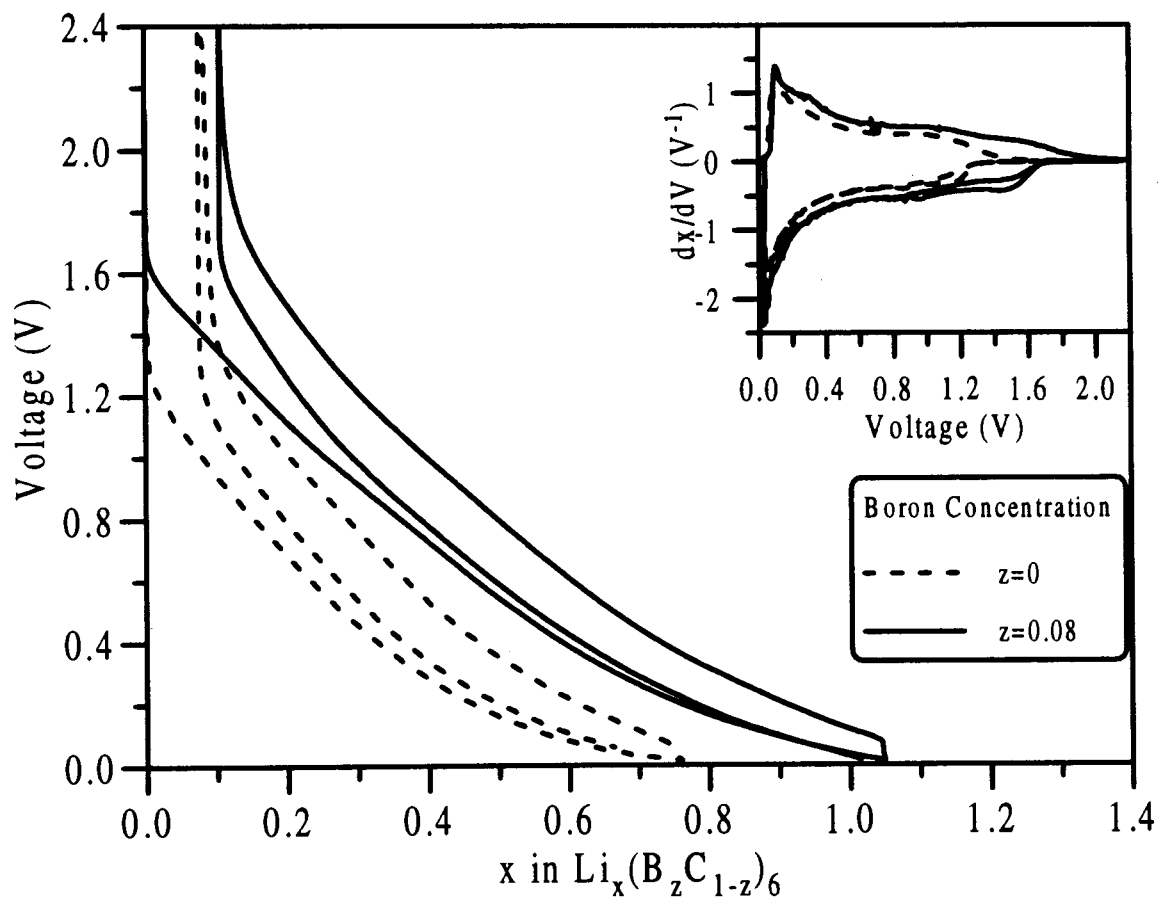


Figure 5-11 Cell voltage vs. x in $\text{Li}_x(\text{B}_z\text{C}_{1-z})_6$ for the first cycle and second discharge of cells made from $\text{B}_{0.08}\text{C}_{0.92}$ (solid), cycled at 3.72 mA/g , and pure carbon produced by CVD from benzene at 900°C . The inset shows the derivative, dx/dV , for the same two cells.

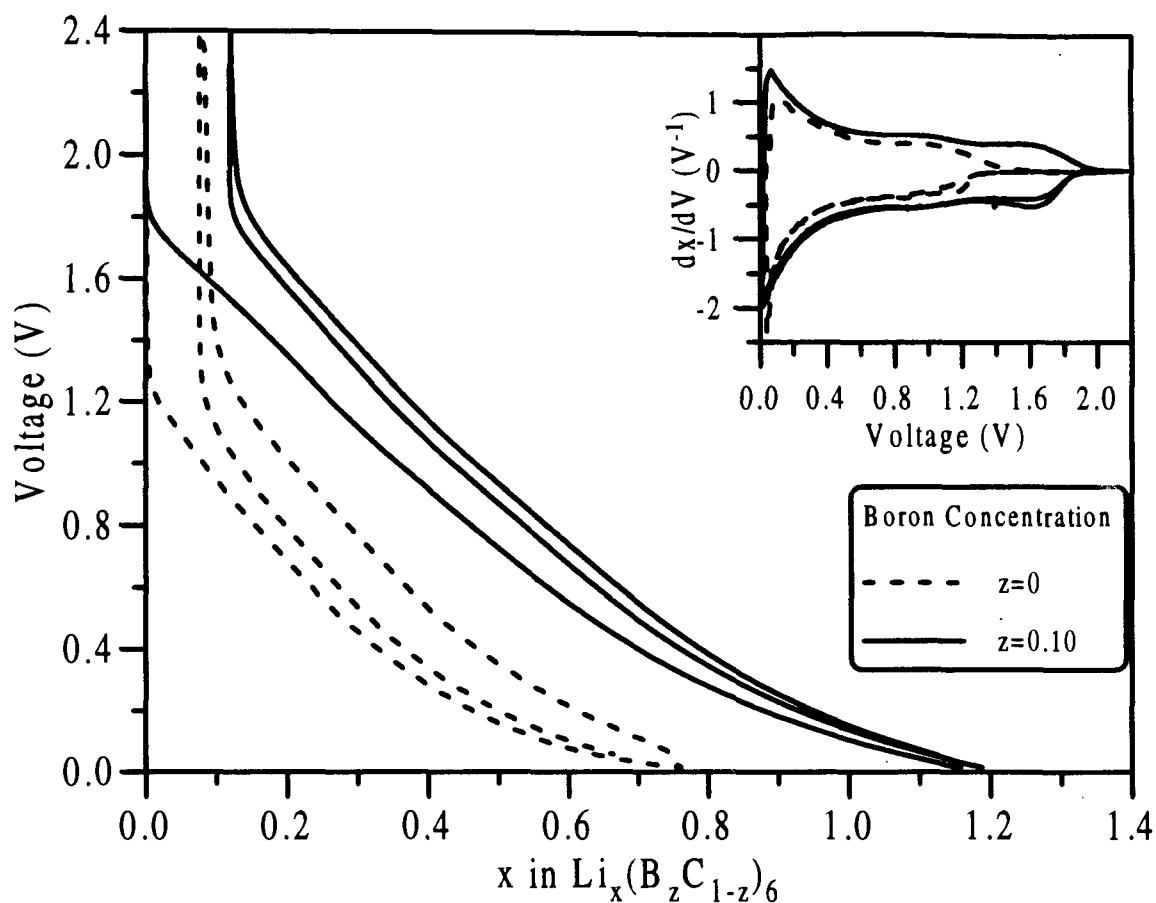


Figure 5-12 Cell voltage vs. x in $\text{Li}_x(\text{B}_z\text{C}_{1-z})_6$ for the first cycle and second discharge of cells made from $\text{B}_{0.10}\text{C}_{0.90}$ (solid), cycled at 3.72 mA/g, and pure carbon produced by CVD from benzene at 900°C. The inset shows the derivative, dx/dV , for the same two cells.

Figure 5-11 compares a $\text{Li}/\text{Li}_x(\text{B}_{0.08}\text{C}_{0.92})_6$ cell cycled at 3.72 mA/g to the same CVD benzene cell. The reversible capacity has increased dramatically to $x_{\text{max}}=0.95$, almost as much as the maximum in graphite. Most of this new capacity is from the high voltage region, where the area under the derivative curve has grown considerably, but there are measurable capacity gains at all voltages. $\text{Li}/\text{Li}_x(\text{B}_{0.10}\text{C}_{0.90})_6$ cells cycled at 3.72 mA/g were used to obtain the voltage and dx/dV curves in Figure 5-12. The reversible capacity in this cell now exceeds that of graphite, $x_{\text{max}}=1.08$. There is also a plateau which is now visible, centered at ~1.6 V, which appears as a broad peak in the derivative. Figure 5-13 shows a cell with a $\text{B}_{0.115}\text{C}_{0.885}$ electrode, cycled at 7.44 mA/g; x_{max} is 1.07, approximately the same as for the $\text{B}_{0.10}\text{C}_{0.90}$ cell. The derivative shows that the capacity at high voltage continues to

increase, indicating that this sample does indeed have more boron, while the capacity at low voltage decreases somewhat. This behaviour can be understood in light of the fact that the $B_{0.10}C_{0.90}$ cell contains no 12-Crown-4 ether, giving it better ionic conductivity. The improved conductivity decreases the polarization of the cell (the voltage difference between charge and discharge) compared to cells with 12-Crown-4 ether, allowing longer discharge before reaching the low voltage trip point. The capacity and plateau length continue to increase in the $Li/Li_x(B_{0.17}C_{0.83})_6$ cell shown in Figure 5-14, with an x_{max} of 1.16. The current for this cell was 7.44 mA/g.

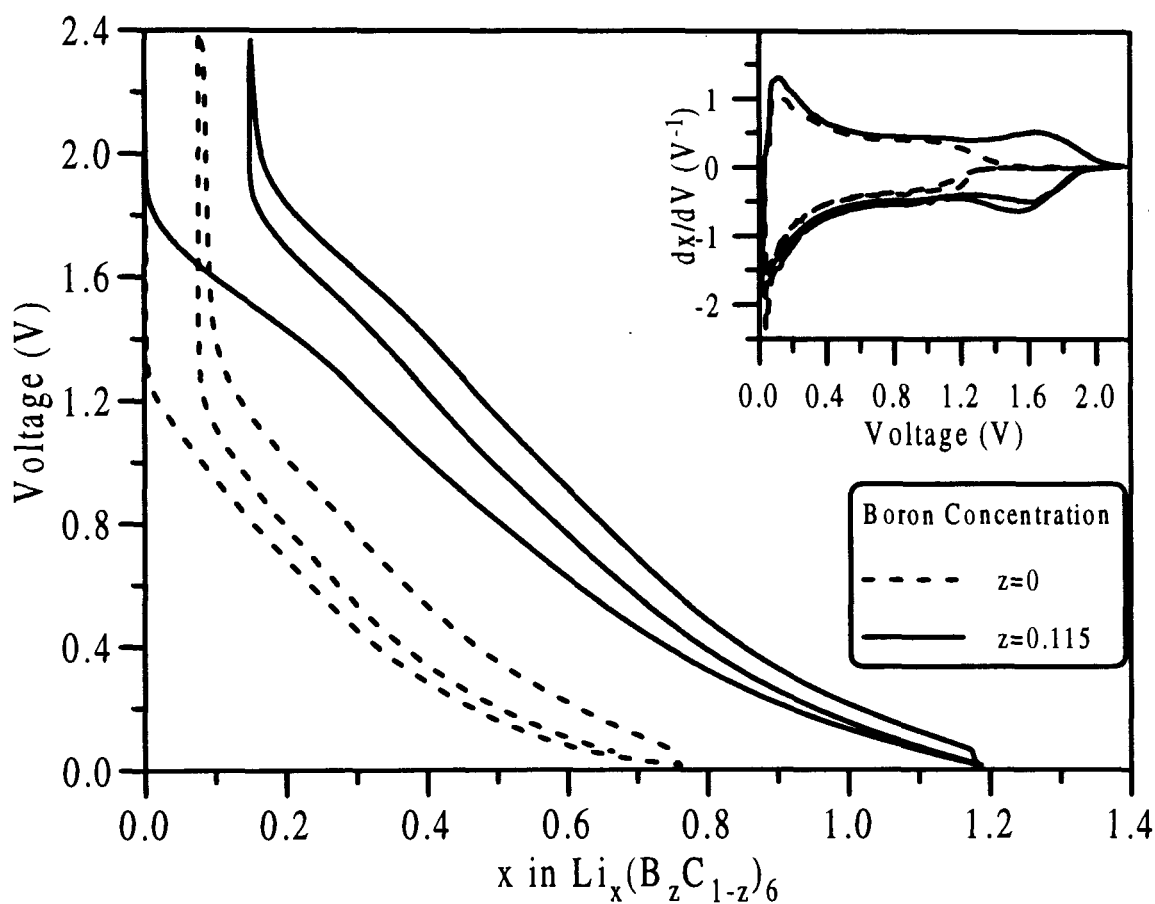


Figure 5-13 Cell voltage vs. x in $Li_x(B_zC_{1-z})_6$ for the first cycle and second discharge of cells made from $B_{0.115}C_{0.885}$ (solid), cycled at 7.44 mA/g, and pure carbon produced by CVD from benzene at 900°C. The inset shows the derivative, dx/dV , for the same two cells.

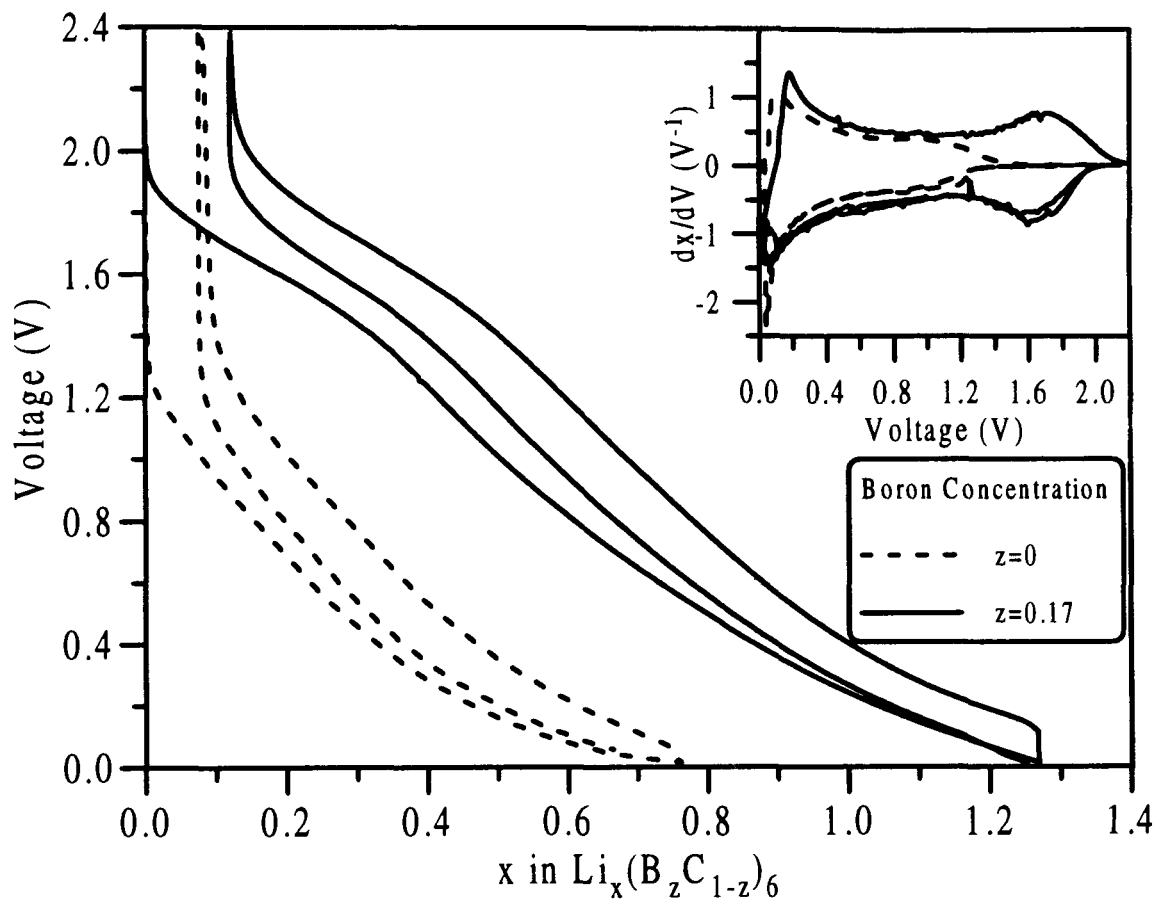


Figure 5-14 Cell voltage vs. x in $\text{Li}_x(\text{B}_z\text{C}_{1-z})_6$ for the first cycle and second discharge of cells made from $\text{B}_{0.17}\text{C}_{0.83}$ (solid), cycled at 7.44 mA/g, and pure carbon produced by CVD from benzene at 900°C. The inset shows the derivative, dx/dV , for the same two cells.

For comparison, cells were made from B_4C powder (Aesar 99+%) and a mixture of XP Coke and Boron powder (Johnson Matthey 99+%, 1 μm) such that the final stoichiometry was $\text{B}_{0.19}\text{C}_{0.81}$. Both these electrodes contained 5% Super S carbon black as a conducting additive. The B_4C cells showed no capacity beyond the very small amount due to the Super S carbon. The voltage curve of the boron/carbon mixture is shown in Figure 5-15 and appears exactly like pure coke, with a reversible capacity of $x_{\text{max}}=0.55$ in Li_xC_6 . The first discharge shows an irreversible capacity of $\Delta x=0.2$ centered at 0.75 V, most likely due to electrolyte decomposition. Neither of these cells shows behaviour that is similar in any way to the samples produced by CVD.

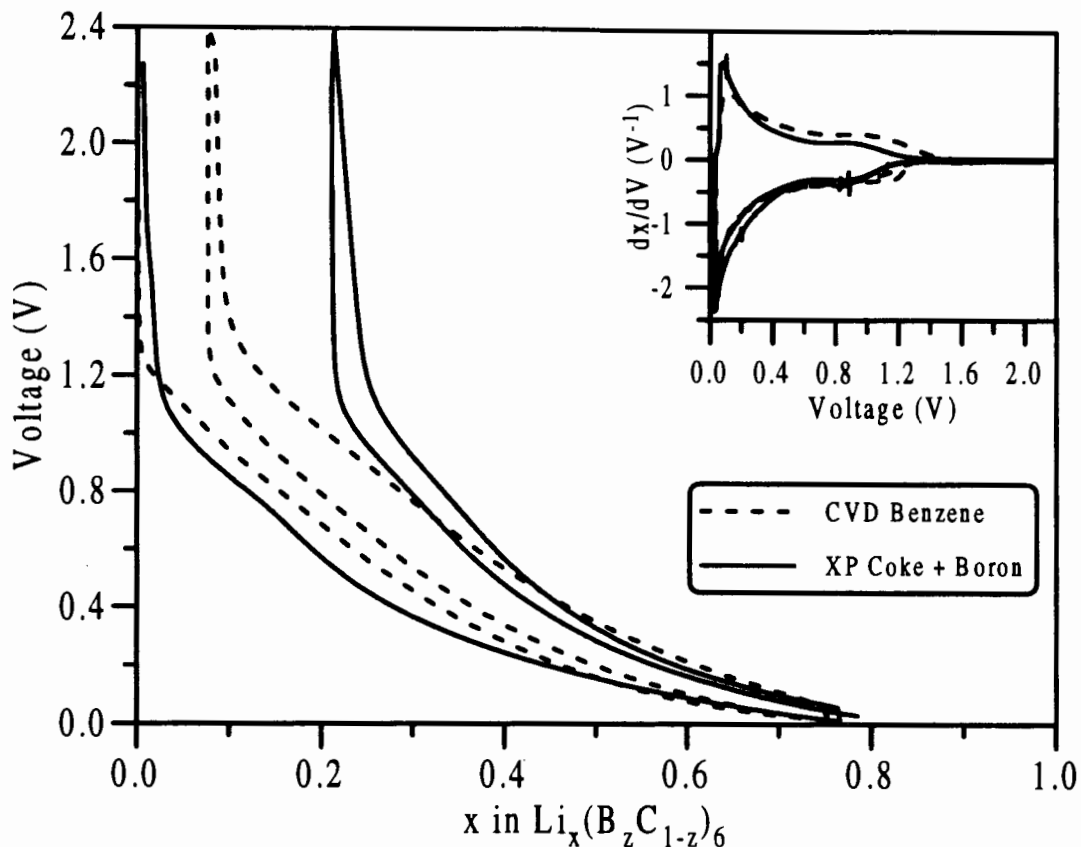


Figure 5-15 Cell voltage vs. x in $\text{Li}_x(\text{B}_z\text{C}_{1-z})_6$ for the first cycle and second discharge of cells made from a mixture of XP Coke and 20% boron powder (solid), cycled at 7.44 mA/g, and pure carbon produced by CVD from benzene at 900°C. The inset shows the derivative, dx/dV , for the same two cells.

Figure 5-16 is a comparison of the voltage curves of the six B_zC_{1-z} samples as a function of boron concentration. Each curve is shifted up sequentially by 1.0 V for clarity. The dramatic changes in profile and capacity are seen clearly, with the growth of the high voltage plateau at ~1.6 V. The irreversible capacity in the first cycle varies between 40 and 60 mAh/g for these materials, similar to that of pure carbon made from benzene by CVD at 900°C. The polarization does not change significantly between the $\text{B}_{0.03}\text{C}_{0.97}$ cell and the $\text{B}_{0.17}\text{C}_{0.83}$ cell (except for the cell with no 12-Crown-4 ether), which were both cycled at the same rate, showing that the rate capability is apparently not affected by boron concentration. This means that the cell impedance does not change appreciably with changing boron concentration.

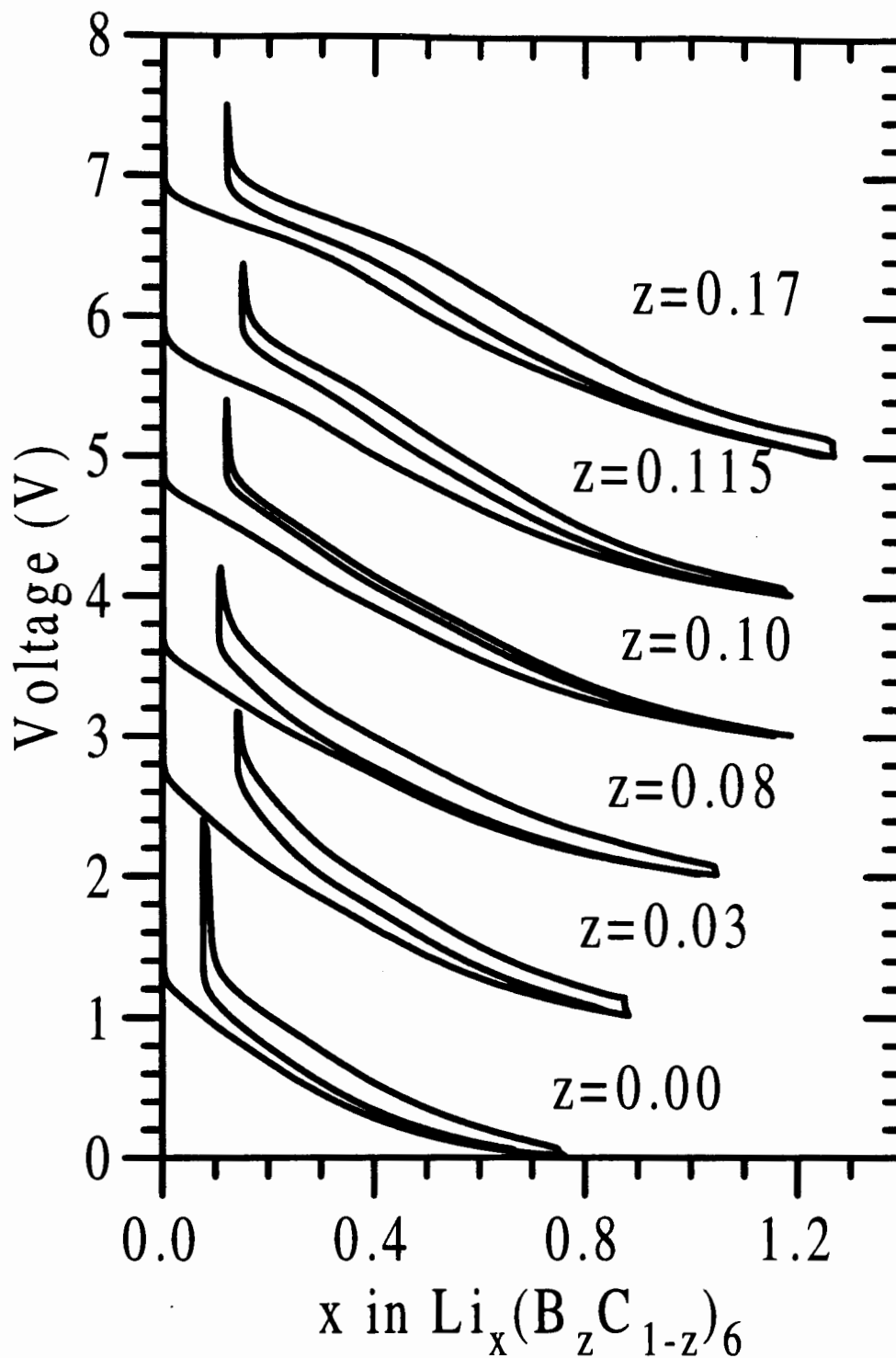


Figure 5-16 A comparison of voltage curves of $\text{Li}/\text{Li}_x(\text{B}_z\text{C}_{1-z})_6$ cells as a function of boron concentration. Each curve is shifted up sequentially by 1.0 V for clarity.

Figure 5-17 shows the reversible capacity, obtained by averaging the first charge and the second discharge capacities, versus the boron concentration. The capacity increases dramatically as the boron concentration increases. The capacity of the $B_{0.10}C_{0.90}$ is anomalously high due to the lack of 12-Crown-4 in the electrolyte.

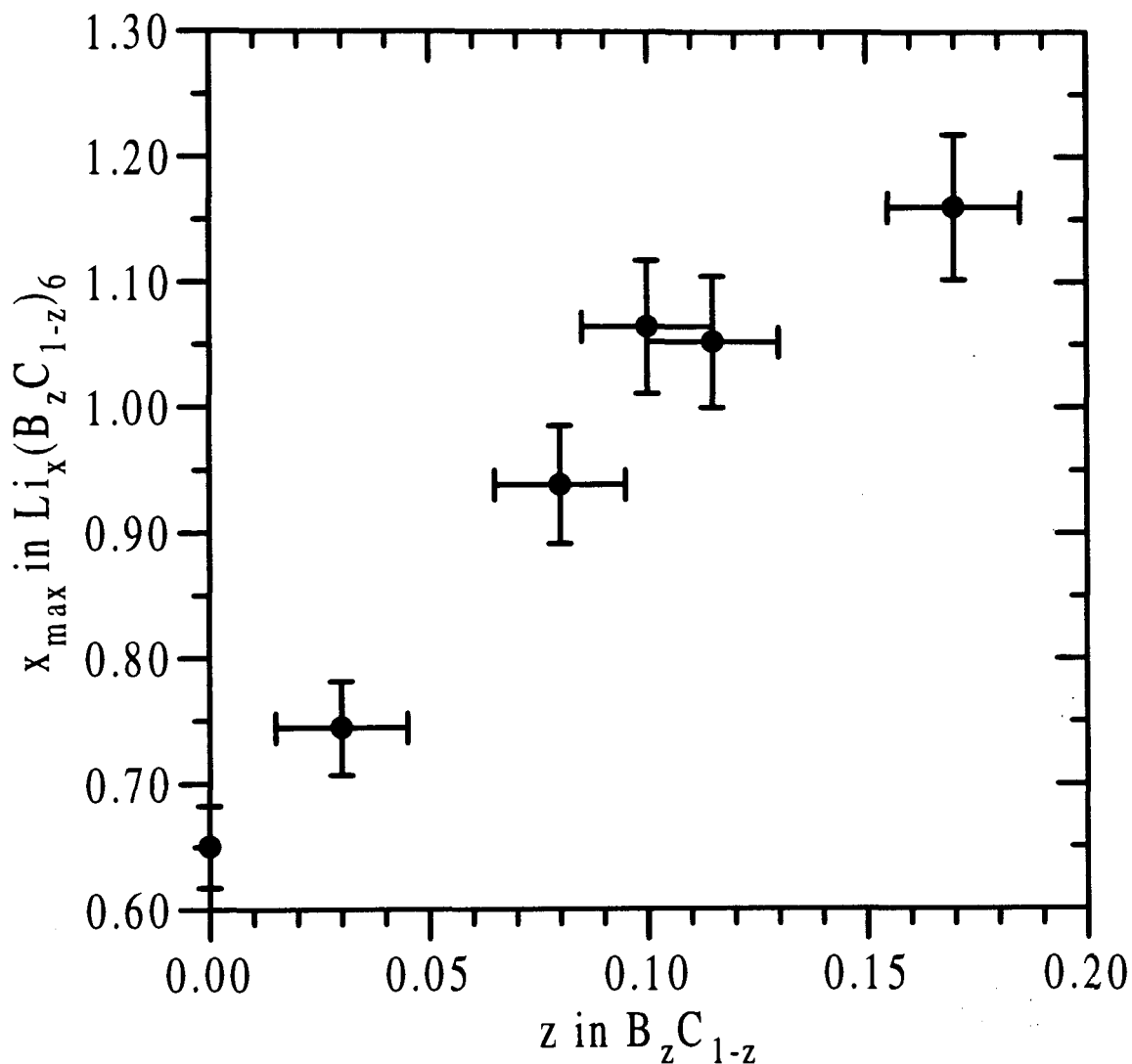


Figure 5-17 Reversible capacity vs. boron concentration in $Li/Li_x(B_zC_{1-z})_6$ cells made from B_zC_{1-z} . Capacities are calculated from the average of the first charge and second discharge.

The behaviour of these cells as a function of boron concentration can be understood qualitatively if the boron is thought of as an electron acceptor. Boron has three valence electrons, one less than carbon, and thus, when substituted into a carbon lattice, acts as an

electron acceptor. That is, there are fewer electrons than expected in the proximity of the boron atom and it is ready to accept more since it is incorporated in a compound whose global properties expect four valence electrons to be contributed from each atom. When lithium is intercalated into the carbon, it acts as an electron donor, donating most of its 2s electrons to the carbon host.³⁶ Therefore the presence of boron strengthens the chemical bond between the intercalated Li and the boron-carbon host compared to the pure carbon host. As a result of the increased bond strength, the chemical potential of the lithium in these boron-substituted carbons is decreased relative to unsubstituted carbon. Since $V = -\mu/e$, the cell voltage increases.

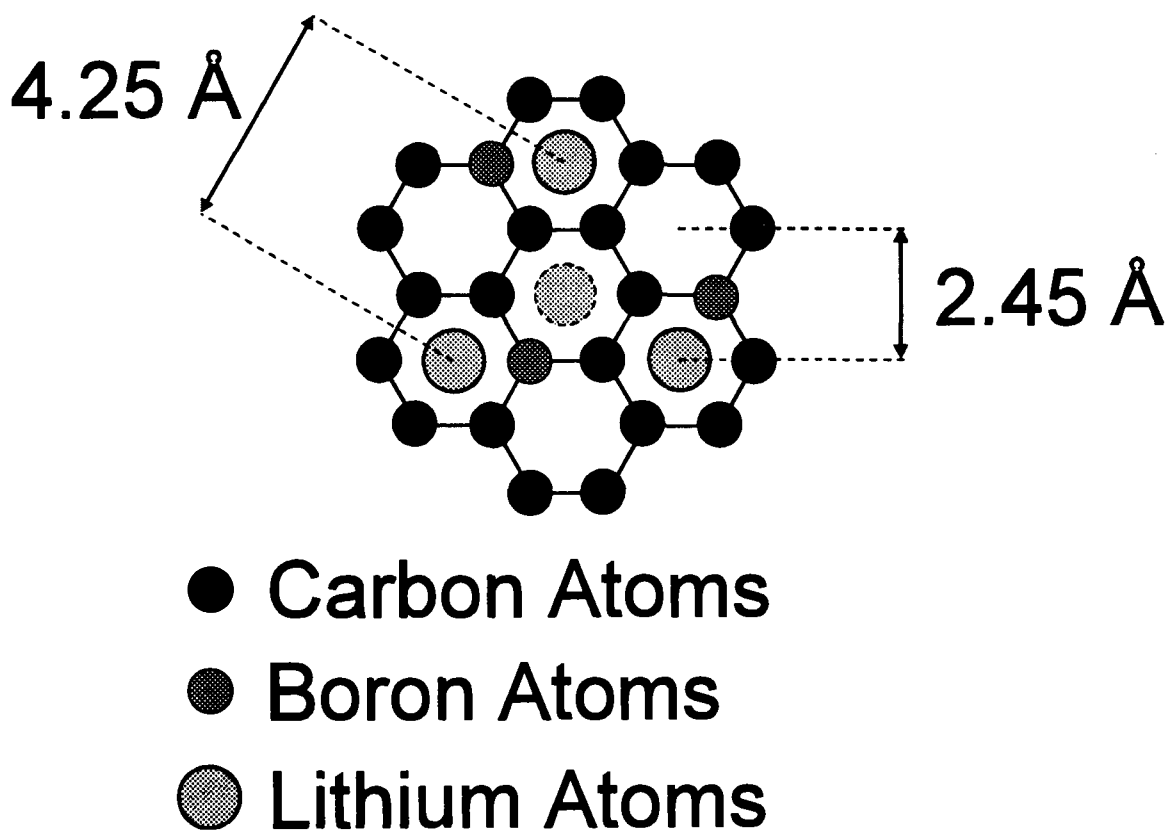


Figure 5-18 Schematic drawing of the lithium sites on a single layer of boron-substituted carbon. The dashed circle represents the site for additional lithium beyond $x=1$ in $\text{Li}_x(\text{B}_2\text{C}_{1-x})_6$

We now need to consider why the addition of boron causes a capacity increase. LiC_6 has one lithium atom centered between adjacent AA stacked carbon layers in every third

honeycomb, as shown by the solid large circles in Figure 5-18, with a near neighbor Li-Li distance of 4.25 Å. We assume that the binding energy $E(x)$, with respect to lithium metal, of these intercalated lithiums is given by E_0 . Experimentally E_0 is near 0.1 eV. If additional lithium atoms can be intercalated, they occupy sites with three neighbouring lithium atoms, each 2.45 Å away, as shown in Figure 5-18 by the dashed large circle. These sites have three additional interactions, which we call J , that are screened Coulomb repulsions between the lithium ion and its positively-charged, nearest-neighbor lithium ions. Therefore, for $1 \leq x \leq 2$ in Li_xC_6 , the binding energy is given by $E(x) = E_0 - 3J$. As lithium is intercalated beyond $x=2$, there are three more nearest-neighbor interactions, also at 2.45 Å. Therefore the binding energy over the range $2 \leq x \leq 3$ in Li_xC_6 is $E_0 - 6J$. Unfortunately, in graphite, $E_0 - 3J$ and $E_0 - 6J$ are apparently both less than zero, and thus x is limited to $x \leq 1$ in Li_xC_6 . But if boron is substituted for some of the carbon, the binding energy E_0 is increased to $E_0 + \Delta$. This effect may be large enough to make $E_0 + \Delta - 3J > 0$ and thus make the $1 \leq x \leq 2$ region accessible to intercalation. A qualitative sketch of the voltage of boron-substituted and unsubstituted graphite is presented in Figure 5-19a, where the region below $V=0$ is not accessible to intercalation.

However, Figure 5-19a does not represent the voltage that we observe from our boron-substituted carbons. Our samples are all completely turbostratically disordered, like petroleum coke. This causes a distribution of binding energies³⁷ which give rise to a sloped voltage curve, like that shown in Figure 5-19b. When boron is substituted into this disordered structure the resulting voltage curve is shifted up, again leading to more capacity. This simple model does not explain the presence of the plateaus at ~ 1.6 V, shown in Figure 5-16. These may be explained by a slightly more complicated model including the effect of the boron on the unoccupied density of electron states in the host available to accept electrons from the intercalated lithium.¹⁵ A lattice gas model attempting to explain this behaviour will be explored in Chapter 6.

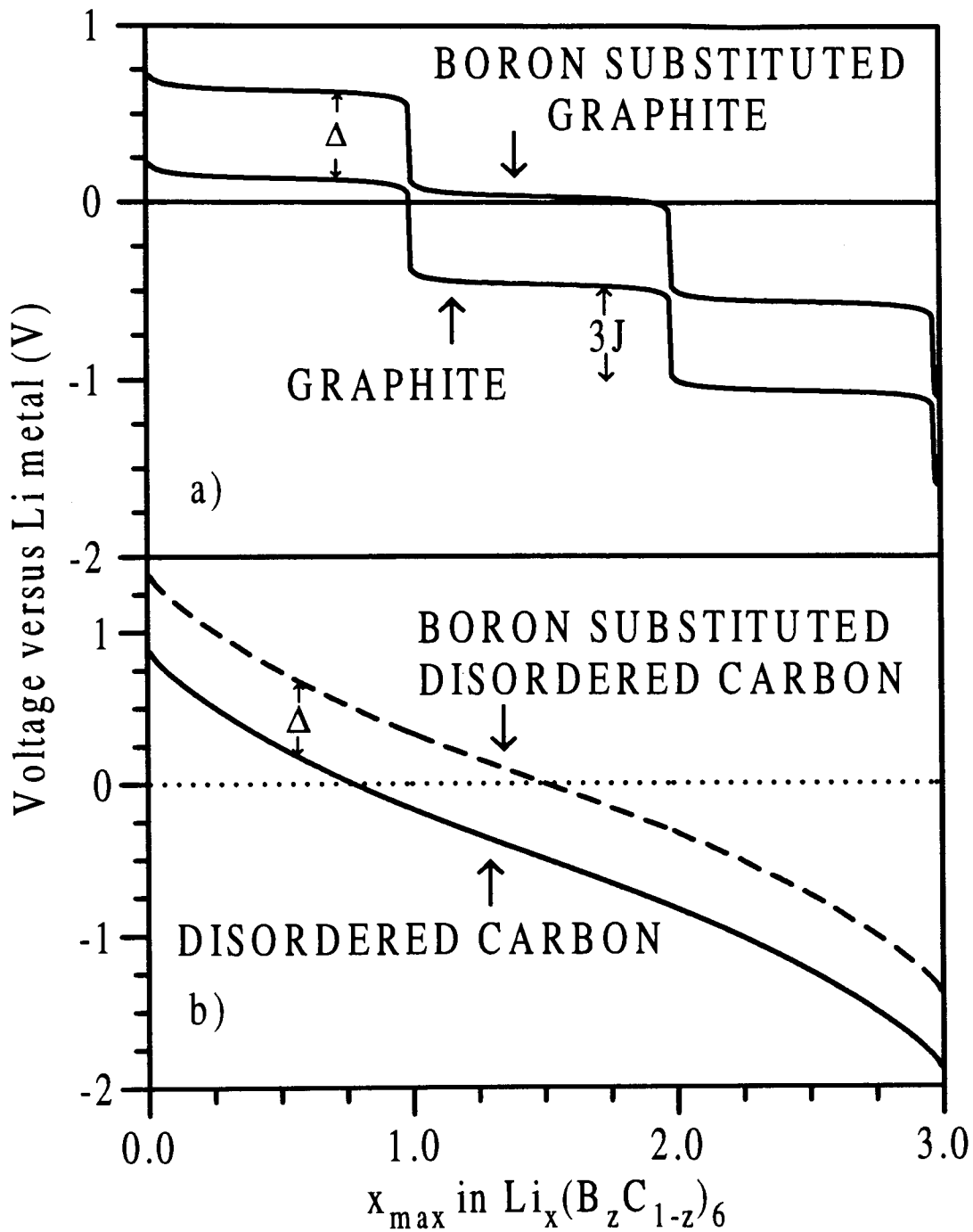


Figure 5-19 Qualitative sketch of the voltage curves of (a) graphite, and (b) disordered carbon, both unsubstituted and boron-substituted; $3J$ is the nearest neighbor repulsion between lithium ions on the lattice, separated by 2.45\AA ; Δ is the increase in binding energy caused by the addition of boron. The region below $V=0$ is not accessible for intercalation.

5.5 *In-situ* Diffraction

It is very useful to be able to study the structure of an intercalation host as a function of the concentration of intercalated lithium. Although the positions of the lithium ions may not be located, due to their low X-ray scattering power, the changes to the host structure, which may include simple expansion (or contraction) or phase transitions to new crystal structures, can be determined. The historical method of performing such experiments is to prepare a series of samples with varying lithium concentration, and measure each sample individually. There are a number of problems associated with such a process, including: (1) time consuming sample preparation, (2) chemical instability of the samples in air, and (3) the difficulty in aligning all samples identically in the diffractometer.

An alternate, and more convenient, method is *in-situ* X-ray diffraction. In this method an electrochemical cell is prepared in a specially designed *in-situ* cell, that has a beryllium window to allow penetration of the X-rays. In the experiment the cell is charged and discharged, allowing continuous variation in the lithium concentration, while repeated X-ray diffraction scans are made. This process has none of the disadvantages of the multiple sample method, since only one sample is required, the cell is not removed from the diffractometer during the course of the experiment, and the cell is sealed, preventing air contact. Because the cell is being continuously cycled, the length of time required for each diffractometer scan must be small compared to the cycling time, or the structure will change significantly during the course of one scan. In addition, the cell must be cycled slowly enough that the intercalation system is close to equilibrium. If this condition is not met, large lithium concentration gradients will exist, smearing out the diffraction peaks. An alternate method that avoids these kinetics problems uses a potentiostat to step the voltage. The cell is then allowed to come to equilibrium at each voltage before an X-ray diffraction measurement is made. The disadvantage of this method is that the cell is normally removed from the diffractometer between scans, and great care must be taken to ensure accurate alignment each time a scan is made. This method is employed here.

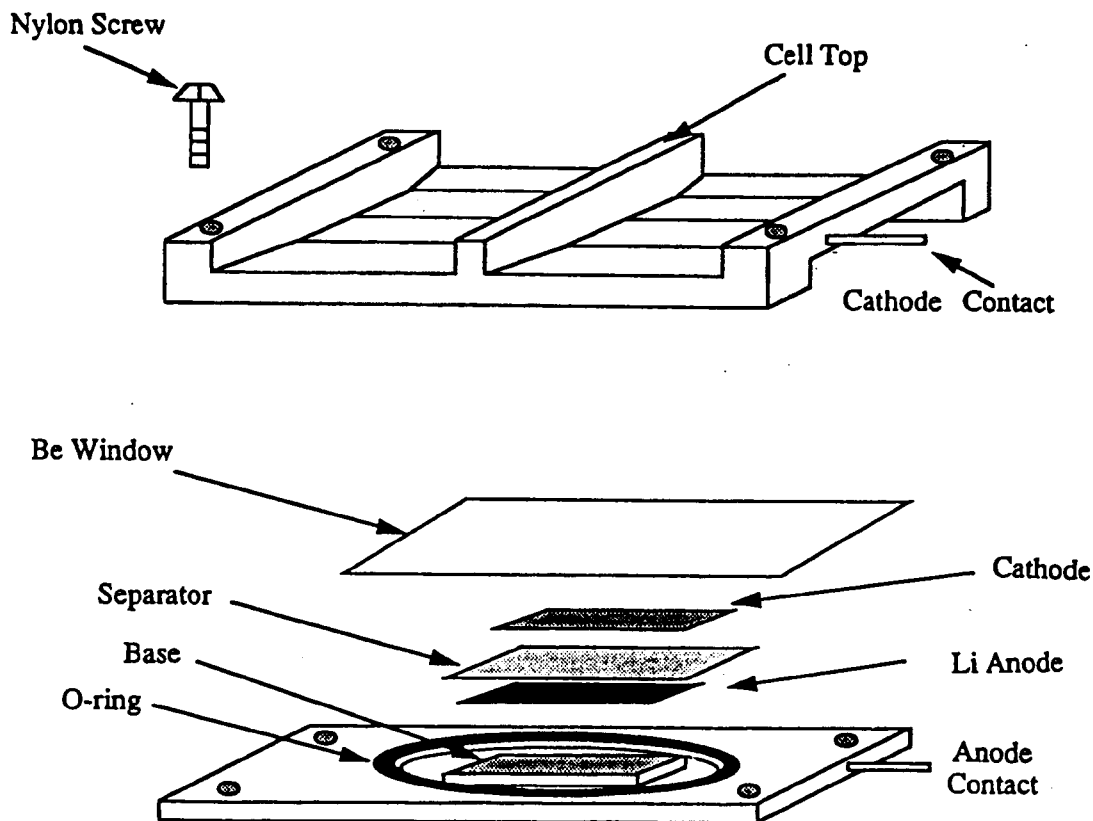


Figure 5-20 Exploded view of X-ray diffraction in-situ cell.

A schematic of the cell design used in these experiments is shown in Figure 5-20. It is functionally identical to the coin cell shown in Figure 5-7, except for the addition of the Be window. The cathode was prepared by making a slurry from the powder, Super S, PVDF, and NMP, as described previously, and spreading the slurry directly onto the Be window. The Be/electrode was then heated to 110°C for several hours to allow evaporation of the NMP. The electrode area was then trimmed to the appropriate size with a scalpel. The cell was assembled in an argon filled glove-box, after pressure wetting the electrode and separator with 1M $\text{LiN}(\text{CF}_3\text{SO}_2)_2$ dissolved in 50/50 (v/v) propylene carbonate and ethylene carbonate (PC/EC). The base is made of stainless steel and the cell top frame is either aluminum or brass. The bar across the cell top is to provide structural stiffness, and does not appear in the diffraction pattern because it is out of the diffractometer focus. The base plate extends out beyond the cell top and is covered with a plastic film so that when it is clamped

into the diffractometer the cell is electrically isolated and will not short circuit.

The potentiostat used was a Keithley 236 Current/Voltage Source Unit, operating in its potentiostat mode. Voltage steps varied, depending on the area of the voltage curve being studied, but were typically 0.1V. The current was allowed to drop below 20 μ A before the cell was removed and diffraction measurement taken. The voltage was measured after the scan as well, and was typically 0.01 V to 0.02 V away from the set voltage. This post-scan voltage was taken as the equilibrium cell voltage for that scan in subsequent calculations. The diffractometer used was the same Philips diffractometer described in Chapter 4. The incident slit was 0.5° , while the receiving slit was 0.2mm, providing a resolution of $\sim 0.02 \text{ \AA}$ at $2\theta=25^\circ$, which is more than adequate for the broad peaks in these samples. Only the (002) Bragg peak was measured, with scans from 20° - 30° , with 0.05° steps, and 6 second count times, for a total scan time of 20 minutes.

To determine the lithium concentration from the equilibrium voltage of the cell, a coin cell with an electrode of the same material was cycled at constant current on the charger system. Because the coin cell is not at equilibrium when cycled at constant current, the following process was employed to determine the equilibrium voltage. The $V(t)$ data was converted to $V(x)$ for both charge and discharge, seen in Figure 5-21. The two curves, charge and discharge, were then fit with a 7th degree polynomial, to get an analytic expression for $V(x)$. The charge and discharge were then averaged for the same value of x , and fit to get an analytic function for $x(V_{\text{average}})$. This average voltage is very close to the equilibrium voltage measured potentiostatically.

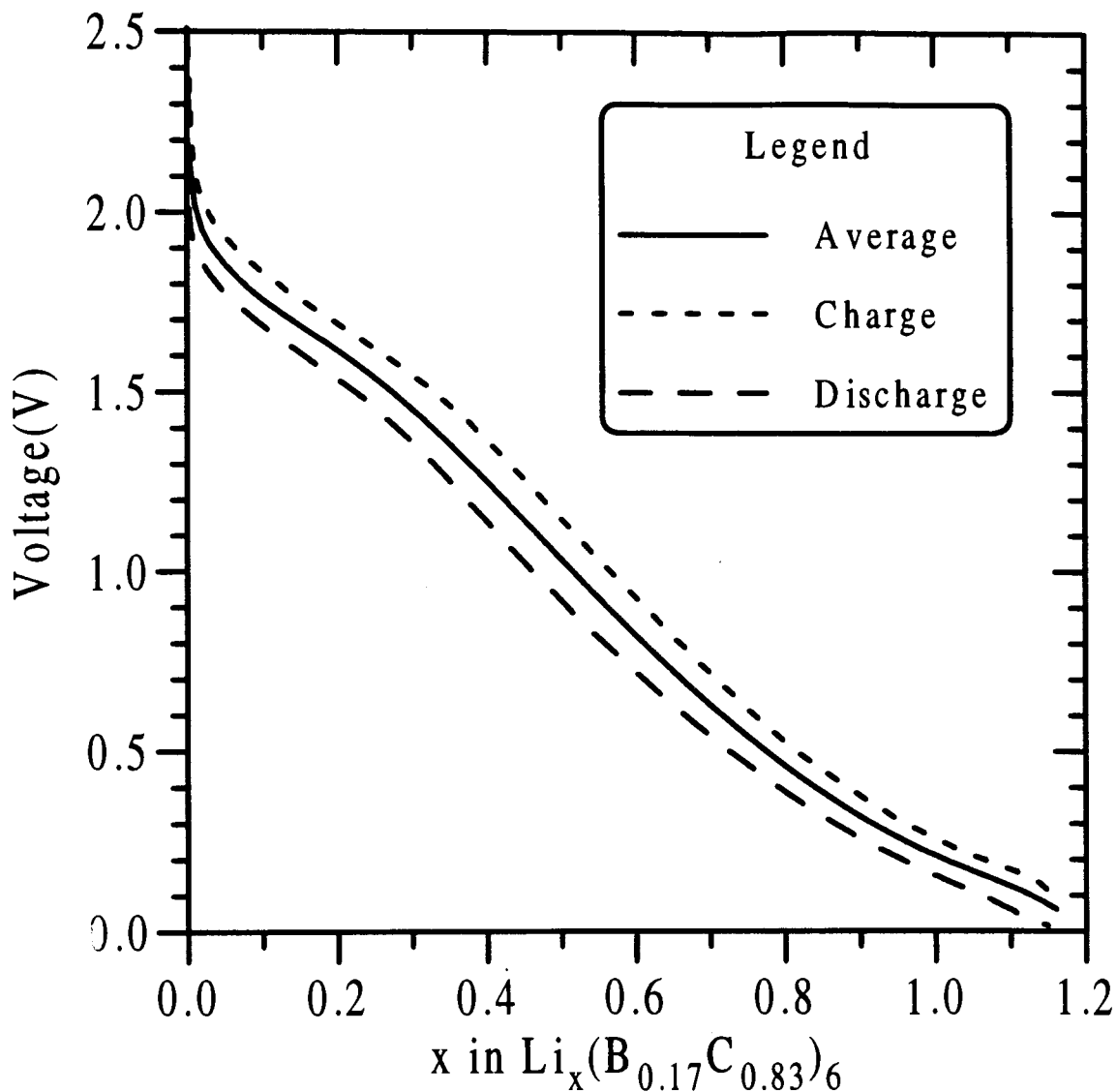


Figure 5-21 Determination of the equilibrium voltage for a $\text{Li}/\text{Li}_x(\text{B}_{0.17}\text{C}_{0.83})_6$ cell

For each measured voltage, a value of x was determined from $x(V_{\text{average}})$, and d_{002} of the diffraction peak was plotted versus x . The results for $\text{B}_{0.17}\text{C}_{0.83}$ are presented in Figure 5-22, along with data for graphite for reference. On discharge (intercalation) the layers expand, and on charge (de-intercalation) they contract, as is usual in layered structures. This behaviour is convincing evidence that intercalation is occurring, and not some reversible chemical reaction. There are two interesting features to note: (1) the hysteresis in the layer spacing, and (2) the large increase in layer spacing with intercalation compared to graphite.

The apparent hysteresis in the layer spacing is probably due to the fact that the cell is not completely equilibrated when the measurement is made, and the estimated equilibrium spacing is shown in the figure by the solid line. The large increase in layer spacing compared to graphite is harder to explain. Figure 5-23 shows the d_{002} spacing versus x for a $\text{Li}/\text{Li}_x(\text{B}_{0.08}\text{C}_{0.92})_6$ *in-situ* cell. The initial layer spacing is larger, and the final spacing smaller, for this cell than for the $z=0.17$ cell.

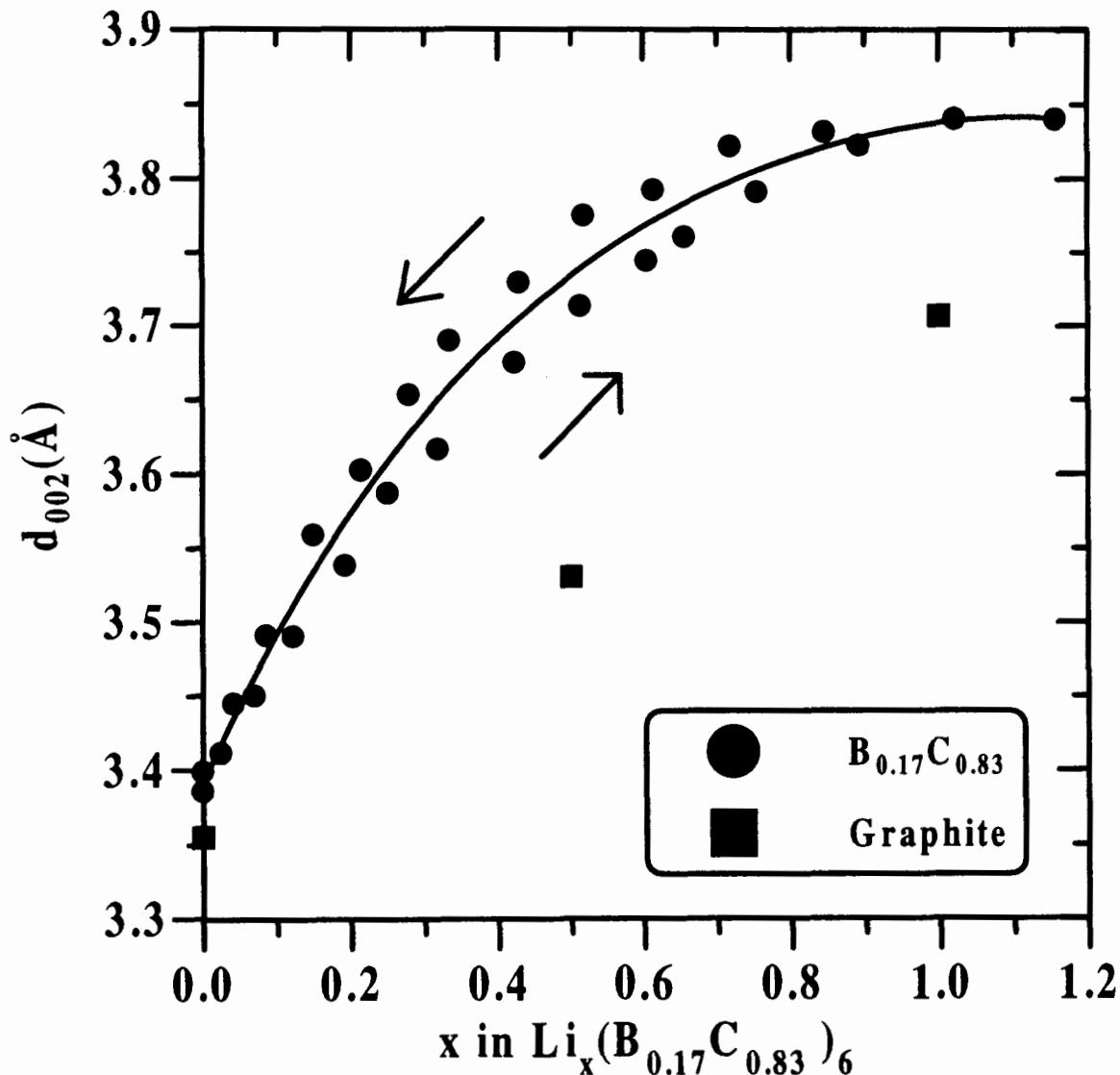


Figure 5-22 Average layer spacing versus lithium concentration in $\text{Li}_x(\text{B}_{0.17}\text{C}_{0.83})_6$. The solid line is a guide to the eye.

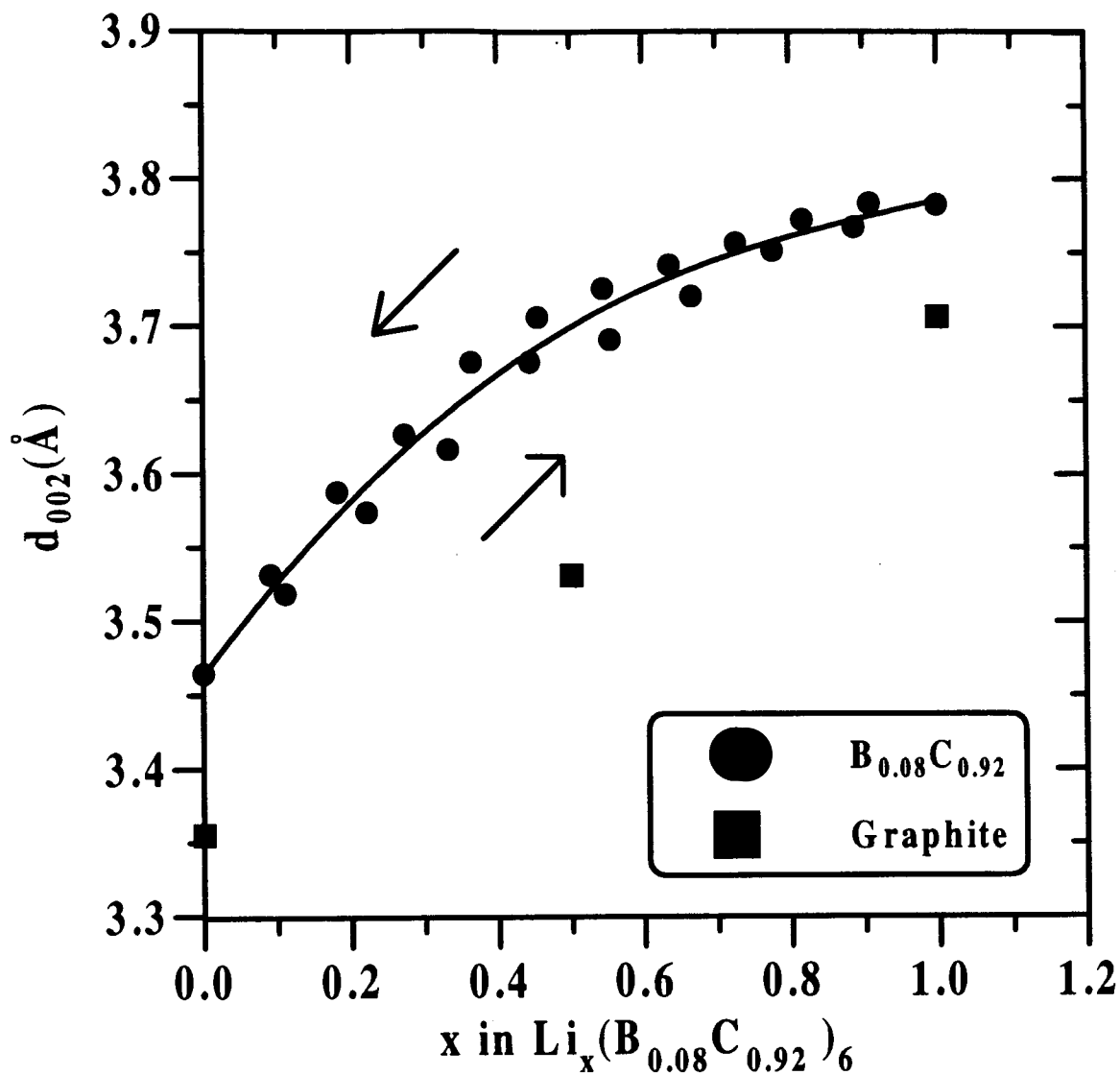


Figure 5-23 Average layer spacing versus lithium concentration in $\text{Li}_x(\text{B}_{0.08}\text{C}_{0.92})_6$. The solid line is a guide to the eye.

The total expansion in d_{002} for the $\text{B}_{0.17}\text{C}_{0.83}$ cell was 0.46 Å, compared to 0.35 Å for graphite,³² 0.32 Å for $\text{B}_{0.08}\text{C}_{0.92}$, and 0.22 Å for petroleum coke.³⁷ The fractional expansion, $\Delta d_{002}/\Delta x$, between $x=0$ and $x=0.5$ for graphite, petroleum coke, $\text{B}_{0.08}\text{C}_{0.92}$ and $\text{B}_{0.17}\text{C}_{0.83}$ are 0.35 Å, 0.44 Å, 0.48 Å and 0.75 Å, respectively. Part of the additional expansion in the B_zC_{1-z} samples is due to the fact that the layers are “pinned” in their turbostratically disordered positions, and can not switch to AAA stacking, as graphite does, when

intercalated. This does not allow the lithium to “nest” in the centers of carbon honeycombs above and below, and forces the layers further apart, as illustrated in Figure 5-24. This behavior is seen in the larger fractional expansion of petroleum coke than graphite.

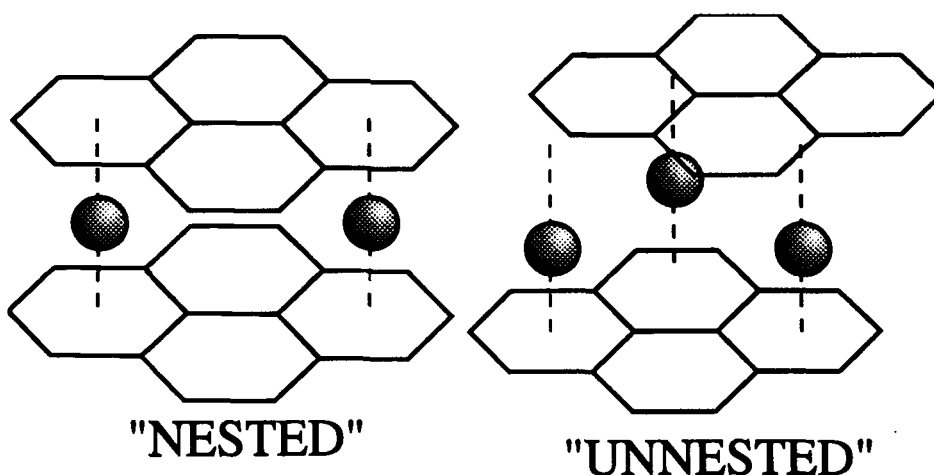


Figure 5-24 Drawing of nested and unnested coordination of lithium ions

An additional cause of the large expansion could be the formation of a quasi-double layer of lithium between the layers. If the additional lithium, beyond $x=1$, is incorporated into sites with 2.45 Å Li-Li nearest neighbor separation (when the Li ions are in the same plane), as suggested in Figure 5-18, then the repulsions may be decreased by increasing the distance between Li ions. This can be achieved by “puckering” the layers of intercalated lithium, causing an increase in the average layer spacing, as seen in Figure 5-25. Whether this occurs or not may be able to be determined by neutron diffraction, but the small sample sizes available and the disorder of the structure would make this experiment difficult.

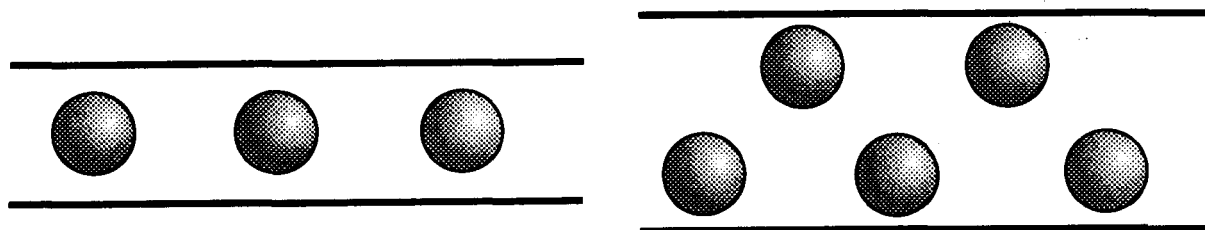


Figure 5-25 Puckering of intercalated lithium layers

5.6 Heat Treated Samples - Results and Discussion

The samples prepared in the heat treatment study described in Chapter 4, were used to make test cells in the same procedure as for the unheated powder samples, using the 1M LiPF₆ in EC/DEC electrolyte. They were cycled at 50 hour rates, and their voltage $V(Q)$, and derivative $-\partial Q/\partial V(V)$ curves calculated. The amount of charge, Q , was used rather than the lithium concentration, x , because the exact composition of the samples was unknown after the heat treatment.

The voltage curves of the pure carbon and B_{0.15}C_{0.85} cells are shown in Figure 5-26 and Figure 5-27, respectively, as a function of heat treatment temperature. For the pure carbon, the capacity of the cells decrease with temperature, while the shape of the curve remains basically unchanged. The capacity of the boron-substituted carbon decreases even more drastically, but the profile also changes. The 1.6 V plateau is considerably shorter by 1200°C, and is completely gone by 1500°C.

The differences in the electrochemical behaviour of the samples are best seen in the derivative curves in Figure 5-28. Only the charge side of the curves are shown. The untreated samples, at 900°C, show the same behaviour as the as-deposited samples presented earlier, with the peak at ~1.6 V growing with increasing boron concentration. This peak then diminishes with increasing heat treatment temperature of the electrode materials, until at 1500°C it is entirely gone. The derivative curves of the B_zC_{1-z} samples heated to 1500°C are quite similar to the pure carbon derivative curve seen in the bottom panel of Figure 5-28. The only major difference is the appearance of a small peak centered at approximately 0.95 V in the 1500°C pure carbon curve that is not present in the other 1500°C curves.

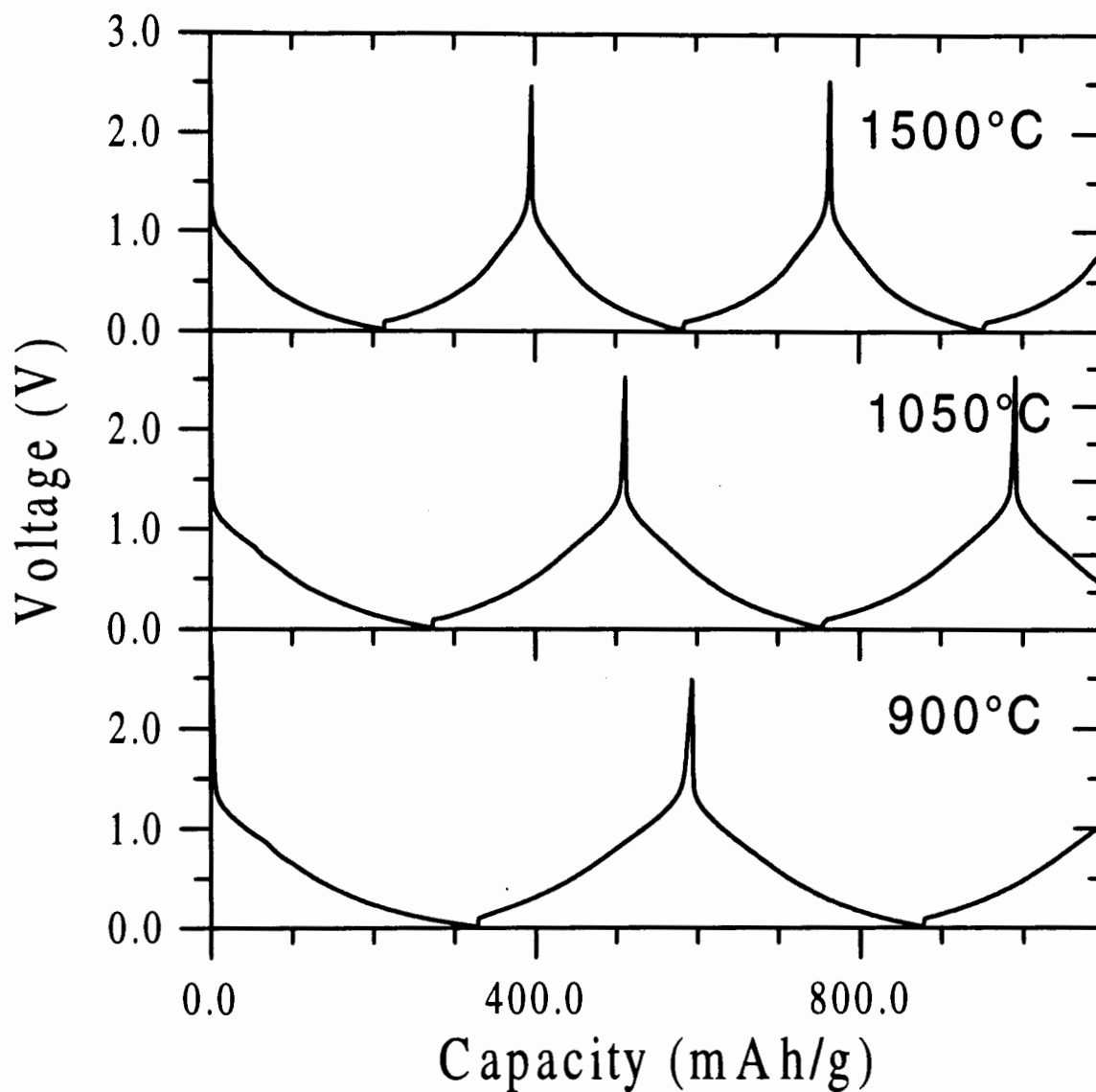


Figure 5-26 Voltage versus capacity for cells made from a pure carbon produced by CVD of benzene at 900°C, heated to a series of temperatures. The capacity scale is continuous, and actual cycle capacity is the difference between the capacities at the beginning and end of the cycle.

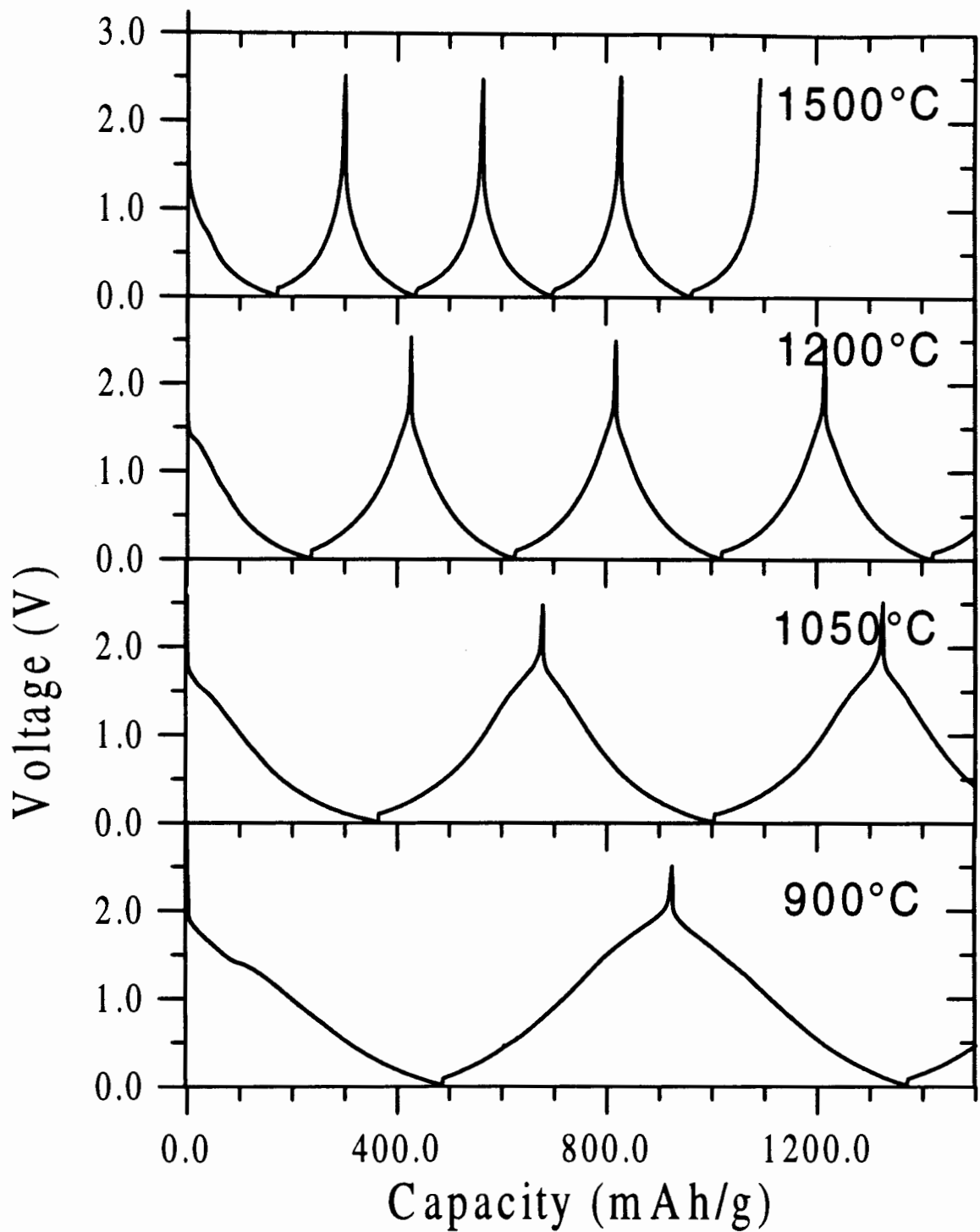


Figure 5-27 Voltage versus capacity for cells made from $B_{0.15}C_{0.85}$, heated to a series of temperatures. The capacity scale is continuous, and actual cycle capacity is the difference between the capacities at the beginning and end of the cycle.

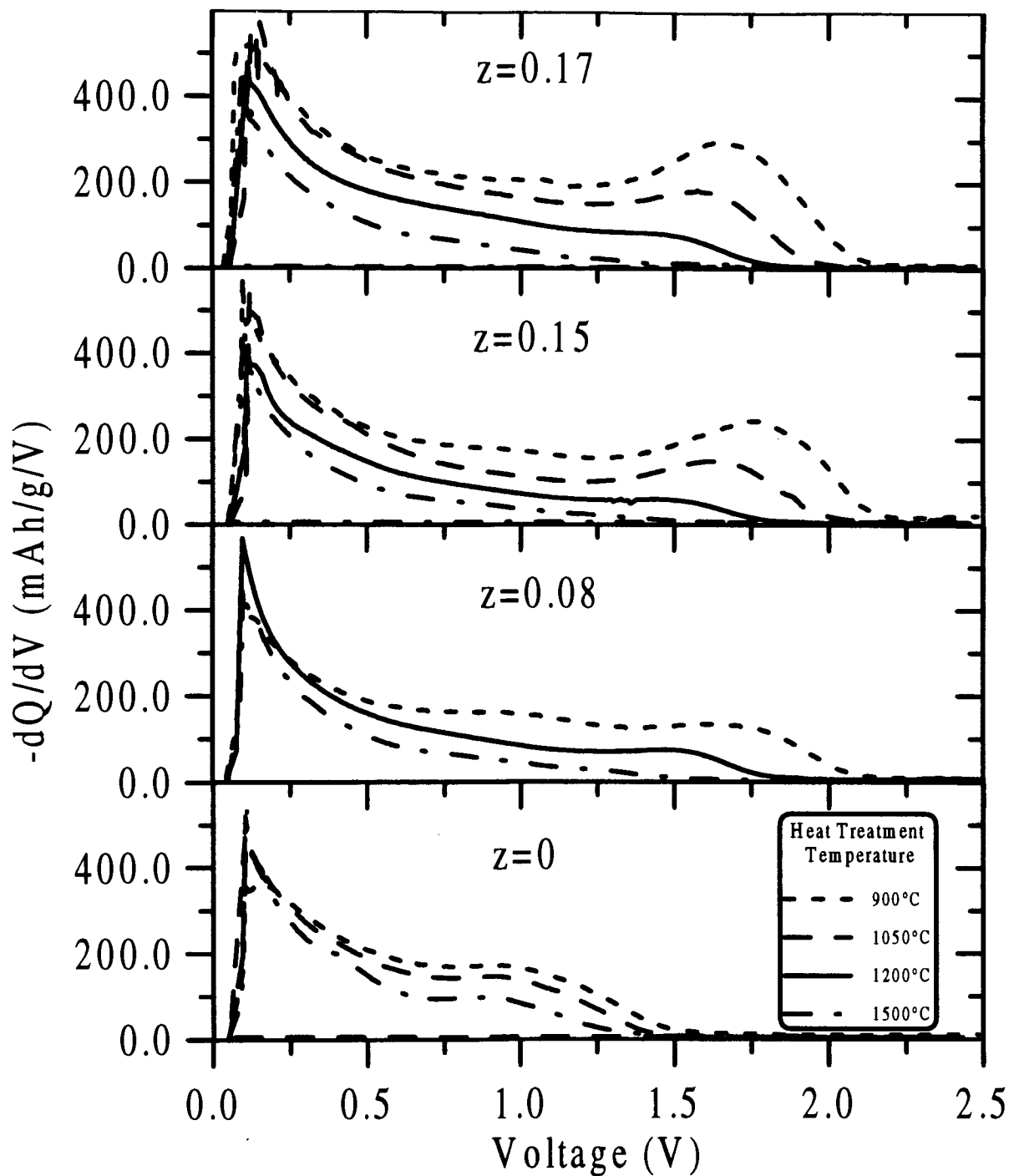


Figure 5-28 Derivative curves for charge only of Li test cells made from heat treated B_2C_{1-z} samples.

The discharge capacity of the 2nd cycle, which is approximately equal to the reversible capacity, is plotted versus heat treatment temperature for the four samples. The general behaviour is for the capacity to decrease with temperature, as seen also by the area under the derivative curves of Figure 5-28. The samples with highest boron concentration decrease most quickly, while those with little or no boron decrease more slowly. The final capacity, at 1500°C, is highest for the pure carbon sample, and lowest for the highest boron concentration sample.

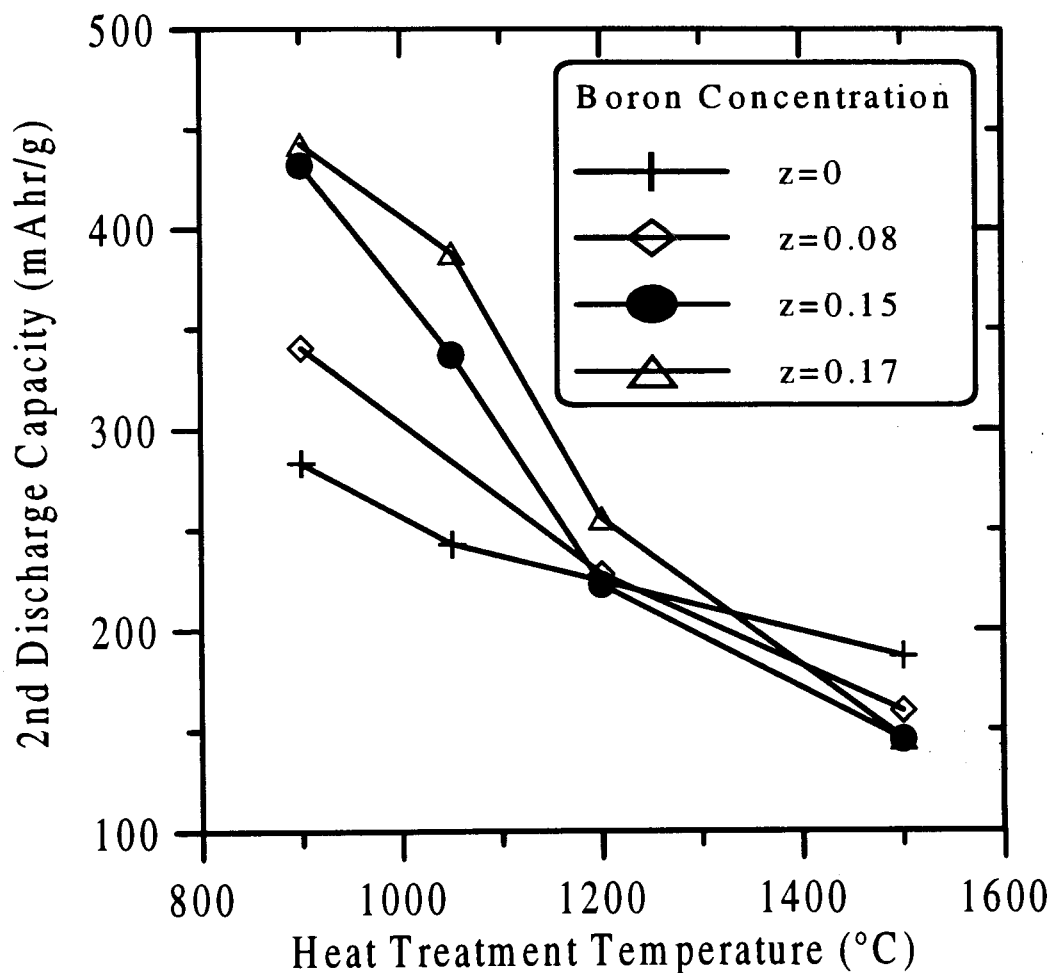


Figure 5-29 2nd discharge capacity versus heat treatment temperature for Li test cells made from heat treated B_zC_{1-z} samples.

This behaviour can be quite easily understood. From the X-ray diffraction results we know that the B_zC_{1-z} is phase separating into B_4C and B_zC_{1-z} , with decreasing z' as the heat treatment temperature is increased. From the derivative curves in Figure 5-28 we can see that this process is essentially complete by 1500°C , leaving only a two phase mixture of B_4C and C. The derivatives of the boron containing samples at 1500°C appear similar to pure carbons at $\sim 2000^\circ\text{C}$, due to the catalytic effect of the boron on graphitization. Figure 5-30 shows the derivative curves of the B_zC_{1-z} samples heated to 1500°C in the region of the 0.95 V peak, compared to Conoco petroleum pitch heated to 2200°C . Note the absence of the peak in the Conoco and B_zC_{1-z} samples for $z > 0$. Since pure carbons reach a minimum in capacity at $\sim 2000^\circ\text{C}$, the total area under the derivative curve is less than the pure carbon at 1500°C .

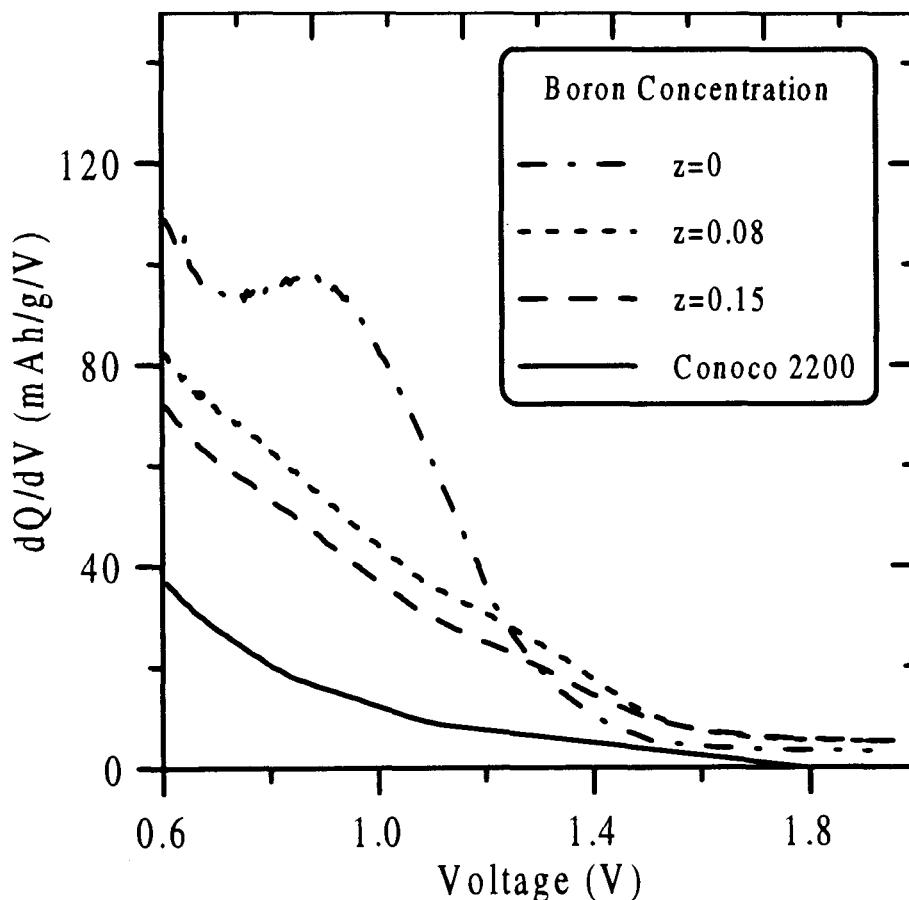


Figure 5-30 Derivative curves for the charge only in the region of the 0.95 V peak for B_zC_{1-z} samples heated to 1500°C and Conoco petroleum pitch heated to 2200°C .

The trends in the capacity arise from the same process. As the boron-substituted carbon phase separates into B_4C and C, the additional capacity due to the effect of the boron is lost, as is the capacity due to the carbon which becomes part of the B_4C , which is unable to intercalate lithium. The higher boron concentration samples, have more boron to lose, and more B_4C to produce, causing a faster decline in capacity. In addition, the higher boron concentration samples graphitize faster with temperature, further decreasing the capacity. Both of these factors lead to final capacities which are lowest for the highest initial boron concentration.

The net result is that heat treatment is not a viable method to increase the capacity or flatten the voltage curve of B_2C_{1-z} , since phase separation occurs before either of these effects can be seen. It may not be possible to check whether a voltage curve such as in the sketch in Figure 5-19a is possible, since an ordered boron-substituted graphite has not yet been produced.

5.7 Conclusions

We have observed three effects of substitutional boron on the electrochemical intercalation of lithium in carbon: (1) the appearance of a high voltage plateau, centered near 1.6 V versus lithium metal, (2) an increase in reversible capacity that grows larger with increasing boron concentration, and (3) an increase in the 002 layer spacing expansion with intercalation, compared to graphite. We have proposed a conceptual model to account for this behavior, but need a better model to qualitatively understand the effects of boron. This will be covered in Chapter 6.

We have also shown that heat treatment to 1500°C is sufficient to allow the boron to fully phase separate into B_4C and C, as evidenced by the complete lack of the high voltage plateau in samples heated to this temperature. The carbons containing boron also showed increased graphitization at 1500°C compared to pure carbon. Further study of heat-treated B_2C_{1-z} is probably not warranted for use as an intercalation host.

Chapter Six

6. Lattice Gas Model of Intercalation

6.1 Introduction

As seen in earlier chapters, the voltage curve, $V(x)$, can vary a great deal, depending on the composition and structure of the host. Modeling this behaviour can provide useful information about the intercalation process in some cases. Even for simple, highly crystalline materials, exact calculation of the chemical potential as a function of lithium concentration by *ab initio* methods is extremely difficult, and has been achieved only recently. It requires total energy calculations for a series of clusters, of varying lithium concentration, for each phase that the intercalated host may go through. To my knowledge this has only been performed for one system: Li-Al alloying.⁶⁹ For disordered systems, such as the one under study here, this method is not possible. In the absence of an exact method, phenomenological methods are used. Historically voltage curves have been calculated using a lattice gas model of lithium atoms on sites in the host lattice.

6.1.1 Thermodynamics of Intercalation

In Chapter 5 we determined that the equilibrium voltage of an electrochemical cell with lithium as the anode is given by:

$$V(x) = -\frac{[\mu_{cathode}(x) - \mu_{anode}]}{e} \quad \text{Equation 6-1}$$

where:

$$\mu = \left[\frac{\partial G}{\partial n} \right]_{P,T} \quad \text{Equation 6-2}$$

and:

$$G = G(n, P, T) = U - TS + P\nu \quad \text{Equation 6-3}$$

where n is the number of atoms of lithium transferred, U is the internal energy, T is the temperature, S is the entropy, P is the pressure and ν is the volume. In an electrochemical cell the volume is constant and the changes in pressure are generally small, and thus the requirement for our model is to provide approximations of the internal energy and entropy.

6.1.2 Lattice Gas Model Applied to Lithium Intercalation

To determine $\mu(x)$ and therefore $V(x)$, we need to choose a model. Lattice gas models have been used many times in the past to study intercalation systems.^{70,71,72} In this model we assume that the intercalated lithium atoms may only occupy specific sites in the lattice of the host compound, and that only one atom at a time may occupy a given site at a given time. The intercalating lithium atoms must move from site to site, but this motion is assumed not to affect the thermodynamics of the system.⁷³ A model for this behavior called activated hopping assumes that the lithium atoms reside in potential wells much deeper than kT , and hop quickly from site to site. The application of a lattice gas model to intercalation in carbons will be discussed in the following section.

6.2 Lattice Gas Model for Lithium Intercalation in Carbon

6.2.1 Mean Field Solution for Graphite

Applying the lattice gas model to graphite is relatively straightforward. We will confine the interactions to a site energy term that corresponds to the binding energy of the lithium atom to the graphite host, and in-plane interactions between screened lithium atoms. Interactions between screened lithium ions in different layers are smaller, but are necessary to reproduce staging phenomena.⁷⁰ Because we are not interested in staging, which does not occur in $\text{Li}_x(\text{B}_2\text{C}_{1-z})_6$ due to structural disorder, a 2-dimensional, in-plane, model will suffice. The 2-D lattice of sites for graphite, corresponding to the centers of the carbon honeycombs, is a triangular lattice.

In graphite, because of its structural order, intercalated lithium atoms occupy sites with the same nearest neighbor carbon environment. We therefore expect that the site energy, E , will be independent of site. The interaction between lithium ions on adjacent sites, J , is taken to be repulsive. The internal energy, including only nearest neighbour interactions, can be defined as:

$$U = \sum_{i=1}^{3N} E_0 x^i + \frac{1}{2} \sum_{\langle i,j \rangle} J x^i x^j \quad \text{Equation 6-4}$$

where $3N$ is the number of sites, x^i is the occupation of site i (0 or 1), and $\langle i,j \rangle$ is the sum over nearest neighbours. The system can be divided into three sublattices, commensurate with the expected LiC_6 structure, as shown in Figure 6-1.

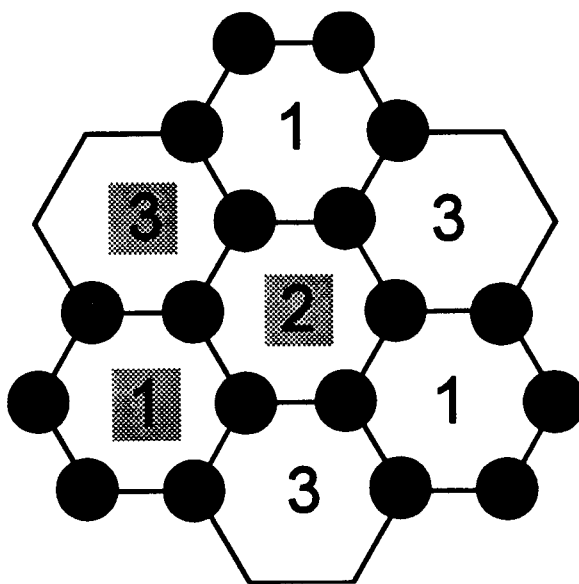


Figure 6-1 The in-plane structure of graphite, showing the three sublattices.

The fractional occupations of the sub-lattices are taken to be x_1 , x_2 and x_3 , and the fractional occupation of the complete lattice, x , is given by the sum of the three sublattice occupations (to be comparable to x in Li_xC_6):

$$x = x_1 + x_2 + x_3 \quad \text{Equation 6-5}$$

The mean field approximation is then applied to each sublattice. In this approximation, within each sublattice, the lithium atoms are assumed to be randomly distributed on the sites, in spite of the interaction. Each site is assumed to interact with the average concentration on the adjacent sublattices. This process of decomposing the lattice of sites into sublattices and applying the mean field approximation to each sublattice is called the Bragg-Williams Approximation.⁷⁴

The internal energy can be defined as:

$$U = N[E_0x + 3J(x_1x_2 + x_2x_3 + x_1x_3)] \quad \text{Equation 6-6}$$

and the entropy can be calculated for each sublattice as the entropy to put $N_i=x_iN$ atoms randomly on N sites:

$$S_i = k \ln \left[\frac{(N)!}{(x_iN)!((1-x_i)N)!} \right] \quad \text{Equation 6-7}$$

The total entropy is the sum of the sublattice entropies, $S=S_1+S_2+S_3$. Combining equations 6-6 and 6-7 and applying Stirling's approximation, the free energy for large N is:

$$G = N \left[E_0x + 3J(x_1x_2 + x_2x_3 + x_1x_3) + kT \sum_{i=1}^3 [x_i \ln x_i + (1-x_i) \ln(1-x_i)] \right] \quad \text{Equation 6-8}$$

The chemical potential of each sublattice, μ_i , can then be calculated as:

$$\mu_i = E_0 + 3J(x_j + x_k) + kT \ln \frac{x_i}{1-x_i} \quad \text{Equation 6-9}$$

where the first term is the site-independent binding energy, the second term is the near-neighbor repulsive interaction with the average occupation of the three sites on each of the two adjacent sublattices, and the third term is due to the configurational entropy of putting xN atoms on N sites (dS/dn_i). Solving for x_i , we get:

$$x_i = \frac{1}{e^{[(E_0 + 3J(x_j + x_k) - \mu)/kT]} + 1} \quad \text{Equation 6-10}$$

Because the three sublattices are in equilibrium, their chemical potentials are equal, and this equation holds for all sublattices. Thus to solve for the concentration as a function of voltage: (1) appropriate choices must be made for E_0 and J , (2) the desired chemical potential and temperature must be given, and (3) initial guesses of the sublattice concentrations x_2 and x_3 must be made. Given these values, x_1 can be calculated, then used to calculate x_2 , and then x_3 . This process can be repeated iteratively until self-consistent values of the sublattice concentrations are obtained. A new chemical potential is then chosen and the process repeated until we obtain the complete $x(\mu)$. This data can be plotted as $V(x)$, giving a calculated voltage curve.

The solid line in Figure 6-2 shows the voltage curve as a function of x , calculated by the procedure described above. The values used in this calculation were $E_0 = -0.1$ eV, $J = -0.25$ eV, and $T = 300$ K. The $0 \leq x \leq 1$ region looks much like the experimental $V(x)$ for lithium intercalating in graphite, except for the notable absence of staging. The region of the curve where $V < 0$ is not accessible to intercalation, and is thus not verifiable by experiment. The voltage drops at $x=1$ and $x=2$ are equal to $3J$, as discussed in Chapter 5, and the average voltage of the first plateau is set by the site energy, E_0 . The entropy term, through the temperature, affects the "rolling off" of the curve when sublattice concentrations are near 0 or 1.

The dashed line shows the number of iterations required to reach self-consistency. When the number of iterations becomes large (at $x \approx 0.1, 1.1, 1.9$, and 2.9), the ordering of the lithium atoms between the sublattices is changing quickly. The peak at $x \approx 0.1$ is due to the transition from a random distribution with $x_1 = x_2 = x_3$, to an ordered one with two sublattices empty, and one filling. At $x=1$ one of the sublattices is full and the other two begin to fill equally. At $x \approx 1.1$ there is a transition to one sublattice full, one empty, and one filling. This continues until $x \approx 1.9$, where one of the sublattices is empty and the other two become equal. At $x=2$, two of the sublattices are full and the third begins to fill. Finally at $x \approx 2.9$, the

occupancy of all sublattices becomes equal until they are all full.

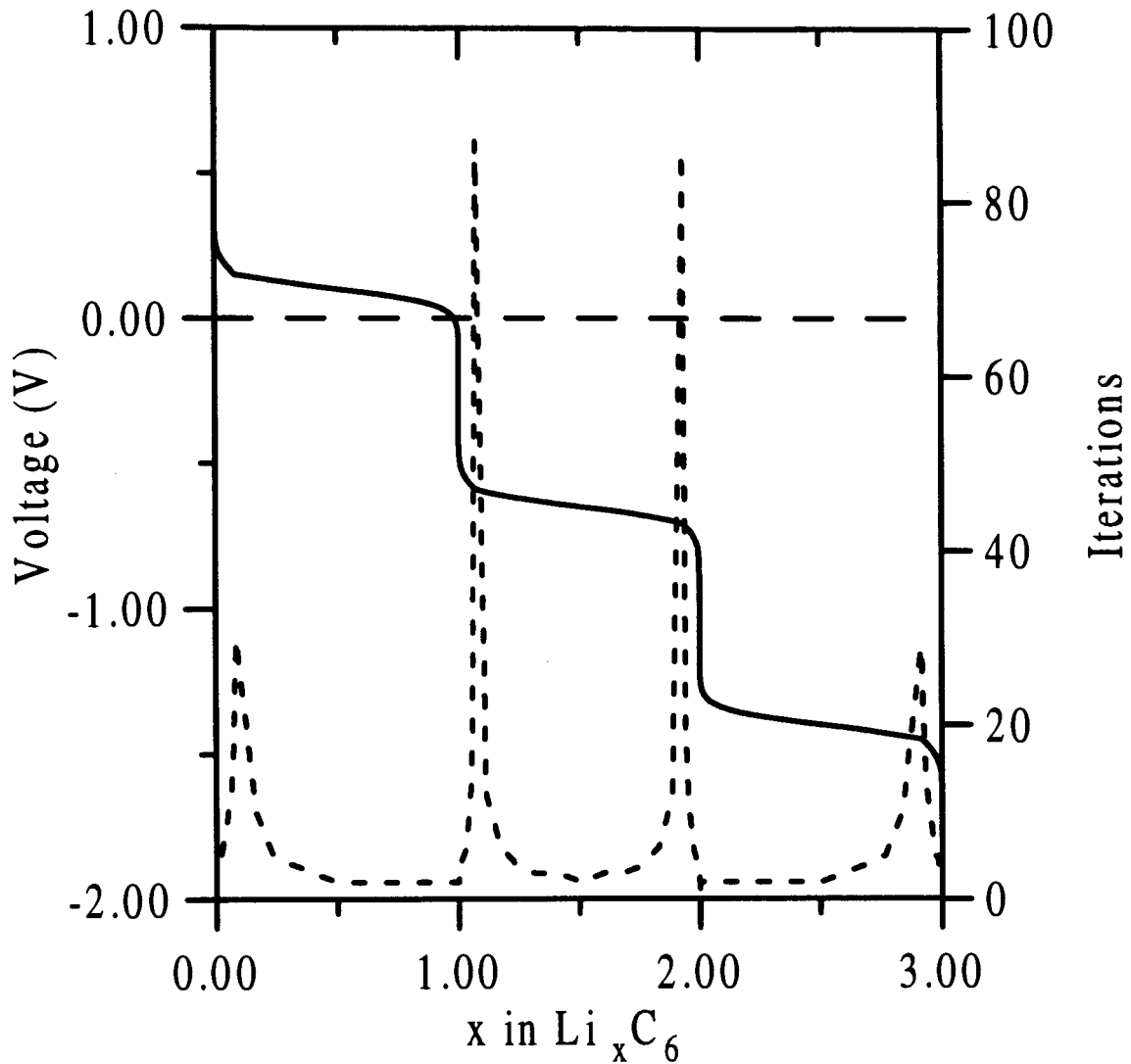


Figure 6-2 Mean field calculation of Li/Graphite voltage curve (solid) and number of iterations required to reach self-consistency (short-dash). The voltage of lithium metal is marked by the long dashes at zero volts.

6.2.2 Mean Field Solution for Disordered Carbon

In a turbostratically disordered carbon, such as petroleum coke, the environment of the lithium atoms, and thus the site energy, E , varies from site to site. A density of sites, $n(E)$, can be defined for each sublattice,⁷⁵ such that:

$$\int_{-\infty}^{+\infty} n(E) dE = 1 \quad \text{Equation 6-11}$$

The average concentration of lithium in sublattice i , x_i , in Li_xC_6 is given by:

$$x_i = \int_{-\infty}^{+\infty} n(E) \tilde{x}_i(E, \mu, T, x) dE \quad \text{Equation 6-12}$$

where \tilde{x}_i is the average occupation of all sites of sublattice i with energy E . Again applying mean field theory, we assume that the repulsive interaction, J , depends only on the average sublattice concentrations of the other sublattices: x_j and x_k . The entropy is then due to randomly arranging $\tilde{x}_i n(E)N$ atoms on $n(E)N$ sites. The chemical potential is then given by:

$$\mu_i = E + 3J(x_j + x_k) + kT \ln \frac{\tilde{x}_i}{1 - \tilde{x}_i} \quad \text{Equation 6-13}$$

This equation can be solved for \tilde{x}_i :

$$\tilde{x}_i = \frac{1}{e^{(E+3J(x_j+x_k)-\mu)/kT} + 1} \quad \text{Equation 6-14}$$

and substituting the result into Equation 6-12. Solving for x_i then gives us:

$$x_i = \int_{-\infty}^{+\infty} \frac{n(E) dE}{e^{(E+3J(x_j+x_k)-\mu)/kT} + 1} \quad \text{Equation 6-15}$$

If we set $n(E) = \delta(E - E_0)$, we reproduce Equation 6-10 for graphite. However, for coke we expect to have a distribution of site energies. Following Greissen,⁷⁵ we can choose a rectangular density of sites such that:

$$n(E) = \frac{1}{2\Delta} \quad \text{for} \quad E_0 - \Delta < E < E_0 + \Delta \quad \text{Equation 6-16}$$

and

$$n(E) = 0$$

otherwise

Equation 6-17

When this density of sites is substituted into Equation 6-15, the result can be integrated to give us an expression for x_i :

$$x_i = 1 + \frac{kT}{2\Delta} \ln \left[\frac{1 + e^{(E_0 + 3J(x_j + x_k) - \mu)/kT} e^{-\Delta/kT}}{1 + e^{(E_0 + 3J(x_j + x_k) - \mu)/kT} e^{+\Delta/kT}} \right]$$

Equation 6-18

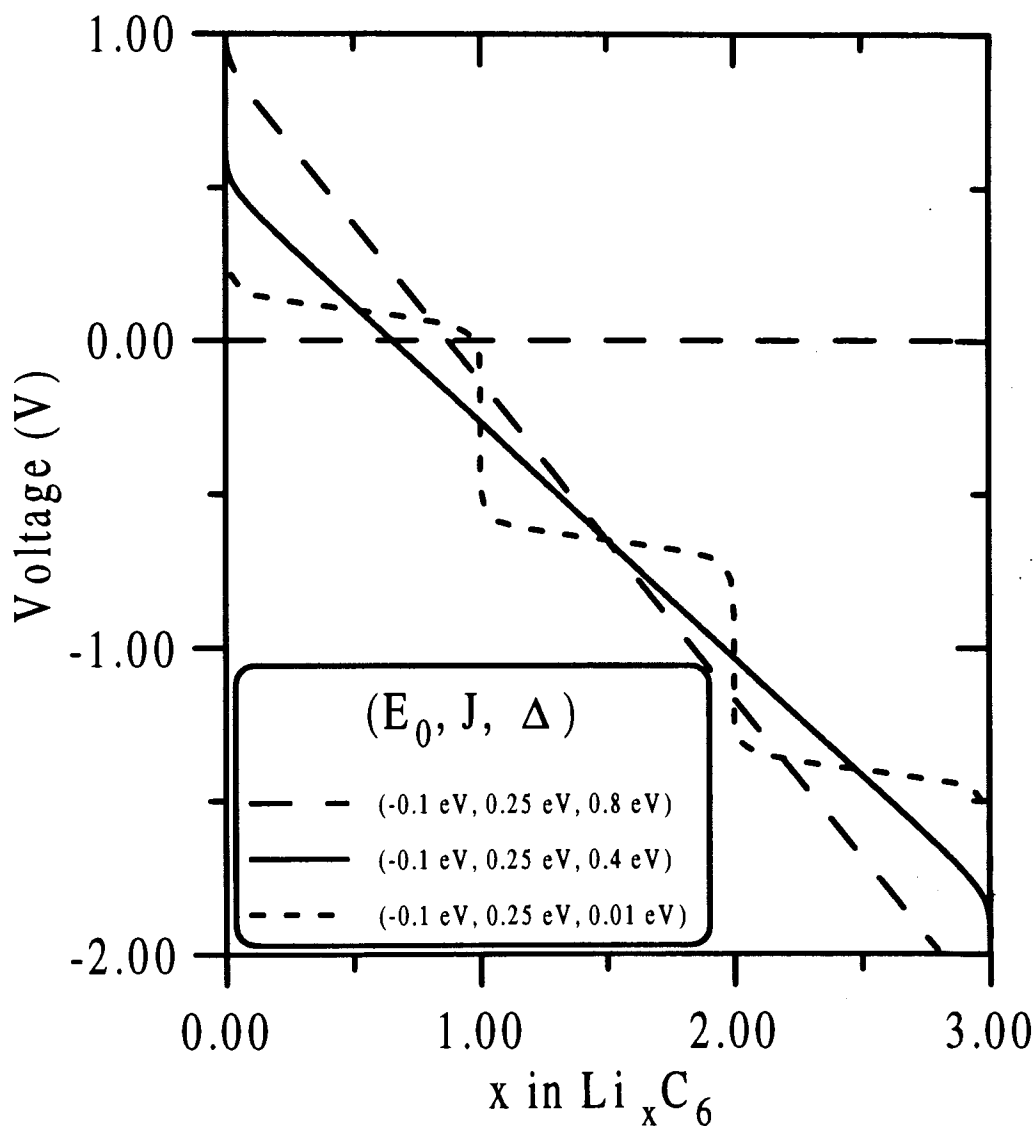


Figure 6-3 Mean field calculation of Li/Coke voltage curve, for $\Delta=0.8$ eV, 0.4 eV, and 0.01 eV.

This expression was used to iteratively solve for $x(\mu)$, as was done for graphite, and results are shown in Figure 6-3 for three values of the half width of the density of sites. Note that the voltage curve becomes increasingly sloped as Δ increases and the profile of $V(x)$ is straight, except for the effects of entropy at x near 0 and 3. The ordering that was evident in graphite is only present in the sample with small Δ . This occurs because for sufficiently large binding energy variation, lithium atoms will occupy sites of lowest energy, rather than ordering on the lattice. The same reasoning also explains the absence of staged phases in turbostratically disordered carbons.³⁷

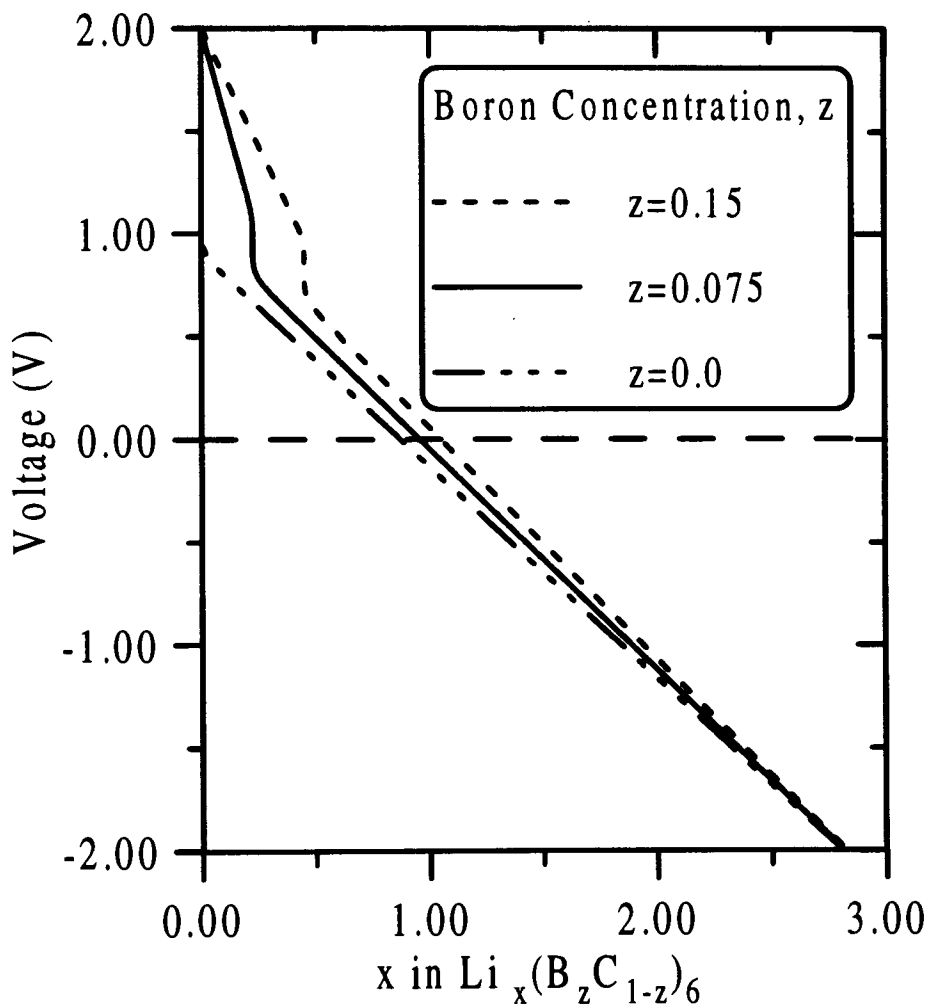


Figure 6-4 Mean field calculation of $\text{Li}/\text{B}_z\text{C}_{1-z}$ voltage curve, for $z=0.15$, 0.075 , and 0.0 , using double rectangular density of sites. Other parameters are described in the text.

6.2.3 Mean Field Solution for B_zC_{1-z}

The method of treating the effect of substituted boron on the intercalation of lithium in carbon is more difficult. Although a simple distribution of site energies can qualitatively reproduce the $V(x)$ behaviour of a Li/Coke intercalation system, the exact cause of the binding energy variation is not well understood. Why, for instance are there so many sites with binding energy greater than for graphite, which one might think has relatively good binding sites? Due to this lack of understanding, it is difficult to be more exact about the effects of boron substitution than the approximation of binding energy variation used for disordered carbons. For this reason we chose a double peaked density of sites: (1) one peak corresponding to those lithium atoms in the vicinity of a boron atom, and (2) one peak the same as for a disordered carbon. The boron peak is shifted to higher binding energy and has an area proportional to the boron concentration, z , while the carbon peak is unshifted and proportional to $1-z$.

6.2.3.1 Double Rectangle Density of Sites

The first choice of $n(E)$ is from Griessen, who used the double rectangular density of sites to model hydrogen absorption in metal alloys,⁷⁵ although he chose symmetric densities, rather than proportional to concentration, as are used here:

$$n_b(E) = \frac{z}{2\Delta_b} \quad \text{for} \quad E_b - \Delta_b < E < E_b + \Delta_b$$

$$n_c(E) = \frac{1-z}{2\Delta_c} \quad \text{for} \quad E_c - \Delta_c < E < E_c + \Delta_c$$

where the b subscript refers to the boron sites and c refers to the carbon sites. A drawing of this density of sites versus energy is shown in Figure 6-5a. E_b and E_c are the average binding energy to the boron and carbon sites respectively. Each of these terms can be substituted into Equation 6-15 and integrated independently to give the following expression for x_i :

$$x_i = z \left(1 + \frac{kT}{2\Delta_b} \ln \frac{1 + e^{(E_b + 3J(x_j + x_k) - \mu)/kT} e^{-\Delta_b/kT}}{1 + e^{(E_b + 3J(x_j + x_k) - \mu)/kT} e^{+\Delta_b/kT}} \right) + (1-z) \left(1 + \frac{kT}{2\Delta_c} \ln \frac{1 + e^{(E_c + 3J(x_j + x_k) - \mu)/kT} e^{-\Delta_c/kT}}{1 + e^{(E_c + 3J(x_j + x_k) - \mu)/kT} e^{+\Delta_c/kT}} \right) \quad \text{Equation 6-19}$$

The iterative calculation of the sublattice concentrations yields the $V(x)$ curves shown in Figure 6-4, for $z=0, 0.075$ and 0.15 . For all three curves: $E_b=-1.6$ eV, $E_c=-0.1$ eV, $\Delta_b=0.4$ eV $\Delta_c=0.8$ eV, $J=0.25$ eV and $T=300$ K. Comparison of Figure 6-4 with experimental data from Chapter 5 shows a qualitative similarity, with the appearance of the lengthening plateau centered at 1.6 V. The drop in voltage between the upper and lower plateaus is much sharper than experimentally observed. To more accurately model the real voltage curve a more complicated expression for the density of sites is required.

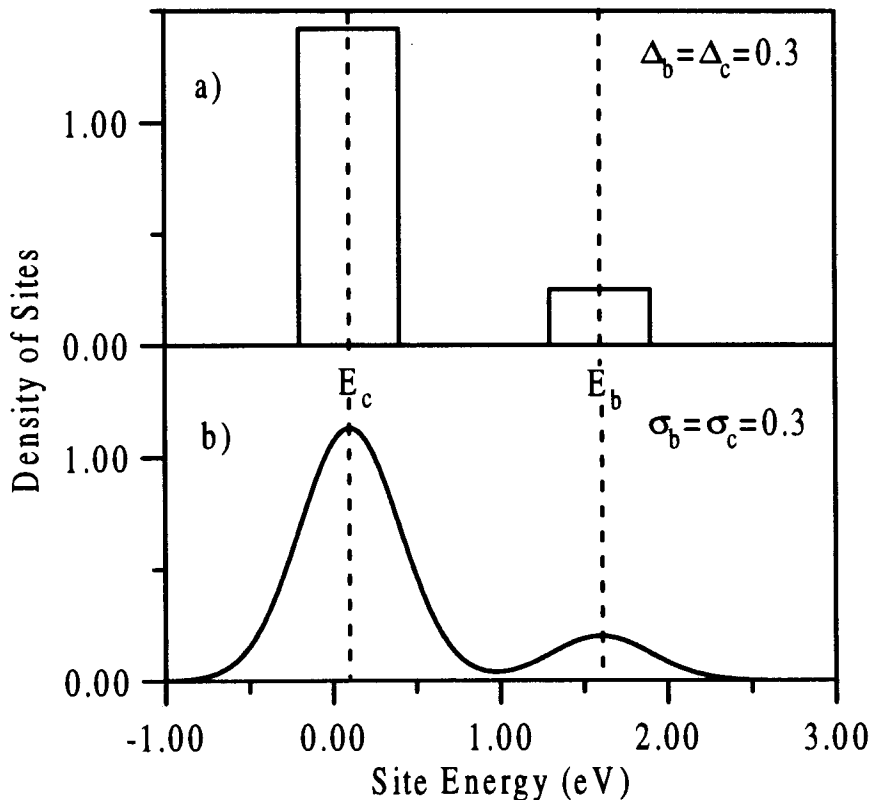


Figure 6-5 (a) Double rectangular and (b) double Gaussian models of the density of sites versus binding energy in B_2C_{1-z}

6.2.3.2 Gaussian Density of Sites

A common choice for the density of sites is a Gaussian distribution. For the boron substituted carbon a double Gaussian is more appropriate. We choose the density of sites as:

$$\begin{aligned} n_b(E) &= \frac{z}{\sqrt{2\pi\sigma_b^2}} \exp\left\{-\frac{(E-E_b)^2}{2\sigma_b^2}\right\} \\ n_c(E) &= \frac{1-z}{\sqrt{2\pi\sigma_c^2}} \exp\left\{-\frac{(E-E_c)^2}{2\sigma_c^2}\right\} \end{aligned} \quad \text{Equation 6-20}$$

where σ_b and σ_c are the standard deviations of the boron and carbon distributions, respectively. This choice of density of sites is pictured in Figure 6-5b. The equation for x_i becomes:

$$x_i = \int_{-\infty}^{+\infty} \frac{\frac{z}{\sqrt{2\pi\sigma_b^2}} \exp\left\{-\frac{(E-E_b)^2}{2\sigma_b^2}\right\} + \frac{1-z}{\sqrt{2\pi\sigma_c^2}} \exp\left\{-\frac{(E-E_c)^2}{2\sigma_c^2}\right\}}{e^{(E+3J(x_j+x_k)-\mu)/kT} + 1} dE \quad \text{Equation 6-21}$$

which has no analytical solution. In this work the integral was estimated in each iteration by the TRAPZD subroutine from Numerical Recipes in Fortran⁷⁶. This subroutine calculates the N'th stage refinement of an extended trapezoidal rule, and is called N times to perform the integral. In this work, ten calls was found to be sufficient to provide a consistent estimate of the integral.

Figure 6-6 shows a comparison of the calculated $V(x)$ for three values of the boron concentration: $z=0$, $z=0.075$ and $z=0.15$. The other parameters are: $T=300$ K, $\sigma_b=\sigma_c=0.3$ eV, $J=0.25$ eV, $E_b=-1.6$ eV and $E_c=-0.1$ eV. The curves look similar to those seen in Figure 6-4 for the double rectangular density of sites, but the drop between the upper and lower voltage plateaus has softened. Increasing the overlap in the Gaussians decreases this drop further.

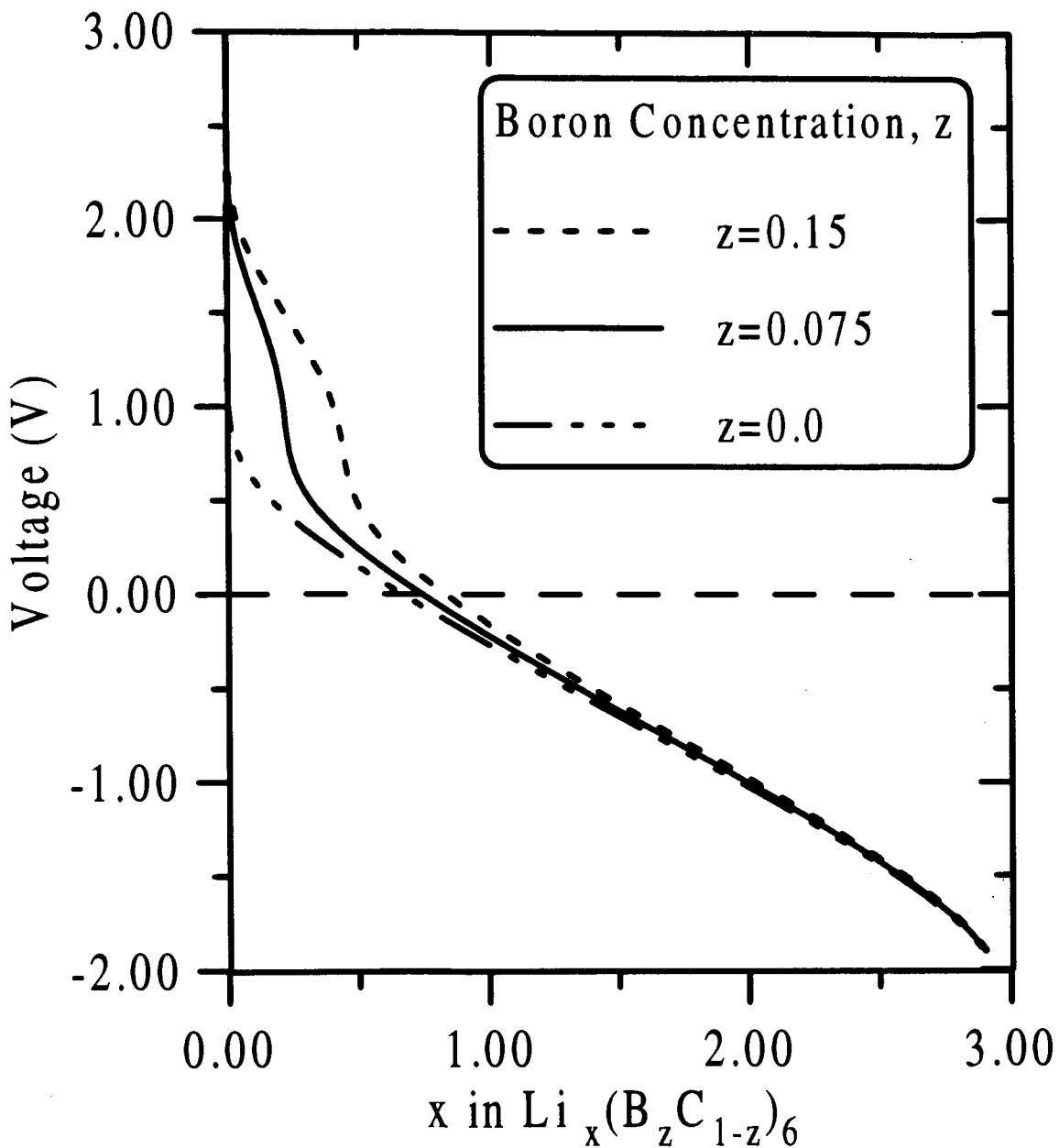


Figure 6-6 Mean field calculation of $\text{Li}/\text{B}_2\text{C}_{1-z}$ voltage curve, for $z=0.15$, 0.075 , and 0.0 , using double Gaussian density of sites. Other parameters are described in the text.

Figure 6-7 shows the effect of changing the distribution widths, σ_b and σ_c , on the calculated voltage curves of samples with $z=0.15$. Note that when σ_c becomes small enough, ordering occurs on the low voltage plateau.

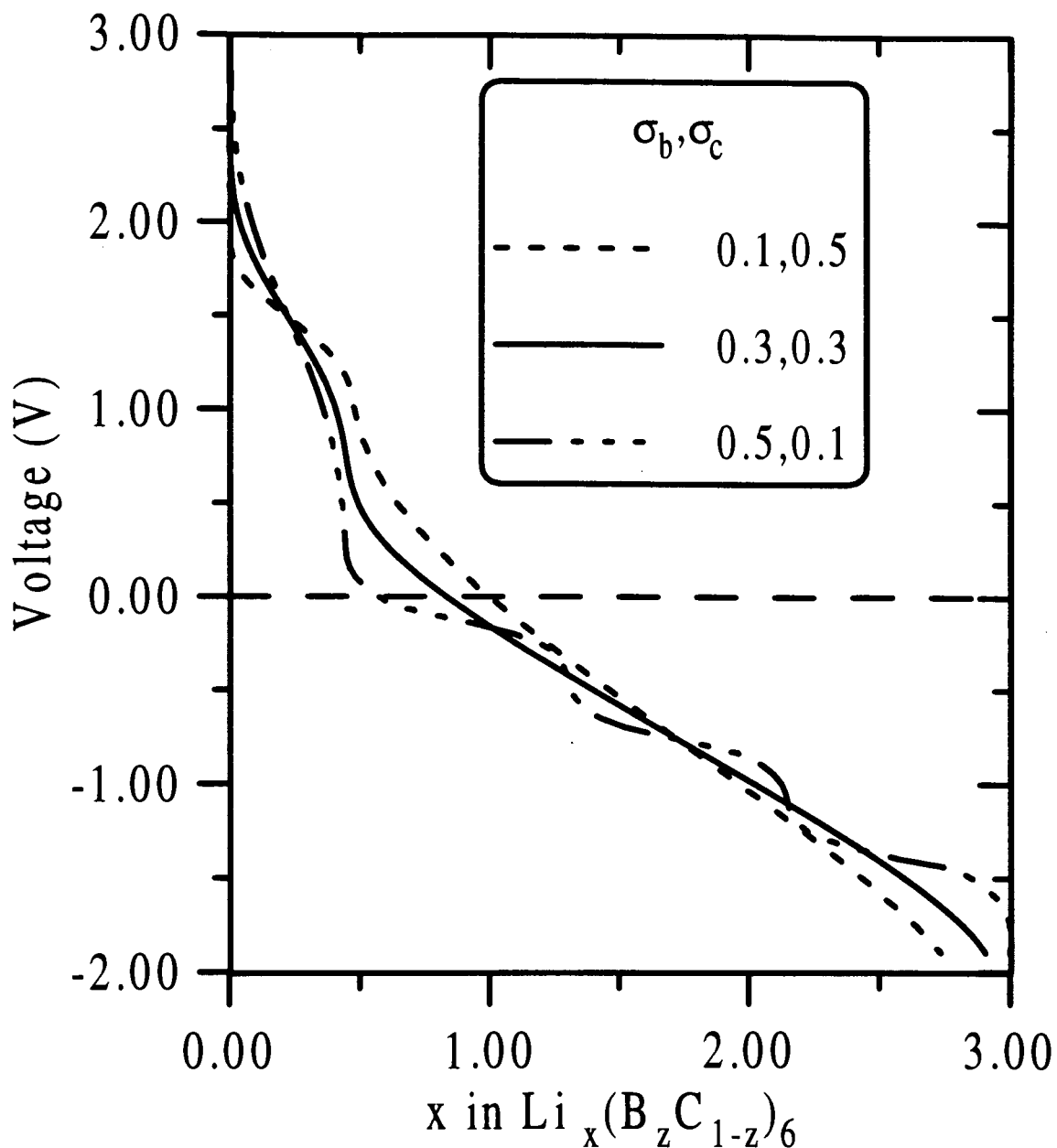


Figure 6-7 Mean field calculation of $\text{Li}/\text{B}_{0.15}\text{C}_{0.85}$ voltage curve using double Gaussian density of sites, and varying the distribution widths, σ_b and σ_c . Other parameters are described in the text.

Figure 6-8 is a comparison of the average voltage versus x of a $\text{Li}/\text{B}_{0.17}\text{C}_{0.83}$ cell, determined by averaging the first charge and second discharge (as described in the section on *in-situ* diffraction in Chapter 5), with a $V(x)$ curve calculated using the double Gaussian density of sites. The parameters of the calculation were: $z=0.12$, $E_b=-1.65$ eV, $E_c=-0.05$ eV,

$J=0.15$ eV, $\sigma_b=0.2$ eV and $\sigma_c=0.7$ eV. The fit is fairly good except in the region below $V=0.5$, which is most likely due to the inadequacy of the model density of sites. A comparison of the calculated and experimental $-\partial x/\partial V$ can be seen in Figure 6-9, for the same data as in Figure 6-8. The roughness of the fit is more apparent in this figure. Because the data is for the charge of the cell, it is shifted up slightly in voltage, accounting for the lack of alignment between the high voltage peaks.

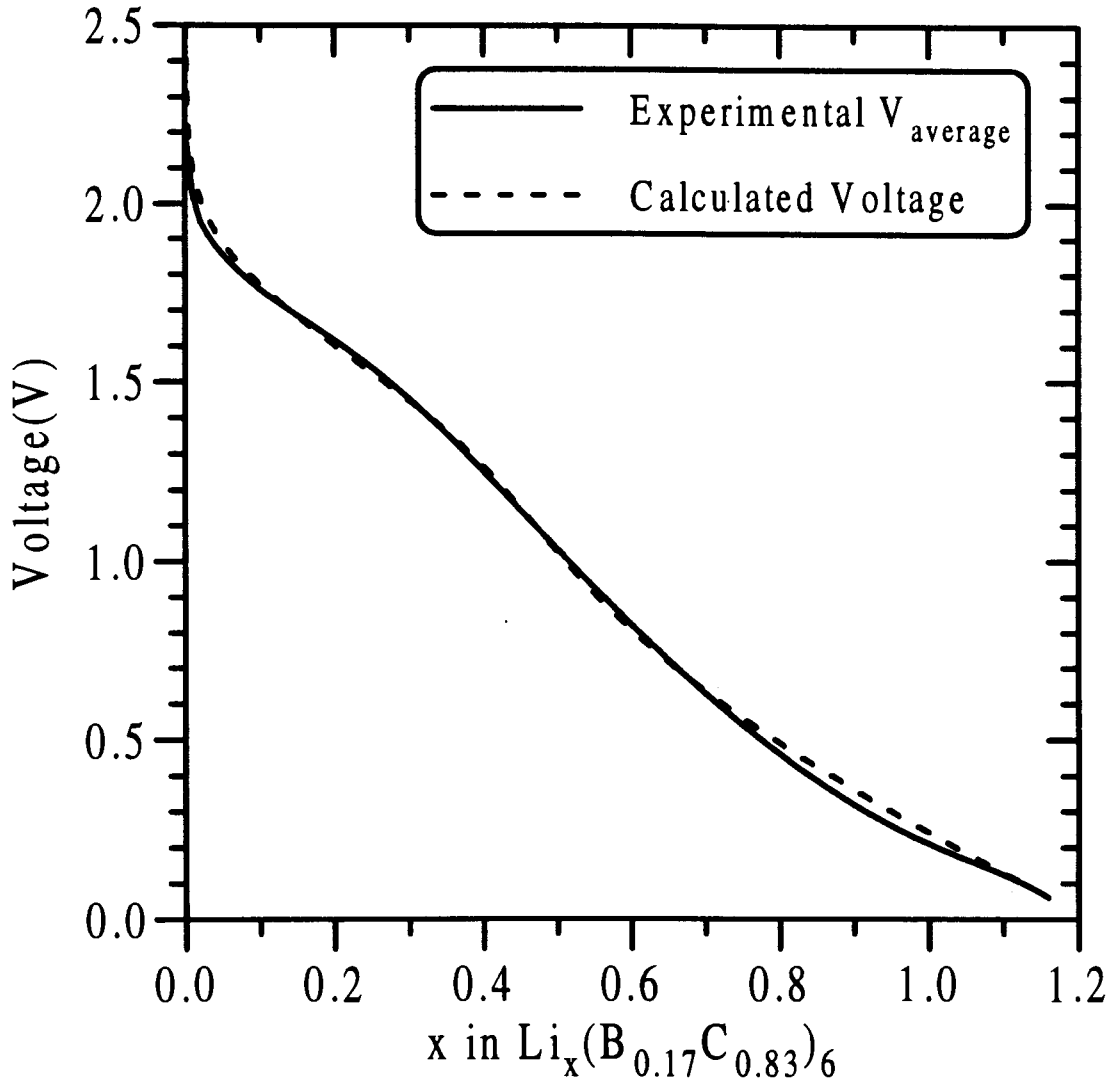


Figure 6-8 Comparison of $\text{Li}/\text{B}_{0.17}\text{C}_{0.83}$ voltage, from average of first charge and second discharge, with mean field calculation of voltage using double Gaussian density of sites and parameters described in the text.

The fit to the data is surprisingly good, considering the simplicity of the model. The fact that we fit the data from a material that we believe has $z=0.17$ with a model using $z=0.12$ suggests three possibilities: (1) our boron concentration is incorrect, (2) our model incorrectly weights the effect of boron or (3) all of the boron in the material is not substitutional. It is unlikely that our boron concentration is out by 5%, although 2% is possible. The model's treatment of the effect of boron is very simplistic and could well be incorrect. For the very high boron concentration samples, a boron containing impurity is evident in the X-ray absorption spectra, and thus may contribute to a decrease in the substituted boron.

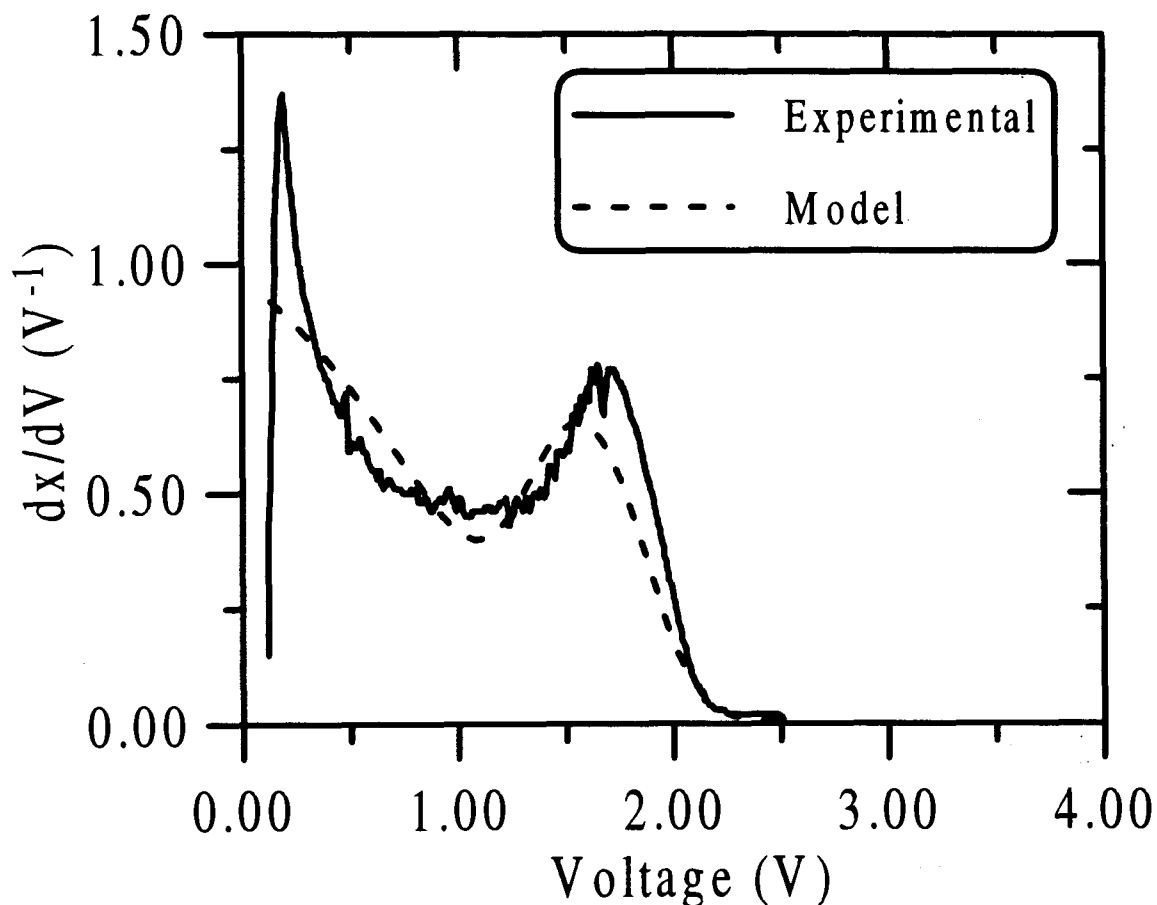


Figure 6-9 Comparison of the derivative curves of the charge of a $\text{Li/B}_{0.17}\text{C}_{0.83}$ cell (solid) with that calculated in mean field approximation. Parameters are the same as for Figure 6-8.

It is also unclear what would cause the distribution width of the boron-shifted

Gaussian to be only 0.2 eV, while that of the carbon Gaussian is 0.7 eV. Again this may be due to an oversimplification of the model, or it may arise from the width of the density of electronic states to which the lithium 2s electrons are being donated.

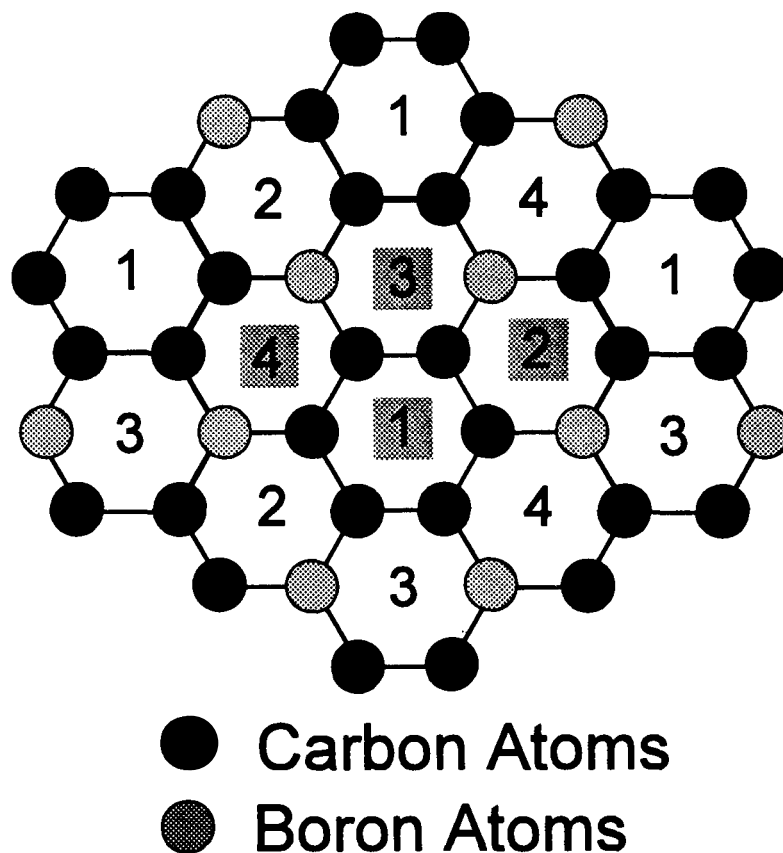


Figure 6-10 In plane structure of BC_3 showing the four sublattices.

6.2.4 Mean Field Solution for BC_3

To determine the voltage curve from lithium intercalation in a pure BC_3 material that was in-plane ordered but could exhibit turbostratic disorder, we applied the simple single rectangular density of sites model used for pure disordered carbons (see Section 6.2.2). For the ordered structure proposed by Bartlett *et al.*,¹⁷ the lattice must be divided into three sublattices of honeycombs containing two boron atoms, and one sublattice with only carbon atoms. Figure 6-10 shows the BC_3 lattice divided into four sublattices, with sublattice 1 containing only carbon atoms. The sites between the boron atoms are assumed to be shifted up in binding energy with respect to the pure carbon sites. Each sublattice interacts with two

of each of the other three sublattices, making the interaction term $2J(x_j+x_k+x_l)$. The solution for x_i is then:

$$x_i = 1 + \frac{kT}{2\Delta} \ln \left[\frac{1 + e^{(E_i + 2J(x_j+x_k+x_l) - \mu)/kT} e^{-\Delta/kT}}{1 + e^{(E_i + 2J(x_j+x_k+x_l) - \mu)/kT} e^{+\Delta/kT}} \right] \quad \text{Equation 6-22}$$

where $E_i = E_c$ for sublattice 1, and $E_i = E_b$ for sublattices 2,3,4. Note that x is now in $\text{Li}_x(\text{BC}_3)_2$.

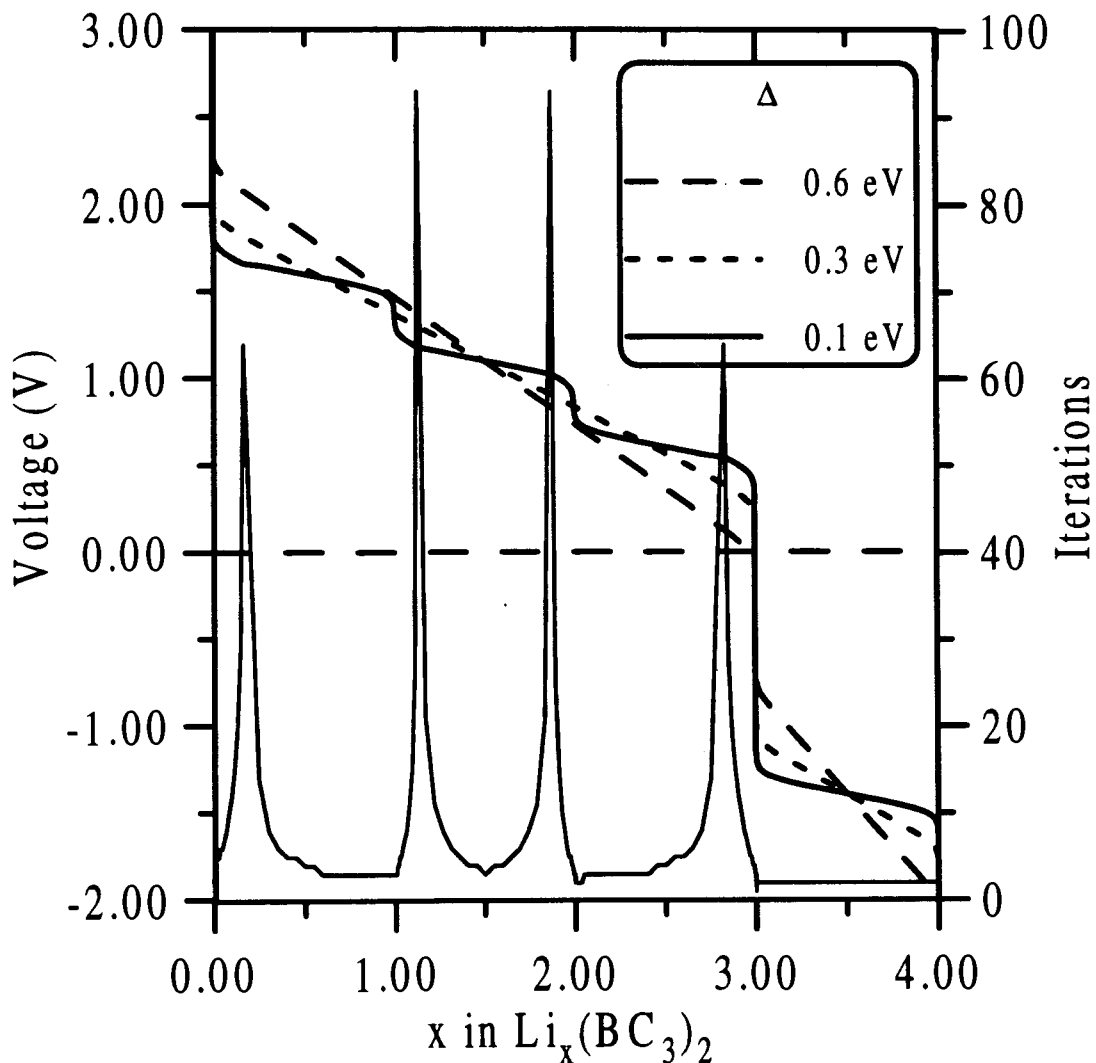


Figure 6-11 Mean field calculation of Li/BC_3 voltage curve, for $\Delta=0.6$ eV, 0.3 eV, and 0.1 eV. Also shown are the number of iterations required to reach self-consistency for the $\Delta=0.1$ eV calculation.

The results of the calculated voltage curves are seen in Figure 6-11, with $E_b = -1.6$ eV, $E_c = -0.1$ eV, $J = 0.25$ eV, $T = 300$ K, and $\Delta = 0.6$ eV, 0.3 eV, and 0.1 eV. The voltage curve for $\Delta = 0.1$ eV shows ordering phase transitions, and as illustrated by the number of iterations taken to reach self-consistency, also shown in the figure. In this case the ordering is such that the three boron sublattices fill first and then the carbon sublattice. According to this model, the capacity of this material (above 0 V) should be $x=3$ in $\text{Li}_x(\text{BC}_3)_2$, or 858 mAh/g, if it can be made. Of course the interaction, J , and the range of possible half-widths are not known, and may be quite different from those in the solid solution, B_zC_{1-z} .

Chapter Seven

7. Recent Advances in Carbonaceous Anodes

The objectives of this chapter are to place the work done in this thesis in a historical perspective, and to review some of the recent advances in the reversible capacities of carbonaceous materials, both pure and containing significant concentrations of other elements.

During the 1980's, rechargeable lithium batteries with lithium metal as the anode were the subject of much interest. Most of the research conducted was into cathode materials, such as MoS_2 , Mo_6S_8 , TiS_2 and various forms of manganese oxides, in an effort to improve energy density and voltage characteristics. On the anode side research focused on methods of decreasing the reactivity of the lithium metal by cell engineering, electrolyte choice, or alloying with aluminum. With the fires caused by Molicel® batteries in cellular phones in Japan in 1989, the industry was forced to find a safer technology, which it did in the form of lithium-ion cells. These cells included two lithium intercalation materials, and no metallic lithium.

New searches were then required to find the best anode and cathode materials. Air-stable cathode materials containing lithium had to be synthesized that were capable of being reversibly intercalated. This search has focused on LiNiO_2 , LiCoO_2 and various lithium manganese oxides, with only LiCoO_2 currently used in commercially available cells. This race continues.

Carbons were soon determined to be the materials of choice for anodes in lithium-ion cells, due to the fact that their lithium intercalation potentials are only 0.1 to 1 V above lithium metal, depending on the type of carbon, and thus the cell voltage is only 0.1 to 1 V less than a cell made with lithium metal as the anode. Carbons such as graphite had a

theoretical specific capacity of 372 mAh/g, were fairly cheap, and, after some development, could perform reliably for over 1000 cycles, much superior to lithium metal. But with the competitiveness of the battery industry, the need for ever higher energy densities pushed the quest for higher specific capacity carbons. At that time, however, very few of the hundreds of available carbons had been tested to determine their specific capacity. In addition, hundreds of thousands of other carbons could conceivably be produced by pyrolysis of available organics, or by deposition from vapors. Only a few materials such as graphite, petroleum coke, and heated petroleum pitches had been studied. It was unknown whether it was possible to produce carbons with higher capacity than graphite, and a lot of the development focused on getting the best performance possible out of graphite and coke, by reducing parasitic side reactions through heat treatment and improving cycle life. It was in this atmosphere that the race for high capacity carbons began.

These new carbonaceous materials will be dealt with in two parts. The first section will deal with the effects caused by the incorporation of additional elements, and the second will describe the new high capacity disordered carbons, containing only carbon and hydrogen.

7.1 The Effect of Phosphorus, Boron, Nitrogen and Silicon on Lithium Intercalation in Carbon

Additional elements can be incorporated into carbon in several ways: (1) substitutionally, as in B_zC_{1-z} , (2) chemically bonded in a non-substitutional manner, and (3) as a dispersed mixture. One of the earliest reported carbons with capacity exceeding graphite was prepared from poly-furfuryl alcohol polymerized using phosphoric acid,⁷⁷ and pyrolyzed at 800°C. The reported capacity was 450 mAh/g. The voltage curve for a similar material, pyrolyzed at 600°C, is shown in Figure 7-1.⁷⁸ It shows very large hysteresis and irreversible capacity. Both of these features make use as a practical anode unlikely. The mechanisms for both the increased capacity and the hysteresis were not understood.

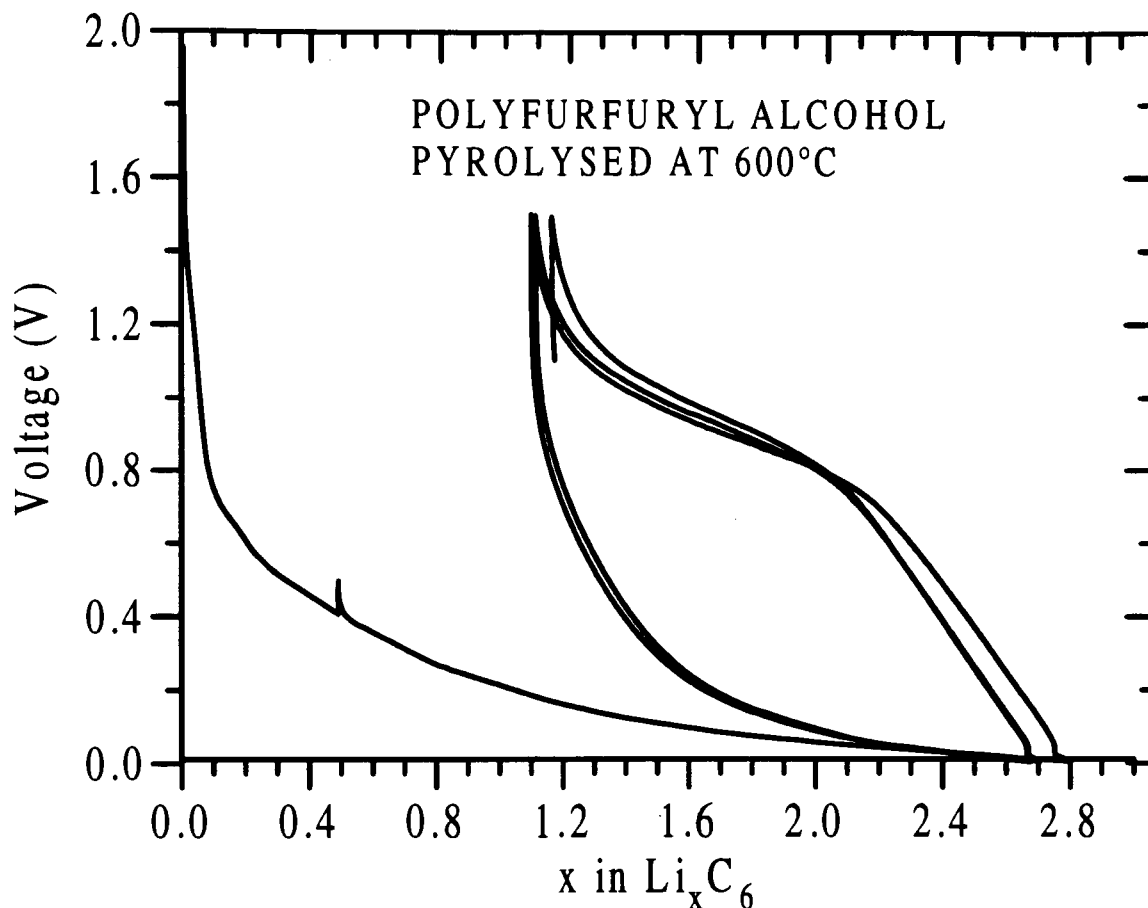


Figure 7-1 Voltage curve of phosphorus-containing polyfurfuryl alcohol, pyrolyzed at 600°C.

As early as May 1992 there have been reports on the use of BC_2N as a lithium-ion anode.^{79,80} These materials were synthesized by CVD by the methods of Bartlett, from acetonitrile (CH_3CN) and boron trichloride at 1000°C. The exact stoichiometry was not reported. They reported slight increases in voltage and reversible capacity, with a maximum of $\Delta x=0.58$ in Li_xBC_2N , which is equal to 318 mAh/g. This is slightly more than for a petroleum coke heated to the same temperature, but less than for graphite.

In October 1992, at the Fall meeting of the Electrochemical Society, we presented cell data for thin B_2C_{1-z} films on metal substrates, with estimated capacities. The aim was to show the dramatic changes in the voltage curves with boron concentration. Due to the large uncertainty in the electrode masses, no capacities greater than 372 mAh/g were reported. At

about the same time we were seeing evidence from powder cells that the capacity could indeed exceed that of graphite, but could not report this while we were seeking to patent. The first evidence of additional capacity was presented in a poster at the 1993 CAP Congress in June 1993. More complete pictures were presented at the Fall Electrochemical Society Meeting 1994, in New Orleans (October 1993), on a poster at the 7th International Meeting on Lithium Batteries in Boston (May 1994), and in the Journal of the Electrochemical Society (April 1994).

Following the early work on B_2C_{1-2} , Weydanz *et al.*⁸¹ prepared nitrogen containing carbons from CVD of ammonia and acetylene as well as thermal decomposition of pyridine and acetonitrile. The cells had similar reversible capacities, regardless of nitrogen content, but the irreversible capacities increased with increasing nitrogen concentration. This suggests that an irreversible reaction occurs between lithium and at least some of the nitrogen present. There is also a shift in the voltage curve, so that the capacity begins at slightly lower voltage. This is consistent with our model of boron as an electron acceptor, and nitrogen as an electron donor. The binding energy between the lithium and the host will be weakened slightly by presence of the nitrogen, causing a downward shift in the voltage. The lack of great improvement in the case of BC_2N can also be understood, since the effects of the boron and nitrogen approximately cancel.

More recently Wilson *et al.* prepared silicon containing carbons both by CVD⁸² and by pyrolysis of silicon containing polymers.⁸³ The CVD samples were produced from source mixtures of either tetrachlorosilane ($SiCl_4$) or dimethyl-dichlorosilane ($(CH_3)_2Cl_2Si$) with benzene at atmospheric pressure and 950°C. Silicon concentrations were determined using a Thermogravimetric Analyzer (TGA), by reacting the samples with air while heating to 950°C, and taking the mass of the resulting white powder as pure SiO_2 . The silicon can not be substitutional for carbon in the graphite structure because silicon bonds tetrahedrally and is incapable of planar (sp^2) bonding. In their model they propose that the silicon atoms are nano-dispersed, either singly, or in groups too small to diffract coherently. A drawing of this model is presented in Figure 7-2, with the pure disordered carbon in (a) and the nano-dispersed silicon in carbon in (b). The nature of the bonding between the silicon and carbon

is unknown. The net effect though, is to allow lithium to bond to the silicon as it is intercalated. The voltage at which Li-Si alloying occurs is approximately 0.3 V with respect to lithium metal.

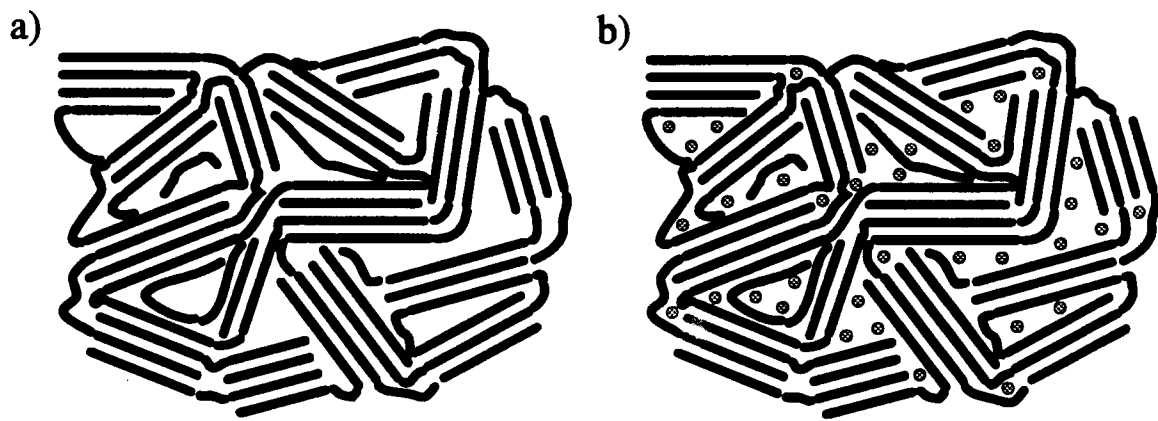


Figure 7-2 Schematic drawing of (a) disordered carbon and (b) nano-dispersed silicon in disordered carbon.

Figure 7-3 shows the voltage curve of a cell made from a sample with 11% Si, produced at 950°C from dimethyl-dichlorosilane and benzene, compared to a sample made from pure benzene under the same conditions. Two features are immediately apparent in the comparison. The irreversible capacity on the first discharge of the Si containing sample is ~160 mAh/g, compared to ~60 mAh/g for the pure carbon cell, and the reversible capacities are ~480 mAh/g and ~300 mAh/g, respectively. On inspection of the derivative curve in the inset, it can be seen that most of the new capacity is between 0.2 V and 0.8 V, and thus may be due to the reversible reaction of lithium with silicon. The irreversible capacity during the first discharge occurs in two places: (1) between 1.0 V and 1.2 V, and (2) between 0 V and 0.2 V. The high voltage irreversible capacity is likely due to formation of the passivating film, but the low voltage area is new, and may correspond to the irreversible reaction of lithium with some of the silicon. The voltage and reversibility of the reaction likely depends on the bonding of the silicon atoms to carbon and other silicon atoms.

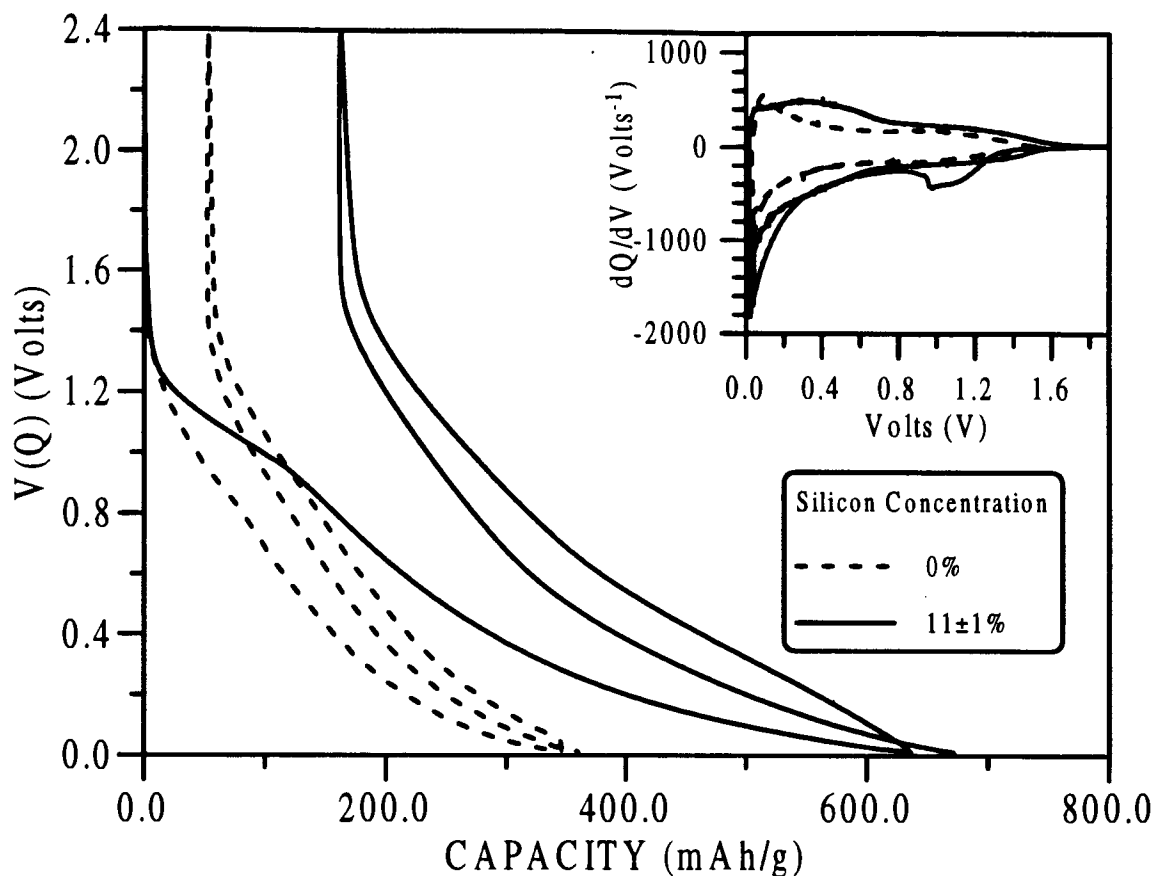


Figure 7-3 Voltage curve for $\text{Li/Si}_2\text{C}_{1-z}$ cells from reference 82. The solid curve is for a sample prepared from 1:1 $(\text{CH}_3)_2\text{Cl}_2\text{Si:C}_6\text{H}_6$ and the dashed curve corresponds to a sample produced from pure benzene. Both samples were prepared by CVD at 950°C .

Pyrolysis of silicon-containing polymers was performed both by Wilson *et al.*,⁸³ using polymethylphenylsiloxane and polyphenylsesquisiloxane, and more recently by Xue *et al.*⁸⁴, on a series of epoxy-silanes with varying silicon stoichiometries. All of these samples were extremely disordered, with diffraction peaks suggestive of a glass, rather than a disordered graphite. Both these types of samples showed large irreversible (150-425 mAh/g) and reversible (400-775 mAh/g) capacities, but with a 0.5 V hysteresis between charge and discharge. Study of these materials continue, and interest is great due to their large reversible capacities, but their value is presently limited by their large irreversible capacities.

7.2 High Capacity Disordered Carbons

Concurrently with the increase in capacity in the carbons containing elemental

additives, the capacity of unsubstituted, disordered carbons has also risen dramatically. With this increase has come a new understanding of some of the factors that affect lithium intercalation in carbons. Much of this new information is reviewed by Dahn *et al.* in Science.⁸⁵ Figure 7-4 is from that paper, and plots the reversible capacities of many carbons as a function of their heat treatment temperature. The carbons of commercial relevance as lithium-ion anodes are divided into three regions: (1) Graphitic carbons, (2) Both soft and hard carbons heated to between 500°C and 800°C, and (3) some hard carbons heated to ~1000°C. Representative voltage curves of carbons from each of these regions are shown in Figure 7-5. Each of these regions will be dealt with individually in the following three sections.

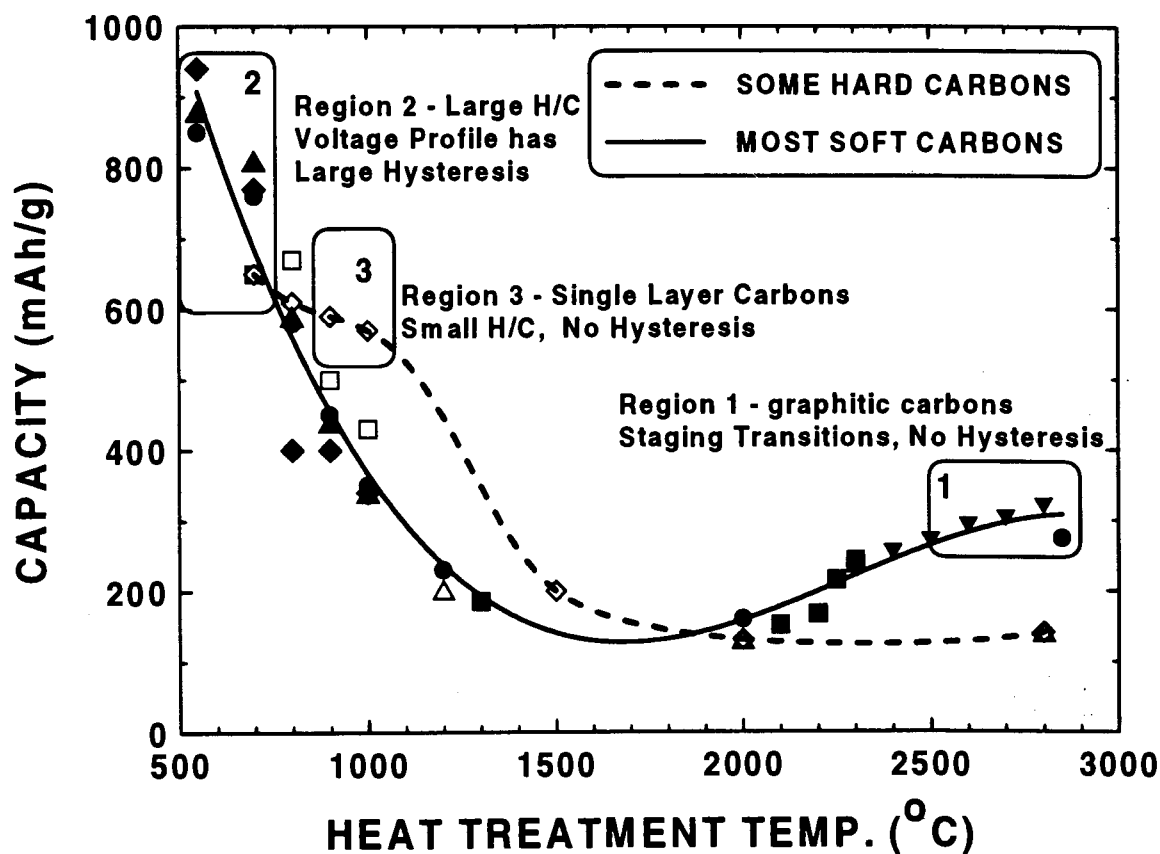


Figure 7-4 The master graph of reversible capacity for lithium plotted versus heat-treatment temperature for a variety of carbon samples from reference 85. The three regions of commercial relevance are marked.

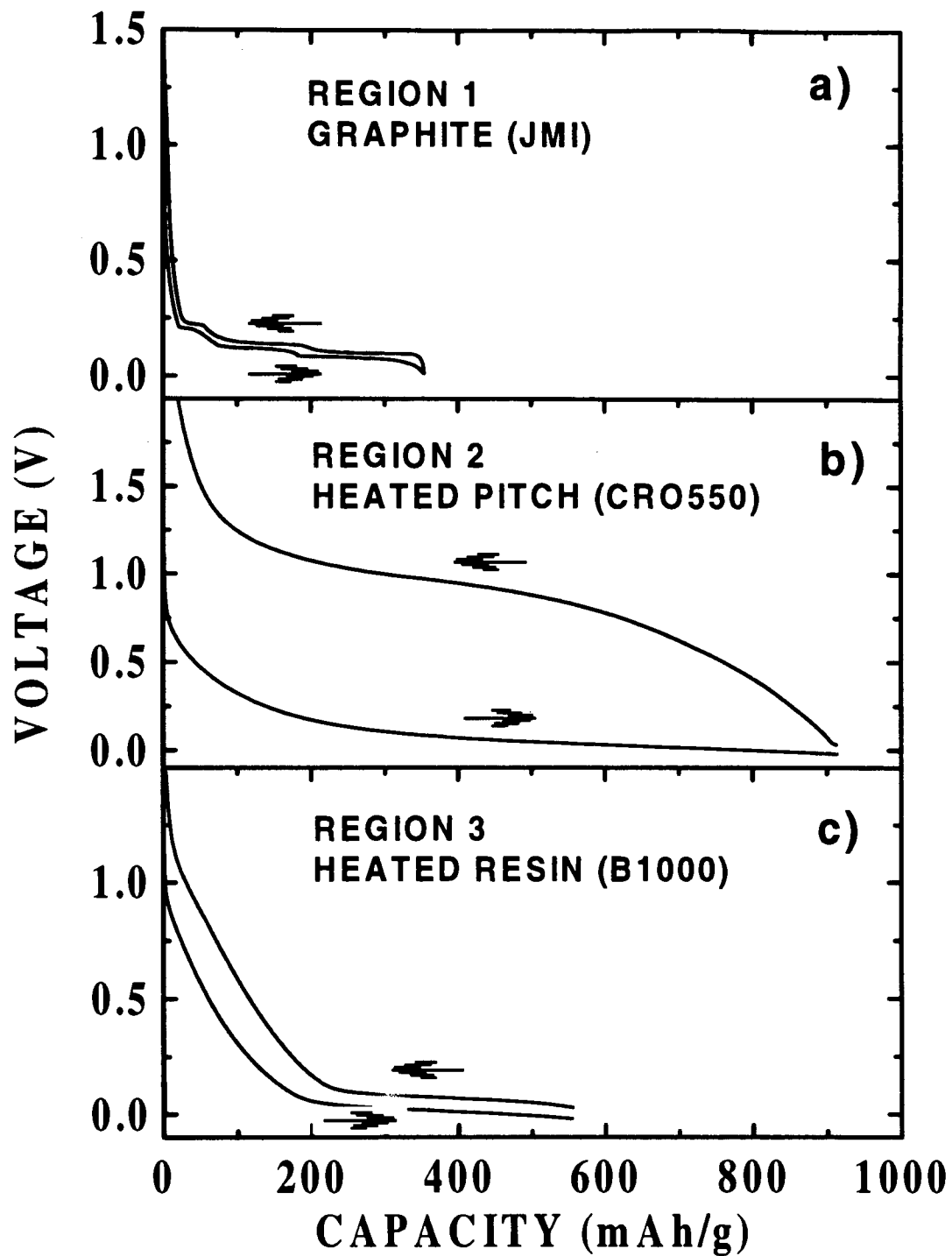


Figure 7-5 Second cycle voltage curves of carbons representative of regions 1,2 and 3. a) Johnson-Matthey Synthetic Graphite, b) Crowley petroleum pitch heated to 550°C and c) resole resin heated to 1000°C.

7.2.1 Region 1:

Region 1 includes the very graphitic carbons, and the details of intercalation in graphite have been described earlier in this thesis. A representative voltage curve for JMI graphite is seen in Figure 7-5a. For graphitic carbons with turbostratic disorder the capacity varies with P as $x_{\max}=(1-P)$ (as seen in Figure 2-9), suggesting that no lithium can be intercalated between parallel layers which are turbostratically misaligned.⁸⁶ For soft carbons P decreases with temperature between 2000°C and 3000°C.

7.2.2 Region 2:

In the past two years many Region 2 materials have been produced from a wide variety of organic precursors, heated to temperatures between 500°C and 800°C^{87,88,89}. They all have voltage curves similar to that seen for the CRO550 sample in Figure 7-5b, with very large capacity, approaching 1000 mAh/g, but also large hysteresis between charge and discharge. The irreversible capacity is also typically quite large. The phosphorus containing carbon produced by the pyrolysis of a furfuryl alcohol polymer at 600°C, mentioned in Section 7.1, also appears to fit in this region, and it becomes apparent that the phosphorus is probably not involved in the intercalation process. A number of explanations have been put forward to explain the behaviour of carbons in this region. Mabuchi *et al.*⁸⁷ believed that lithium was being inserted into cavities within the material. This is not likely because one would expect that the chemical potential of the lithium deposited in these cavities to be very close to that of lithium metal, giving an average cell voltage of the order of tens of millivolts, instead of >0.1 V as observed. In addition, no hysteresis in the voltage profile would be expected. Further evidence against this possibility was provided by Liu *et al.*,⁹⁵ who reported that the microporosity of many of these materials is very low.

Another explanation was put forward by Sato *et al.*,⁸⁸ who proposed that the lithium ions in the intercalated carbon occupy nearest neighbor sites in each layer. However, like the case for B_2C_{1-2} , this would require that there is a mechanism (such as an electron acceptor) present to overcome the screened Coulomb repulsion between ions on nearest neighbor sites. There is also no explanation of the voltage hysteresis.

One fact noted by Yata *et al.*⁸⁹ was that these carbons had a significant fraction of hydrogen, and thus they referred to them as “polyacenic semiconductors.” In fact, all of the carbons from references 87,88 and 89 that had high capacities, also had hydrogen to carbon atomic ratios of ~ 0.2 . Figure 7-6 shows the reversible capacity of region 2 carbons versus their H/C atomic ratio taken from Zheng *et al.*⁹⁰ The solid line is the capacity expected if one lithium atom can be accommodated for each hydrogen atom, starting with a base capacity of 250 mAh/g for intercalation in the carbon. Data from reference 87 are also included.

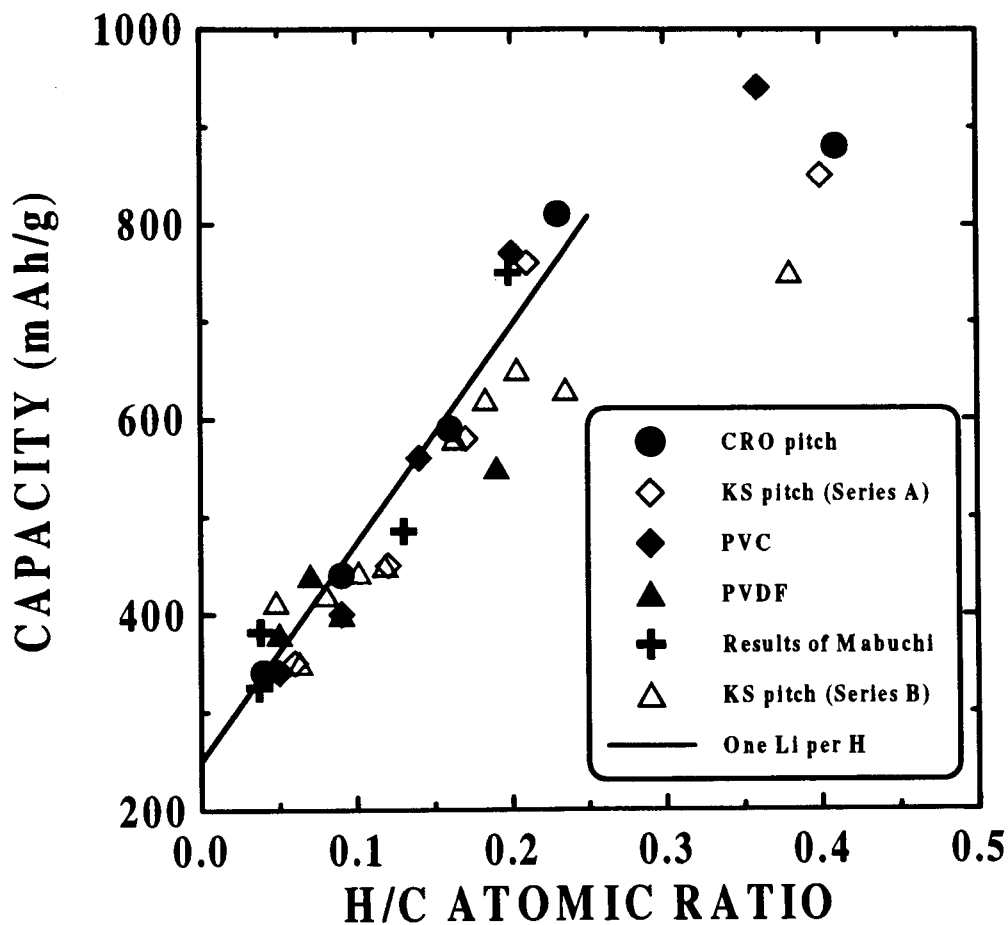


Figure 7-6 Reversible capacity of carbons from region 2 as a function of their hydrogen to carbon ratio. The samples include Crowley Pitch (CRO), Kureha Pitch (KS Series A and B), polyvinylchloride (PVC) and polyvinylidene fluoride (PVDF) heated to temperatures between 550°C and 1000°C as well as data from reference 87.

The exact reason for the effect of hydrogen on the reversible capacity is still not well understood, but Dahn *et al.* have proposed the following hypothesis.⁸⁵ It is known that charge transfer from alkali metal atoms to hydrogen in carbon occurs in graphite-alkali-hydrogen materials.⁹¹ Therefore it is not unreasonable to expect that a lithium atom will bond in the vicinity of a hydrogen atom and transfer part of its 2s electron to the hydrogen. This would affect the hydrogen-carbon bond, leading to changes in the host structure. These changes may be activated processes, leading to a hysteresis in the voltage curve. They do not speculate as to the exact nature of the Li-H-C bonding.

7.2.3 Region 3:

Carbons in region 3 tend to be hard carbons, produced by the pyrolysis of cross-linked polymers at temperatures near 1000°C. These materials have reversible capacities of 500 to 600 mAh/g on a low voltage plateau, near zero volts, and little hysteresis in the voltage curve, as seen in Figure 7-5c. Some of the reports of voltage curves for carbons in this region include: Takahashi *et al.*,⁹² Omaru *et al.*⁹³ using pyrolyzed polyfurfuryl alcohol, Sonobe⁹⁴ *et al.* using pyrolyzed petroleum pitch and Liu *et al.* using pyrolyzed epoxy novolac resins.⁹⁵

Ishikawa *et al.*⁹⁶ proposed that the large capacity was due to the filling of micropores in the carbon with lithium clusters. This would give a very low voltage plateau, because the lithium atoms would be only very weakly bound with respect to lithium metal. This is consistent with the experimentally observed behavior. By contrast, Liu *et al.*⁹⁵ showed that these carbons were made up with a large fraction of single layers, stacked like a “house of cards”. They proposed that lithium could be adsorbed to both sides of the graphene sheets, leading to an increased capacity over graphite, which only has one lithium layer per graphene sheet. For 100% single layer carbon this would lead to a capacity of Li_2C_6 or 740 mAh/g. Figure 7-7 plots the reversible capacity as a function of the single layer fraction for a series of epoxy novolac resins heated to 900°C to 1100°C.

Small-angle scattering shows that the pore sizes of these carbons are of the order of 15 Å in diameter.⁶³ The two views, pore-filling and surface adsorption, are actually the same

when the pore size is small, because adsorbed lithium will completely fill the pores. Both of these models predict very low voltage plateaus. The sloping part of the voltage curve in Figure 7-5c is due to intercalation between stacks that have two or more layers.

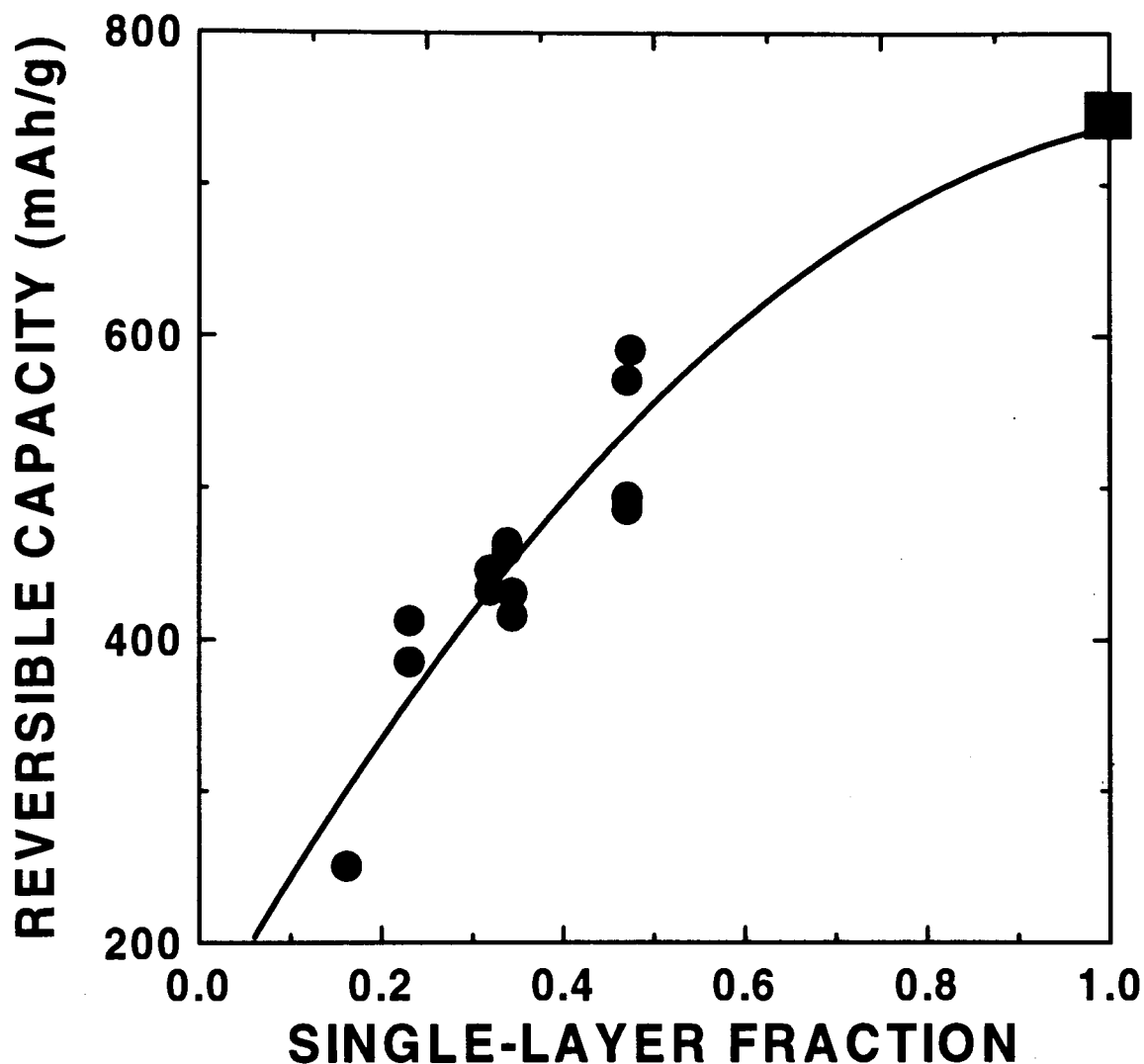


Figure 7-7 The reversible capacity of region 3 carbons prepared from epoxy-novolac resins heated between 900°C and 1100°C as a function of their single-layer fraction. The square point is a calculation corresponding to complete absorption on both sides of a carbon consisting of only single-layers. The line is a guide to the eye.

Recent evidence from Xue *et al.*⁶³ also supports this view of the microstructure of the Region 2 carbons. They measured the BET surface area (N_2 adsorption), small angle X-ray scattering (SAX) and methylene blue adsorption of a series of epoxy-resin based carbons as

a function of mass lost to oxidation. They observed an increase in pore opening size, but not in pore size, with oxidation. This is correlated with an increase in the irreversible capacity and a decrease in the reversible capacity as the pore opening becomes large enough to admit electrolyte, causing a passivating film to be formed on the pore surfaces.

7.3 Conclusions

There are several promising types of high capacity carbons, all of which are presently under investigation for use in lithium-ion cells. Of the carbons containing other elements, the most promising are the materials produced by the pyrolysis of silicon-containing polymers. They are relatively cheap to produce, and have reversible capacities of up to nearly 800 mAh/g. The major problems that need addressing are the large irreversible capacity and hysteresis of ~0.5 V. The Region 1, graphitic carbons are currently used as commercial anodes, but will likely be replaced if new high capacity carbons can be made to cycle well, and safely. The Region 2 hydrogen containing, carbons have the highest reversible capacities, but also have large irreversible capacity and hysteresis. The high voltage of de-intercalation would result in a lithium-ion cell with a discharge voltage ~1 V lower than for a present, commercial cell. If not adequately compensated by increased capacity, this would lower the energy density of the cell. The irreversible capacity requires additional cathode material to replace the lithium that is lost, also decreasing energy density. The region 3, single layer carbons are probably the most promising of all. The reversible capacities are potentially up to 740 mAh/g, with low irreversible capacity and no hysteresis. With the extremely low voltage plateau, a lithium-ion cell containing one of these materials will have the maximum possible voltage for the given cathode material.

Chapter Eight

8. Conclusions

8.1 Summary of Contributions of this Thesis

In this thesis we have presented the experimental results for the synthesis, characterization and lithium intercalation in B_zC_{1-z} , for $0 \leq z \leq 0.17$. In addition, we have presented both qualitative and semi-quantitative models to understand the effects of boron substitution on the intercalation of lithium in carbons.

In the synthesis of the B_zC_{1-z} films we basically followed the method of Bartlett.⁴² We, along with many other groups,^{56, 97, 98, 99} confirmed this synthesis method. In the characterization of the films we presented some interesting new results, including: (1) the variation of boron concentration in the samples with the ratio of BCl_3 to C_6H_6 ; (2) grazing incidence diffraction of the thin films to illustrate the decreasing layer spacing and increasing ordering with increasing boron concentration; (3) rocking curves on the films deposited on quartz to provide a measurement of the mosaic spread; (4) the angle dependence of the X-ray absorption, providing further evidence for the substitutional incorporation of the boron; and (5) the phase separation of B_zC_{1-z} into B_4C and C in the temperature range 1200°C to 1500°C.

Of these contributions, the first is extremely important since it allows the determination of other properties, including the intercalation of lithium, as a function of boron concentration. Our paper¹⁰⁰ was, to the best of our knowledge, the first report of a series of samples with varying boron concentration produced at the same temperature. This work has been recently confirmed in Figure 6 of Cermignani *et al.* (1995).⁵⁶ The study of the effect of boron concentration on the graphitic order of the carbons continues where earlier studies left off^{18, 38} (at a maximum of 2.35 atomic percent boron), and shows that the layer

spacing can be decreased to that of graphite at 900°C with the addition of approximately 15% boron. The rocking curves determined that the films grow in a generally oriented manner, with the average c-axis parallel to the normal to the substrate, but with a fairly broad mosaic spread of 5.5° full width at half maximum. The angle dependent XAS measurements we presented in the same paper also provided what we believe was the best evidence to date of the substitutional incorporation of boron, rather than interlayer or interstitial incorporation, or presence as another chemical species.

The study of the electrochemical intercalation of lithium in B_2C_{1-z} provided many interesting results, and has not been duplicated elsewhere (with the exception of patent applications of questionable validity that are addressed in Section 8.3). Measurements of the voltage curves of the B_2C_{1-z} materials have shown striking variations in both the voltage profile and reversible capacity as a function of lithium concentration. These results have been of great interest, particularly to the battery community, which at that time had never seen capacities larger than that of graphite. The variation of layer spacing with intercalated lithium concentration, as measured by *in-situ* diffraction, is larger than expected for a pure carbon, and suggests possible mechanisms for the additional reversible capacity that was observed. Finally, the study of the samples that had been heat-treated confirmed that the boron was separating into a phase that was incapable of intercalating lithium, and that further heating to change electrochemical properties was pointless.

The final goal of this thesis was to try to provide an understanding of the intercalation of lithium in B_2C_{1-z} by modeling the voltage curves using a lattice gas model. Although the model is very qualitative, the result is a model that fits the data reasonably well. It suggests that most of the features in the voltage curve are due to the shape of the density of sites with binding energy, and not other factors such as entropy or ordering phase transitions, and that the boron concentration determines the number of sites with a shifted binding energy. This means that the shape of the density of sites versus binding energy is very close to that of $-\partial x/\partial V$ versus voltage, and a more accurate model would have to reproduce this more complicated shape.

8.2 Future Work

There are many other potential projects that are suggested by the work in this thesis. A careful study of the variation of all of the available deposition parameters would most likely provide a higher boron concentration product, as well as changes in crystallographic order. Better methods of boron concentration determination could be employed to produce more accurate results. A neutron diffraction study of the fully intercalated B_2C_{1-z} sample may be able to determine the location of the lithium ions in the intercalated host, providing that the initial sample is ordered enough. Finally, another useful project would be the investigation of much cheaper synthesis route, that still produces a substitutional product. This would probably involve the low temperature (<1000°C) pyrolysis of a polymer than contains boron atoms in six-member rings, so that no reordering of the boron takes place. With the possible exception of the last project, none of these would be of great interest to the battery industry, but may be of interest to academic scientists interested in the B_2C_{1-z} material and its properties.

8.3 Technological Application of B_2C_{1-z}

We reported the reversible capacity of the B_2C_{1-z} materials first in June 1993 (delayed due to patent application filing). The highest specific capacity we achieved was 420 mAh/g, significantly higher than graphite, and higher still than the disordered carbons that were the material of choice at the time for commercial lithium-ion cells. The downside of these materials was the large voltage range over which the capacity was available, which would produce a lower voltage lithium-ion cell, as well as the prohibitive cost of the CVD method. Still, the material was thought worthy of patenting and we applied for U.S., Japanese and European patents for electron acceptor containing electrode materials, with the rights assigned to Moli Energy (1990) Ltd.

Japanese companies have also believed boron substituted carbons worth patenting, with Matsushita Electric Industrial Co. Ltd.¹⁰¹ and Sanyo Electric Co. Ltd.¹⁰² filing patent applications including the use of BC_3 as a lithium-ion anode in June 1992 and February 1993 respectively. The Matsushita patent does not include any information about the synthesis of

BC₃, but does include voltage curves claiming to come from Li/BC₃ cells. The voltage curve is completely flat at 0.1 V, with a total capacity of ~350 mAh/g. This “data” looks like no data that we have ever seen for a real cell. The voltage is similar to that of graphite, but with no staging. In our opinion the data is clearly not real. The wording in the document is also strikingly similar to that used by us at the Fall Electrochemical Meeting in Toronto (1992).

The Sanyo patent does describe the synthesis method. It suggests mixing petroleum coke with B₄C, B₂O₃, B or a boron halide (BCl₃, BF₃, BBr₃, or BI₃) and heating to between 2000°C and 3000°C. No evidence that BC₃ has been made is presented and from the work presented here, this synthesis method would not produce a substitutional material. The reported d₀₀₂ is 3.78 Å, much larger than expected for a carbon heated to this temperature range, especially in the presence of boron, which should catalytically graphitize the sample. The voltage curve of a cell claimed to be Li/BC₃, slopes between 0 and 1 V and looks very much like that of petroleum coke, except with a reversible capacity of 375 mAh/g. Furthermore the same curve is claimed for both BC₃ and BC₃N. This patent is full of inconsistencies which make it unlikely that the authors have synthesized or made cells from a substitutional BC₃.

The obvious question is whether or not a B₂C_{1-z} material is likely to be used as an anode in a commercial lithium-ion cell? This seems unlikely in view of the startling recent advances in the reversible capacities of highly disordered pure and silicon-containing carbons, and the prohibitive cost of manufacturing the B₂C_{1-z} by chemical vapor deposition. One possibility is the incorporation of an electron acceptor along with the disorder needed to produce a very high capacity anode. If an alternate, cheap, synthesis route is discovered, another potential application for this, or other electron acceptor materials, is as an all carbon cell. One electrode would be a pure carbon of region 3 (see Figure 7-5), with a voltage near 0V, and the other electrode, an electron acceptor substituted carbon, with a voltage >1.5V, producing a cell voltage of approx. 1.2-1.5V, the same as Nickel-Cadmium or alkaline cells. Lithium can be introduced into coin-size cells by placing the carbon electrode on top of a piece of lithium foil and sealing the cell, allowing the lithium to intercalate directly. For small cells the amount of heat generated in this short circuit is small enough not to damage

the cell. In this way no lithium needs to be included in the initial electrodes. The advantage of this type of cell may be longer cycle life, and light weight.

In any case, the study of B_zC_{1-z} helped to dispel the belief that graphite's 372 mAh/g specific capacity was an unbreakable barrier and led the way to attempts to fabricate silicon substituted carbons that instead produced nano-dispersed silicon with even higher reversible capacities. In addition, it aided in the understanding of the effect of substituted elements on the voltage curve of carbons, which may help direct future work.

References

- ¹ A.Volta, Phil. Trans., 1800, **90**, 403
- ² N.J.Sinsted, Ann. Physik Chem., 1854, **92**, 21
- ³ D.Guyomard and J.M.Tarascon, Adv. Mater. **1994**, 408.
- ⁴ S.R.Ovishinsky, M.A.Fetcenko and J.Ross, Science **260**, 176 (1993).
- ⁵ PC Computing Magazine, December 1994, p128
- ⁶ M.S.Whittingham, Science **192**, 1126 (1976).
- ⁷ J.R.Dahn, U. von Sacken, M.W.Juzkow and H.Al-Janaby, J. Electrochem. Soc. **138**, 2207 (1991).
- ⁸ S.Hossain, in D.Linden (ed) Handbook of Batteries, 2nd edition, McGraw-Hill, New York, 1995, pp. 36.1-36.77.
- ⁹ M.Armand, in D.W.Murphy, J.Broadhead and B.C.H.Steele (eds), Materials for Advanced Batteries, Plenum, New York, 1980, p. 145.
- ¹⁰ T.Nagaura and K.Tozawa, Progress in Batteries and Solar Cells **9**, 209 (1990).
- ¹¹ J.M.Tarascon and D.Guyomard, J. Electrochem. Soc., **138**, 2864 (1991).
- ¹² D.Guérard and A.Hérolde, Carbon **13**, 337 (1975).
- ¹³ U. von Sacken, E.Nodwell, A.Sundher and J.R.Dahn, Solid State Ionics **69**, 284 (1994).
- ¹⁴ J.R.Dahn, A.K.Sleigh, Hang Shi, J.N.Reimers, Q.Zhong and B.M.Way, Electrochimica Acta **38**, 1179 (1993).
- ¹⁵ J.R Dahn, J.N Reimers, A.K. Sleigh and T. Tiedje, Phys. Rev. B **45**, 3773 (1992).
- ¹⁶ C.E. Lowell, J.Am. Ceram.Soc. **50**, 142 (1967).
- ¹⁷ J.Kouvetakis, R.B.Kaner, M.L.Sattler and N.Bartlett, J. Chem. Soc. Chem. Commun. **1986**, 1758 (1986).
- ¹⁸ Claude A. Klein in Chemistry and Physics of Carbon, Volume 2, p. 228 (1966).
- ¹⁹ R.M.Wentzcovitch, D.Tomanek, S.G.Louie and M.L.Cohen, Bull. Am. Phys. Soc. **33**, 427 (1988).
- ²⁰ D.L.Fecko, L.E.Jones, and P.A.Thrower, Carbon **31**, 637 (1993).
- ²¹ R.R.Haering, Can. J. Phys. **36**, 352 (1958), and the references within.
- ²² R.E.Franklin, Proc. Roy. Soc. (London) A **209**, 196 (1951).
- ²³ B.E.Warren, X-ray Diffraction, Addison-Wesley, Reading, Massachusetts, 1969, p. 253.
- ²⁴ Hang Shi, J.N.Reimers, and J.R.Dahn, J Appl. Crystallogr. **26**, 827 (1993).
- ²⁵ A.Herold, Bull. Soc. Chim. Fr. **187**, 999 (1955).
- ²⁶ M.S.Dresselhaus and G.Dresselhaus, Adv. in Physics **30**, 139 (1981).
- ²⁷ M.B.Dines, Mat. Res. Bull. **10**, 287 (1975).
- ²⁸ W.R.McKinnon, Chem. Solid State Mater. **5**, 163 (1995).
- ²⁹ J.Friedel, Advances in Physics **3**, 446 (1954).
- ³⁰ S.A.Safran, Phys. Rev. Lett. **44**, 937 (1980).

-
- ³¹ S.E.Millman and G.Kirczenow, Phys. Rev. B **28**, 3482 (1983).
- ³² J.R. Dahn, Phys Rev. B **44**, 9170 (1991).
- ³³ N.Daumas and A.Herold, C.R. Hebd. Seanc. Acad. Sci., Paris C **268**, 373 (1969).
- ³⁴ J.E.Fischer in A.P.LeGrand and S.Flandrois (eds), Chemical Physics of Intercalation, Plenum, New York, 1987, p.47.
- ³⁵ Kambe, M.S.Dresselhaus, G.Dresselhaus, S.Basu, A.R.McGhie, and J.E.Fischer, Materials Science and Engineering **40**, 1 (1979).
- ³⁶ S.Doyen-Lang, A.Charlier, L.Lang, M.F.Charlier, and E.McRae, Synthetic Metals **58**, 95 (1993).
- ³⁷ J.R. Dahn, Rosamaria Fong, M.J. Spoon, Phys Rev. B **42**, 6424 (1990).
- ³⁸ S.Marinkovic, in The Chemistry and Physics of Carbon, Volume 19, pp. 1-64.
- ³⁹ D.E.Soule, Proceedings of the Fifth Conference on Carbon, Vol.1, Pergamon Press, Elmsford, N.Y., 1962, p.13.
- ⁴⁰ J.W.McClure, Phys. Rev. **119**, 606 (1960).
- ⁴¹ M.E.Preil, D.P.DiVencenzo, R.C.Tatar and J.E.Fischer, Proceedings of the 15th ACS Carbon Conference, Univ. of Pennsylvania, Philadelphia, 1981, p.72.
- ⁴² J.Kouvetakis, R.B.Kaner, M.L.Sattler and N.Bartlett, J. Chem. Soc. Chem. Commun. **1986**, 1758 (1986).
- ⁴³ J. Kouvetakis, T. Sasaki, C. Shen, R. Hagiwara, M. Lerner, K.M. Krishnan and Neil Bartlett, Synthetic Metals **34**, 1 (1989).
- ⁴⁴ B.C.Shen, O.K.Tse, J.Kouvetakis, K.M.Krishnan, K.M.Yu and N.Bartlett, unpublished.
- ⁴⁵ L.E.Jones, D.A.Fecko and P.A.Thrower, Proceedings of the fifth International Carbon Conference, Essen, Germany, 22-26 (1992).
- ⁴⁶ W.E.Sawyer and A.Man., U.S. Patent #229,335, June 29, 1880.
- ⁴⁷ C.F.Powell in *Vapor Deposition*, Ed. by C.F.Powell, J.H.Oxley and J.M.Blocher, Jr, Wiley, New York, p.250 (1966).
- ⁴⁸ J.N.Pring and W.Fielding, J. Chem. Soc., **95**, 1497 (1909).
- ⁴⁹ M.Formstecher and E.Ryskevich, Compt. rend., **221**,558 (1945).
- ⁵⁰ R.Feidenhans'l, Surf. Sci. Rep. **10**, pp. 105-188 (1989).
- ⁵¹ L.E.Davis, N.C.MacDonald, P.W.Palmberg, G.E.Riach and R.E.Weber, Handbook of Auger Electron Spectroscopy, 2nd edition, Physical Electronics Division, 1978.
- ⁵² Joachim Stohr, NEXAFS Spectroscopy, Springer-Verlag New York (1992), p118.
- ⁵³ Joachim Stohr, NEXAFS Spectroscopy, Springer-Verlag New York (1992), p34.
- ⁵⁴ D.A.Fischer, R.M.Wentzcovitch, R.G.Carr, A.Contineza, and A.J.Freeman, Phys. Rev B **44**, 1427 (1991).
- ⁵⁵ K.H.Tan, G.M.Bancroft, L.L.Coatsworth and B.W.Yates, Can. J. Phys. **60**, 131 (1982).
- ⁵⁶ W.Cermignani, T.E.Paulson, C.Onneby, and C.G.Pantano, Carbon **33**, 367 (1995).
- ⁵⁷ W.Ruland, Acta Crystallogr. **18**, 992 (1985).
- ⁵⁸ R.G.Wyckoff, Crystal Structures, 2nd ed. (Krieger, Malabar, FL, 1982), Vol.1.
- ⁵⁹ D.A.Fischer, R.M.Wentzcovitch, R.G.Carr, A.Contineza, and A.J.Freeman, Phys. Rev B **44**, 1427 (1991).

-
- ⁶⁰ J.R.Dahn, J.N.Reimers, T.Tiedje, Y.Gao, A.K.Sleigh, W.R.McKinnon and S.Cramm, *Phys. Rev. Lett.* **68**, 835 (1992).
- ⁶¹ JCPDS CD-ROM Version 2.14, International Center for Diffraction Data, Newtown, Pennsylvania, 1993.
- ⁶² E.Rossen, J.N.Reimers and J.R.Dahn, *Solid State Ionics* **62**, 53 (1993).
- ⁶³ J.S.Xue and J.R.Dahn, accepted in *J. Electrochem. Soc.*, July 1995.
- ⁶⁴ T.Zheng, J.N.Reimers, and J.R.Dahn, *Phys. Rev. B* **51**, 734 (1995).
- ⁶⁵ E.Peled, *J. Electrochem. Soc.* **126**, 2047 (1979).
- ⁶⁶ R.Fong, U.von Sacken and J.R.Dahn, *J. Electrochem. Soc.* **140**, 2009 (1990).
- ⁶⁷ Z.X.Shu, R.S.McMillan, and J.J.Murray, *J. Electrochem. Soc.*, **140**, 922 (1993).
- ⁶⁸ R.T.K.Baker, P.S.Harris, R.B.Thomas and R.J.Waite, *J. Catal.* **30**, 86 (1973).
- ⁶⁹ J.N.Reimers and J.R.Dahn, *Phys. Rev. B* **47**, 2995 (1993).
- ⁷⁰ J.R.Dahn, PhD. Thesis (1982), University of British Columbia, Vancouver, Canada.
- ⁷¹ W.R.McKinnon, *Solid State Comm.* **40**, 343 (1981).
- ⁷² W.R.McKinnon, PhD. Thesis (1980), University of British Columbia, Vancouver, Canada.
- ⁷³ W.R.McKinnon, PhD. Thesis (1980), University of British Columbia, Vancouver, Canada, p 41.
- ⁷⁴ W.L.Bragg and E.J.Williams, *Proc. Roy. Soc. (London)* **A145**, 699 (1934).
- ⁷⁵ R.Griessen, *Phys. Rev B* **47**, 7575 (1983).
- ⁷⁶ W.H.Press, B.P.Flannery, S.A.Teukolsky and W.T.Vetterling, *Numerical Recipes (Fortran Version)*, Cambridge University Press, New York, 1990, p. 111.
- ⁷⁷ Y. Nishi et al., European Patent Application 89115940.2, August 29 (1989).
- ⁷⁸ J.R.Dahn, A.K.Sleigh, Hang Shi, B.M.Way, W.J.Weydanz, J.N.Reimers, Q.Zhong, and U.von Sacken, in G. Pistoia (ed), *Lithium Batteries - New Materials, Developments, and Perspectives*, Elsevier, North Holland, 1993, pp. 1-47.
- ⁷⁹ M.Morita, T.Hanada, H.Tsutsumi, Y.Matsuda and M.Kawaguchi, *J. Electrochem. Soc.* **139**, 1227 (1992).
- ⁸⁰ Y.Matsuda, M.Morita, T.Hanada and M.Kawaguchi, *J. Power Sources* **43**, 75 (1993).
- ⁸¹ W.J.Weydanz, B.M.Way, T.van Buuren and J.R.Dahn, *J. Electrochem. Soc.* **141**, 900 (1994).
- ⁸² A.M.Wilson and J.R.Dahn, *J. Electrochem. Soc.* **142**, 326 (1995).
- ⁸³ A.M.Wilson, J.N.Reimers, E.W.Fuller and J.R.Dahn **74**, 249 (1994).
- ⁸⁴ J.S.Xue, K.Myrtle, and J.R. Dahn, accepted by *J. Electrochem. Soc.*, April 1995.
- ⁸⁵ J.R.Dahn, T.Zheng, Y.Liu and J.S.Xue, submitted to *Science*, April 1995.
- ⁸⁶ T.Zheng, J.N.Reimers and J.R.Dahn, *Phys. Rev. B* **51**, 734 (1995).
- ⁸⁷ A.Mabuchi, K.Tokumitsu, H.Fujimoto and T.Kasuh, 7th International meeting on Lithium Batteries, May 15-20, (1994) Boston, Massachusetts, U.S.A., paper I-A-10, p207 of extended abstracts.
- ⁸⁸ K.Sato, M.Noguchi, A.Demachi, N.Oki and M.Endo, *Science* **264**, 556 (1994).

-
- ⁸⁹ S.Yata, H.Kinoshita, M.Komori, N.Ando, T.Kashiwamura, T.Harada, K.Tanaka and T.Yamabe, *Synthetic Metals* **62**, 153 (1994).
- ⁹⁰ T.Zheng, Y.Liu, E.W.Fuller, S.Tseng, U.von Sacken and J.R.Dahn, submitted to *J. Electrochem. Soc.*, January 1995.
- ⁹¹ T.Enoki, S.Miyajima, M.Sano and H.Inokuchi, *J. Mater. Res.* **5**, 435 (1990).
- ⁹² Y.Takahashi, J.Oishi, Y.Miki, M.Yoshimura, K.Shibahara and H.Sakamoto, 35th Battery Symposium in Japan, Nov 14-16 (1994), Nagoya, Japan, paper 2B05, extended abstracts, page 39.
- ⁹³ A.Omaru, H.Azuma, M.Aoki, A. Kita and Y.Nishi, paper #25, 182nd meeting to the electrochemical society, Toronto, Canada (1992), Extended Abstracts of the Battery Division, p 34.
- ⁹⁴ N.Sonobe, M.Ishikawa and T.Iwasaki, 35th Battery Symposium in Japan, Nov 14-16 (1994), Nagoya, Japan, paper 2B09, extended abstracts, page 47.
- ⁹⁵ Y.Liu, J.S.Xue, T.Zheng and J.R.Dahn, Submitted to *Carbon*, April 1995.
- ⁹⁶ M.Ishikawa, N.Sonobe, H.Chuman and T.Iwasaki, 35th Battery Symposium in Japan, Nov 14-16 (1994), Nagoya, Japan, paper 2B10, extended abstracts, page 49.
- ⁹⁷ D.L.Fecko, L.E.Jones and P.A.Thrower, *Carbon* **31**, 637 (1993).
- ⁹⁸ F.Saugnac, F.Teyssandier and A.Marchand, *Journal de Physique IV* **1**, C2-673 (1991).
- ⁹⁹ A.Derre, L.Filipozzi and F.Peron, *Journal de Physique IV* **3**, C3-673 (1993).
- ¹⁰⁰ B.M.Way, J.R.Dahn, T.Tiedje, K.Myrtle and M.Kasrai, *Phys. Rev. B* **46**, 1697 (1992).
- ¹⁰¹ Y.Bito, H.Murai, M.Hasegawa and S.Ito, U.S. Patent #5,229,226, July 20, 1993.
- ¹⁰² M.Fujimoto, N.Yoshinaga, K.Ueno, K.Moriwaki and K.Nishio, U.S. Patent #5,358,805, October 25, 1994.